T2R2 東京科学大学 リサーチリポジトリ
Science Tokyo Research Repository

論文 / 著書情報
Article / Book Information

題目(和文)	
Title(English)	Design method for high-rise base-isolated buildings with active control considering maximum response and maximum control force
著者(和文)	陳引力
Author(English)	Yinli Chen
出典(和文)	学位:博士(学術), 学位授与機関:東京工業大学, 報告番号:甲第11860号, 授与年月日:2022年3月26日, 学位の種別:課程博士, 審査員:佐藤 大樹,元結 正次郎,盛川 仁,大風 翼,古谷 寛
Citation(English)	Degree:Doctor (Academic), Conferring organization: Tokyo Institute of Technology, Report number:甲第11860号, Conferred date:2022/3/26, Degree Type:Course doctor, Examiner:,,,,
学位種別(和文)	博士論文
Type(English)	Doctoral Thesis

Powered by T2R2 (Science Tokyo Research Repository)

Tokyo Institute of Technology

Ph.D. Dissertation

Design method for high-rise base-isolated buildings with active control considering maximum response and maximum control force

Author:
Yinli Chen

Supervisor:
Assoc. Prof. Daiki Sato

Course of Urban Design and Built Environment
Department of Architecture and Building Engineering
School of Environment and Society

February 23, 2022

Abstract

The title of this dissertation is “Design method for high-rise base-isolated buildings with active control considering maximum response and maximum control force” and it consists of 6 chapters.

The combination of base-isolation and active structural control (active base-isolation) improves the the control performance by adjusting the natural period and damping ratio of the control system, and many researches show the effectiveness of active base-isolated buildings, there were still few applications of active base-isolated buildings. A significant reason for it could be considered as the control system designed in black-box approaches, causing a limited design outlook.

Chapter 1 *"Introduction"* explains the background of passive base-isolation, active base-isolation, shortcomings and limitations of a trial-and-error design method for control system. Moreover, Chapter 1 introduces the conventional design method for earthquake-resistant design and passive wind-resistant design, and the concept of equivalent model of active control system. Furthermore, Chapter 1 shows the research methodology to extend these passive design methods to active base-isolation.

Chapter 2 *"Linear earthquake-resistant design"* expresses the dependency of the maximum responses and control force on the design parameters of the control system using the equivalent model of the control system considering a linear base-isolated structures. Chapter 2 also presents a design method for determining the design parameters of the control system that satisfies the restrictions on maximum responses and control force without trial-and-error approaches and numerical simulations.

Chapter 3 *"Nonlinear earthquake-resistant design"* extends the estimation methods for maximum responses and control force and design presented at Chapter 2 to a nonlinear base-isolated structures. Equivalent linearization method is used to replace a nonlinear hysteretic damper with a linear spring and linear dash-pot.

Chapter 4 *"Wind-resistant design on along-wind direction"* proposes the estimation method for the mean displacement and mean control force, gust factor for displacement and control force to estimate the maximum displacement and maximum control force on along-wind direction. The gust-factor method is extended to active base-isolation using the proposed estimation method. Moreover, Chapter 4 also develops a design method for along-wind direction without trial-and-error approaches and numerical simulations.

Chapter 5 *"Wind-resistant design on across-wind direction"* proposes the estimation method for the standard deviation of displacement and control force, peak factor for displacement and control force to estimate the maximum displacement and maximum control force on across-wind direction. The peak-factor method is extended to active base-isolation using the proposed estimation method. Then, Chapter 4 also develops a design method for along-wind direction without trial-and-error approaches and numerical simulations.

Chapter 6 *"Switch of feedback gain for wind-resistant and earthquake-resistant"* shows the switch method of feedback gain.

Chapter 7 *"Conclusion"* shows the the conclusion and the future works of this dissertation.

This study proposed the methods for estimating the maximum responses and maximum control force of active base-isolated buildings subjecting to earthquake and wind disturbances. Moreover, this study devised the design methods for active base-isolated buildings considering both earthquake and wind disturbances that eliminates the trial-and-error approaches and numerical simulations. Thus, this study contributes the structural engineering in civil engineering, and it deserves Ph. D.

Acknowledgments

I would first like to thank my supervisor, associate professor **Daiki Sato**, who accepted me at my master's course and did not mind about my undergraduate major, making it possible for me to research structural engineering. Your insightful feedback advice, invaluable advice, and continuous support pushed me to sharpen my thinking and brought my work to a higher level. I am also grateful to Professor **Jinhua She**, who provides me professional advice on control engineering. I would like to thank Dr. **Kou Miyamoto** for his precious academic advice. Besides, Dr. **Kou Miyamoto** also helped me a lot to understand Japanese culture and adjust to life in Japan.

Special thanks to the **Japan Society for the Promotion of Science** (research fellow DC1) and **SOFTech** (JST Program on Open Innovation Platform with Enterprises, Research Institute, and Academia) for supporting my Ph.D. research. Special thanks to the **Rotary Yoneyama Memorial Foundation** for providing me the scholarship during my master's course, which enabled me to be more concentrated on my study. I especially thank Mr. **Yoshikazu Tanaka**, my counselor in Tsuzuki Rotary Club, and **Kenho Kusumi**, the chairman of RID2590 Yoneyama alumni association in 2018. They kindly spent their precious time even operating hours to help me not only get familiar with Rotary International but also help me to integrate into the Japanese culture.

I must express my very profound gratitude to my parents, without whom the accomplishment would not have been possible.

Last but not least, I would like to thank **Xu Zhang**, who spends most treasured time with me, and accompanied me through the difficult times during my Ph.D. career. Fortunately having you and making our own cozy memories. You complete me.

Thanks for all your encouragement!

February 23, 2022

List of Symbols

$\mathbf{A}$	System matrix	B	Width
$\mathbf{B_F}$	Input matrix for wind force	$\mathbf{B_g}$	Input matrix for ground acceleration
$\mathbf{B_h}$	Input matrix for hysteretic damper	$\mathbf{B_u}$	Input matrix for control force
c	Damping coefficient	$\mathbf{C}$	Damping matrix
$c_{cr,0}$	Critical damping coefficient for natural period of isolator	$\mathbf{C_d}$	Output matrix for displacement response
$C_{F,i}(t)$	Wind coefficient of ith story	C_g	Overturning moment coefficient
C'_g	Standard deviation of overturning moment coefficient	$c_{h,\mathrm{eq}}$	Equivalent damping coefficient of hysteretic damper
$\mathbf{C_s}$	Damping matrix of superstructure	c_v	Damping coefficient of viscous damper
c_{eq}	Equivalent damping coefficient of system	D	Depth
E	Input energy of earthquake	e	Estimation error
$\mathbf{E_F}$	Input matrix of wind force	E_H	Wind velocity profile factor
$\mathbf{E_u}$	Input matrix of control force	F_0	Restoring force of isolator
F_D	Along-wind force spectral factor	F_h	Restoring force of hysteretic damper
f_h	Force of hysteretic damper	F_v	Force of viscous damper
g	Ground acceleration	g_D	Peak factor for displacement
G_D	Gust factor for displacement	g_u	Peak factor for control force
G_u	Gust factor for control force	H	Height
h	Height of story	H_D	Transfer function of displacement
H_u	Transfer function of control force	I_H	Turbulence intensity at reference height
J	Standard LQR performance index	$\tilde{J}$	LQR performance index
k	Stiffness	$\mathbf{K}$	Stiffness matrix
K_{D}	Wind direction factor	k_h	Initial stiffness of hysteretic damper
$\mathbf{K_P}$	State-feedback gain	$\mathbf{K_{PD}}$	Feedback gain for displacement
$\mathbf{K_{PV}}$	Feedback gain for velocity	$k_{\mathrm{R}w}$	Conversion factor of return period
$\mathbf{K_s}$	Stiffness matrix of superstructure	L_H	Turbulence scale at reference height
m	Mass of structure	$\mathbf{M}$	Mass matrix
M_D	Generalized mass	M_{D1}	Eneralized mass (assuming $\beta = 1$)
N	Number of cases	$\mathbf{P}$	Solution of Riccati equation

p_{ij}	Entry of P	$\mathbf{Q}$	Standard LQR weighting matrix for displacement
$\tilde{\mathbf{Q}}$	LQR weighting matrix for displacement	q_1	Standard weighting entry
$\tilde{q}_1$	Weighting entry	q_2	Standard weighting entry
$\tilde{q}_2$	Weighting entry	q_H	Speed pressure of wind velocity
R	Standard LQR weighting matrix for control force	R_D	Resonance factor for along-wind vibration
S_A	Absolute-acceleration-response spectrum	S_C	Control-force spectrum
S_D	Displacement-response spectrum	S_D	Size effect factor
${}_pS_V$	Pseudo-velocity-response spectrum	S_V	Velocity-response spectrum
t	Time	T	Natural period
T_0	Natural period of isolator	T_s	Natural period of superstructure
u	Control force	U_0	Basic wind velocity
U_H	Wind velocity	v_D	Level crossing rate
W_a	Dissipated energy of actuator	W_h	Dissipated energy of hysteretic damper
W_v	Dissipated energy of viscous damper	$x(t)$	Displacement response
$\mathbf{X}(t)$	Displacement vector	$\ddot{x}_g$	Ground acceleration
x_{hy}	Yield displacement of hysteretic damper	$\mathbf{z}(t)$	State vector
α	Story-shear-force ratio	α'	Exponent of power law for wind speed profile
α_{hy}	Shear-force ratio of yield force of hysteretic damper	α_u	Shear-force ratio of control force
α_u	Shear-force ratio of control force (displacement component)	α_u	Shear-force ratio of control force (velocity component)
β	LQR design parameter	ΔD	Dissipated energy of hysteretic damper in one cycle
ΔW	Dissipated energy of viscous damper in one cycle	γ	Second stiffness rate of hysteretic damper
λ	Mode correction factor of general wind force	μ	Maximum plasticity rate
ω	Natural angular frequency	ω_s	Natural angular frequency of super structure
ϕ	Mode shape	ϕ_D	Mode shape correction factor
π	Ratio of the circumference of a circle to its diameter	ρ_a	Density of air
ρ_s	Density of superstructure	σ	Standard deviation
σ_D	Standard deviation of displacement	σ_u	Standard deviation of control force

τ	Exponent of power law for the first translational vibration mode	ζ	Damping ratio
ζ_s	Damping ratio of superstructure	ζ_v	Damping ratio of viscous damper
$\hat{\square}$	Response of equivalent linear model	$\bar{\square}$	Mean component of parameter
$\square_{\mathrm{ABS}}$	ABS method	$\square_{\mathrm{AIJ}}$	Parameter of AIJ
$\square_{\mathrm{eq}}$	Parameter of equivalent model	$\square_{\mathrm{est}}$	Estimation value
$\square_{\mathrm{lim}}$	Design limitation	$\square_{\mathrm{max}}$	Maximum value
$\square_{\mathrm{m}i}$	i-th mode	$\square_{\mathrm{sim}}$	Simulation results
$\square_{\mathrm{SRSS}}$	SRSS method	$\square_{\mathrm{tar}}$	Target value
$\square_{\mathrm{WTE}}$	Parameter of WTE		

Contents

CHAPTER 1

Introduction

1.1 Background of the Study

Base-isolation minimize damages of superstructures and makes possible for resuming operation after violent earthquakes [1.1]. Its effectiveness of base-isolation has been validated via theoretical analysis, experiment and disaster site survey [1.2]. Especially, the Great Hanshin earthquake in 1995 triggered a great demand for base-isolation, thus, its application increasing sharply after 1995 in Japan. In other areas, such as the USA, Asia, and Europe, the application of base-isolation has also received significant attention [1.1].

Base-isolated structures are popular for constructing hospitals, public buildings, and other essential facilities that sensitive to the absolute acceleration [1.2]. For example, some precision machine factories install base-isolation devices to suppress the absolute acceleration response. Moreover, the height of buildings tends to increase recently, especially in center of metropolises, and the base-isolation also applied to high-rise buildings to simultaneously improve land utilization and safety of the of the building [1.3].

base-isolation response by installing a relatively softer story under the superstructure to increase the natural period of the structure and dissipate input energy of earthquake disturbance at isolation story. However, a high-rise building usually has a long natural period, applying base-isolation to a high-rise building will further increasing the natural period of the structure. The wind load increases as the height of the building increases, thus, designing of high-rise buildings should consider both the influence of wind load and earthquake load. wind disturbance and earthquake disturbances have different characteristics. Earthquake inputs its disturbance by the ground acceleration and its short-period is dominant. The softer bearing of base-isolation is effectiveness for earthquake disturbance. On the other hand, different from earthquake, wind load acts directly on the superstructure and its long-period component is dominant. Moreover, the mean wind force may not induce large acceleration but excessive displacement of isolation layer, and it cannot be mitigated by just increasing the damping. The most effective way is to increase the stiffness of isolation system, but it affects the seismic performance. Thus, there is a trade-off on adjusting the stiffness of the structure between earthquake-resistant design and wind-resistant design.

There are some researches and experiments on passive base-isolation lock-type device to switch the stiffness of the isolation layer between earthquake-resistant design and wind-resistant design [1.4–1.9]. This study considers applying active control to base-isolation (active base-isolation) to address this trade-off problem. Active control calculates the appropriate control input by a using the vibration responses of the building observed by sensors, and generates the control input by active control devices. There are many method to construct an active control system, and the most applied method for active structural control is the feedback control. Feedback control determines the control input by the observed responses (i.e., displacement and velocity) multiplied by the feedback gain. The feedback adjusts both the natural period and damping ratio of the active control system to achieve the target control performance [1.10, 1.11]. Thus, an active base-isolated building can enlarges its natural period to avoid the dominant period of earthquake disturbance and shortens its the natural period to avoid the dominant period of wind disturbance only by switching the feedback gain to earthquake pattern and wind pattern. It uses sensors or observers to obtain the essential responses of the structure. The design of feedback gain mainly uses pole-placement method or linear-quadratic regulator (LQR) method [1.10]. The pole-placement method are usually used to design the feedback gain for a single-degree-of-freedom (single-DOF) model that achieves the target dynamic characteristics (natural period and damping ratio) [1.10]. On the other hand, the LQR method are widely used to design the feedback gain for a multi-DOFs model. Instead of selecting all of poles for each mode of control system, LQR method conveniently selects appropriate weights for response and control input, determines the feedback gain by minimizing the cost function of weighted responses and control force.

In the theoretical research, not only the conventional method based on LQR control (also called optimal control, optimal regulator, etc.), but also the research using $H\infty$ control has been conducted in order to consider the uncertainty of system identification [1.12]. Moreover, Loh et al. conducted an full-scale experiment using an active tendon, and confirmed the effectiveness of active control for suppressing a full-scale building [1.13]. Furthermore, the control technology, absolute vibration control, was devised to reduce the absolute acceleration of buildings by constructing the base-isolated building in absolute coordinate axis system, and the latest active base-isolated building using the absolute vibration control technology was constructed in Japan [1.14]. It was shown that the control performance was excellent when combined with the conventional base-isolation structure [1.15].

The total number of passive base-isolated buildings in Japan is now over 40 thousands [1.1]. Compare to the passive base-isolated buildings, even if the effectiveness of active base-isolation is proved theoretically and experimentally, the total number of it (even concluding semi-active control) in the world is only 4 [1.16] (see Table 1.1). The reasons for the very low number of implemented active base-isolated buildings could be considered as the following items:

(1) Cost

As have been mentioned before, active control needs sensors, computers, control devices to observer response, calculate control input, and act control force. All these devices and instruments requires high performance and high sensitiveness. Moreover, active control requires huge input energy to control a heavy building. Furthermore, after the construction, active control system also needs routine maintenance to confirm its status. All these parts require a lot of costs.

(2) Reliability

Construction of the control system requires system identification and calculation control force requires observed responses. If the system identification and sensor have error, the reliability may not be guaranteed. Moreover, because active control requires outside energy suppling for operating the control devices, the its behavior during power failure also can not be guaranteed.

(3) Lack of legal framework and social awareness

Because of few implemented active base-isolated buildings, the legal framework and the social awareness of active control is still not inadequate. Thus, it is difficult to identify the responsibility of each party.

(4) Limited design perspective

Typically, an active control system is design by a trial-and-error approach, because the dependency of the maximum responses and maximum control force on design parameters are not theoretically expressed. Moreover, the maximum displacement response and maximum control force of a control system are typically determined via numerical simulations. An active base-isolated building has a lot of design parameters, such as the natural period of the superstructure, damping of the superstructure, stiffness and damping of isolation layer, hysteretic damper. Thus, determining these parameters a trial-and-error approach is highly complicated due to the significant amount of guessing and testing, and the prolonged simulation time involved in the process.

Table 1.1
Constructed active base-isolated buildings

Name of building	Control strategy	Design method
Gymnasium, Yagami campus of Keio university (semi-active base-isolation, 2001) [1.16]	Feedback control	LQR
South Building, Mita campus of Keio university (semi-active base-isolation, 2005)	Feedback control	LQR
Obelisk, Yozemi Tower of Yoyogi Seminar Main School (semi-active base-isolation, 2008)	Feedback control	Bilinear optimal-control
Technical Research Institute Main Building of Obayashi corporation (active base-isolation, 2010)	Feedforward control & Feedback control	Absolute-vibration control & pole-placement

1.2 Previous studies

Conventional passive earthquake-resistant design

Seismic-resistant designs widely uses the response-spectrum method, which illustrates the relationship between the maximum responses and dynamics characteristics of SDOF structures, to design buildings [1.17]. Design manuals usually give response spectra of design earthquake waves, and base-isolated buildings can be assumed as SDOF structures because the stiffness of the isolation layer is much softer than the superstructure. Therefore, using the given response spectra, the parameters of a base-isolated building can be easily selected without trial-and-error approaches and numerical simulations that satisfy the design criteria.

Conventional passive wind-resistant design

Wind load contains the mean force generated by the mean velocity pressure. The mean displacement of a building subjected to wind load on along-wind direction can be easily estimated by the static balance using the mean wind force. The gust factor for displacement, a scalar, was also developed to estimate the maximum displacement on along-wind direction without numerical simulations [1.18].

On across-wind direction, as vortex-induced vibration does not contain the mean component, the peak-factor method is used to estimate the maximum displacement. The standard deviation of displacement is estimated by power spectral density of wind force multiplied by the transfer function of the model [1.18]. using the estimated standard deviation of displacement and proposed peak-factor, the maximum displacement on across-wind direction also can be estimated without numerical simulations.

Limitation of conventional passive design methods

The dependency of the dynamic characteristics of the control system on the controller is not theoretically expressed at present, passive design methods for earthquake-resistant design and can not be used for active control. Moreover, The control force for operating the control devices is very large as expected for structural control, thus, the estimating the maximum control force is also important. It is also necessary to develop a method for estimating maximum control force without numerical simulations.

Equivalent model

Fujii et al. performed research on a single degree-of-freedom (SDOF) semi-active structural control system, and theoretically clarified the influence of LQR weighting matrices on the dynamics characteristics of the control system [1.19]. Elumalai et al. in a study on the SDOF magnetic levitation system, presented an algebraic method for calculating the LQR weighting matrices [1.20]. Using the equivalent model of the control system presented by Fujii et al. and Elumalai et al., the dependency of the dynamics characteristics of a control system on the design parameters is theoretically expressed. However, the model used by Fujii et al. did not consider structural internal damping, limiting its applicability to active-base-isolated buildings, which usually contains high structural internal damping.

Moreover, these methods did not consider limitations with respect to the maximum required control force. The estimation of the required control force is important to select an appropriate actuator to perform active structural control.

However, the method proposed by Fujii et al. and Elumalai et al. did not consider nonlinearity of the isolation layer, causing it only suit for a linear model. Hysteretic dampers are used in most of base-isolated buildings [1.21, 1.22] because of theirs low cost, simple structure, long-term reliability, and easy implementation [1.23, 1.24]. To extend the response-spectrum method to active base-isolation, it is necessary to consider the nonlinearity of hysteretic dampers installed in isolation layers.

1.3 Objectives and content structure of this study

The objective of this study is to develop simple methods for estimating the maximum responses and maximum control force of a feedback control system subjected to earthquake disturbance and wind disturbance. The estimation methods need neither numerical simulations nor trail-and-error that simplifies the design procedure and provide a good perspective at the first stage of design to select the design parameters for both structure and controller. The highlights of the methods are shown below.

Earthquake-resistant design

This study constructs an equivalent linear method (a passive model with a linear spring and linear dash-pot) of an single-DOF active nonlinear model (a model with a controller and nonlinear hysteretic damper) . Using the equivalent linear method, the dynamic characteristics of the control system is theoretically expressed and the maximum responses of an active nonlinear model is easily estimated by response spectra. Moreover, a new spectrum, control-force spectrum, is proposed to estimate the maximum control force without numerical simulations. Furthermore, a control system design method subjected to wind disturbance for determining design parameters that satisfies design criteria is proposed.

Wind-resistant design

An multi-DOFs equivalent model of an active model is constructed. This study extends the gust-factor method and peak-factor method for displacement to active control on along-wind and across-wind directions, respectively, using the constructed equivalent model. Moreover, This study also devises gust factor and peak factor for control force too estimate the maximum control force with out numerical simulations. Furthermore, a control system design method subjected to earthquake disturbance for determining design parameters that satisfies design criteria is proposed.

The content structure of this study are given below.

Content structure of this study

Chapter 1 *"Introduction"* explains the background of passive base-isolation, active base-isolation, shortcomings and limitations of a trial-and-error design method for control system. Moreover, Chapter 1 introduces the conventional design method for earthquake-resistant design and passive wind-resistant design, and the concept of equivalent model of active control system. Furthermore, Chapter 1 shows the research methodology to extend these passive design methods to active base-isolation.

Chapter 2 *"Linear earthquake-resistant design"* expresses the dependency of the maximum responses and control force on the design parameters of the control system using the equivalent model of the control system considering a linear base-isolated structures. Chapter 2 also presents a design method for determining the design parameters of the control system that satisfies the restrictions on maximum responses and control force without trial-and-error approaches and numerical simulations.

Chapter 3 *"Nonlinear earthquake-resistant design"* extends the estimation methods for maximum responses and control force and design presented at Chapter 2 to a nonlinear base-isolated structures. Equivalent linearization method is used to replace a nonlinear hysteretic damper with a linear spring and linear dash-pot.

Chapter 4 *"Wind-resistant design on along-wind direction"* proposes the estimation method for the mean displacement and mean control force, gust factor for displacement and control force to estimate the maximum displacement and maximum control force on along-wind direction. The gust-factor method is extended to active base-isolation using the proposed estimation method. Moreover, Chapter 4 also develops a design method for along-wind direction without trial-and-error approaches and numerical simulations.

Chapter 5 *"Wind-resistant design on across-wind direction"* proposes the estimation method for the standard deviation of displacement and control force, peak factor for displacement and control force to estimate the maximum displacement and maximum control force on across-wind direction. The peak-factor method is extended to active base-isolation using the proposed estimation method. Then, Chapter 4 also develops a design method for along-wind direction without trial-and-error approaches and numerical simulations.

Chapter 6 *"Switch of feedback gain"* shows the switch procedure of feedback gain between earthquake-resistant pattern and wind-resistant pattern, and shows simulation results of the control system subjected to a different disturbance of a pattern considered at design.

Chapter 7 *"Conclusion"* shows the the conclusion and the future works of this dissertation.

This study proposed the methods for estimating the maximum responses and maximum control force of active base-isolated buildings subjecting to earthquake and wind disturbances. Moreover, this study devised the design methods for active base-isolated buildings considering both earthquake and wind disturbances that eliminates the trial-and-error approaches and numerical simulations.

References

[1.1] The Japan Society of Seismic Isolation, Recent trends in seismic isolation buildings [in Japanese], Tech. rep., The Japan Society of Seismic Isolation (2018).
URL `http://www.jssi.or.jp/menshin/doc/keizoku2.pdf`

[1.2] G. P. Warn, K. L. Ryan, A review of seismic isolation for buildings: Historical development and research needs, Buildings 2 (3) (2012) 300–325. `doi:10.3390/buildings2030300`.

[1.3] Y. Tanaka, N. Fukuwa, J. Tobita, M. Mori, Development and analysis of database for base-isolated buildings in Japan, AIJ Journal of Technology and Design 17 (35) (2011) 19–84. `doi:10.3130/aijt.17.79`.

[1.4] I. ISHIDE, A. NISHIMURA, M. YAMAMOTO, H. YONEDA, A. OGAWA, K. TAKAKU, 21188 development of an oil damper which has passive type lock mechanism for seismic isolation : Part1: Background of development and the mechanism, in: Summaries of technical papers of Annual Meeting, Vol. B-2, Architectural Institute of Japan, 2010, pp. 375–376.
URL `https://ci.nii.ac.jp/naid/110008123905/en/`

[1.5] S. FUTATSUGI, A. NISHIMURA, M. YAMAMOTO, H. YONEDA, 21189 development of an oil damper which has passive type lock mechanism for seismic isolation : Part2: Analytical study of a seismically isolated building with the developed oil damper, in: Summaries of technical papers of Annual Meeting, Vol. B-2, Architectural Institute of Japan, 2010, pp. 377–378.
URL `https://ci.nii.ac.jp/naid/110008123906/en/`

[1.6] A. NISHIMURA, M. YAMAMOTO, I. ISHIDE, S. FUTATUGI, R. YOSHIDA, 21214 development of an oil damper which has passive type lock mechanism for seismic isolation : Part3: The design outline of super high rise building with seismic isolation, in: Summaries of technical papers of annual meeting, Vol. B-2, Architectural Institute of Japan, 2013, pp. 427–428.
URL `https://ci.nii.ac.jp/naid/110009682580/en/`

[1.7] R. YOSHIDA, M. YAMAMOTO, A. NISHIMURA, S. FUTATUGI, I. ISHIDE, 21215 development of an oil damper which has passive type lock mechanism for seismic isolation : Part4: Dynamic analysis result, in: Summaries of technical papers of annual meeting, Vol. B-2, Architectural Institute of Japan, 2013, pp. 429–430.
URL `https://ci.nii.ac.jp/naid/110009682581/en/`

[1.8] M. AWANO, S. YOSHIDA, K. TAGA, M. TADA, 21292 development of wind-load resisting shear pins for a high rise mid-height seismic isolation building : (part 1)abstraction of a shear pin and seismic response analysis, in: Summaries of technical papers of Annual Meeting, Vol. B-2, Architectural Institute of Japan, 2011, pp. 583–584.
URL `https://ci.nii.ac.jp/naid/110009518905/en/`

[1.9] S. YOSHIDA, M. AWANO, S. MUKAIDE, A. TAKADA, K. TAGA, M. TADA, 21293 development of wind-load resisting shear pins for a high rise mid-height seismic isolation building : (part 2)performance evaluation test of a shear pin, in: Summaries of technical papers of Annual Meeting, Vol. B-2, Architectural Institute of Japan, 2011, pp. 585–586.
URL `https://ci.nii.ac.jp/naid/110009518906/en/`

[1.10] A. Preumont, A. Seto, Active control of structures, John Wiley & Sons, Inc., 2008.

[1.11] K. Miyamoto, D. Sato, J. She, A new performance index of lqr for combination of passive base isolation and active structural control, Engineering Structures 157 (2018) 280 – 299. `doi:10.1016/j.engstruct.2017.11.070`.

[1.12] N. MECHBAL, E. NOBREGA, Spatial H∞ Approach to Damage Tolerant Active Control, working paper or preprint (Jan. 2015).
URL `https://hal.archives-ouvertes.fr/hal-01102749`

[1.13] C.-H. Loh, P.-Y. Lin, N.-H. Chung, Experimental verification of building control using active bracing system, Earthquake Engineering & Structural Dynamics 28 (10) (1999) 1099–1119. `doi:https://doi.org/10.1002/(SICI)1096-9845(199910)28:10<1099::AID-EQE857>3.0.CO;2-\#`.

[1.14] O. YOSHIDA, M. KAGEYAMA, T. SANO, H. K. F. ENDO, T. WATANABE, M. YAMANAKA, Application of active base isolation system using absolute vibration control technology [in Japanese], TRANSACTIONS OF THE JAPAN SOCIETY OF MECHANICAL ENGINEERS Series C 78 (789) (2012) 1632–1643. `doi:10.1299/kikaic.78.1632`.

[1.15] Y. Ikeda, Active and semi-active vibration control of buildings in japan—practical applications and verification, Structural Control and Health Monitoring 16 (2009) 703 – 723. `doi:10.1002/stc.315`.

[1.16] The Japan Society of Seismic Isolation, Seismic isolation structure research report [in Japanese], Tech. rep., The Japan Society of Seismic Isolation (2020).

[1.17] Architectural Institute of Japan, Design Recommendations for Seismically Isolated Buildings, Architectural Institute of Japan, 2016.

[1.18] Architectural Institute of Japan, AIJ Recommendations for Loads on Buildings, Architectural Institute of Japan, 2015.

[1.19] T. Fujii, H. Fujitani, Y. Mukai, Performance evaluation of semi-active optimal control system by MR damper, Journal of Structural and Construction Engineering (Transactions of AIJ) 78 (689) (2013) 1237–1245. `doi:10.3130/aijs.78.1237`.

[1.20] V. K. Elumalai, R. G. Subramanian, A new algebraic LQR weight selection algorithm for tracking control of 2 DoF torsion system, Archives of Electrical Engineering 66 (1) (2017) 55 – 75. `doi:10.1515/aee-2017-0005`.

[1.21] M. Higashino, S. Okamoto, Response Control and Seismic Isolation of Buildings, Routledge, 2006. `doi:10.4324/9780203018866`.

[1.22] A. Salem Milani, M. Dicleli, Systematic development of a new hysteretic damper based on torsional yielding: part I—design and development, Earthquake Engineering & Structural Dynamics 45 (6) (2016) 845–867. `doi:https://doi.org/10.1002/eqe.2684`.

[1.23] X. D. Nguyen, L. Guizani, Analytical and numerical investigation of natural rubber bearings incorporating U-shaped dampers behaviour for seismic isolation, Engineering Structures 243 (2021) 112647. `doi:https://doi.org/`.

[1.24] D. R. Teruna, T. A. Majid, B. Budiono, Experimental study of hysteretic steel damper for energy dissipation capacity, Advances in Civil Engineering 2015 (631726). `doi:10.1155/2015/631726`.

CHAPTER 2

Linear earthquake-resistant design

2.1 Introduction

The combination of base-isolation and active control adjusts the dynamic characteristics that achieves high control performance, and many researches shows its efficiency [2.1–2.4]. Since the dependency of the maximum responses and maximum control force of a control system on design parameters was not theoretically expressed, the conventional design process for a control system mainly uses a trial-and-error approach [2.5, 2.6]. A base-isolated building with active control has many design parameters, such as isolated period, isolated damping, and controller, etc. Moreover, design limitation for a base-isolated building with active control also contains the restrictions on both responses (i.e., displacement, velocity and absolute acceleration) and control force. Thus, selecting parameters of a base-isolated building with active control that satisfies all design limitations usually requires much guess, testing and numerical simulations, causing a limited design outlook [2.5, 2.6].

In conventional passive earthquake-resistant design, the response spectra, expressing the dependency of the maximum response to the natural period and damping ratio for a passive model, are widely used in structural design to select the desired dynamic characteristics [2.7]. If the concept of response spectra can be broadened to active structural control, the selection of the natural period, passive damper and controller that satisfies the design limitation, will be simplified. To realize this idea, we consider the equivalent model to express the dynamic characteristics of an active model (a model with active control device).

Fujii et al. performed research on the single degree-of-freedom (SDOF) semi-active structural control system, and theoretically clarified the influence of the LQR weighting matrices on the dynamic characteristics of the control system [2.8]. However, the model used by Fujii et al. did not consider structural internal damping, limiting its applicability and made it incompatible with the model of the PBI structure combined with ASC. Elumalai et al. in a study on the SDOF magnetic levitation system, presented an algebraic method for calculating the LQR weighting matrices [2.9]. This achieved the equivalent natural angular frequency and equivalent damping ratio, but Elumalai et al. did not consider limitations with respect to the maximum required control force, making it inadequate for application to the ASC. Kohiyama et al. developed a method to estimate the maximum response and control force for feedback control systems [2.10, 2.11]. However, the methods proposed by Kohiyama et al. need to construct the modal expression for the dynamics of the system and did not present the spectrum of the maximum control force, making it difficult applying in design.

This section constructed the equivalent model of the active model to theoretically express the dependency of the dynamic characteristics on the design parameters. Using the natural period and damping ratio of the equivalent model , the maximum responses are easily estimated by the conventional response spectra. This section also devises a new control-force spectrum, theoretically expressing the dependency of the maximum control force to the natural period and passive damper, using only the conventional response spectra and no additional numerical simulations. This section proposes a control-system design method for an SDOF model using the control-force spectrum. The design method calculates the range of the combination of the natural period, passive damper, and maximum control force that satisfies the restrictions. This method requires neither trial-and-error nor numerical simulations. So, it simplifies the design procedure. Since the isolation story is usually much softer than the superstructure, base-isolated buildings can be considered as SDOF models [2.7]. Therefore, this method can be used to design a base-isolated building with active control. Finally, a design example for a base-isolated building with active control is used to validate the efficacy of the design methodology.

2.2 Earthquake wave and mathematic model

2.2.1 Earthquake waves for simulation

This Chapter uses 4 earthquake waves, Taft NS, El Centro 1940 NS, JMA Kobe NS, and Code Hachinohe, to carry out numerical simulations. The earthquake waves used in this section are standardized to 1.5 times of Level II of Japan earthquake resistant design standard. The peak ground velocity (PGV) of Taft NS, El Centro 1940 NS, and JMA Kobe NSare standardized to 0.75 m/s (1.5 times of Level II of Japan earthquake resistant design standard). Moreover, Code Hachinoheis a code earthquake wave, which was generated from the recorded earthquake waves, the 1995 JMA Kobe NS wave, to met the code response spectrum presented by the Japan seismic-resistant design standard. The pseudo-velocity response spectrum, ${}_pS_V$, of Code Hachinoheis 1.2 m/s (1.5 times of Level II of Japan earthquake resistant design standard [2.12]) for a structure with a damping ratio of 5% after a corner period of 0.64 s (Fig. 2.4 (b)).

Figs. 2.1~2.4 show the waves and pseudo-velocity response spectrum of Taft NS, El Centro 1940 NS, JMA Kobe NS, and Code Hachinohe. Table 2.1 shows the peak ground acceleration (PGA) and PGV of Taft NS, El Centro 1940 NS, JMA Kobe NS, and Code Hachinohe.

Table 2.1
PGA and PGV of Taft NS, El Centro 1940 NS, JMA Kobe NS, and Code Hachinohe waves

Wave	PGA [m/s^2]	PGV [m/s]
Taft NS	6.27	0.75
El Centro 1940 NS	6.74	0.75
JMA Kobe NS	6.72	0.75
Code Hachinohe	5.99	0.66

2.2.2 Mathematic model

In this chapter, we use a base-isolated building (Fig. 2.5). The superstructure of the building is assumed to be a rigid body, because the stiffness of the isolation layer is usually smaller than that of the superstructure [2.7]. Thus, in this study, we describe a base-isolated building as an SDOF model (active model, Fig. 2.6).

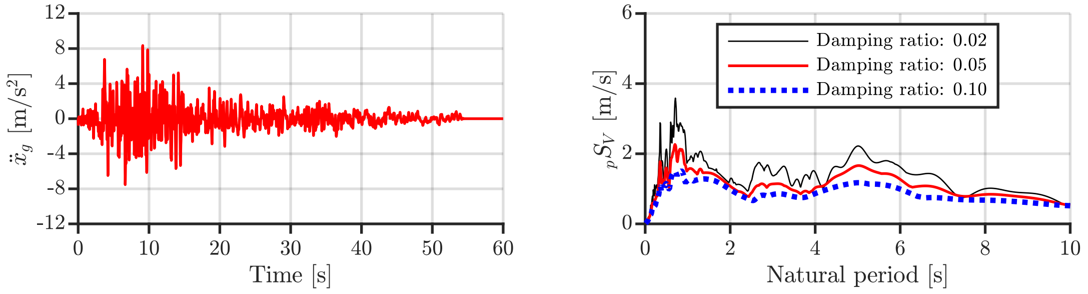

(a) accelerogram **(b)** pseudo-velocity response spectrum

Figure 2.1: Taft NS wave

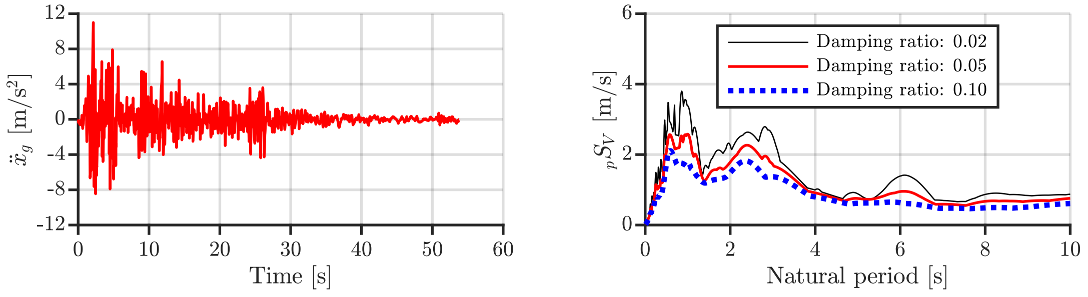

(a) accelerogram **(b)** pseudo-velocity response spectrum

Figure 2.2: El Centro 1940 NS wave

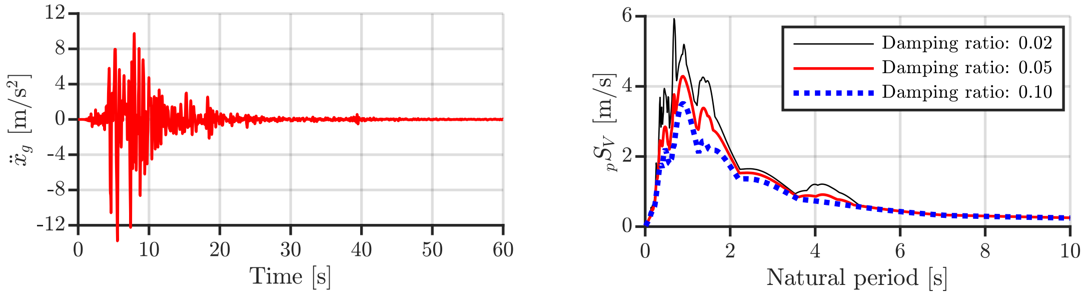

(a) accelerogram **(b)** pseudo-velocity response spectrum

Figure 2.3: JMA Kobe NS wave

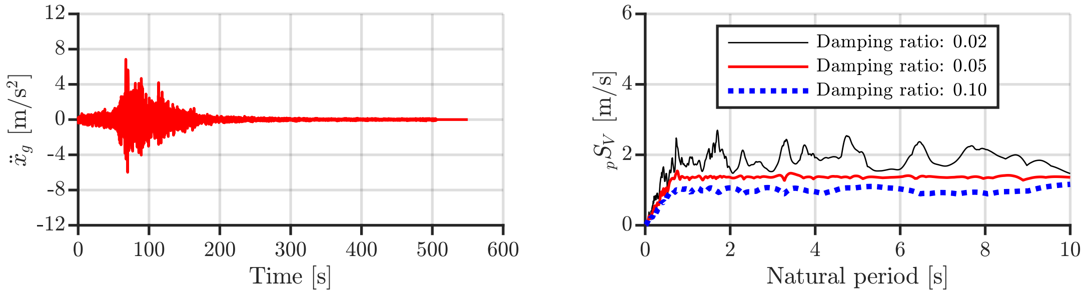

(a) accelerogram **(b)** pseudo-velocity response spectrum

Figure 2.4: Code Hachinohe wave

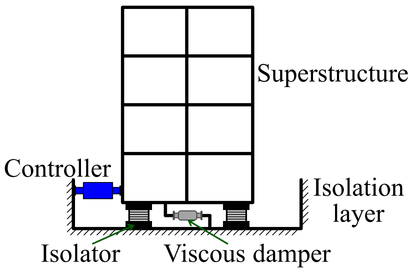

Figure 2.5: base-isolated building

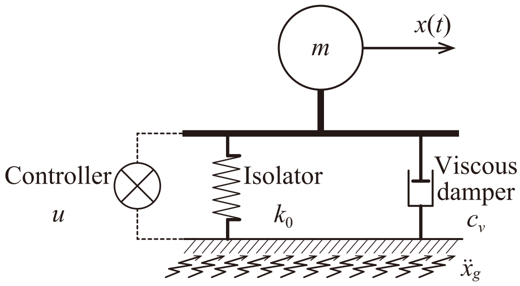

Figure 2.6: mathematic model

The isolation layer of the model contains a linear isolator, linear viscous dampers, and an actuator. The restoring force of the isolator F_0 is proportional to the displacement (Fig. 2.7 (a)); the force of the viscous damper F_v is proportional to the velocity (Fig. 2.7 (b)).

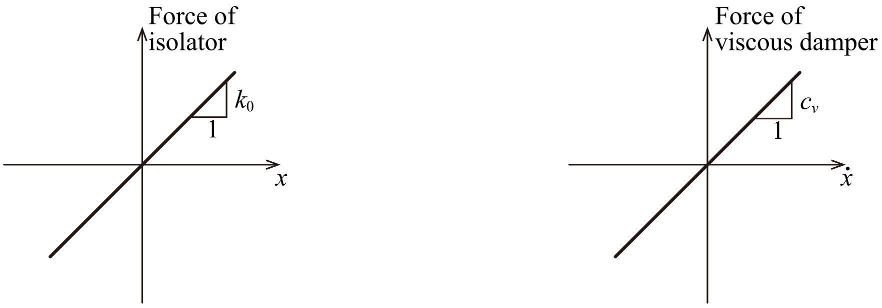

(a) Force of isolator **(b)** Force of viscous damper

Figure 2.7: Force of isolator and viscous damper

The dynamics of the active model are described by the following equation:

$$m\ddot{x}(t) + c_v\dot{x}(t) + k_0x(t) = -m\ddot{x}_g(t) - u(t), \tag{2.1}$$

where m is the mass; c_v is the damping-coefficient of the viscous damper; k_0 is the stiffness-coefficient of the isolator; $x(t)$, $\dot{x}(t)$, and $\ddot{x}(t)$ are the response displacement, response velocity, and response acceleration, respectively; $\ddot{x}_g(t)$ is the ground acceleration; $u(t)$ is control force. k_0 and c_v are defined by

$$k_0 = m\omega_0^2 = m\frac{4\pi^2}{T_0^2} \text{ and} \tag{2.2}$$

$$c_v = 2\zeta_v\sqrt{mk_0}, \tag{2.3}$$

where ω_0 is the natural angular frequency of the structure; T_0 is the natural period of the isolator; ζ_v is the damping ratio of the viscous damper. The state-space representation of

(2.1) is

$$\dot{\mathbf{z}}(t) = \mathbf{A}\mathbf{z}(t) + \mathbf{B_g} - m\ddot{x}_g - \mathbf{B_u}u(t), \tag{2.4}$$

where $\mathbf{z}(t)$ is a state vector; $\mathbf{A}$ is the system matrix; $\mathbf{B_u}$ is the input matrix for $u(t)$; $\mathbf{B_g}$ is the input matrix for $\ddot{x}_g(t)$, defined by

$$\mathbf{z}(t) = \begin{bmatrix} x(t) & \dot{x}(t) \end{bmatrix}^{\mathrm{T}}, \tag{2.5a}$$

$$\mathbf{A} = \begin{bmatrix} 0 & 1 \\ -\dfrac{k_0}{m} & -\dfrac{c_v}{m} \end{bmatrix}, \text{ and} \tag{2.5b}$$

$$\mathbf{B_u} = \begin{bmatrix} 0 & \dfrac{1}{m} \end{bmatrix}^{\mathrm{T}}. \tag{2.5c}$$

$$\mathbf{B_g} = \begin{bmatrix} 0 & -1 \end{bmatrix}^{\mathrm{T}}. \tag{2.5d}$$

Fig. 2.8 shows the block-diagram of the control system used in this study.

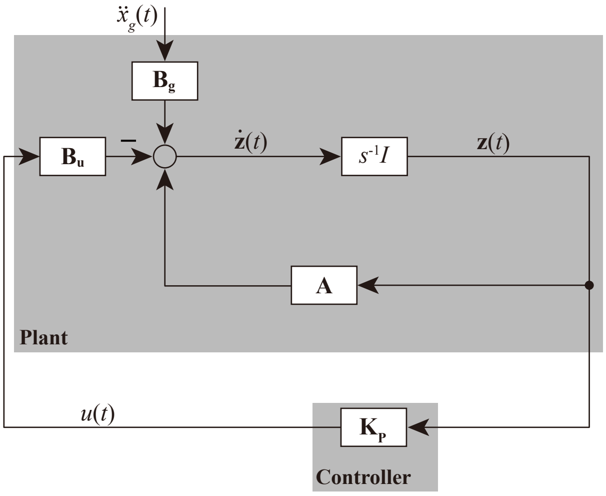

Figure 2.8: Block diagram of control system (linear earthquake-resistant design)

Feedback control law

$$u(t) = \mathbf{K_P}\mathbf{z}(t) \tag{2.6}$$

is used, where $\mathbf{K_P}$ is the state-feedback gain.

2.3 Equivalent model of active model

In this study, the equivalent model is defined as a model with a linear spring and dash-pot, and the responses of the equivalent model are the same as those of the active model (a model with ASC device) [Fig. 2.9, $x_{\mathrm{eq}}(t) = x(t)$].

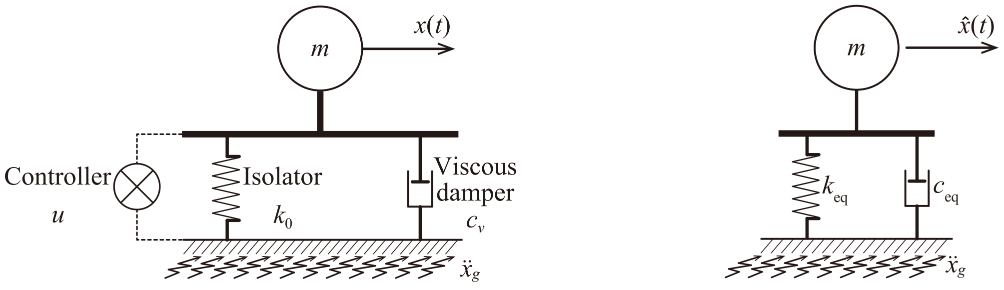

(a) Active model **(b)** Equivalent model

Figure 2.9: Active model and equivalent model ($\hat{x}(t) = x(t)$)

This section introduces the method for constructing an equivalent model of an active model to theoretically express the relationship between the vibration characteristics (natural period and damping ratio) of an active model and its design parameters.

2.3.1 Construction of equivalent model of active model

Representing (2.6) yields

$$u(t) = \mathbf{K}_{\mathbf{P}}\mathbf{z}(t) \begin{bmatrix} K_{PD} & K_{PV} \end{bmatrix} \begin{bmatrix} x(t) \\ \dot{x}(t) \end{bmatrix} = K_{PD}x(t) + K_{PV}\dot{x}(t), \tag{2.7}$$

where K_{PD} and K_{PV} are the feedback gain for displacement and velocity, respectively.

Substituting (2.7) into (2.1) yields

$$m\ddot{x}(t) + c_v\dot{x}(t) + k_0x(t) = -m\ddot{x}_g - K_{PD}x(t) - K_{PV}\dot{x}(t). \tag{2.8}$$

Representing (2.8) yields

$$m\ddot{x}(t) + c_{\mathrm{eq}}\dot{x}(t) + k_{\mathrm{eq}}x(t) = -m\ddot{x}_g, \tag{2.9}$$

where k_{eq} and c_{eq} are the equivalent stiffness and the equivalent damping coefficient (Fig.

2.9):

$$k_{\mathrm{eq}} = k_0 + K_{PD} \text{ and} \tag{2.10a}$$

$$c_{\mathrm{eq}} = c_v + K_{PV}. \tag{2.10b}$$

Thus, the equivalent natural angular frequency, equivalent natural period, and equivalent damping ratio (ω_{eq}, T_{eq}, and ζ_{eq}) are obviously defined as the following equation using the equivalent stiffness and equivalent damping coefficient (k_{eq} and c_{eq}):

$$\omega_{\mathrm{eq}} = \sqrt{\frac{k_{\mathrm{eq}}}{m}}, \tag{2.11a}$$

$$T_{\mathrm{eq}} = \frac{2\pi}{\omega_{\mathrm{eq}}}, \text{ and} \tag{2.11b}$$

$$\zeta_{\mathrm{eq}} = \frac{c_{\mathrm{eq}}}{2m\omega_{\mathrm{eq}}}. \tag{2.11c}$$

Using the equivalent natural period, and equivalent damping ratio (T_{eq} and ζ_{eq}), the maximum responses (displacement, velocity, and absolute acceleration) of the control system can be estimated by the conventional response spectra.

Moreover, solving (2.10) and (2.11) yield the presented calculation formula for determining the feedback gain (K_{PD} and K_{PV}) that achieving the target equivalent natural period, and equivalent damping ratio ($T_{\mathrm{eq,tar}}$ and $\zeta_{\mathrm{eq,tar}}$):

$$K_{PD} = k_{\mathrm{eq,tar}} - k_0 = m(\omega_{\mathrm{eq,tar}}^2 - \omega_0^2) = 2\pi m\left(\frac{1}{T_{\mathrm{eq,tar}}^2} - \frac{1}{T_0^2}\right) \text{ and} \tag{2.12a}$$

$$K_{PV} = c_{\mathrm{eq,tar}} - c_v = 2m(\omega_{\mathrm{eq,tar}}\zeta_{\mathrm{eq,tar}} - \omega_0\zeta_0) = 4\pi m\left(\frac{\zeta_{\mathrm{eq,tar}}}{T_{\mathrm{eq,tar}}} - \frac{\zeta_v}{T_0}\right). \tag{2.12b}$$

In addition, if the feedback gain, K_P, is designed by linear-quadratic regulator (LQR) method, the presented calculation formula for determining the LQR weighting matrices are shown at Appendix 2A.

2.3.2 Numerical verification

This section uses Taft NS, El Centro 1940 NS, JMA Kobe NS, and Code Hachinohe waves (Figs. 2.1~2.4) to verify the validity of the presented equivalent model of the active model.

The natural period of the isolator, T_0, and damping ratio of the viscous damper, ζ_v, are 3 s and 0.01, respectively.

Fig. 2.10 shows the comparison between the response spectra of Taft NS wave and the maximum response of the equivalent calculated from numerical simulation results. Figs. 2.11~2.13 show that for El Centro 1940 NS, JMA Kobe NS, and Code Hachinohe waves, respectively. From Figs. 2.10~2.13, it can be seen that the maximum responses of the equivalent model matches well to the response spectra. Therefore, the accuracy of the equivalent model is confirmed.

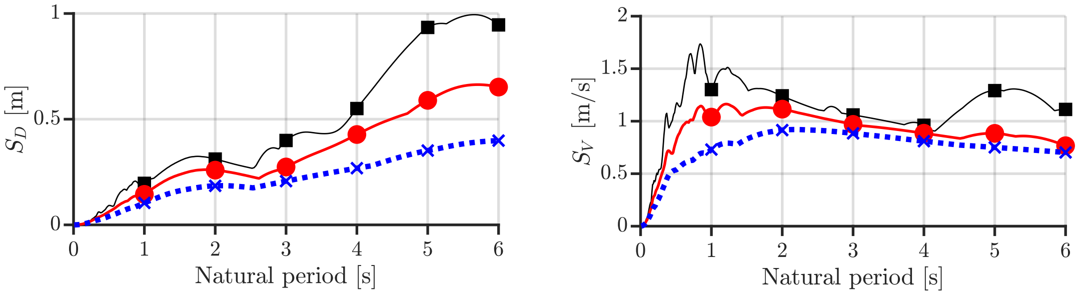

(a) Displacement response spectrum

(b) Velocity response spectrum

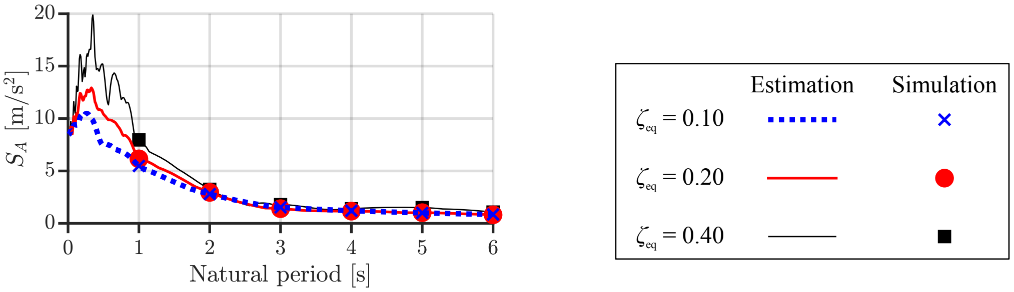

(c) absolute acceleration response spectrum

Figure 2.10: Response spectra of Taft NS

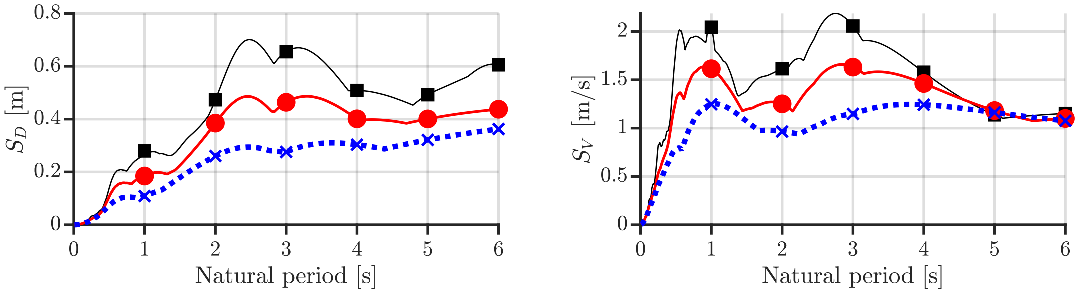

(a) Displacement response spectrum

(b) Velocity response spectrum

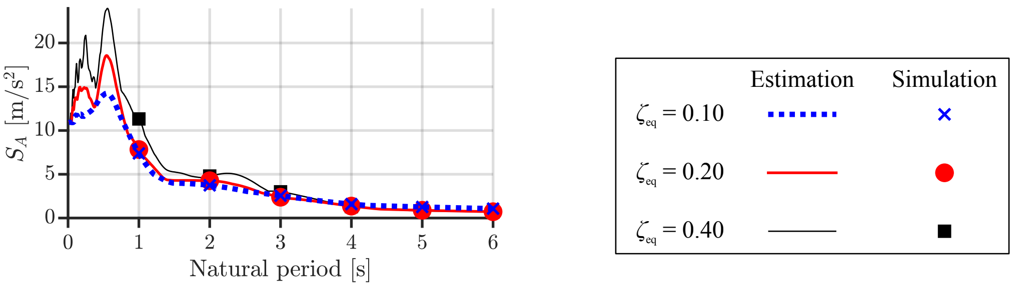

(c) absolute acceleration response spectrum

Figure 2.11: Response spectra of El Centro 1940 NS

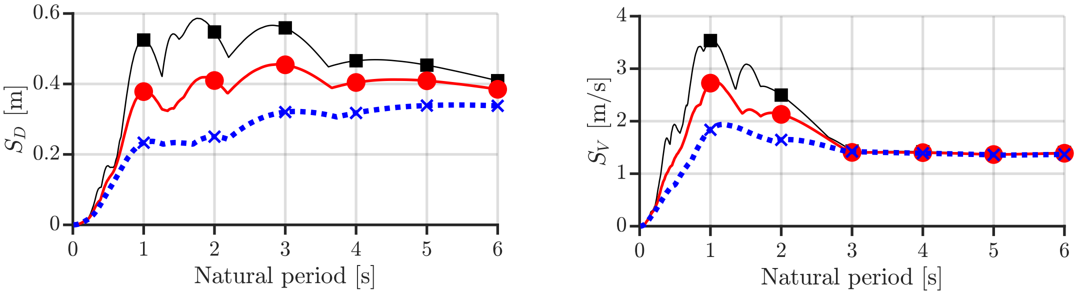

(a) Displacement response spectrum **(b)** Velocity response spectrum

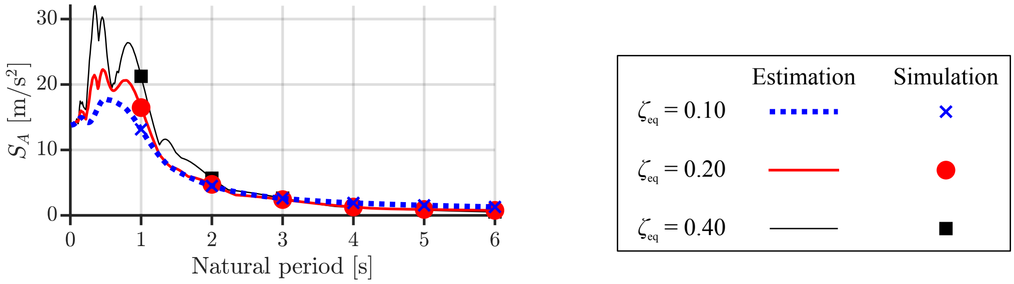

(c) absolute acceleration response spectrum

Figure 2.12: Response spectra of JMA Kobe NS

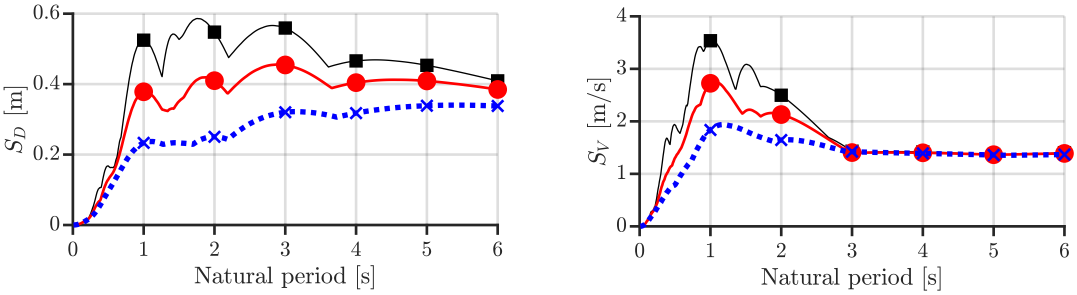

(a) Displacement response spectrum **(b)** Velocity response spectrum

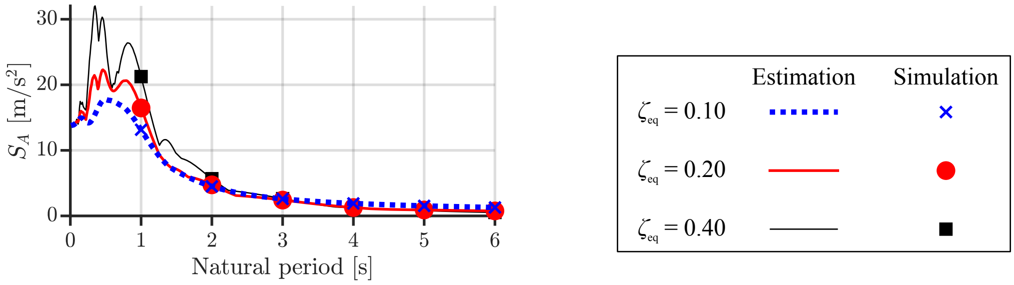

(c) absolute acceleration response spectrum

Figure 2.13: Response spectra of Code Hachinohe

2.4 Control-force spectrum

This section devises the control-force spectrum for an ASC model, which expresses the dependency of the maximum control force on the all parameters for designing the control system. This section also uses the numerical examples to check the accuracy of the proposed control-force spectrum.

2.4.1 Derivation of the control-force spectrum

Substituting (2.12) in the control law, (2.6), the control force can be estimated by the following equation:

$$u(t) = (k_{\mathrm{eq}} - k_0)x(t) + (c_{\mathrm{eq}} - c_v)\dot{x}(t). \tag{2.13}$$

Thus, the maximum control force, $u_{\max}$, is

$$u_{\max} = \max\left\{\left|(k_{\mathrm{eq}} - k_0)x(t) + (c_{\mathrm{eq}} - c_v)\dot{x}(t)\right|\right\}. \tag{2.14}$$

Since the phase of displacement response is usually unequal to that of velocity response, the maximum displacement response and velocity response do not appear simultaneously in most cases. Therefore,

$$u_{\max} \leq \left|k_{\mathrm{eq}} - k_0\right| \max\left\{|x(t)|\right\} + \left|c_{\mathrm{eq}} - c_v\right| \max\left\{|\dot{x}(t)|\right\}. \tag{2.15}$$

From the response spectra of the earthquake, the maximum responses are estimated without numerical simulations:

$$\max\left\{|x(t)|\right\} = S_D(T_{\mathrm{eq}}, \zeta_{\mathrm{eq}}) \text{ and} \tag{2.16a}$$

$$\max\left\{|\dot{x}(t)|\right\} = S_V(T_{\mathrm{eq}}, \zeta_{\mathrm{eq}}), \tag{2.16b}$$

where $S_D(T_{\mathrm{eq}}, \zeta_{\mathrm{eq}})$ and $S_V(T_{\mathrm{eq}}, \zeta_{\mathrm{eq}})$ are the maximum displacement response and the maximum velocity response refer to the displacement response spectrum and the velocity response spectrum of the earthquake, respectively.

Substituting (2.16) into (2.15) yields

$$u_{\max} \le \left|k_{\text{eq}} - k_0\right| S_D(T_{\text{eq}}, \zeta_{\text{eq}}) + \left|c_{\text{eq}} - c_v\right| S_V(T_{\text{eq}}, \zeta_{\text{eq}}). \tag{2.17}$$

The maximum control force, $u_{\max}$, divided by the weight of the structure, mg, yields the maximum shear-force coefficient of the maximum control, $\alpha_{u,\max}$:

$$\alpha_{u,\max} = \frac{u_{\max}}{mg} \le \alpha_{uD,\max} + \alpha_{uV,\max}\,, \tag{2.18}$$

where

$$\alpha_{uD,\max} = \frac{\left|k_{\text{eq}} - k_0\right|}{mg} S_D(T_{\text{eq}}, \zeta_{\text{eq}}) \text{ and} \tag{2.19a}$$

$$\alpha_{uV,\max} = \frac{\left|c_{\text{eq}} - c_v\right|}{mg} S_V(T_{\text{eq}}, \zeta_{\text{eq}}). \tag{2.19b}$$

From (2.18), the shear-force coefficient of the maximum control force, $\alpha_{u,\max}$, contains both the displacement component, S_D, and the velocity component, S_V. Since the maximum displacement and velocity usually do not appear at the same time, this study uses the square root of the sum of squares (SRSS) method [2.13] to estimate the maximum shear-force coefficient of the control force and defines the following estimation equation as the control-force spectrum, S_C:

$$S_C(T_0, \zeta_v, T_{\text{eq}}, \zeta_{\text{eq}}) := \sqrt{\alpha^2_{uD,\max} + \alpha^2_{uV,\max}}. \tag{2.20}$$

The control-force spectrum, S_C, estimates the maximum control force only using the response spectra of the equivalent model and does not require additional numerical simulations, and it is a function of the natural period of the structure, T_0, the damping ratio of the structure, ζ_v, the equivalent natural period, T_{eq}, and the equivalent damping ratio, ζ_{eq}.

In addition, the comparison of the control-force spectrum between SRSS method and absolute sum (ABS) method is shown at Appendix 4B.

2.4.2 Numerical verification

Figs. 2.14~2.17 show control-force prediction spectra for Taft NS, El Centro 1940 NS, JMA Kobe NS, and Code Hachinohe waves with different damping ratios (0.01 and 0.05).

From Figs. 2.14~2.17, the following results are obtained.

1. The maximum control force decreases as the damping of the viscous damper, ζ_0.

2. The maximum control force decreases as the equivalent damping ratio, ζ_{eq}, increases if $T_{\mathrm{eq}} < 1$ s.

3. The maximum control force increases as the equivalent damping ratio, ζ_{eq}, increases if $T_s = T_{\mathrm{eq}}$.

4. The maximum control force increases as the equivalent natural period, T_{eq}, increases if $T_{\mathrm{eq}} > 6$ s only for the case of Art Hachinohe.

The detailed analysis of the above results are given at Appendix C.

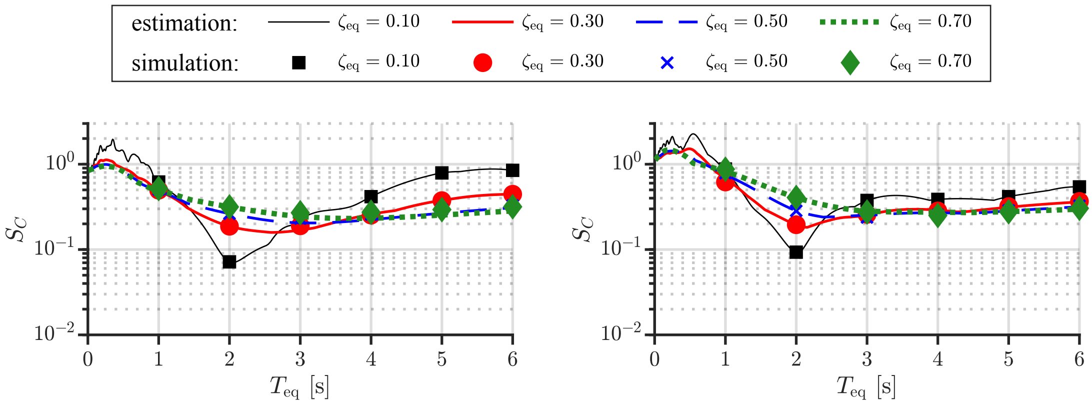

(a) Taft NS

(b) El Centro 1940 NS

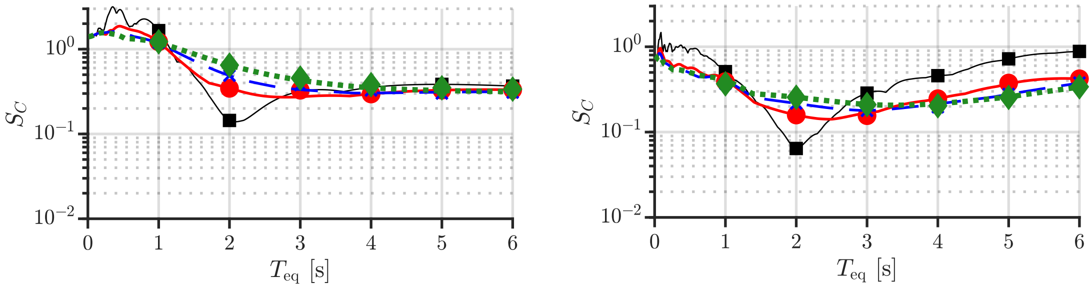

(c) JMA Kobe NS

(d) Code Hachinohe

Figure 2.14: Control-force spectra ($T_0 = 2$ s and $\zeta_v = 0.01$)

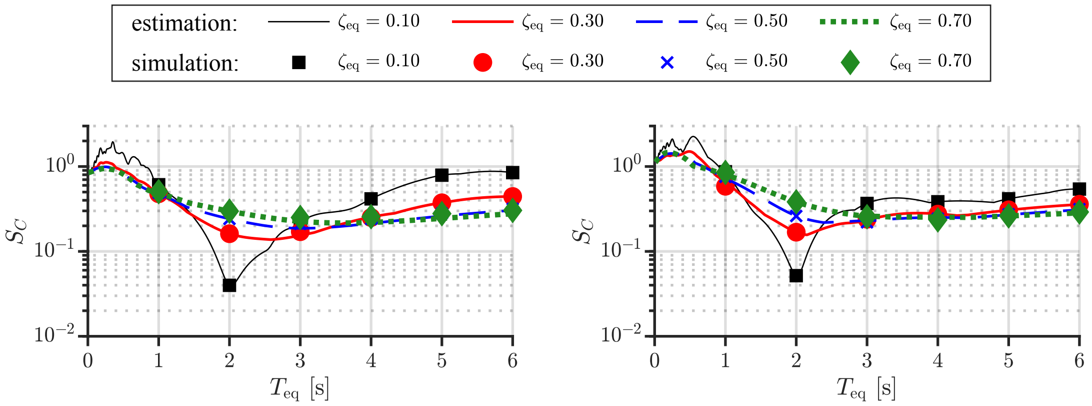

(a) Taft NS

(b) El Centro 1940 NS

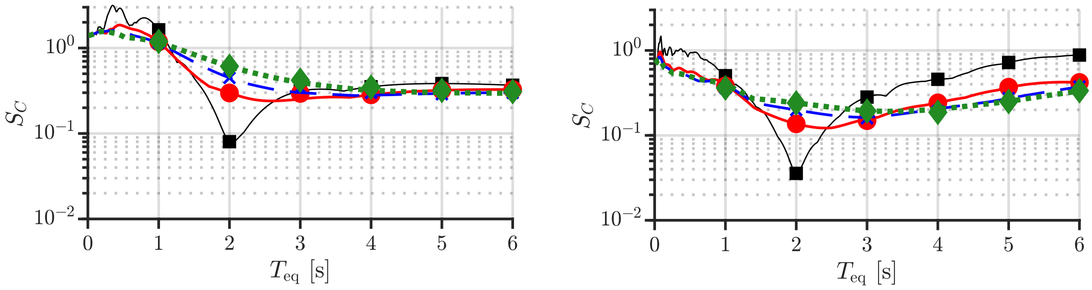

(c) JMA Kobe NS

(d) Code Hachinohe

Figure 2.15: Control-force spectra ($T_0 = 2$ s and $\zeta_v = 0.05$)

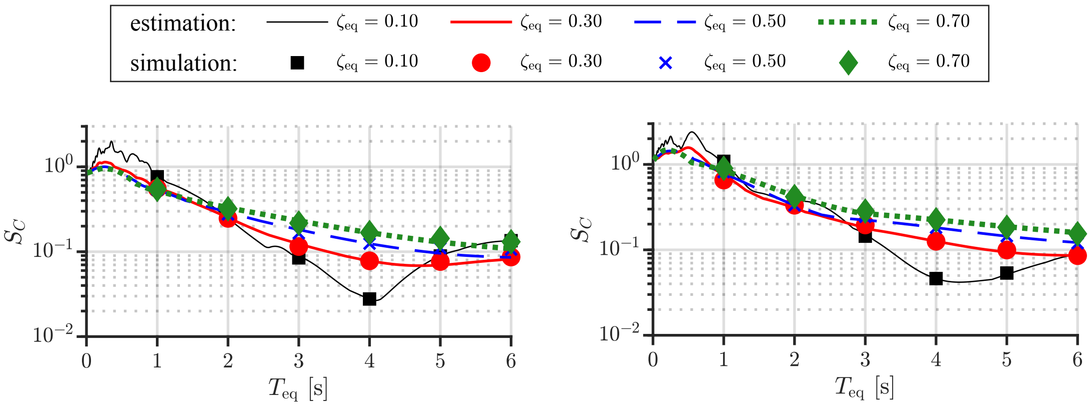

(a) Taft NS **(b)** El Centro 1940 NS

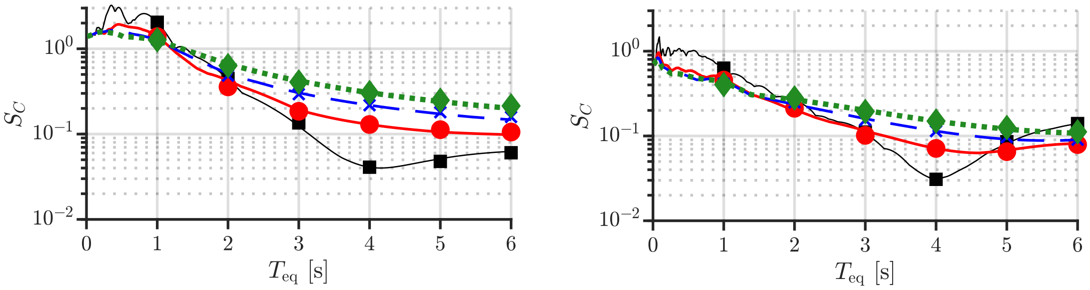

(c) JMA Kobe NS **(d)** Code Hachinohe

Figure 2.16: Control-force spectra (T_0 = 4 s and ζ_v = 0.01)

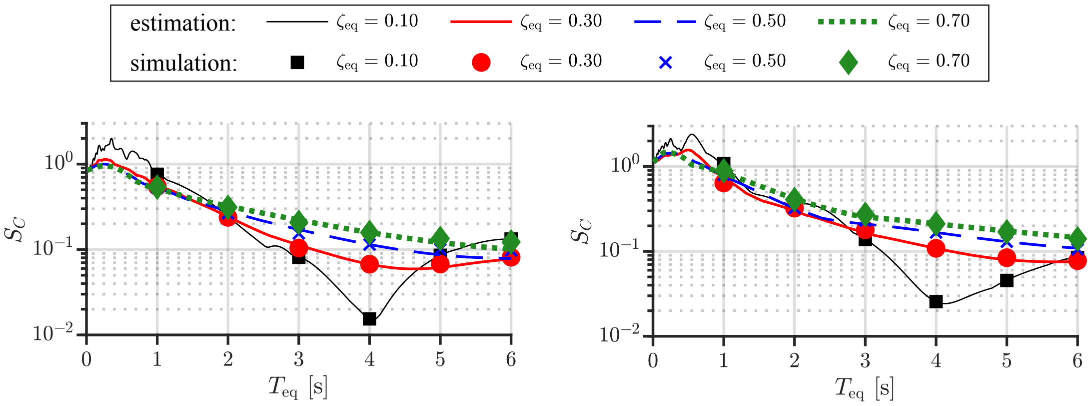

(a) Taft NS **(b)** El Centro 1940 NS

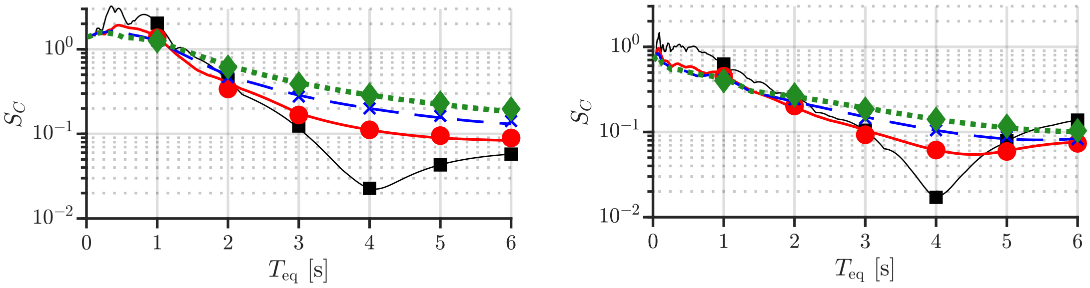

(c) JMA Kobe NS **(d)** Code Hachinohe

Figure 2.17: Control-force spectra (T_0 = 4 s and ζ_v = 0.05)

2.5 Design method

This section devises a design method for PBI structures with ASC for determining the damping ratio and natural period of the structure, and maximum control force that satisfies these restrictions using the response spectra and control-force spectrum. This section also uses a design example to confirm the accuracy of the design method.

2.5.1 Design algorithm

Step 1. Specifies the design conditions:

design earthquake wave,

mass of the structure (m),

restrictions of the maximum responses (displacement, x_{lim}, velocity, $\dot{x}_{\mathrm{lim}}$, and absolute acceleration, $\{\ddot{x}+\ddot{x}_g\}_{\mathrm{lim}}$),

restrictions of natural period and damping ratio of structure ($T_{s,\mathrm{lim}}$ and $\zeta_{s,\mathrm{lim}}$), and

restriction of shear-force coefficient of control force ($\alpha_{u,\mathrm{lim}}$).

Step 2. Uses the response spectra of the design earthquake wave to select the target equivalent model (equivalent natural period, $T_{\mathrm{eq,tar}}$, and equivalent damping ratio, $\zeta_{\mathrm{eq,tar}}$) that satisfies the limitations on the maximum responses set at Step 1.

Step 3. Uses the control force prediction spectrum estimating the maximum control force of the equivalent model selected at Step 2. If all design limitations ($T_{0,\mathrm{lim}}$, $\zeta_{v,\mathrm{lim}}$, and $\alpha_{u,\mathrm{lim}}$) are satisfied, specifies appropriate values for T_0 and ζ_v, then go to the next step. If not, go back to Step 2 and select another equivalent model.

Step 4. Substituting the target equivalent natural period, $T_{\mathrm{eq,tar}}$, target equivalent damping ratio, $\zeta_{\mathrm{eq,tar}}$, natural period of isolator, T_0, and damping ratio of viscous damper, ζ_v, into (2.12) to calculate the feedback gain, $\mathbf{K_P}$.

2.5.2 Design example

Step 1. Design earthquake wave:

Code Hachinohe wave (Fig. 2.4).

This sections only shows the design procedure for using the code response spectrum [2.7]. Selecting of the design wave is important in order to consider the influence of response spectrum and phase component. The additional analysis of the influence of the phase component is shown at Appendix 2D.

Mass of the structure:

$m = 1$ kg.

Restrictions of the maximum response:

$x_{\text{lim}} = 60$ cm, $\dot{x}_{\text{lim}} = 80$ cm/s, and $\left\{\ddot{x} + \ddot{x}_g\right\}_{\text{lim}} = 80$ cm/s^2.

Restrictions of natural period and damping ratio of structure:

1 s $\leq T_{0,\text{lim}} \leq$ 4 s and $0.01 \leq \zeta_{v,\text{lim}} \leq 0.1$.

Restriction of shear-force coefficient of control force:

$\alpha_{u,\text{lim}} = 0.06$.

Step 2. Fig. 2.18 (a) shows the displacement response spectrum and absolute acceleration response spectrum of the Art Hachinohe wave, and Fig. 2.18 (b) shows the velocity response spectrum of the Art Hachinohe wave. From Fig.s 2.18, it can be seen that increasing the damping ratio over 40% cannot achieve a higher performance; thus, we do not consider the cases with a damping ratio large than 40%. We select the following equivalent model:

$T_{\text{eq,tar}} = 6$ s and $\zeta_{\text{eq,tar}} = 0.40$,

which satisfies the restrictions on the maximum responses set at Step 1.

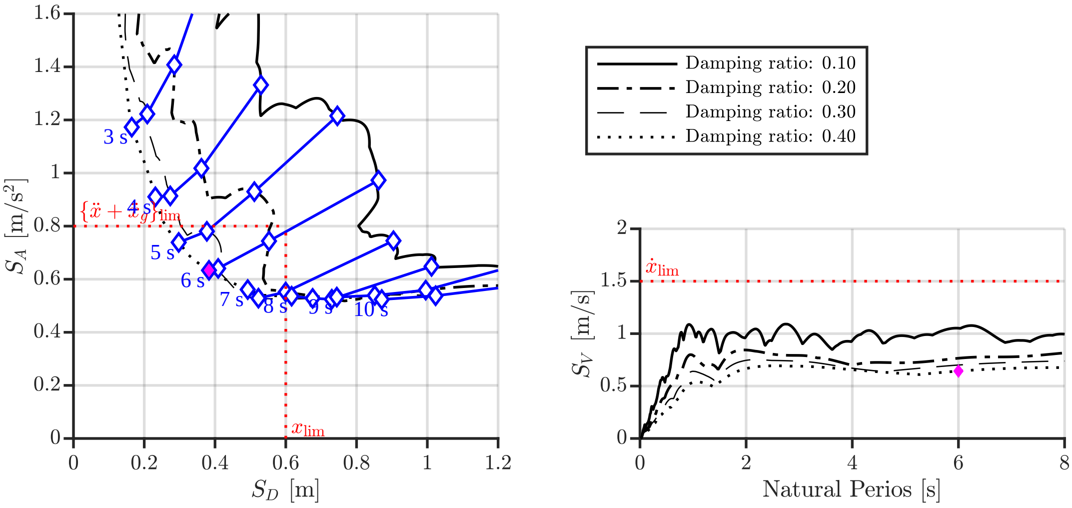

(a) S_D-S_A relationship

(b) Velocity response spectrum

Figure 2.18: Response spectra of Code Hachinohe wave (design example for linear earthquake-resistant design method)

Step 3. Figure 2.19 shows the control-force spectrum calculated by (2.20). From Figure 2.19, we select the structure with the natural period $\boldsymbol{T_0 = 4}$ **s** and damping ratio $\boldsymbol{\zeta_v = 0.05}$ that meets all restrictions set at Step 1.

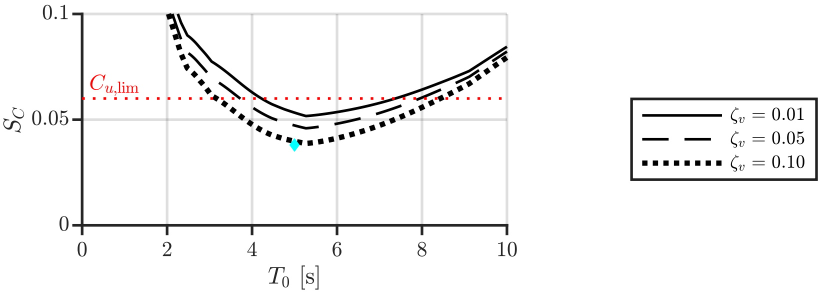

Figure 2.19: Control-force spectrum of Code Hachinohe wave (design example for linear earthquake-resistant design method, $T_{\mathrm{eq}} = 6$ s and $\zeta_{\mathrm{eq}} = 0.04$)

Step 4. Substituting the target equivalent natural period, $T_{\mathrm{eq,tar}} = 6$ s, target equivalent damping ratio, $\zeta_{\mathrm{eq,tar}} = 0.40$, natural period of isolator, $T_0 = 4$ s, and damping ratio of viscous damper, $\zeta_v = 0.05$, into (2.12), the feedback gain is obtained: $K_P = [-1.37,\ 0.52]$.

Figure 2.20 shows the time-history waves of responses of the model selected in the design example of the design method. From Figure 2.20, it can be seen that all of the restrictions are met. Therefore, the efficiency of the design method is validated.

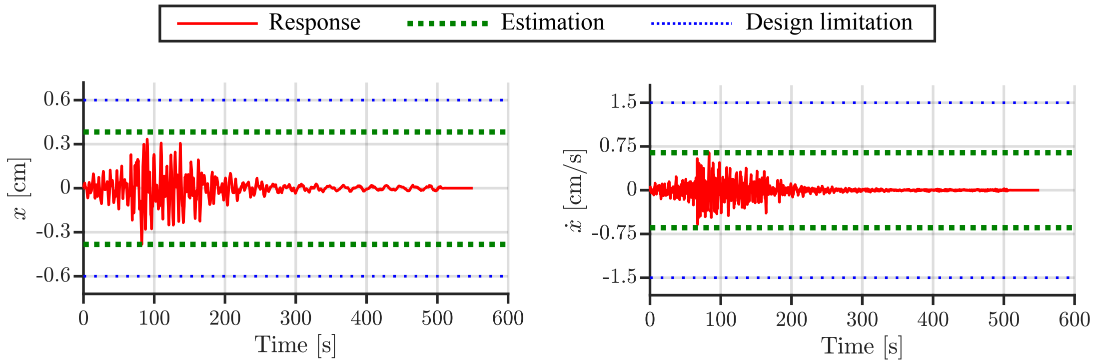

(a) Displacement **(b)** Velocity

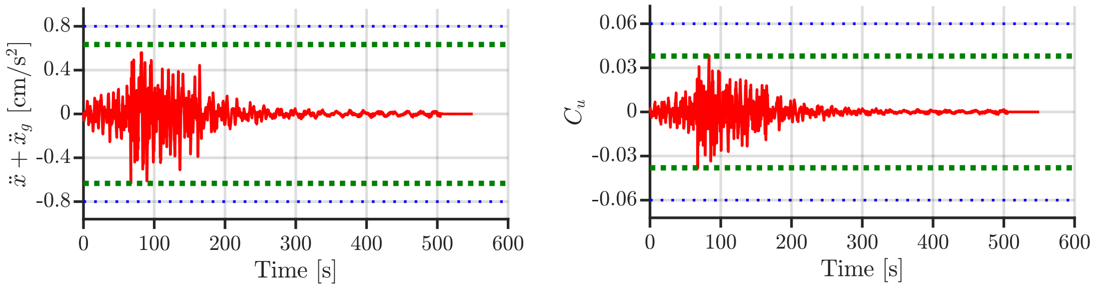

(c) Absolute acceleration **(d)** Shear-force ratio of control force

Figure 2.20: Time-history wave of design example (Code Hachinohe wave, $T_0 = 4$ s, $\zeta_s = 0.10$, $T_{\text{eq}} = 6$ s, $\zeta_{\text{eq}} = 0.40$)

2.6 Conclusion

This section developed the control-force spectrum, which estimates the maximum control force for feedback control systems without numerical simulations. The control-force spectrum theoretically estimates the maximum control force and expresses the dependency of the maximum control force on all design parameters (T_0, ζ_0, T_{eq}, and ζ_{eq}). Numerical examples have shown that the estimation errors of the control-force prediction spectra are less than 20% for most cases. This section also developed the design method, which illustrates the possible design area of the feedback gain and building satisfying the design limitations eliminating the trial-and-error approaches and numerical simulations. Finally, this section used the design example to confirm the validity of the proposed design method. From the numerical examples, this section clarified the following 4 points:

(1) If $T_{\mathrm{eq}} = T_0$, there are no estimation errors for all cases. The reason for it is that the control force only contains the velocity component when $T_{\mathrm{eq}} = T_0$.

(2) Since the phase difference usually occurs between the displacement response and velocity response, the estimation error may occur if $T_{\mathrm{eq}} \neq T_0$.

(3) The maximum control force decreases as the equivalent damping ratio increases in the resonance range.

(4) The maximum shear-force coefficient of control force increases as the equivalent damping ratio, ζ_{eq}, increases if $T_{\mathrm{eq}} = T_0$.

Appendix 2A Dependency of the vibration characteristics of control system on LQR weighting matrices

2A.1 Setting of LQR weighting matrices

The linear-quadratic regulator (LQR) method is a wild used method to design the feedback gain of a control system. The LQR approach minimizes a performance index that includes a state of the system (including displacement and velocity), control forces, and their weights to improve the vibration characteristics of the system and minimize control energy. LQR approach is thus suitable for vibration control [2.14–2.18] and is widely used in active structural control [2.5].

This section theoretically expresses the dependency of the dynamics characteristics of the control system on weighting matrices and presents a method for determining the LQR weighting matrices that achieves the target dynamics characteristics.

The standard LQR method is an optimization problem using weighting matrices as its design parameters to determine the state-feedback gain K_P by minimizing the following performance index:

$$\tilde{J} = R\int_0^\infty \left[\mathbf{z}^\mathrm{T}(t)\frac{\tilde{\mathbf{Q}}}{R}\mathbf{z}(t) + u^\mathrm{T}(t)u(t)\right]\mathrm{d}t, \tag{2.21}$$

where $R(>0)$ is the weighting matrix for control force, and $\tilde{\mathbf{Q}}$ (≥ 0) is the weighting matrix for the state. This section considers the following weighting matrix for the state:

$$\tilde{\mathbf{Q}} = \begin{bmatrix} \tilde{q}_1 & 0 \\ 0 & \tilde{q}_2 \end{bmatrix}. \tag{2.22}$$

The problem of optimizing $\tilde{J}$ in (2.21) is equal to that of optimizing

$$J = \int_0^\infty \left[\mathbf{z}^\mathrm{T}(t)\mathbf{Q}\mathbf{z}(t) + u^\mathrm{T}(t)u(t)\right]\mathrm{d}t, \tag{2.23}$$

where,

$$\mathbf{z} = \begin{bmatrix} \dfrac{\tilde{q}_1}{R} & 0 \\ 0 & \dfrac{\tilde{q}_2}{R} \end{bmatrix} = \begin{bmatrix} q_1 & 0 \\ 0 & q_2 \end{bmatrix}. \tag{2.24}$$

So, we can set $R = 1$ and focus on the adjustment of Q. Solving (2.23), the feedback gain

K_P is given as

$$\mathbf{K_P} = \mathbf{B_u^T P}, \tag{2.25}$$

where $\mathbf{P}$ (≥ 0 and symmetrical) is the solution of the following algebraic Riccati equitation [2.5]:

$$\mathbf{A^T P} + \mathbf{PA} - \mathbf{PB_u B_u^T P} + \mathbf{Q} = \mathbf{0}. \tag{2.26}$$

2A.2 Analytical solution of algebraic Riccati equitation

This section drives the analytical solution of the algebraic Riccati equitation.

The solution of the algebraic Riccati equitation is a positive definite symmetrical matrix:

$$\mathbf{P} = \begin{bmatrix} p_{11} & p_{12} \\ p_{12} & p_{22} \end{bmatrix}, \tag{2.27}$$

Substituting (2.5), (2.24), and (2.27) into (2.26) yields

$$\begin{aligned}
&\begin{bmatrix} 0 & -k_0/m \\ 1 & -c_0/m \end{bmatrix} \begin{bmatrix} p_{11} & p_{12} \\ p_{12} & p_{22} \end{bmatrix} + \begin{bmatrix} p_{11} & p_{12} \\ p_{12} & p_{22} \end{bmatrix} \begin{bmatrix} 0 & 1 \\ -k_0/m & -c_0/m \end{bmatrix} \\
&- \begin{bmatrix} p_{11} & p_{12} \\ p_{12} & p_{22} \end{bmatrix} \begin{bmatrix} 0 \\ 1/m \end{bmatrix} \begin{bmatrix} 0 & 1/m \end{bmatrix} \begin{bmatrix} p_{11} & p_{12} \\ p_{12} & p_{22} \end{bmatrix} + \begin{bmatrix} q_1 & 0 \\ 0 & q_2 \end{bmatrix} \\
&= \begin{bmatrix} 0 & 0 \\ 0 & 0 \end{bmatrix},
\end{aligned} \tag{2.28}$$

that is

$$\begin{bmatrix} -2\dfrac{k_0}{m}p_{12} + q_1 - \dfrac{p_{12}^2}{m^2} & p_{11} - \dfrac{c_0}{m}p_{12} - \dfrac{k_0}{m}p_{22} - \dfrac{p_{12}p_{22}}{m^2} \\ p_{11} - \dfrac{c_0}{m}p_{12} - \dfrac{k_0}{m}p_{22} - \dfrac{p_{12}p_{22}}{m^2} & 2p_{12} - 2\dfrac{c_0}{m} + q_2 - \dfrac{p_{22}^2}{m^2} \end{bmatrix} = \begin{bmatrix} 0 & 0 \\ 0 & 0 \end{bmatrix}. \tag{2.29}$$

Expanding (2.29) yields

$$-2\frac{k_0}{m}p_{12} + q_1 - \frac{p_{12}^2}{m^2} = 0, \tag{2.30a}$$

$$2p_{12} - 2\frac{c_0}{m} + q_2 - \frac{p_{22}^2}{m^2} = 0, \text{ and} \tag{2.30b}$$

$$p_{11} - \frac{c_0}{m}p_{12} - \frac{k_0}{m}p_{22} - \frac{p_{12}p_{22}}{m^2} = 0. \tag{2.30c}$$

The elements of the P matrix, such as p_{11}, p_{12}, and p_{22} are obtained using the algebraic Riccati equitation in (2.26):

$$p_{12} = -mk_0 \pm \sqrt{m^2k_0^2 + m^2q_1}, \tag{2.31a}$$

$$p_{22} = -mc_0 \pm \sqrt{m^2c_0^2 + 2m^2p_{12} + m^2q_2}, \text{ and} \tag{2.31b}$$

$$p_{11} = \frac{c_0}{m}p_{12} + \frac{k_0}{m}p_{22} + \frac{p_{12}p_{22}}{m^2}. \tag{2.31c}$$

Moreover, given that P is a semi-positive matrix, it yields

$$p_{11} \geq 0, \quad p_{22} \geq 0, \quad p_{11} \cdot p_{22} \geq p_{12}^2. \tag{2.32}$$

Finally, p_{12} and p_{22} are defined as

$$p_{12} = -mk_0 + \sqrt{m^2k_0^2 + m^2q_1} \text{ and} \tag{2.33a}$$

$$p_{22} = -mc_0 + \sqrt{m^2c_0^2 + 2m^2p_{12} + m^2q_2}. \tag{2.33b}$$

From (2.33) and (2.31c), the analytical solution of the algebraic Riccati equitation is obtained using the SDOF model.

2A.3 Calculation formula for determining LQR weighting matrices to achieve target vibration characteristics

This section constructs the equivalent model of the active model, and then theoretically expresses the dependency of the dynamics of the equivalent model on the LQR weighting matrices.

Substituting (2.5c) and (2.27) into (2.25) gives the analytical solution of the feedback gain, $\mathbf{K_P}$, of the LQR:

$$\mathbf{B}_\mathbf{u}^\mathrm{T}\mathbf{P} = \begin{bmatrix} 0 & \frac{1}{m} \end{bmatrix} \begin{bmatrix} p_{11} & p_{12} \\ p_{12} & p_{22} \end{bmatrix} = \begin{bmatrix} \frac{p_{12}}{m} & \frac{p_{22}}{m} \end{bmatrix} = \begin{bmatrix} K_{PD} & K_{PV} \end{bmatrix}, \tag{2.34}$$

where K_{PD} and K_{PV} are

$$K_{PD} = \sqrt{k_0^2 + q_1} - k_0 \text{ and} \tag{2.35a}$$

$$K_{PV} = \sqrt{c_0^2 - 2mk_0 + 2\sqrt{m^2k_0^2 + m^2q_1} + q_2} - c_0. \tag{2.35b}$$

Substituting (2.34) into (2.10), the dependency of k_{eq} and c_{eq} on LQR weighting matrices is

$$k_{\text{eq}} = k_0 + K_{PD} = \sqrt{k_0^2 + q_1} \text{ and} \tag{2.36a}$$

$$c_{\text{eq}} = c_0 + K_{PV} = \sqrt{c_0^2 + 2\sqrt{m^2k_0^2 + m^2q_1} - 2mk_0 + q_2}. \tag{2.36b}$$

Using (2.36), we theoretically express the dependencies of the stiffness coefficient and the damping coefficient of the equivalent model on the LQR weighting matrices.

From (2.36a), k_{eq} is dependent on k_0 and q_1. When $q_1 = 0$, the value of k_{eq} is equal to k_0, and the value of k_{eq} increases as q_1 increases. From (2.36b), c_{eq} is dependent on c_0, k_0, m, q_1 and q_2. When $q_1 = q_2 = 0$, the value of c_{eq} is equal to c_0, and the value of c_{eq} increases as q_1 or q_2 increases. However, the influence of q_1 on c_{eq} is smaller than that of q_2, given that q_1 is in the double route.

As is commonly known, the natural angular frequency ω_{eq}, natural period T_{eq}, and damping ratio ζ_{eq} of the equivalent model are

$$\omega_{\text{eq}} = \sqrt{\frac{k_{\text{eq}}}{m}}, \tag{2.37a}$$

$$T_{\text{eq}} = \frac{2\pi}{\omega_{\text{eq}}}, \text{ and} \tag{2.37b}$$

$$\zeta_{\text{eq}} = \frac{c_{\text{eq}}}{2m\omega_{\text{eq}}}. \tag{2.37c}$$

Solving (2.37) yields a calculation formula for the determination of the LQR weighting entries to achieve desired vibration characteristics without a trial-and-error approach.

Solving (2.36a) and (2.36b), the entries of Q, such as q_1 and q_2, can be determined by

$$q_1 = k_{\text{eq,tar}}^2 - k_0^2 \text{ and} \tag{2.38a}$$

$$q_2 = c_{\text{eq,tar}}^2 - c_0^2 + 2mk_0 - 2\sqrt{m^2k_0^2 + m^2q_1}. \tag{2.38b}$$

Furthermore, if the control system is represented in a controllable canonical form, (2.38) is identical to that proposed by Elumalai *et al* [2.9].

(2.38) is used to yield the calculation formula for the determination of the LQR weighting entries so as to achieve the desired vibration characteristics without a trial-and-error approach. The calculation procedure of the LQR weight selection method is summarized below:

Step 1. Specify the natural period and damping ratio of the structure (T_0 and ζ_0), and calculate the value of k_0 and c_0 using (2.2) and (2.3).

Step 2. Specify the desired natural period and damping ratio of the control system ($T_{\text{eq,tar}}$ and $\zeta_{\text{eq,tar}}$), and calculate the value of $k_{\text{eq,tar}}$ and $c_{\text{eq,tar}}$ using (2.2) and (2.2).

Step 3. Substitute $k_{\text{eq,tar}}$ and k_0 into (2.38a), and calculate q_1 in the weighting matrix $\mathbf{Q}$.

Step 4. Substituting $c_{\text{eq,tar}}$, m, k_0, c_0 and q_1 calculated in Step 3 into (2.38b), calculate q_2 in the weighting matrix $\mathbf{Q}$. If $q_2 \geq 0$, use the calculated values of q_1 and q_2 to design the control system. If $q_2 < 0$, go back to Step 2 and review $T_{\text{eq,tar}}$ or $\zeta_{\text{eq,tar}}$, because it is inconsistent with the semi-positive limitation of $\mathbf{Q}$.

Fig. 2.21 presents the flowchart for the calculation method of weighting entries q_1 and q_2.

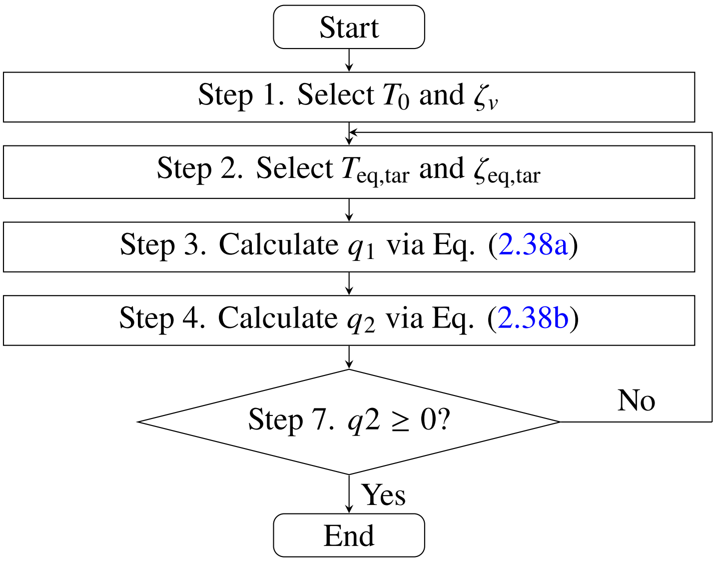

Figure 2.21: Flowchart for calculating weighting entries to achieve target vibration characteristics

Appendix 2B Control-force spectrum: SRSS method vs. ABS method

This section uses the FEMA P695 wave list [2.19] to verify the accuracy of the control-force spectrum, S_C. Table 2.2 shows the information of the FEMA P695 wave list. The parameters of the models used in this section are shown below:

T_0: 2 s, 4 s, and 6s;

ζ_v: 0.01 and 0.05;

T_{eq}: 0.01~10 s per 0.01 s;

ζ_{eq}: 0.1, 0.3, 0.5, and 0.7.

Table 2.2
FEMA P695 wave list [2.19]

No.	Name	Recording station	Year - M.	PGA [cm/s^2] comp. 1	PGA [cm/s^2] comp. 2	PGV [cm/s] comp. 1	PGV [cm/s] comp. 2
1	Northridge	Beverly Hills - Mulhol	1994 - 6.7	407.00	506.00	58.89	62.57
2	Northridge	Canyon Country - WLC	1994 - 6.7	344.00	472.00	22.00	44.86
3	Duzce	Bolu	1999 - 7.1	713.00	806.00	56.43	62.03
4	Hector Mine	Hector	1999 - 7.1	260.00	330.00	28.52	41.67
5	Imperial Valley	Delta	1979 - 6.5	233.00	344.00	25.93	32.93
6	Imperial Valley	El Centro Array #11	1979 - 6.5	357.00	372.00	34.41	42.09
7	Kobe	Nishi-Akashi	1995 - 6.9	499.00	493.00	37.24	36.54
8	Kobe	Shin-Osaka	1995 - 6.9	238.00	208.00	37.77	27.85
9	Kocaeli	Duzce	1999 - 7.5	306.00	351.00	58.80	46.33
10	Kocaeli	Arcelik	1999 - 7.5	214.00	147.00	17.67	39.53
11	Landers	Yermo Fire Station	1992 - 7.3	240.00	148.00	51.27	29.72
12	Landers	Coolwater	1992 - 7.3	278.32	408.66	275.47	433.74
13	Loma Prieta	Capitola	1989 - 6.9	518.00	434.00	34.94	29.16
14	Loma Prieta	Gilroy Array #3	1989 - 6.9	544.00	360.00	35.66	44.61
15	Manjil	Abbar	1990 - 7.4	504.70	487.06	42.41	50.69
16	Superstition Hills	El Centro Imp. Co.	1987 - 6.5	351.00	253.00	46.30	40.82
17	Superstition Hills	Poe Road (temp)	1987 - 6.5	437.00	294.00	35.65	32.74
18	Cape Mendocino	Rio Dell Overpass	1992 - 7.0	378.00	538.00	43.72	41.81
19	Chi-Chi	CHY101	1999 - 7.6	346.00	431.00	70.52	114.93
20	Chi-Chi	TCU045	1999 - 7.6	487.06	348.88	12.67	20.54
21	San Fernando	LA - Hollywood Stor	1971 - 6.6	206.00	171.00	18.81	14.81
22	Friuli	Tolmezzo	1976 - 6.5	344.00	309.00	22.00	30.75

Two methods, the absolute sum (ABS) method and the square root of the sum of squares (SRSS) method, are used to compare the estimation errors:

$$S_{C,\text{ABS}} := \alpha_{uD,\max} + \alpha_{uV,\max} \text{ and} \tag{2.39a}$$

$$S_{C,\text{SRSS}} := \sqrt{\alpha_{uD,\max}^2 + \alpha_{uV,\max}^2}. \tag{2.39b}$$

We select the cases of $T_0 = 4$ s, $\zeta_v = 0.01$, component 1 of Imperial Vally wave of El Centro

Array #11 recording (FEMA ID No. 6) and component 1 of Kobe wave of Nishi-Akasaki recording (FEMA ID No. 7) to show the estimation errors. Figure 2.22 presents the estimation errors of the ABS method, and Figure 2.23 presents that of the SRSS method. Besides, the estimation errors, e, are calculated by the following equation:

$$e = \frac{S_C - \alpha_{u,\max}}{\alpha_{u,\max}} \times 100\% \tag{2.40}$$

where $\alpha_{u,\max}$ is the shear-force coefficient of the maximum control force calculated by the numerical simulations (real value). From Figures 2.22 and 2.23, the following results are obtained:

(1) The estimation error of the ABS method is obviously larger than that of the SRSS method.

(2) The estimation error of the ABS method are always larger than 0.

(3) The estimation error of the SRSS method are less than 20% for the two selected cases.

(4) There are no estimation errors for both the ABS method and SRSS method if $T_{\mathrm{eq}} = T_s$ (4 s in Figures 2.22 and 2.23).

Figure 2.24 shows the mean value of the estimation errors, $\bar{e}$, and the standard derivation of the maximum estimation errors, σ_e, using the ABS method and the SRSS method for all equivalent natural periods ($T_s = 4$ s and $\zeta_s = 0.01$). In addition, the mean value and the standard derivation of the estimation errors for all equivalent natural periods, T_{eq}, are calculated by

$$\bar{e} = \frac{\sum e(T_{\mathrm{eq}})}{N_T} \text{ and} \tag{2.41}$$

$$\sigma_e = \sqrt{\frac{\sum \left[e(T_{\mathrm{eq}}) - \bar{e}\right]^2}{N_T}}, \tag{2.42}$$

where N_T is the number of cases of the equivalent natural period (in this section, N_T is 1000). From Figure 2.24, the following results are obtained:

(1) The mean value and standard derivation of the maximum estimation errors of the SRSS method are larger than that of the ABS method.

(2) The estimation errors of the SRSS method are less than 20% for most cases.

Table 2.3 shows the mean value of $\bar{e}$, $\bar{e}_{\text{all}}$, and the mean value of σ_e, $\sigma_{e,\text{all}}$, for all waves of the ABS method and SRSS method:

$$\bar{e}_{\text{all}} = \frac{\sum \bar{e}(\text{FEMA ID No.})}{N_{\text{ID}}} \tag{2.43}$$

$$\bar{\sigma}_{e,\text{all}} = \frac{\sum \sigma_e(\text{FEMA ID No.})}{N_{\text{ID}}} \tag{2.44}$$

where N_{ID} is the number of cases of the waves (in this section N_{ID} is 44).

From Table 2.3, the following results are obtained:

(1) Both the mean value of the estimation error and the standard derivation of the estimation error of the SRSS method are obviously less than that of the ABS method.

(2) The mean values of the standard derivation of the estimation error of the SRSS method for each case are less than 8%.

Thus, this study uses the SRSS method to estimate the maximum control force.

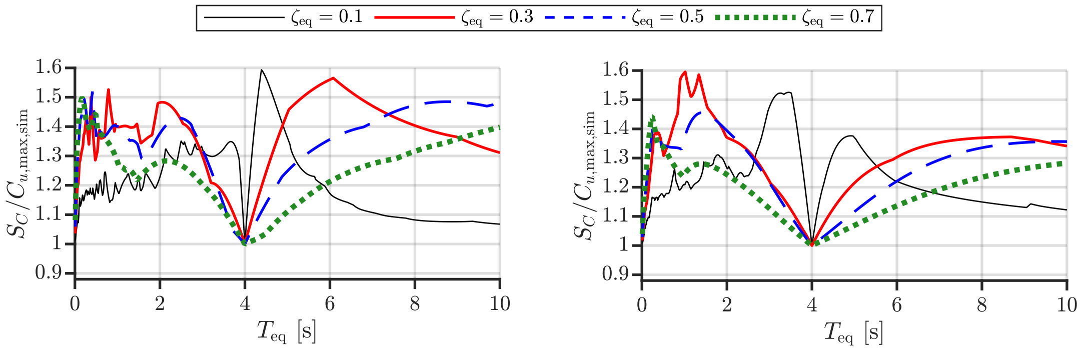

(a) Component 1 of No. 6 wave **(b)** Component 1 of No. 7 wave

Figure 2.22: Accuracy of $S_{C,\text{ABS}}$ ($T_0 = 4$ s, $\zeta_v = 0.01$)

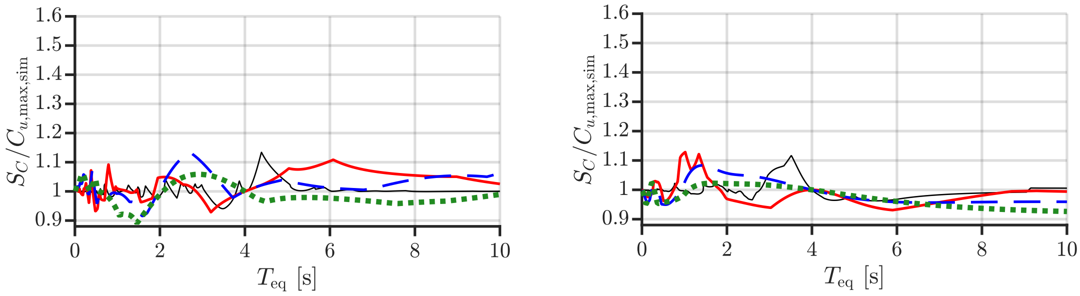

(a) Component 1 of No. 6 wave **(b)** Component 1 of No. 7 wave

Figure 2.23: Accuracy of $S_{C,\text{SRSS}}$ ($T_0 = 4$ s, $\zeta_v = 0.01$)

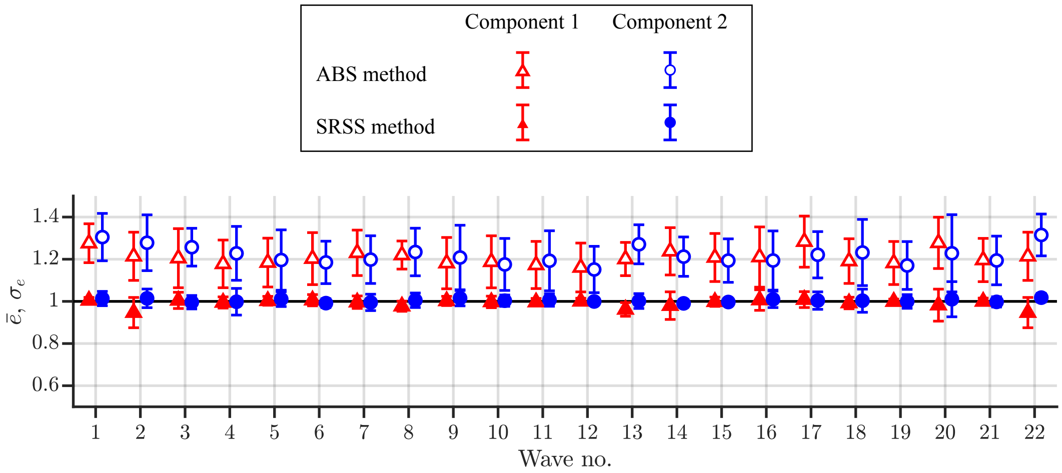

(a) $\zeta_{\mathrm{eq}} = 0.10$

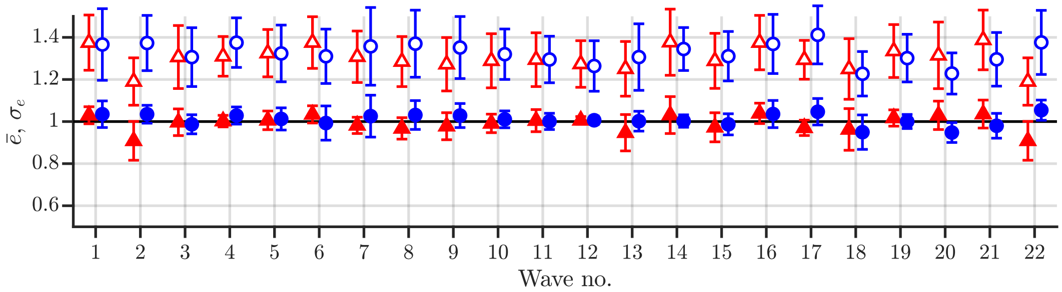

(b) $\zeta_{\mathrm{eq}} = 0.30$

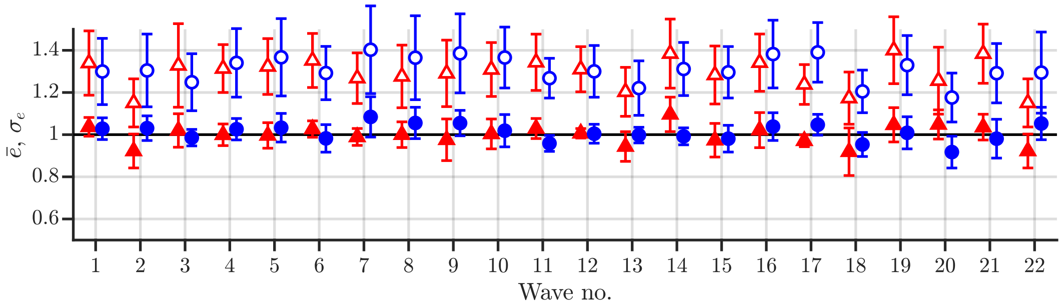

(c) $\zeta_{\mathrm{eq}} = 0.50$

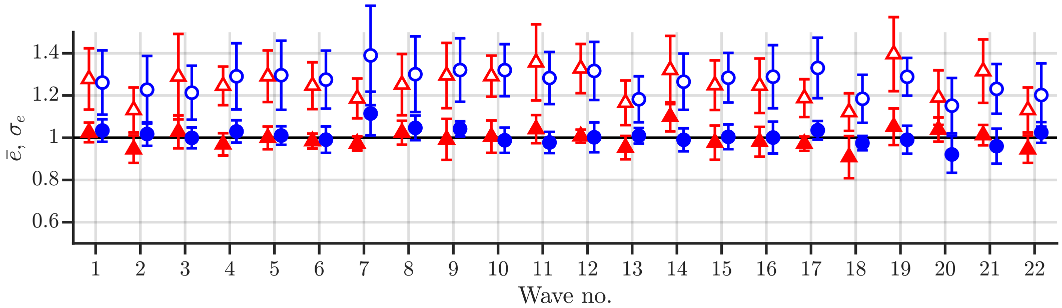

(d) $\zeta_{\mathrm{eq}} = 0.70$

Figure 2.24: Estimation error of control-force spectrum of FEMA waves (T_0 = 4 s, ζ_v = 0.01).

Table 2.3
Estimation error of control-force spectrum of FEMA waves
(T_0 = 4, 5 and 6 s, and ζ_v = 0.01 and 0.05)

T_0	ζ_v	ζ_{eq}	ABS method		SRSS method	
			$\bar{e}_{\mathrm{all}}$	$\bar{\sigma}_{e,\mathrm{all}}$	$\bar{e}_{\mathrm{all}}$	$\bar{\sigma}_{e,\mathrm{all}}$
2 s	0.01	0.10	10.79%	11.92%	−0.04%	2.26%
		0.30	21.21%	14.00%	−0.26%	4.46%
		0.50	25.93%	14.22%	−0.30%	6.04%
		0.70	27.74%	14.26%	−0.64%	6.86%
	0.05	0.10	7.98%	10.17%	−0.04%	1.69%
		0.30	17.36%	15.31%	−0.09%	4.07%
		0.50	23.30%	14.59%	−0.23%	5.46%
		0.70	26.16%	14.31%	−0.52%	6.51%
4 s	0.01	0.10	21.47%	12.46%	−0.27%	4.16%
		0.30	31.56%	14.05%	0.04%	6.82%
		0.50	30.23%	15.89%	0.49%	7.88%
		0.70	26.06%	15.33%	0.23%	7.45%
	0.05	0.10	14.52%	13.42%	−0.10%	3.10%
		0.30	30.31%	13.81%	−0.07%	6.35%
		0.50	30.72%	15.73%	0.55%	7.76%
		0.70	26.86%	15.45%	0.30%	7.52%
6 s	0.01	0.10	27.40%	12.53%	−0.32%	5.60%
		0.30	29.21%	15.03%	−0.26%	7.30%
		0.50	23.45%	15.54%	−0.28%	6.70%
		0.70	19.23%	14.82%	0.16%	6.25%
	0.05	0.10	22.58%	12.32%	−0.23%	4.22%
		0.30	30.29%	14.83%	−0.22%	7.38%
		0.50	24.32%	15.58%	−0.27%	6.85%
		0.70	19.79%	14.88%	0.15%	6.37%

$T_{\mathrm{eq}} = 0.01 \sim 10$ s per 0.01 s (1000 data for each wave)

Appendix 2C Detailed analysis of control-force spectrum

This section analyzes the reason for the results for the numerical examples of the control-force spectrum (Figs. 2.16 and 2.17) using the response spectra of earthquake waves. Figs. 2.25~2.28 show the displacement response spectra, S_D, and velocity response spectra of Taft NS, El Centro 1940 NS, JMA Kobe NS, and Art Hachinohe, respectively.

Result 1:

The maximum control force decreases as the equivalent damping ratio, ζ_{eq}, *increases if* $T_{\mathrm{eq}} < 1$ s.

Reason for result 1:

From Eq.(2.20), the maximum control force increases as the maximum displacement response or maximum velocity response increases. From Figures 2.25~2.28, it can be seen that the maximum displacement response and the maximum velocity response decreases as the equivalent damping ratio increases. Thus the maximum control force decreases as the equivalent damping ratio increases if $T_{\mathrm{eq}} \leq 1$ s.

Result 2:

The maximum control force increases as the equivalent damping ratio, ζ_{eq}, *increases, if* $T_0 = T_{\mathrm{eq}}$.

Reason for result 2:

The value of k_{eq} is equal to k_0 if $T_{\mathrm{eq}} = T_0$. Therefore, from (2.19)

$$\alpha_{uD,\max} = 0 \tag{2.45}$$

is obtained. Substituting (2.45) into (2.20) yields

$$S_C(T_0, \zeta_v, T_{\mathrm{eq}}{=}T_0, \zeta_{\mathrm{eq}}) = \alpha_{uV,\max} = \frac{|c_{\mathrm{eq}} - c_v|}{mg} S_V(T_{\mathrm{eq}}, \zeta_{\mathrm{eq}}) \tag{2.46}$$

Since the values of m, g, c_v, and S_V in (2.46) are constant for one case, the value of S_C increases as equivalent damping increases.

Result 3:

The maximum control force increases as the equivalent natural period, T_{eq}, *increases if* $T_{\mathrm{eq}} > 6$ s *only for the case of Art Hachinohe.*

Reason for result 3:

The Art Hachinohe is an artificial earthquake that minimizes the effects of natural periods of the original waves. The maximum displacement response of a structure increases as the equivalent natural period increases under the Art Hachinohe wave. Since the maximum control force increases as the maximum displacement response, the maximum control force increases as the equivalent natural period, T_{eq}, increases for the case of Art Hachinohe.

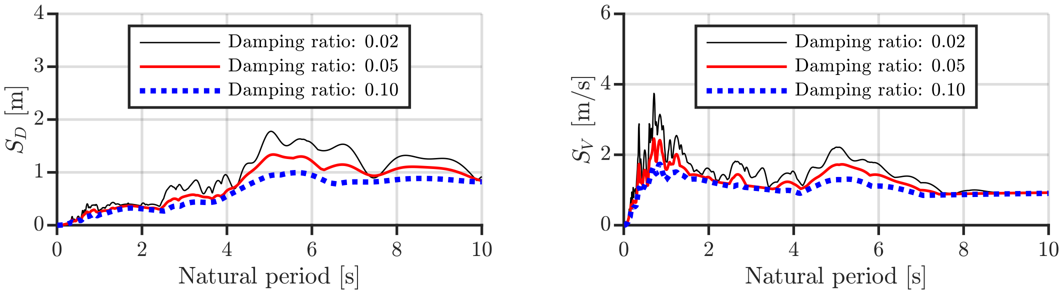

(a) Displacement-response spectrum **(b)** Displacement-response spectrum

Figure 2.25: Displacement-response and Velocity-response spectra of Taft NS wave

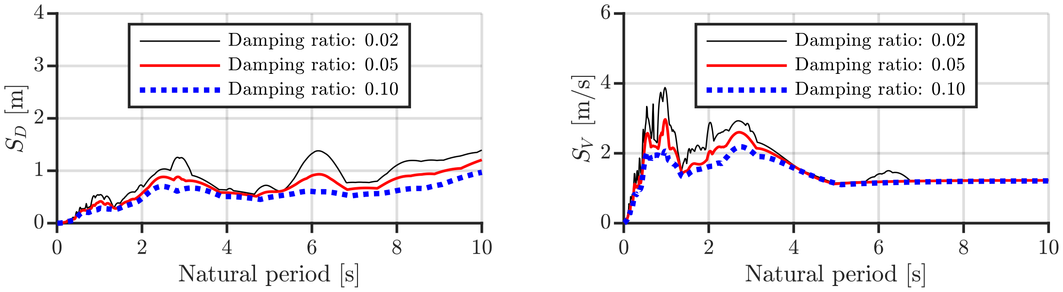

(a) Displacement-response spectrum **(b)** Displacement-response spectrum

Figure 2.26: Displacement-response and Velocity-response spectra of El Centro 1940 NS wave

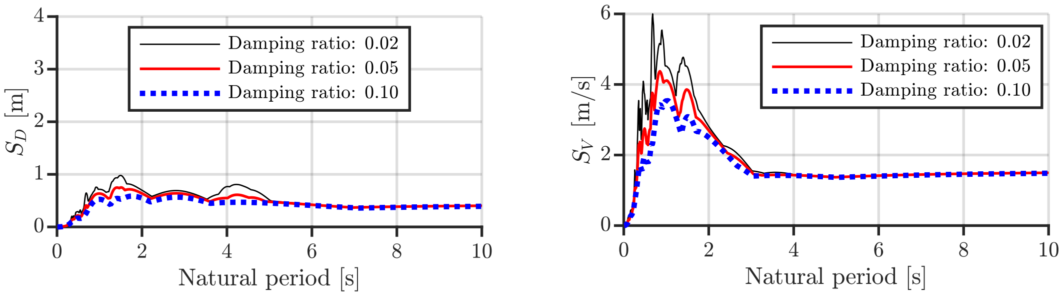

(a) Displacement-response spectrum **(b)** Displacement-response spectrum

Figure 2.27: Displacement-response and Velocity-response spectra of JMA Kobe NS wave

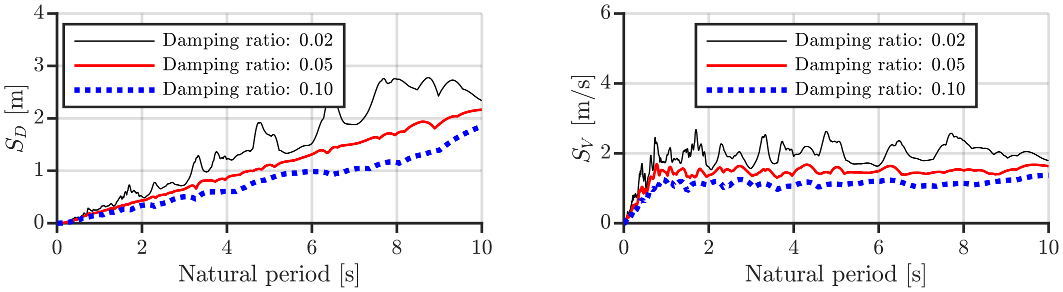

(a) Displacement-response spectrum **(b)** Displacement-response spectrum

Figure 2.28: Displacement-response and Velocity-response spectra of Code Hachinohe wave

Appendix 2D Earthquake wave used in design example

This chapter used 4 earthquakes (Taft NS, El Centro 1940 NS, JMA Kobe NS, and Code Hachinohe), and all these waves are standardized to 1.5 times of Level II of Japan earthquake resistant design standard (see Table 2.1). Fig. 2.29 shows the comparison of response spectra between Taft NS, El Centro 1940 NS, JMA Kobe NS, and Code Hachinohewaves. From Fig. 2.29, it can be seen that the responses of Code Hachinohewave is largest between these 4 waves, if natural period of a structures longer than 2 s. Therefore, the design example of this chapter uses Code Hachinohewave as example.

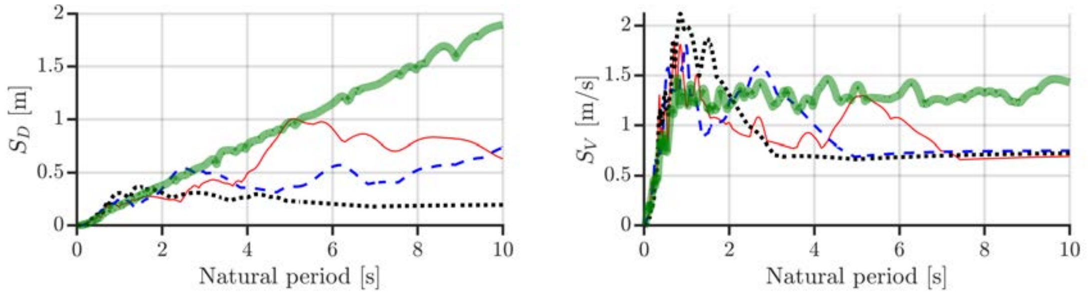

(a) Displacement-response spectrum

(b) Velocity-response spectrum

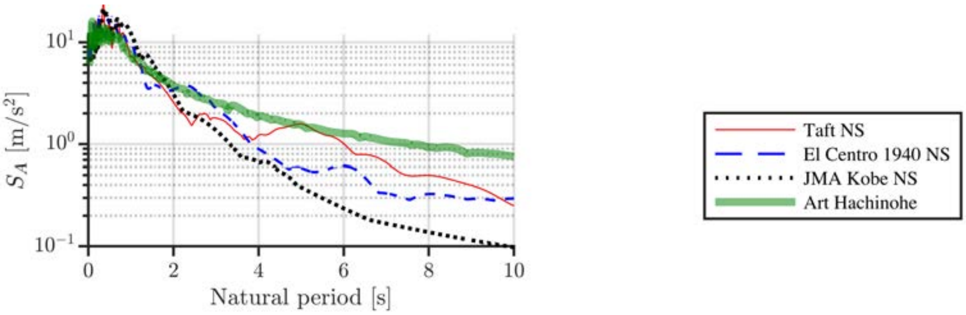

(c) Absolute-acceleration-response spectrum

Figure 2.29: Response spectra: Taft NSvs. El Centro 1940 NSvs. JMA Kobe NSvs. Code Hachinohe

Appendix 2E Responses and control force: single-DOF model vs. multi-DOFs model

The stiffness of the isolation layer of a passive-base-isolated structure is usually much softer than its superstructure and the controller (feedback gain) designed in this section added an equivalent negative stiffness to the isolation layer. Thus, the structure can be modeled as a single-DOF model. This section shows the comparison of responses and control force between SDOF model and MDOF model for the design example. In addition, the parameters of the superstructure are shown at Table 2.4.

Table 2.4
Height, mass, stiffness, and damping coefficient of each story of superstructures for A4 model

Story	h_i [m]	m_i [kg]	k_i [N/m]	c_i [Ns/m]
1	10	1.09×10^6	5.94×10^8	7.56×10^6
2	10	1.09×10^6	5.83×10^8	7.42×10^6
3	10	1.09×10^6	5.61×10^8	7.15×10^6
4	10	1.09×10^6	5.29×10^8	6.73×10^6
5	10	1.09×10^6	4.86×10^8	6.19×10^6
6	10	1.09×10^6	4.32×10^8	5.50×10^6
7	10	1.09×10^6	3.67×10^8	4.67×10^6
8	10	1.09×10^6	2.91×10^8	3.71×10^6
9	10	1.09×10^6	2.05×10^8	2.61×10^6
10	10	1.09×10^6	1.08×10^8	1.37×10^6

(1st natural period: 2 s, 1st damping ratio: 0.02)

Figs. 2.30~2.30 show the comparison of responses between the single-DOF model and multi-DOFs model subjected to Taft NS, El Centro 1940 NS, JMA Kobe NS, and Code Hachinohewaves. Fig. 2.34 shows the comparison of control force between the single-DOF model and multi-DOFs model subjected to Taft NS, El Centro 1940 NS, JMA Kobe NS, and Code Hachinohewaves. From Figs. 2.30~2.34, the following results are obtained:

- There are little differences of maximum responses of the superstructure between stories of the superstructure.
- The maximum responses of the single-DOF model match well to the multi-DOFs model.
- The maximum control force of the single-DOF model match well to the multi-DOFs

model.

Therefore, a single-DOF model can be used to estimated the responses and control force of a multi-DOFs model in earthquake-resistant design.

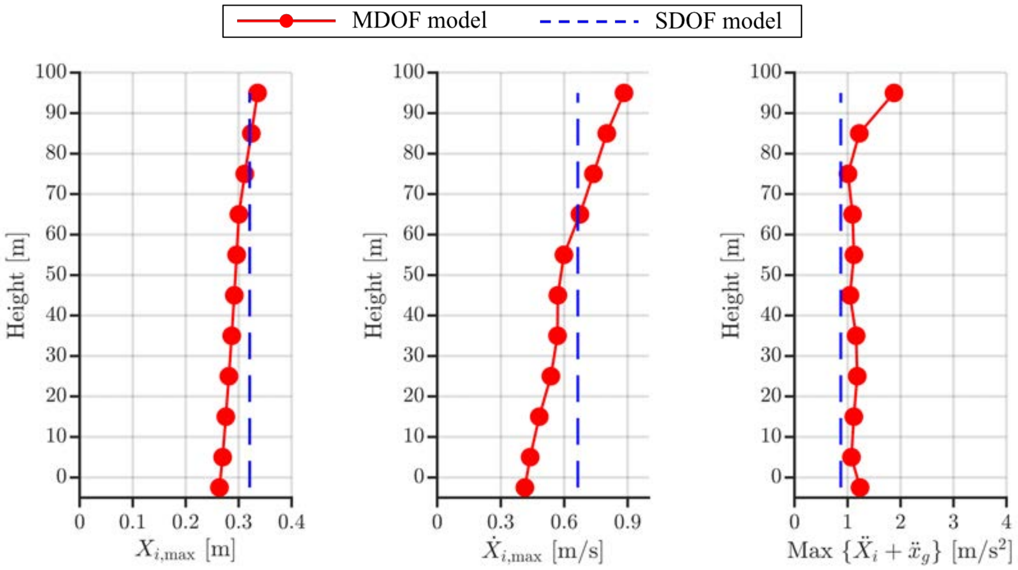

(a) Displacement **(b)** Displacement **(c)** Displacement

Figure 2.30: Responses subjected to Taft NSwave: MDOF model vs. SDOF model

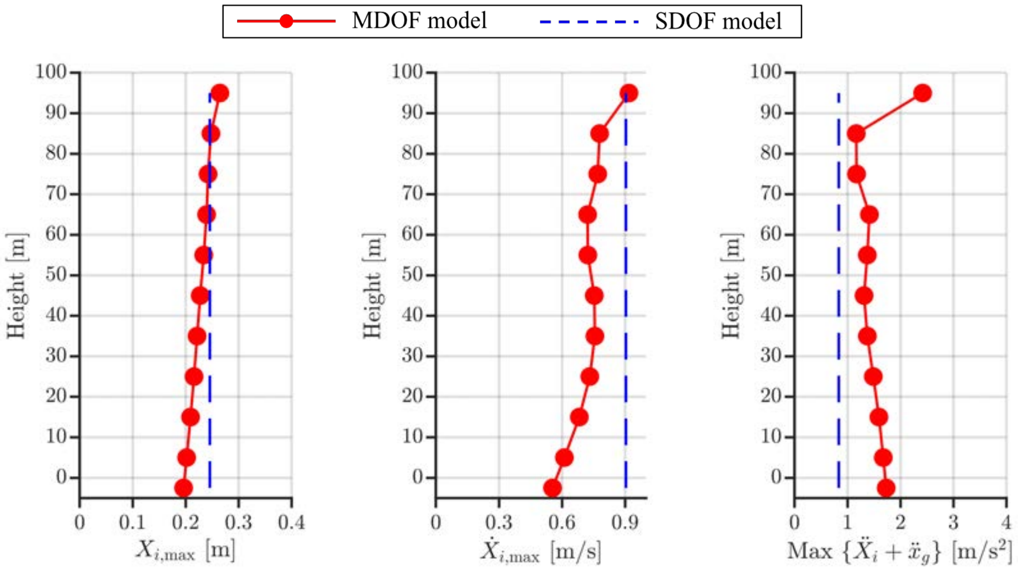

(a) Displacement **(b)** Displacement **(c)** Displacement

Figure 2.31: Responses subjected to El Centro 1940 NSwave: MDOF model vs. SDOF model

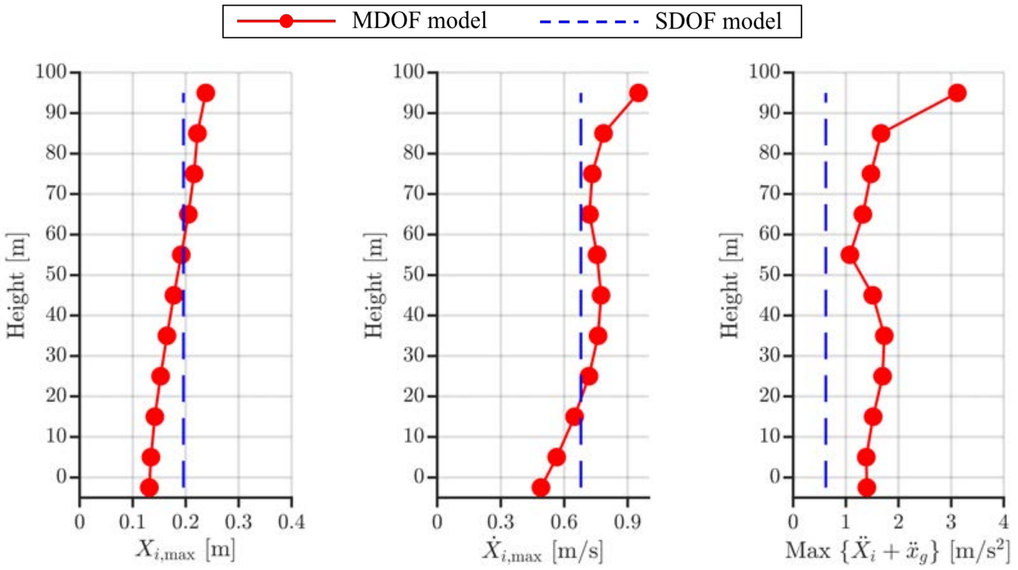

(a) Displacement **(b)** Displacement **(c)** Displacement

Figure 2.32: Responses subjected to JMA Kobe NSwave: MDOF model vs. SDOF model

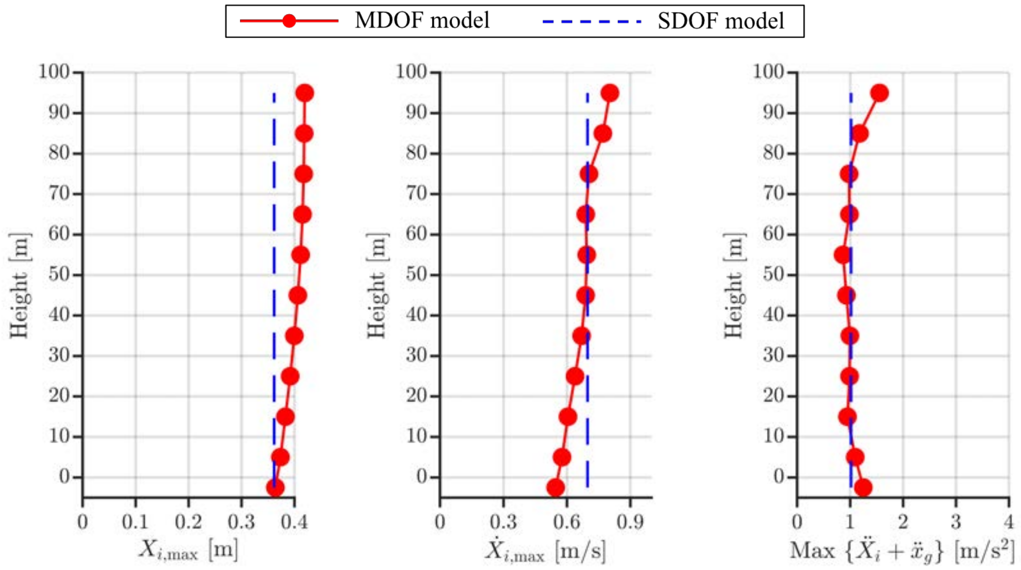

(a) Displacement **(b)** Displacement **(c)** Displacement

Figure 2.33: Responses subjected to Code Hachinohewave: MDOF model vs. SDOF model

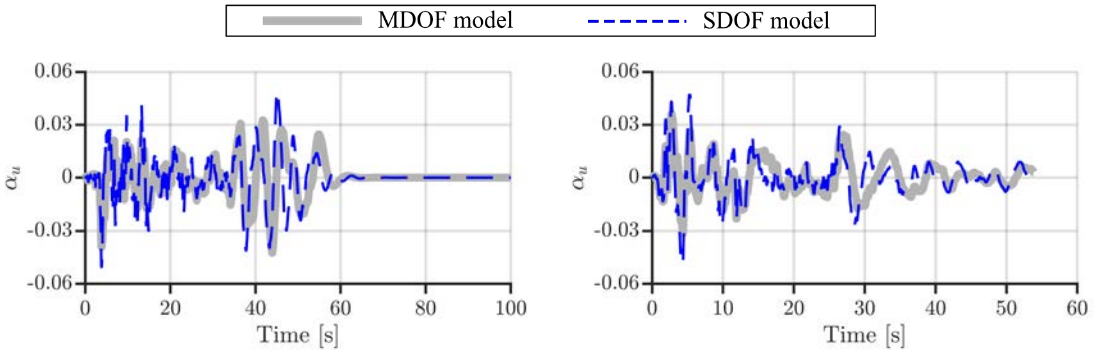

(a) Taft NS **(b)** El Centro 1940 NS

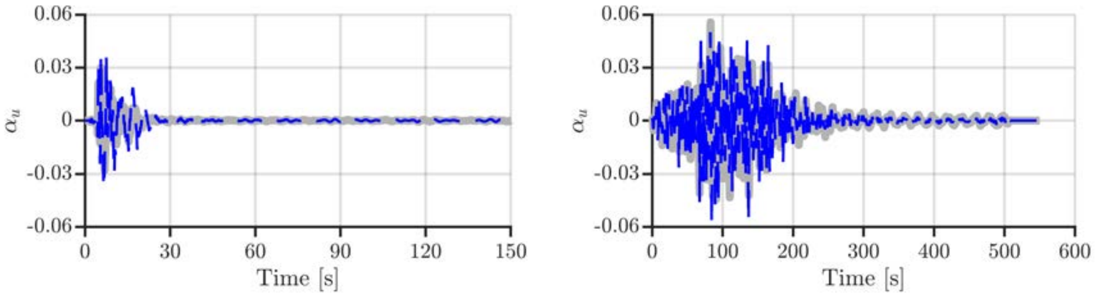

(c) JMA Kobe NS **(d)** Code Hachinohe

Figure 2.34: Control force subjected to Taft NS, El Centro 1940 NS, JMA Kobe NS, and Code Hachinohewaves: MDOF model vs. SDOF model

References

[2.1] Y. Peng, Z. Zhang, Optimal mr damper–based semiactive control scheme for strengthening seismic capacity and structural reliability, Journal of Engineering Mechanics 146 (6) (2020) 04020045. `doi:10.1061/(ASCE)EM.1943-7889.0001768`.

[2.2] K. Miyamoto, D. Sato, J. She, A new performance index of LQR for combination of passive base isolation and active structural control, Engineering Structures 157 (2018) 280 – 299. `doi:10.1016/j.engstruct.2017.11.070`.

[2.3] F. Casciati, J. Rodellar, U. Yildirim, Active and semi-active control of structures – theory and applications: A review of recent advances, Journal of Intelligent Material Systems and Structures 23 (11) (2012) 1181–1195. `doi:10.1177/1045389X12445029`.

[2.4] S. Korkmaz, A review of active structural control: challenges for engineering informatics, Computers & Structures 89 (23) (2011) 2113 – 2132. `doi:10.1016/j.compstruc.2011.07.010`.

[2.5] A. Preumont, A. Seto, Active control of structures, John Wiley & Sons, Inc., 2008.

[2.6] K. Miyamoto, J. She, D. Sato, N. Yasuo, Automatic determination of lqr weighting matrices for active structural control, Engineering Structures 174 (2018) 308–321. `doi:10.1016/j.engstruct.2018.07.009`.

[2.7] Architectural Institute of Japan, Design Recommendations for Seismically Isolated Buildings, Architectural Institute of Japan, 2016.

[2.8] T. Fujii, H. Fujitani, Y. Mukai, Performance evaluation of semi-active optimal control system by MR damper, Journal of Structural and Construction Engineering (Transactions of AIJ) 78 (689) (2013) 1237–1245. `doi:10.3130/aijs.78.1237`.

[2.9] V. K. Elumalai, R. G. Subramanian, A new algebraic LQR weight selection algorithm for tracking control of 2 DoF torsion system, Archives of Electrical Engineering 66 (1) (2017) 55 – 75. `doi:10.1515/aee-2017-0005`.

[2.10] C. Horiguchi, M. Kohiyama, Simultaneous optimization of structural and control systems of a SDOF buildings with a linear quadratic regulator controller aiming at performance-based design, Journal of Structural and Construction Engineering (Transactions of AIJ) [in Japanese] 77 (675) (2012) 715–722. `doi:https://doi.org/10.3130/aijs.77.715`.

[2.11] M. Kohiyama, Prediction of maximum control force of pd-controlled system under stationary white noise, in: 11th International Conference on Structural Safety and Reliability, 2013, pp. 3871–3878. `doi:10.1201/b16387-562`.

[2.12] Architectural Institute of Japan, AIJ Recommendations for Loads on Buildings, Architectural Institute of Japan, 2015.

[2.13] J. M. Kelly, Earthquake-Resistant Design with Rubber, Second Edition, Springer, 1997.

[2.14] K. Miyamoto, J. She, J. Imani, X. Xin, D. Sato, Equivalent-input-disturbance approach to active structural control for seismically excited buildings, Engineering Structures 125 (2016) 392 – 399. `doi:10.1016/j.engstruct.2016.07.028`.

[2.15] M. Al-Dawod, B. Samali, K. Kwok, F. Naghdy, Fuzzy controller for seismically excited nonlinear buildings, Journal of Engineering Mechanics 130 (4) (2004) 407–415. `doi:10.1061/(ASCE)0733-9399(2004)130:4(407)`.

[2.16] K. Miyamoto, D. Sato, J. She, A new performance index of lqr for combination of passive base isolation and active structural control, Engineering Structures 157 (2018) 280 – 299. `doi:10.1016/j.engstruct.2017.11.070`.

[2.17] K. Miyamoto, J. She, D. Sato, N. Yasuo, Automatic determination of lqr weighting matrices for active structural control, Engineering Structures 174 (2018) 308 – 321. `doi:10.1016/j.engstruct.2018.07.009`.

[2.18] P. P. Ong, A. Adnan, K. Kwok, C.-K. Ma, P. Tiong, H. P. Behbahani, Dynamic simulation of unrestrained interlocking tuned liquid damper blocks, Construction and Building Materials 144 (2017) 586 – 597. `doi:https://doi.org/10.1016/j.conbuildmat.2017.03.190`.

[2.19] Federal Emergency Management Agency, Quantification of Building Seismic Performance Factors - FEMA P695, Federal Emergency Management Agency, 2009.

CHAPTER 3

Nonlinear earthquake-resistant design

3.1 Introduction

Chapter 2 proposed a method for estimating the maximum responses and maximum control force of the control system using the equivalent model and response spectra. However, Chapter 2 only considered a linear base-isolation story (only contains linear viscous dampers and linear natural-rubber bearings).

Yielding materials, such as lead rubber bearings, tin rubber bearings, steel dampers, and other metallic materials have hysteretic characteristics, and these devices can be modeled as hysteretic dampers [3.1]. A hysteretic damper dissipates the energy induced by an earthquake through hysteretic plastic deformation of the steel, and because of its low cost, simple structure, long-term reliability, and easy implementation [3.2, 3.3], most of base-isolated buildings installed hysteretic dampers in Japan [3.4–3.6]. To extend the response-spectrum method to active base-isolated buildings, it is necessary to consider the nonlinearity of the isolation layer. In passive earthquake-resistant design, the equivalent linearization method is widely used, and an equivalent linear model are used to estimate the maximum response of a nonlinear model with hysteretic dampers [3.7–3.9]. This chapter extends equivalent models, response spectra and control-force spectrum to active bas-isolation considering nonlinear hysteretic dampers (active nonlinear model).

This chapter proposes a method for constructing an equivalent linear method for an active nonlinear model (an active control system model with hysteretic dampers). This method uses equivalent linear method to replace the controller and nonlinear hysteretic damper to linear springs and dashpots, and constructs the equivalent linear model passive linear model) of the active nonlinear model (SDOF model with actuator and hysteretic dampers). Using the equivalent linear model, the response spectrum and control-force spectrum can be extended to a nonlinear control system to estimate the maximum responses and control force. Moreover, equations for determining the feedback gain for an active nonlinear model that achieves the desired dynamics are also devised herein. Then, using the equivalent linear model and presented equations, a spectrum-based design method for active base-isolated buildings with hysteretic dampers is proposed. The design method simplifies the conventional design procedure using the following three points:

1. It estimates the maximum response of the control system via response spectra.
2. It estimates the maximum control force of the control system via a control force spectrum.
3. It does not require trail-and-error approaches and numerical simulations to determine design parameters that satisfy all design criteria.

This chapter also gives a numerical design example to show the validity of the design method.

3.2 Earthquake wave and mathematic model

3.2.1 Earthquake waves for simulation

This Chapter uses the same earthquake waves with Chapter 2, Taft NS, El Centro 1940 NS, JMA Kobe NS, and Code Hachinohe waves (see Figs. 2.1~2.4 and Table 2.1).

3.2.2 Mathematic model

In this chapter, we use a base-isolated building (Fig. 3.1). The superstructure of the building is assumed to be a rigid body, because the stiffness of the isolation layer is usually smaller than that of the superstructure [3.10]. Thus, in this study, we describe a base-isolated building as an SDOF model (active model, Fig. 3.2).

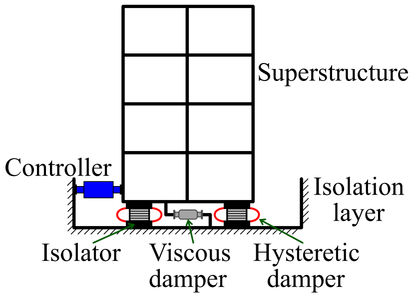

Figure 3.1: Base-isolated building (nonlinear)

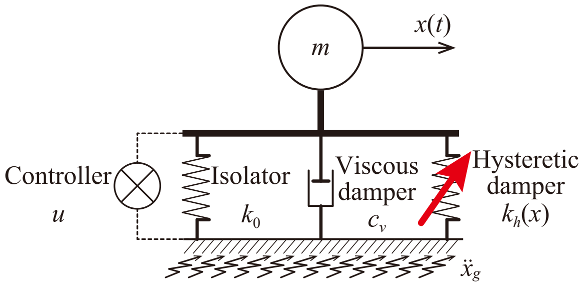

Figure 3.2: Mathematic model (nonlinear)

The isolation layer of the model contains a linear isolator, linear viscous damper, nonlinear hysteretic damper and an actuator. The restoring force of the isolator F_0 is proportional to the displacement (Fig. 3.3 (a)); the force of the viscous damper F_v is proportional to the velocity (Fig. 3.3 (b)).

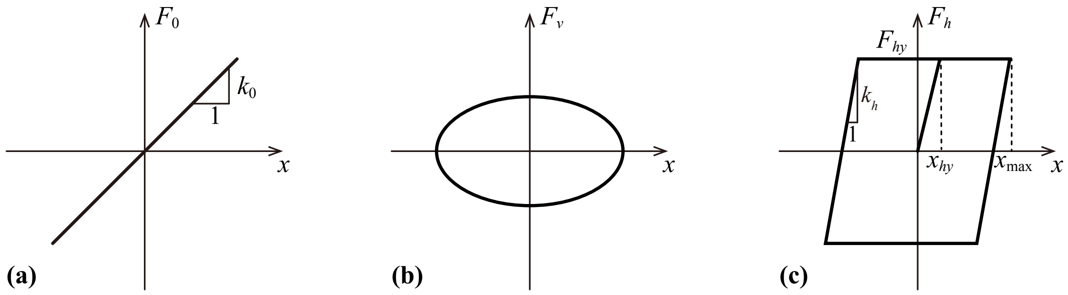

Figure 3.3: Force of (a) isolator, (b) viscous damper, and (c) hysteretic damper (nonlinear model)

The dynamics of the active model are described by the following equation:

$$m\ddot{x}(t) + c_v\dot{x}(t) + k_0x(t) + F_h(x) = -m\ddot{x}_g(t) - u(t), \tag{3.1}$$

$$F_h(x) = k_h f_h(x), \tag{3.2}$$

$$f_h(x) = \begin{cases} x + (x_{\max} - x_{hy}), & -x_{\max} \le x \le -(x_{\max} - 2x_{hy}) \text{ and } \dot{x} \ge 0, \\ x - (x_{\max} - x_{hy}), & x_{\max} - 2x_{hy} \le x \le x_{hy} \text{ and } \dot{x} \le 0, \\ x_{hy}, & -(x_{\max} - 2x_{hy}) \le x \le x_{\max} \text{ and } \dot{x} \ge 0, \\ -x_{hy}, & -x_{\max} \le x \le x_{\max} - 2x_{hy} \text{ and } \dot{x} \le 0, \end{cases} \tag{3.3}$$

where m is the mass; c_v is the damping-coefficient of the viscous damper; k_0 is the stiffness-coefficient of the isolator; F_h is the restoring force of the hysteretic damper; $x(t)$, $\dot{x}(t)$, and $\ddot{x}(t)$ are the displacement, velocity, and acceleration, respectively; $d(t)$ and $u(t)$ are disturbance force and control force, respectively; k_h is the 1st stiffness of the hysteretic damper; $x_{\max}$ is the maximum displacement; x_{hy} is the yield displacement of the hysteretic damper; k_0 and c_v are defined by

$$k_0 = m\omega_0^2 = m\frac{4\pi^2}{T_0^2} \text{ and} \tag{3.4}$$

$$c_v = 2\zeta_v\sqrt{mk_0}, \tag{3.5}$$

where ω_0 is the natural angular frequency of the structure; T_0 is the natural period of the isolator; ζ_v is the damping ratio of the viscous damper.

The state-space representation of (3.1) is

$$\dot{\mathbf{z}}(t) = \mathbf{A}\mathbf{z}(t) - \mathbf{B_h}F_h(t) + \mathbf{B_g}\ddot{x}_g(t) - \mathbf{B_u}u(t). \tag{3.6}$$

where $z(t)$ is a state vector; A is a system matrix; B_u is the input matrix for u; B_d is the input matrix for d; B_h is the input matrix for F_h, defined by

$$\mathbf{z}(t) = \begin{bmatrix} x(t) \\ \dot{x}(t) \end{bmatrix}, \tag{3.7a}$$

$$\mathbf{A} = \begin{bmatrix} 0 & 1 \\ -\frac{k_0}{m} & -\frac{c_v}{m} \end{bmatrix}, \text{ and} \tag{3.7b}$$

$$\mathbf{B_u} = \mathbf{B_h} = \begin{bmatrix} 0 \\ 1/m \end{bmatrix} \tag{3.7c}$$

$$\mathbf{B_g} = \begin{bmatrix} 0 \\ -1 \end{bmatrix}. \tag{3.7d}$$

Fig. 3.4 shows the block-diagram of the control system used in this study.

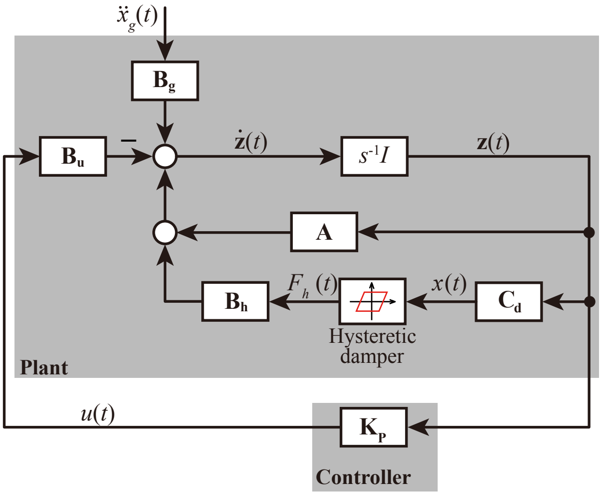

Figure 3.4: Block diagram of control system (nonlinear earthquake-resistant design)

Feedback control law

$$u(t) = \mathbf{K_P z}(t) = \begin{bmatrix} K_{PD} & K_{PV} \end{bmatrix} \begin{bmatrix} x(t) \\ \dot{x}(t) \end{bmatrix} = K_{PD}x(t) + K_{PV}\dot{x}(t), \tag{3.8}$$

is used, where $\mathbf{K_P}$ is the state-feedback gain.

3.3 Equivalent model of active model

Chapter 2 presented the method for constructing an equivalent model of linear control system. This chapter extends the equivalent model to the control system with nonlinear hysteretic dampers located at isolation layer. This section uses equivalent linearization method to substitute the a nonlinear hysteretic damper for a linear spring and linear dashpot. Thus, a nonlinear control system with viscous dampers and hysteretic dampers can be described as a linear model (see Fig. 3.5, $\hat{x}(t) = x(t)$), and the response spectrum and control-force spectrum can be used for a nonlinear control system.

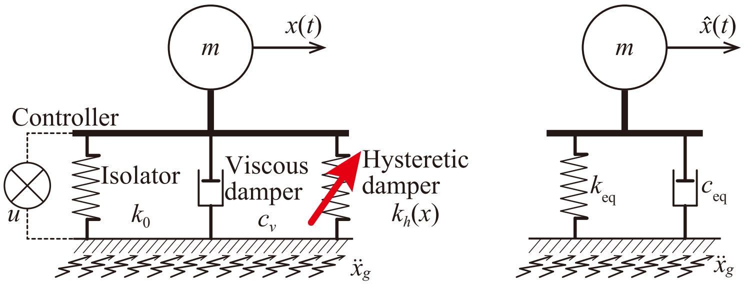

(a) (b)

Figure 3.5: Mathematic models: (a) active nonlinear model and (b) equivalent linear model ($\hat{x}(t) = x(t)$)

3.3.1 Construction of equivalent model of active model

The equivalent linear damper force, $F_{h,\text{eq}}$, of the hysteretic damper is assumed as the following equation:

$$F_{h,\text{eq}}(t) = k_{h,\text{eq}}x(t) + c_{h,\text{eq}}\dot{x}(t), \tag{3.9}$$

where $F_{h,\text{eq}}$ is the equivalent linear damper force of the hysteretic damper, $k_{h,\text{eq}}$ and $c_{h,\text{eq}}$ are the equivalent stiffness and equivalent damping coefficient of the hysteretic damper, respectively.

This paper uses the maximum-stiffness-displacement method to determine the equivalent stiffness and equivalent damping coefficient of the hysteretic damper, $k_{h,\text{eq}}$ and $c_{h,\text{eq}}$ [3.7]. The equivalent stiffness of the hysteretic damper, $k_{h,\text{eq}}$, is determined by the slope of the secant line of the maximum displacement point of the hysteresis curve (Fig. 3.6 (a)):

$$k_{h,\text{eq}} = \frac{F_{h,\max}}{x_{\max}}, \tag{3.10}$$

where $F_{h,\max}$ is the maximum restoring force of the hysteretic damper, and $x_{\max}$ is the maximum displacement.

The maximum restoring force of the hysteretic damper is presented as:

$$F_{h,\max} = \begin{cases} k_h x_{\max} & \text{if } x_{\max} < x_{hy}, \\ F_{hy} & \text{if } x_{\max} \geq x_{hy}. \end{cases} \tag{3.11}$$

The equivalent damping coefficient ($c_{h,\mathrm{eq}}$) of the hysteretic damper is determined by assuming that dissipated energies in one cycle for a linear dashpot and a hysteretic damper are the same (Fig. 3.6).

The energy dissipated by the hysteretic damper in one vibration cycle ΔW (Fig. 3.6 (a)) is

$$\Delta W = 4F_{hy}(x_{\max} - x_{hy}). \tag{3.12}$$

The energy dissipated by the linear dashpot in one vibration cycle of steady-state vibration ΔD (Fig. 3.6 (b)) is

$$\Delta D = \pi c_{h,\mathrm{eq}} \omega_{\mathrm{eq}} x_{\max}^2, \tag{3.13}$$

where ω_{eq} is the natural angular frequency of the equivalent model:

$$\omega_{\mathrm{eq}} = \sqrt{\frac{k_{\mathrm{eq}}}{m}}. \tag{3.14}$$

Assuming $\Delta W = \Delta D$ yields

$$4F_{hy}(x_{\max} - x_{hy}) = \pi c_{h,\mathrm{eq}} \omega_{\mathrm{eq}} x_{\max}^2. \tag{3.15}$$

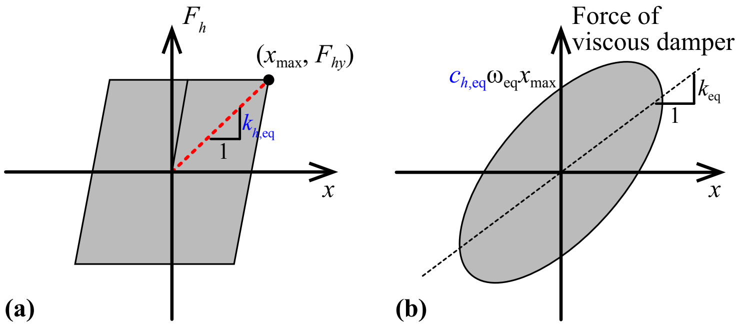

Figure 3.6: Equivalent dynamics characteristics of (a) equivalent stiffness and (b) equivalent damping coefficient: Area of (a) is the same of (b)

Thus, the damping coefficient of the equivalent model is

$$c_{h,\mathrm{eq}} = \frac{4F_{hy}(x_{\max} - x_{hy})}{\pi\omega_{\mathrm{eq}}x_{\max}^2}. \tag{3.16}$$

Substituting (3.8) and (3.9) into (3.1) yields

$$m\ddot{\hat{x}}(t) + c_{\mathrm{eq}}\dot{\hat{x}}(t) + k_{\mathrm{eq}}\hat{x}(t) = -m\ddot{x}_g(t), \tag{3.17}$$

$$k_{\mathrm{eq}} = k_0 + K_{PD} + k_{h,\mathrm{eq}}, \tag{3.18a}$$

$$c_{\mathrm{eq}} = c_v + K_{PV} + c_{h,\mathrm{eq}}, \tag{3.18b}$$

where $\hat{x}$ is the displacement of the equivalent linear model; k_{eq} is the stiffness of the equivalent linear model (equivalent stiffness); c_{eq} is the damping coefficient of the equivalent linear model (equivalent damping coefficient).

Moreover, to achieve the desired dynamic characteristics (k_{eq} and c_{eq}), we decide the controller gains K_P as follow:

$$K_{PD} = k_{\mathrm{eq}} - k_0 - k_{h,\mathrm{eq}}, \tag{3.19a}$$

$$K_{PV} = c_{\mathrm{eq}} - c_0 - c_{h,\mathrm{eq}}. \tag{3.19b}$$

3.3.2 Numerical verification

This section uses Taft NS, El Centro 1940 NS, JMA Kobe NS, and Code Hachinohe waves (Figs. 2.1~2.4) to verify the validity of the presented equivalent linear model of the active model. The natural period of the isolator, T_0, uses 4 s, and the damping ratio of the viscous damper, ζ_v, uses 0.10.

Figs. 3.7~3.14 shows the comparison of the maximum responses between the values of response spectra and equivalent linear models. Note that the maximum responses of the equivalent linear models are calculated from numerical simulation results. From Figs. 3.7~3.14, the following results are obtained:

- The maximum responses of the equivalent linear models matches well to the response spectra. Thus, the efficiency of the equivalent linear are validated.

- The estimation error of the equivalent linear models of the cases $\alpha_{hy} = 0.03$ is larger than that of the cases $\alpha_{hy} = 0.01$.

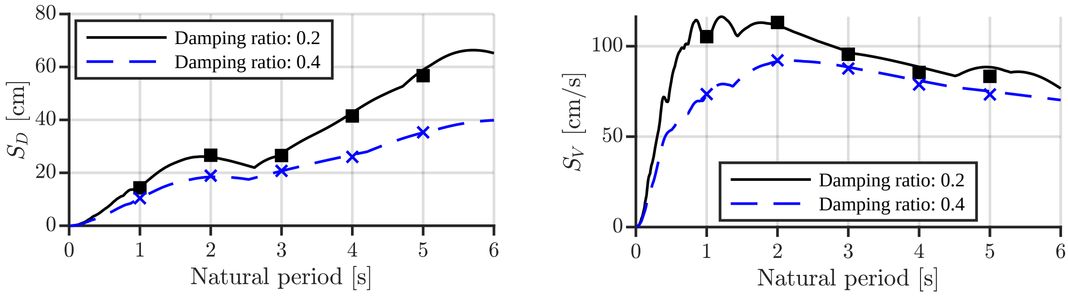

(a) Displacement response spectrum **(b)** Velocity response spectrum

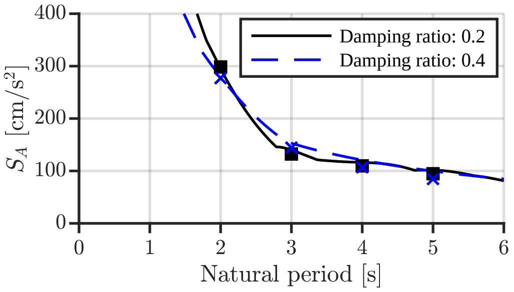

(c) Absolute acceleration response spectrum

Figure 3.7: Response spectra of Taft NS (T_0 = 3 s, ζ_v = 0.01, α_{hy} = 0.01)

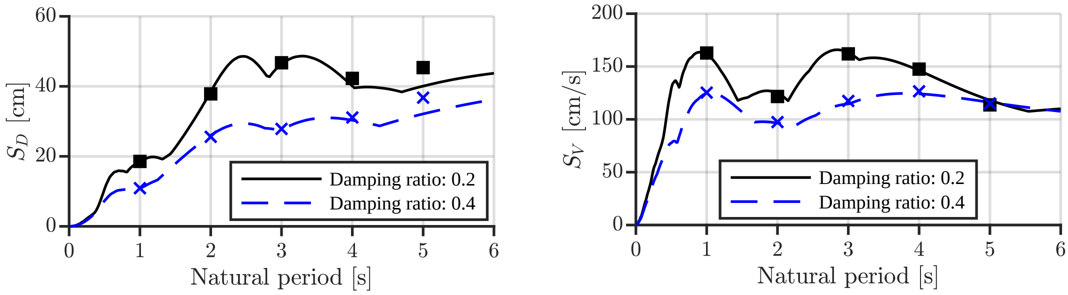

(a) Displacement response spectrum **(b)** Velocity response spectrum

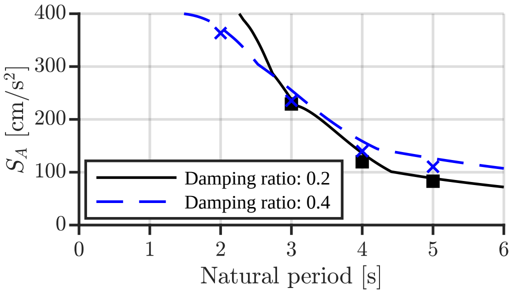

(c) Absolute acceleration response spectrum

Figure 3.8: Response spectra of El Centro 1940 NS (T_0 = 3 s, ζ_v = 0.01, α_{hy} = 0.01)

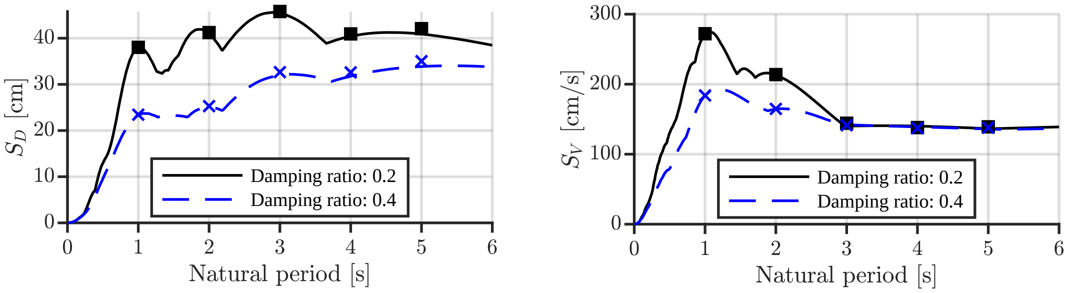

(a) Displacement response spectrum **(b)** Velocity response spectrum

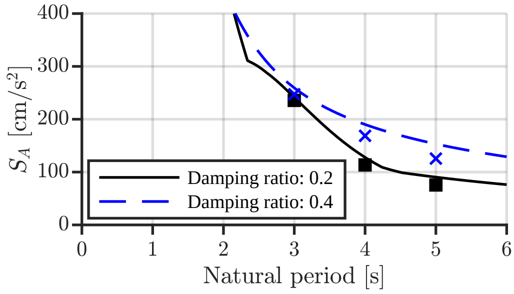

(c) absolute acceleration response spectrum

Figure 3.9: Response spectra of JMA Kobe NS (T_0 = 3 s, ζ_v = 0.01, α_{hy} = 0.01)

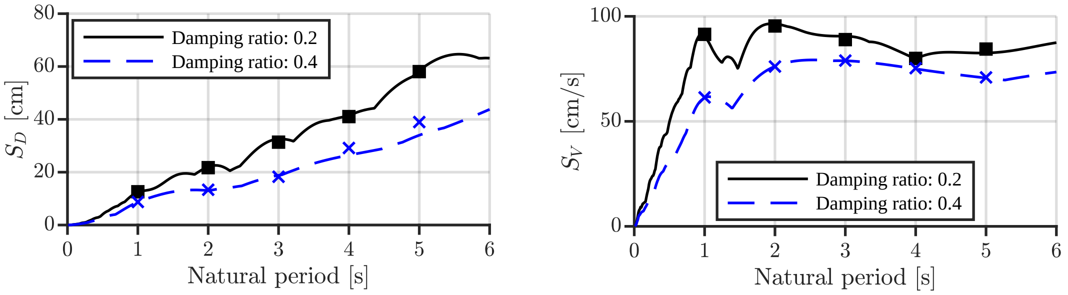

(a) Displacement response spectrum **(b)** Velocity response spectrum

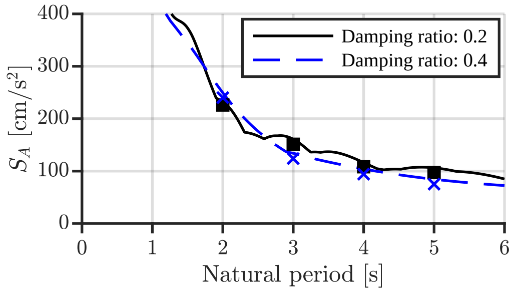

(c) absolute acceleration response spectrum

Figure 3.10: Response spectra of Code Hachinohe (T_0 = 3 s, ζ_v = 0.01, α_{hy} = 0.01)

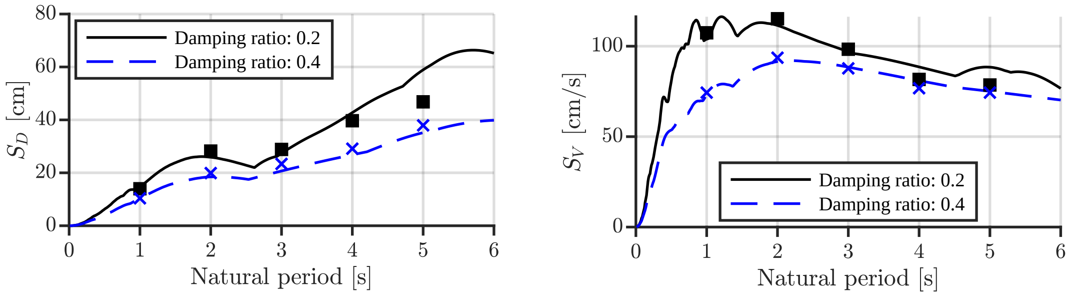

(a) Displacement response spectrum

(b) Velocity response spectrum

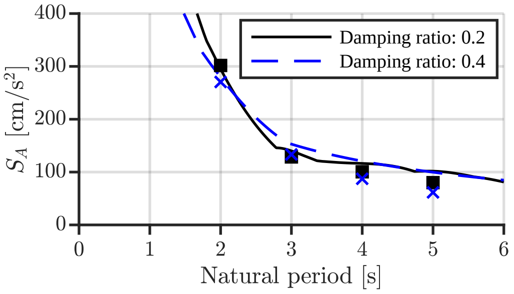

(c) Absolute acceleration response spectrum

Figure 3.11: Response spectra of Taft NS (T_0 = 3 s, ζ_v = 0.01, α_{hy} = 0.03)

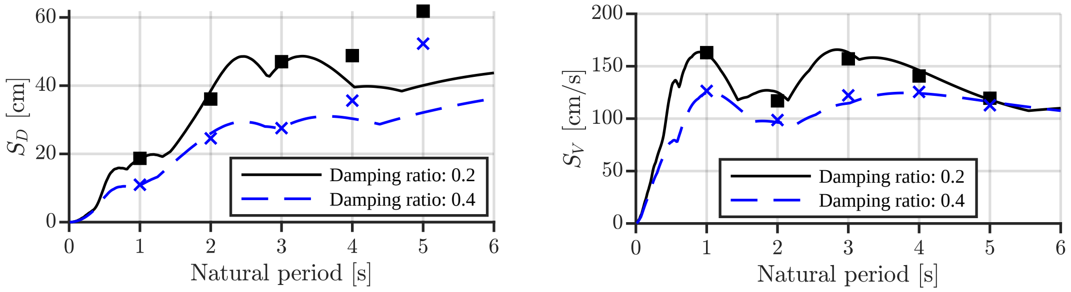

(a) Displacement response spectrum

(b) Velocity response spectrum

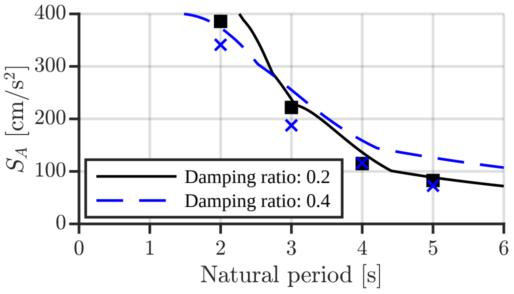

(c) Absolute acceleration response spectrum

Figure 3.12: Response spectra of El Centro 1940 NS (T_0 = 3 s, ζ_v = 0.01, α_{hy} = 0.03)

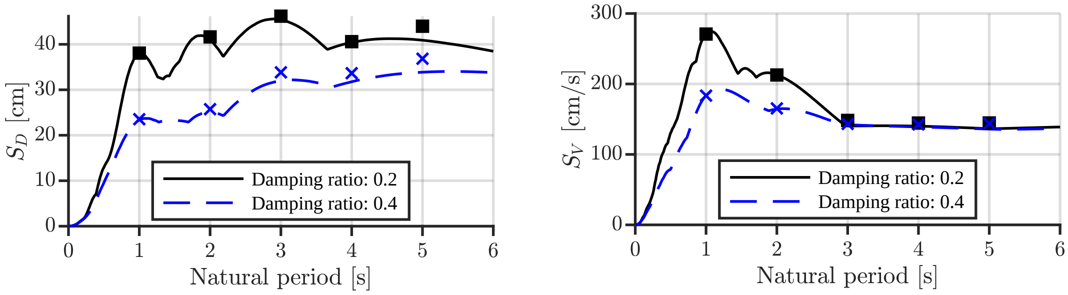

(a) Displacement response spectrum

(b) Velocity response spectrum

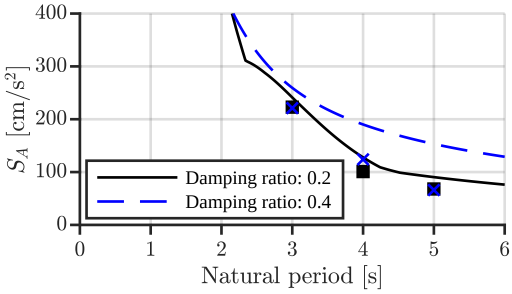

(c) absolute acceleration response spectrum

Figure 3.13: Response spectra of JMA Kobe NS (T_0 = 3 s, ζ_v = 0.01, α_{hy} = 0.03)

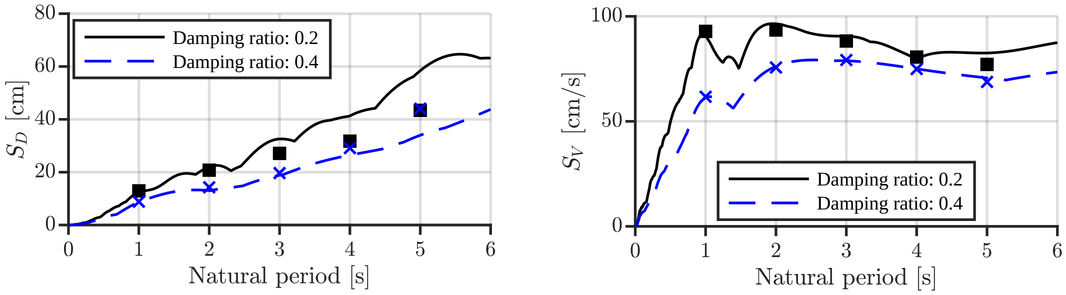

(a) Displacement response spectrum

(b) Velocity response spectrum

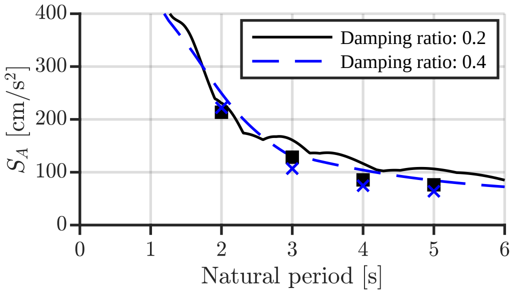

(c) absolute acceleration response spectrum

Figure 3.14: Response spectra of Code Hachinohe (T_0 = 3 s, ζ_v = 0.01, α_{hy} = 0.03)

3.4 Control-force spectrum

This section devises the control-force spectrum for an nonlinear control model, which expresses the dependency of the maximum control force on the all parameters for designing the control system, using the presented equivalent linear model. This section also uses the numerical examples to check the accuracy of the proposed control-force spectrum.

3.4.1 Derivation of the control-force spectrum

Substituting (3.19) in the control law, (3.8), the control force can be estimated by the following equation:

$$u(t) = (k_{\mathrm{eq}} - k_0 - k_{h,\mathrm{eq}})x(t) + (c_{\mathrm{eq}} - c_v - c_{h,\mathrm{eq}})\dot{x}(t). \tag{3.20}$$

Thus, the maximum control force, $u_{\max}$, is

$$u_{\max} = \max\left\{\left|(k_{\mathrm{eq}} - k_0 - k_{h,\mathrm{eq}})x(t) + (c_{\mathrm{eq}} - c_v - c_{h,\mathrm{eq}})\dot{x}(t)\right|\right\}. \tag{3.21}$$

Since the phase of displacement response is usually unequal to that of velocity response, the maximum displacement response and velocity response do not appear simultaneously in most cases. Therefore,

$$u_{\max} \le \left|k_{\mathrm{eq}} - k_0 - k_{h,\mathrm{eq}}\right| \max\left\{|x(t)|\right\} + \left|c_{\mathrm{eq}} - c_v - C_{h,\mathrm{eq}}\right| \max\left\{|\dot{x}(t)|\right\}. \tag{3.22}$$

From the response spectra of the earthquake, the maximum responses are estimated without numerical simulations:

$$\max\left\{|x(t)|\right\} = S_D(T_{\mathrm{eq}}, \zeta_{\mathrm{eq}}) \text{ and} \tag{3.23a}$$

$$\max\left\{|\dot{x}(t)|\right\} = S_V(T_{\mathrm{eq}}, \zeta_{\mathrm{eq}}), \tag{3.23b}$$

where $S_D(T_{\mathrm{eq}}, \zeta_{\mathrm{eq}})$ and $S_V(T_{\mathrm{eq}}, \zeta_{\mathrm{eq}})$ are the maximum displacement response and the maximum velocity response refer to the displacement response spectrum and the velocity response spectrum of the earthquake, respectively.

Substituting (3.23) into (3.22) yields

$$u_{\max} \leq \left|k_{\mathrm{eq}} - k_0 - k_{h,\mathrm{eq}}\right| S_D(T_{\mathrm{eq}}, \zeta_{\mathrm{eq}}) + \left|c_{\mathrm{eq}} - c_v - c_{h,\mathrm{eq}}\right| S_V(T_{\mathrm{eq}}, \zeta_{\mathrm{eq}}). \tag{3.24}$$

The maximum control force, $u_{\max}$, divided by the weight of the structure, mg, yields the maximum shear-force coefficient of the maximum control, $C_{u,\max}$:

$$C_{u,\max} = \frac{u_{\max}}{mg} \leq C_{uD,\max} + C_{uV,\max}\,, \tag{3.25}$$

where

$$C_{uD,\max} = \frac{\left|k_{\mathrm{eq}} - k_0 - k_{h,\mathrm{eq}}\right|}{mg} S_D(T_{\mathrm{eq}}, \zeta_{\mathrm{eq}}) \text{ and} \tag{3.26a}$$

$$C_{uV,\max} = \frac{\left|c_{\mathrm{eq}} - c_v - c_{h,\mathrm{eq}}\right|}{mg} S_V(T_{\mathrm{eq}}, \zeta_{\mathrm{eq}}). \tag{3.26b}$$

From (3.25), the shear-force coefficient of the maximum control force, $C_{u,\max}$, contains both the displacement component, S_D, and the velocity component, S_V. Since the maximum displacement and velocity usually do not appear at the same time, this paper uses the square root of the sum of squares (SRSS) method to estimate the maximum shear-force coefficient of the control force and defines the following estimation equation as the control-force spectrum, S_C:

$$S_C(T_0, \zeta_v, T_{\mathrm{eq}}, \zeta_{\mathrm{eq}}, \alpha_{hy}) := \sqrt{C_{uD,\max}^2 + C_{uV,\max}^2}. \tag{3.27}$$

The control-force spectrum, S_C, estimates the maximum control force only using the response spectra of the equivalent model and does not require additional numerical simulations, and it is a function of the natural period of the structure, T_0, the damping ratio of the structure, ζ_v, the equivalent natural period, T_{eq}, the equivalent damping ratio, ζ_{eq}, and the shear-force ratio of the hysteretic damper.

Using the control-force spectrum proposed in this section, (3.27), the maximum control force are estimated only by the response spectra without additional numerical simulation.

3.4.2 Numerical verification

Figs. 3.15 and 3.16 show control-force prediction spectra for Taft NS, El Centro 1940 NS, JMA Kobe NS, and Code Hachinohe waves with different damping ratios. The natural period of the isolator, T_0, uses 4 s, and the damping ratio of the viscous damper, ζ_v, uses 0.10.

From Figs. 3.15 and 3.16, it can be seen that the maximum control force estimated by control-force spectra matches well to the values of simulation results. Thus, the efficiency of the presented control-force spectra is confirmed.

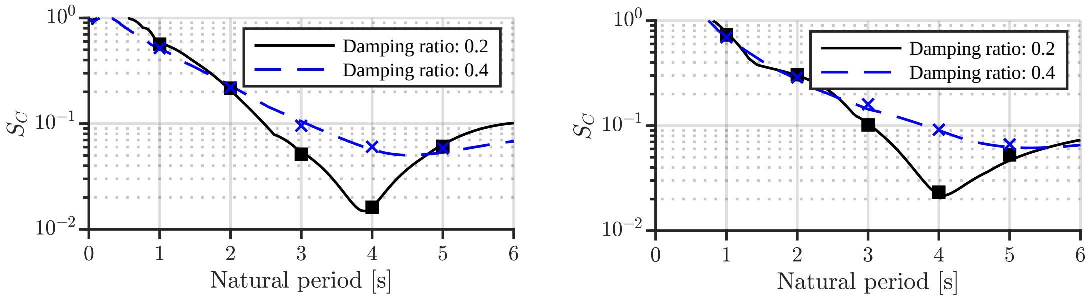

(a) Taft NS **(b)** El Centro 1940 NS

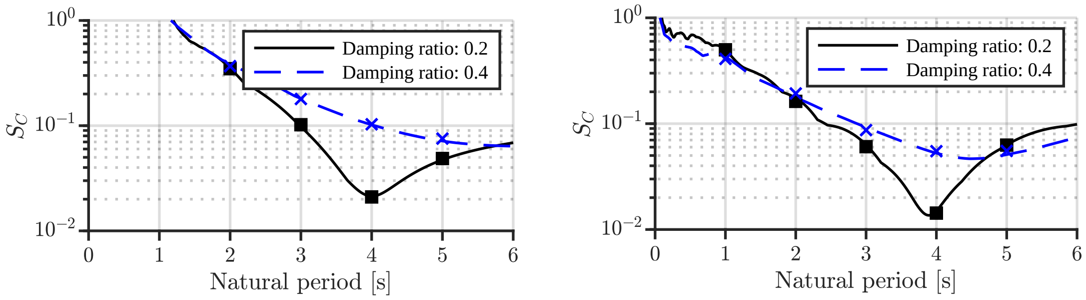

(c) JMA Kobe NS **(d)** Code Hachinohe

Figure 3.15: Control-force spectra (T_0 = 4 s, ζ_v = 0.01, and α_{hy} = 0.01)

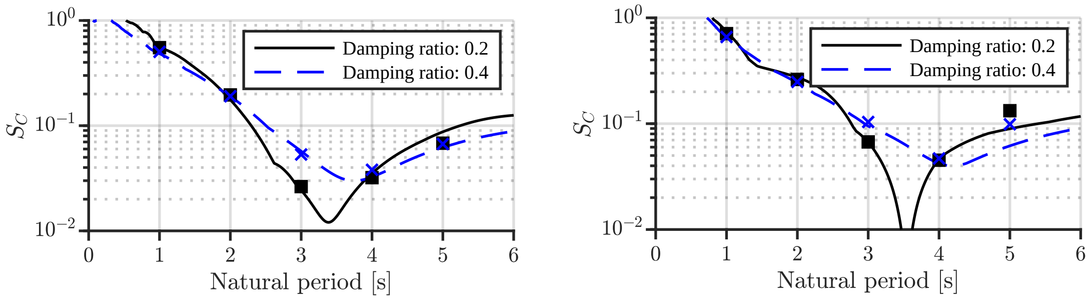

(a) Taft NS **(b)** El Centro 1940 NS

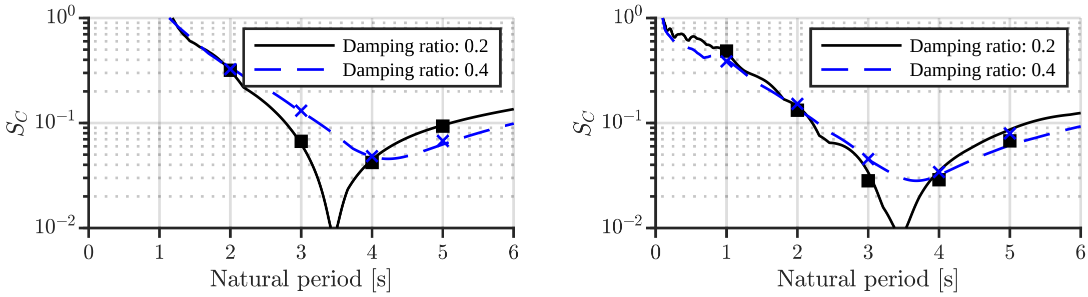

(c) JMA Kobe NS **(d)** Code Hachinohe

Figure 3.16: Control-force spectra (T_0 = 4 s and ζ_v = 0.03)

3.5 Design method

Fig. 3.17 presents the design flowchart presented in this study. This method uses only the response spectrum to estimate the maximum responses and maximum control force of the system and does not require numerical simulations or trial-and-error approaches.

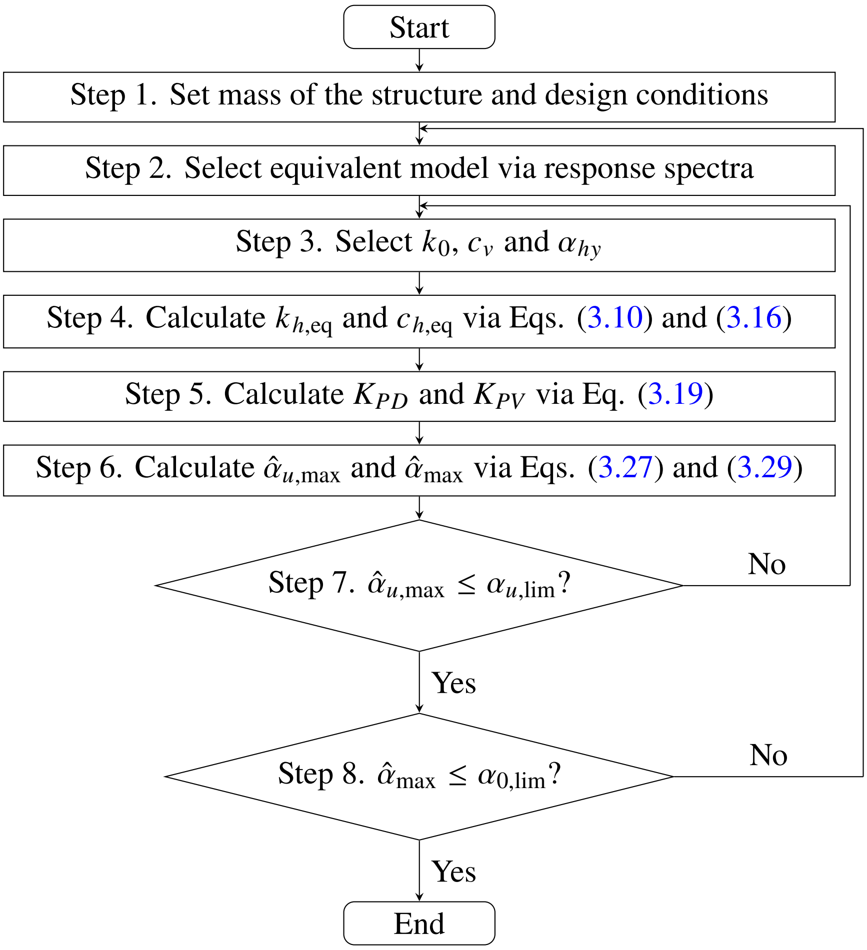

Figure 3.17: Design flowchart (nonlinear earthquake-resistant design)

3.5.1 Design algorithm

Step 1. Provide the mass of the structure and design conditions (design earthquake wave and design criteria).

Step 2. Select the equivalent model (k_{eq} and c_{eq}) using the response spectra of the design earthquake that satisfies the design limitations of the responses set in Step 1.

Step 3. Select the stiffness of the isolator, damping of the viscous damper, and the shear-force ratio of yield force of the hysteretic damper (k_0, c_v, and α_{hy}).

Step 4. Obtain the equivalent stiffness and equivalent damping coefficient of the hysteretic damper ($k_{h,\mathrm{eq}}$ and $c_{h,\mathrm{eq}}$), using Eqs. (3.10) and (3.16), respectively.

Step 5. Obtain the feedback gain, $\mathbf{K_P}$ using Eq. (3.19).

Step 6. Obtain the shear-force ratio of the maximum shear-force ratio of control force, $\alpha_{u,\max}$, using the control-force spectrum, Eq. (3.27):

$$\hat{\alpha}_{u,\max} = \sqrt{(K_{PD}\hat{x}_{\max})^2 + (K_{PV}\dot{\hat{x}}_{\max})^2}; \tag{3.28}$$

obtain the maximum story-shear-force ratio of the equivalent model, $\hat{\alpha}_{u,\max}$, using the square-root of the sum-of-squares [3.11]:

$$\hat{\alpha}_{\max} = \sqrt{(k_{\mathrm{eq}}\hat{x}_{max})^2 + (c_{\mathrm{eq}}\dot{\hat{x}}_{\max})^2}, \tag{3.29}$$

where $\hat{x}_{\max}$ and $\dot{\hat{x}}_{\max}$ are the maximum displacement and maximum velocity of the equivalent linear model, respectively. Note that, the values of $\hat{x}_{max}$ and $\dot{\hat{x}}_{max}$ can be estimated from the spectra in Step 2.

Step 7. If the design limitation of the shear-force ratio of the control force, $\alpha_{u,\mathrm{lim}}$, is satisfied, proceed to the next step. If not, return to Step 3, thereby operating one or both of the following actions:

- Selecting another natural period of the isolator, T_0, which is near the equivalent natural period, T_{eq}.
- Increasing the damping ratio of the viscous damper, ζ_v.

Step 8. If the design limitation of the story-shear-force ratio, $\alpha_{0,\mathrm{lim}}$, is satisfied, end the design. If not, return to Step 2, thereby selecting another equivalent model.

3.5.2 Design example

Step 1. Parameters of the structure: Refer to Table 3.1,

design earthquake wave: ArtKobe-120 (Fig. 2.4),

design criteria: shown at Table 3.2.

Table 3.1
Parameters of design models (nonlinear earthquake-resistant design)

Item	Symbol	Value
Mass [kg]	m	1.00
Natural period of isolator [s]	T_0	4.00
Stiffness of isolator [N/m]	k_0	2.47
Damping ratio of viscous damper	ζ_v	0.05
Damping coefficient of viscous damper [Ns/m]	c_v	0.16
Shear-force ratio of yield force	α_{hy}	0.00~0.05
Initial stiffness [N/m]	k_h	9.80
Secondary stiffness [N/m]	-	0
Yield displacement [m]	x_{hy}	0.03

Table 3.2
Design criteria (nonlinear earthquake-resistant design)

Design limitation of displacement	x_{lim}	0.30 m
Design limitation of velocity	$\dot{x}_{\text{lim}}$	1.50 m/s
Design limitation of absolute acceleration	$\{\ddot{x}+\ddot{x}_g\}_{\text{lim}}$	1.50 m/s^2
Design limitation of shear-force ratio of control force	$\alpha_{u,\text{lim}}$	0.05
Design limitation of shear-force ratio of isolation layer	α_{lim}	0.12

Step 2. Fig. 3.18 shows the displacement-response spectrum (S_D), velocity-response spectrum (S_V), and absolute-acceleration-response spectrum (S_A) of ArtKobe-120. From Fig. 3.18, we select the equivalent model, $T_{\text{eq}} = 4$ s and $\zeta_{\text{eq}} = 0.5$ ($k_{\text{eq}} = 2.47$ N/m and $c_{\text{eq}} = 1.57$ Ns/m), that satisfies design limitations of the displacement ($\hat{x}_{\text{max}} = 0.25$ m), velocity ($\dot{\hat{x}}_{\text{max}} = 0.63$ m/s), absolute acceleration ($\{\ddot{\hat{x}} + \ddot{x}_g\}_{\text{max}} = 1.16$ m/s^2).

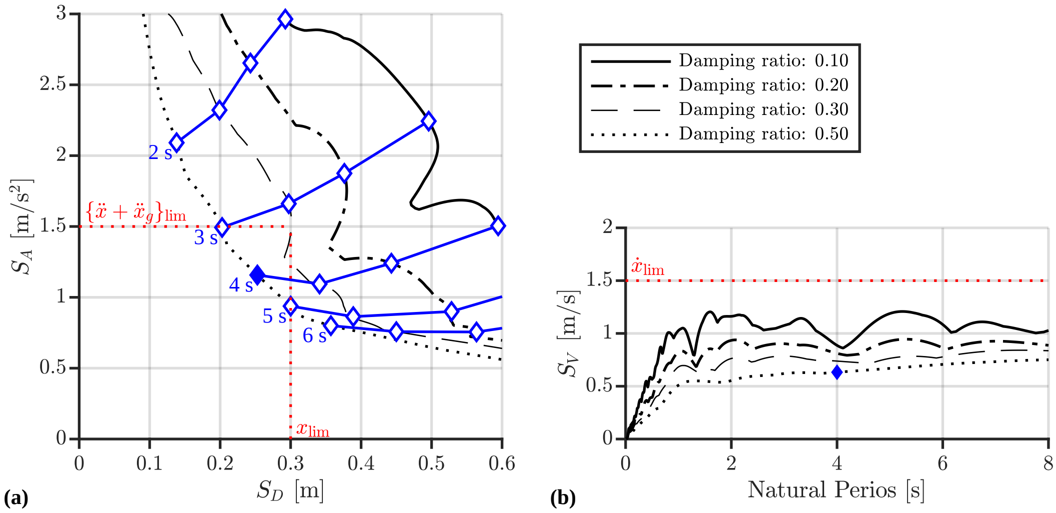

Figure 3.18: Response spectra of Code Hachinohe: (a) S_D against S_A and (b) S_V

Step 3. We select the following 2 models, P and A models. The 2 models have the same shear-force ratio of the yield force of the hysteretic dampers, α_{hy}, but Model P installs more viscous dampers and model A installs less viscous dampers. Thus, the damping coefficient of Model P is larger than that of Model A, and the required control force of Model P is expected to be less than that of Model A.

Model P: $\alpha_{hy} = 0.03$, $T_0 = 4$ s and $\zeta_v = 0.20$ ($k_0 = 2.47$ N/m and $c_v = 0.63$ Ns/m).

Model A: $\alpha_{hy} = 0.03$, $T_0 = 4$ s and $\zeta_v = 0.10$ ($k_0 = 2.47$ N/m and $c_v = 0.31$ Ns/m).

Step 4. Using Eqs. (3.10) and (3.16), the equivalent stiffness and equivalent damping coefficient are obtained. In addition, The estimated maximum displacement of the equivalent model is obtained from the displacement spectrum ($x_{\max} = 0.25$ m, see Fig. 3.18).

Model P:

$$k_{h,\text{eq}} = \frac{F_{h,\max}}{x_{\max}} = \frac{0.02mg}{x_{\max}} = 1.16 \text{ N/m},$$

$$c_{h,\text{eq}} = \frac{4F_{hy}(x_{\max} - x_{hy})}{\pi\omega_{h,\text{eq}}x_{\max}^2} = 0.83 \text{ Ns/m}.$$

Model A:

$$k_{h,\text{eq}} = \frac{F_{h,\max}}{x_{\max}} = \frac{0.02mg}{x_{\max}} = 1.16 \text{ N/m},$$

$$c_{h,\text{eq}} = \frac{4F_{hy}(x_{\max} - x_{hy})}{\pi\omega_{h,\text{eq}}x_{\max}^2} = 0.83 \text{ Ns/m}.$$

Step 5. Using Eq. (3.19b), the feedback gain is obtained:

Model P:

$$K_{PD} = k_{\text{eq}} - k_0 - k_{h,\text{eq}} = 2.47 - 2.47 - 1.16 = -1.16 \text{ N/m},$$

$$K_{PV} = c_{\text{eq}} - c_v - c_{h,\text{eq}} = 1.57 - 0.63 - 0.83 = 0.11 \text{ Ns/m}.$$

Model A:

$$K_{PD} = k_{\text{eq}} - k_0 - k_{h,\text{eq}} = 2.47 - 2.47 - 1.16 = -1.16 \text{ N/m},$$

$$K_{PV} = c_{\text{eq}} - c_v - c_{h,\text{eq}} = 1.57 - 0.31 - 0.83 = 0.43 \text{ Ns/m}.$$

Step 6. From Eqs. (3.28) and (3.29), the maximum shear-force ratio of control force, $\hat{\alpha}_{u,\max}$, and maximum story-shear-force ratio, $\hat{\alpha}_{\max}$, of models 1 and 2 are given below:

Model P:

$$\hat{\alpha}_{u,\mathrm{max}} = \sqrt{(K_{PD}\hat{x}_{\mathrm{max}})^2 + (K_{PV}\dot{\hat{x}}_{\mathrm{max}})^2} = 0.031,$$

$$\hat{\alpha}_{\mathrm{max}} = \sqrt{(k_{\mathrm{eq}}\hat{x}_{max})^2 + (c_{\mathrm{eq}}\dot{\hat{x}}_{\mathrm{max}})^2} = 0.12.$$

Model A:

$$\hat{\alpha}_{u,\mathrm{max}} = \sqrt{(K_{PD}\hat{x}_{\mathrm{max}})^2 + (K_{PV}\dot{\hat{x}}_{\mathrm{max}})^2} = 0.041,$$

$$\hat{\alpha}_{\mathrm{max}} = \sqrt{(k_{\mathrm{eq}}\hat{x}_{max})^2 + (c_{\mathrm{eq}}\dot{\hat{x}}_{\mathrm{max}})^2} = 0.12.$$

Step 7. Since the design limitation of the maximum shear-force ratio of control force of both P and A models are satisfied, $\alpha_{u,\mathrm{max}} \leq \alpha_{u,\mathrm{lim}}$, go to the next step.

Step 8. Since the design limitation of the maximum story-shear-force ratio is satisfied, $\alpha_{\mathrm{max}} \leq \alpha_{0,\mathrm{lim}}$, end the design.

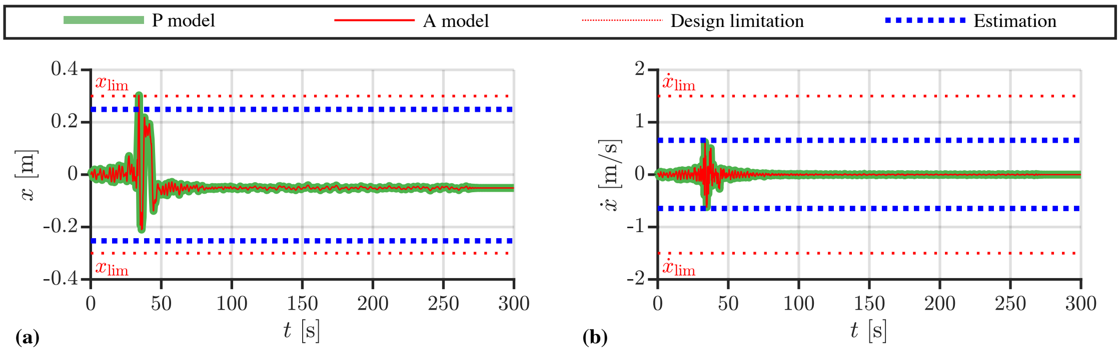

(a) Displacement **(b)** Velocity

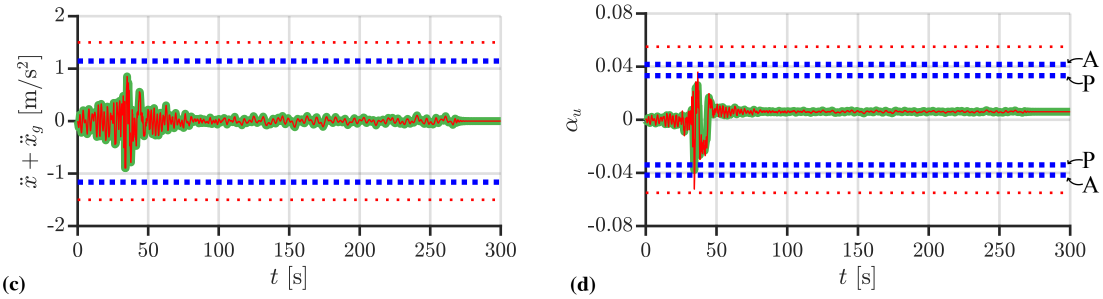

(c) Absolute acceleration **(d)** Shear-force of control force

Figure 3.19: Time-history wave of numerical simulation results for nonlinear earthquake-resistant design example

3.6 Conclusion

In this section, we presented a method for constructing an equivalent linear model for an active nonlinear model. We also devised a method for determining the feedback gain for an active nonlinear model that achieves the desired dynamics. The presented method neither requires an iterative operation to construct the equivalent linear model nor trial-and-error approaches to determine the feedback gain, which is essential for conventional design. Moreover, this section proposes a design method for nonlinear active base-isolation. The design method simplifies the conventional design procedure based on the following points:

1. It estimates the maximum responses of the control system via response spectra.
2. It estimates the maximum control force of the control system via control-force spectrum.
3. It does not require iterative operations to calculate the equivalent stiffness and equivalent damping coefficient of the hysteretic damper.
4. It does not require iterative approaches to determine the feedback gain.

The numerical design example shows the efficiency of the design method.

Appendix 3A Maximum-displacement-stiffness method vs. least-squares method vs. Newmark-Rothenbluth method

Subsection 3.3.1 presented the maximum-displacement-stiffness method for calculating the equivalent stiffness and equivalent damping coefficient of the hysteretic damper ($k_{h,\mathrm{eq}}$ and $c_{h,\mathrm{eq}}$). This section shows other 2 methods, least-square method [3.7] and Newmark-Rosenblueth method [3.7], for calculating $k_{h,\mathrm{eq}}$ and $c_{h,\mathrm{eq}}$, and compares their accuracy. Since the active control component of equivalent model does not has error [3.7], this section uses a passive model (Fig 3.20).

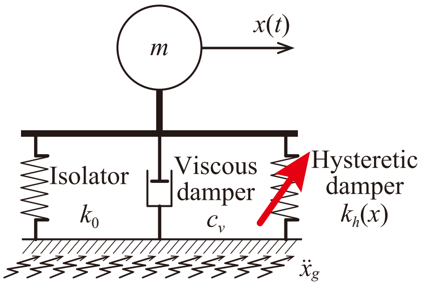

Figure 3.20: SDOF model with hysteretic damper

3A.1 Least-square method

Considering a cosine ground motion,

$$x_g = x_{\max} \cos \omega_{\mathrm{eq}} t, \tag{3.30}$$

inputs on the model. The vibration equation (without ASC) of the model is

$$m\ddot{x}(t) + c\dot{x}(t) + kx(t) + F_h(x) = m\alpha \cos \omega_{\mathrm{eq}} t \tag{3.31}$$

with

$$\alpha = x_{\max}\omega_{\mathrm{eq}}^2. \tag{3.32}$$

Substituting the equivalent force of the hysteretic damper, (3.9), into (3.31) yields

$$m\ddot{x}(t) + c_{\mathrm{eq}}\dot{x}(t) + k_{\mathrm{eq}}x(t) + \epsilon(x, \dot{x}, t) = m\alpha \cos pt, \tag{3.33}$$

with

$$\begin{aligned}\overline{\epsilon^2} &= \overline{\left[k_{h,\mathrm{eq}}x + c_{h,\mathrm{eq}}\dot{x} - k_h f_h(x)\right]^2} \\ &= \frac{\omega_{\mathrm{eq}}}{2\pi}\int_0^{T_{\mathrm{eq}}} \left[k_{h,\mathrm{eq}}x + c_{h,\mathrm{eq}}\dot{x} - k_h f_h(x)\right]^2 \mathrm{d}t \rightarrow \min,\end{aligned} \tag{3.34}$$

where ϵ is the error component.

By minimizing error component, ϵ, the following 2 conditions are obtained:

$$\frac{\partial\overline{\epsilon^2}}{\partial k_{h,\mathrm{eq}}} = 0, \tag{3.35a}$$

$$\frac{\partial\overline{\epsilon^2}}{\partial c_{h,\mathrm{eq}}} = 0. \tag{3.35b}$$

From (3.34) and (3.35) yields

$$\int_0^{T_{\mathrm{eq}}} \left[k_{h,\mathrm{eq}}x + c_{h,\mathrm{eq}}\dot{x} - k_h f_h(x)\right] x\mathrm{d}t, \tag{3.36a}$$

$$\int_0^{T_{\mathrm{eq}}} \left[k_{h,\mathrm{eq}}x + c_{h,\mathrm{eq}}\dot{x} - k_h f_h(x)\right] \dot{x}\mathrm{d}t. \tag{3.36b}$$

Assuming the approximate solution of (3.33) ignoring the error component, ϵ, is

$$x(t) = x_{\max}\cos(\omega_{\mathrm{eq}}t - \phi). \tag{3.37}$$

Substituting

$$\int_0^{T_{\mathrm{eq}}} \dot{x}x\mathrm{d}t = 0 \tag{3.38}$$

into (3.36) yields

$$k_{h,\mathrm{eq}} = \frac{\int_0^{T_{\mathrm{eq}}} k_h f_h(x)x\mathrm{d}t}{\int_0^{T_{\mathrm{eq}}} x^2\mathrm{d}t}, \tag{3.39a}$$

$$c_{h,\mathrm{eq}} = \frac{\int_0^{T_{\mathrm{eq}}} k_h f_h(x)\dot{x}\mathrm{d}t}{\int_0^{T_{\mathrm{eq}}} \dot{x}^2\mathrm{d}t} \tag{3.39b}$$

Assuming $\theta = \omega_{\text{eq}}t - \phi$ yields

$$\begin{aligned} k_{h,\text{eq}} &= \frac{\int_0^{2\pi} k_h f_h(x_{\max}\cos\theta) x_{\max}\cos\theta \mathrm{d}\theta}{\int_0^{2\pi} x_{\max}^2 \cos^2\theta \mathrm{d}\theta} \\ &= k\left[\frac{\int_0^{2\pi} f_h(x_{\max}\cos\theta)\cos\theta \mathrm{d}\theta}{\pi x_{\max}}\right], \end{aligned} \tag{3.40a}$$

$$\begin{aligned} c_{h,\text{eq}} &= \frac{\int_0^{2\pi} k_h f_h(x_{\max}\cos\theta)(-x_{\max}\omega_{\text{eq}}\sin\theta)\mathrm{d}\theta}{\int_0^{2\pi} x_{\max}^2 \omega^2 \sin^2\theta \mathrm{d}\theta} \\ &= -\frac{k_h}{\omega_{\text{eq}}}\left[\frac{\int_0^{2\pi} f_d(x_{\max}\cos\theta)\sin\theta \mathrm{d}\theta}{\pi x_{\max}}\right] \end{aligned} \tag{3.40b}$$

3A.2 Newmark-Rosenblueth method

The Newmark-Rosenblueth method for calculating the equivalent stiffness and equivalent damping are given below:

$$k_{\text{eq}} = \frac{4\pi^2 m}{T_{\text{eq}}^2}, \tag{3.41a}$$

$$c_{\text{eq}} = 2m\zeta_{\text{eq}}\omega_{\text{eq}}, \tag{3.41b}$$

with

$$T_{\text{eq}} = T_0\sqrt{\frac{\mu}{\mu\gamma - \gamma + 1}}, \tag{3.42a}$$

$$\zeta_{\text{eq}} = \frac{c_0}{2\sqrt{k_{\text{eq}}m}} + \frac{2}{\mu\gamma\pi}\ln\frac{\mu\gamma - \gamma + 1}{\mu}, \tag{3.42b}$$

where μ and γ are the maximum plasticity rate and the second stiffness rate, respectively:

$$\mu = \frac{x_{\max}}{x_{hy}}, \tag{3.43a}$$

$$\gamma = \frac{k_0 + k_{h,\text{eq}}}{k_0 + k_h}. \tag{3.43b}$$

3A.3 Numerical examples

This section shows the numerical examples comparing the errors of maximum-displacement-stiffness method, least-square method, and Newmark-Rosenblueth method under El Centro 1940 NS (Fig. 2.2) and Code Hachinohe (Fig. 2.4) waves. Figs. 3.21~3.26 shows the errors of these 3 methods. From Figs. 3.21~3.26, it can be seen that errors of these 3 methods are almost in the same level. Thus, this paper uses the maximum-displacement-stiffness method, the simplest method of theses 3 methods.

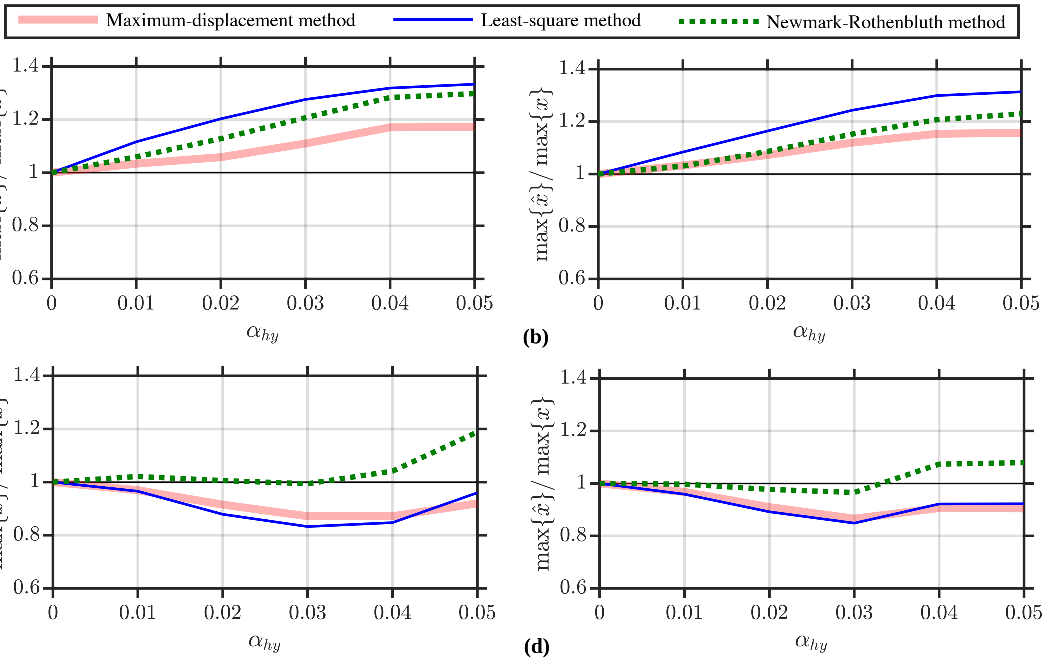

Figure 3.21: Maximum-displacement-stiffness method vs. least-square method vs. Newmark-Rosenblueth method for maximum displacement under El Centro wave : (a) T_0 = 2 s and ζ_v = 0.05, (b) T_0 = 2 s and ζ_v = 0.10, (c) T_0 = 4 s and ζ_v = 0.05, and (d) T_0 = 4 s and ζ_v = 0.10

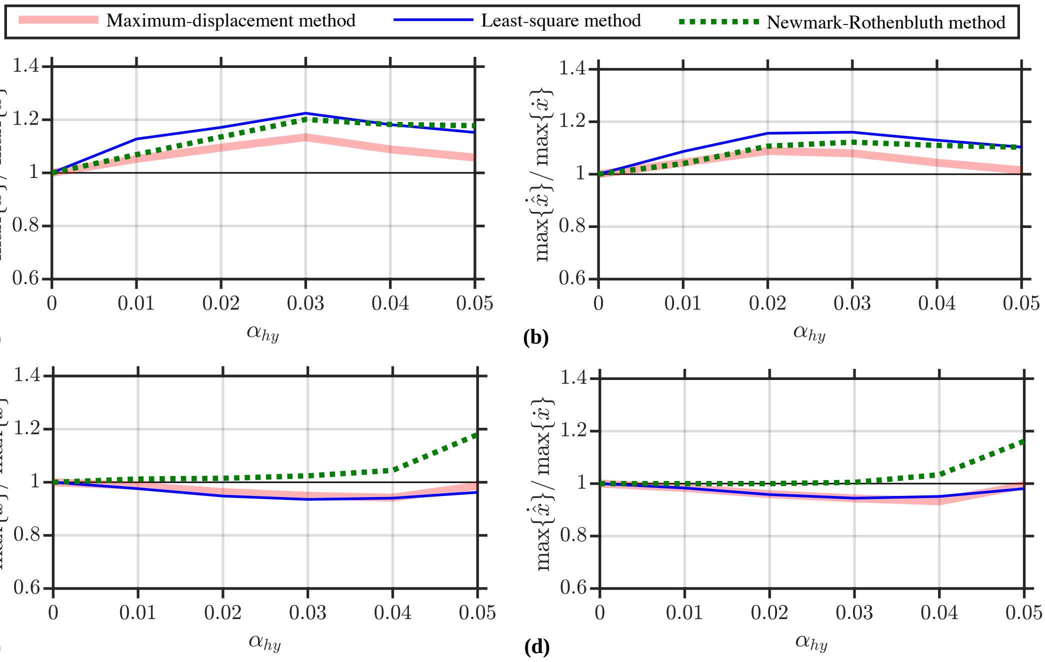

Figure 3.22: Maximum-displacement-stiffness method vs. least-square method vs. Newmark-Rosenblueth method for maximum velocity under El Centro wave : (a) T_0 = 2 s and ζ_v = 0.05, (b) T_0 = 2 s and ζ_v = 0.10, (c) T_0 = 4 s and ζ_v = 0.05, and (d) T_0 = 4 s and ζ_v = 0.10

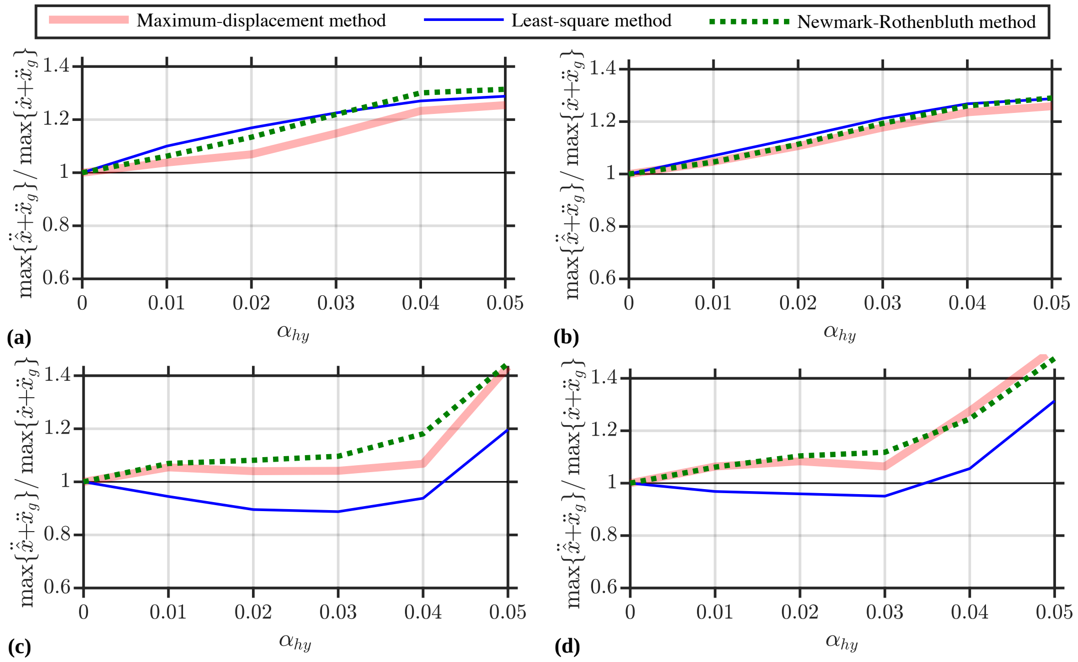

Figure 3.23: Maximum-displacement-stiffness method vs. least-square method vs. Newmark-Rosenblueth method for maximum absolute under El Centro wave : (a) $T_0 = 2$ s and $\zeta_v = 0.05$, (b) $T_0 = 2$ s and $\zeta_v = 0.10$, (c) $T_0 = 4$ s and $\zeta_v = 0.05$, and (d) $T_0 = 4$ s and $\zeta_v = 0.10$

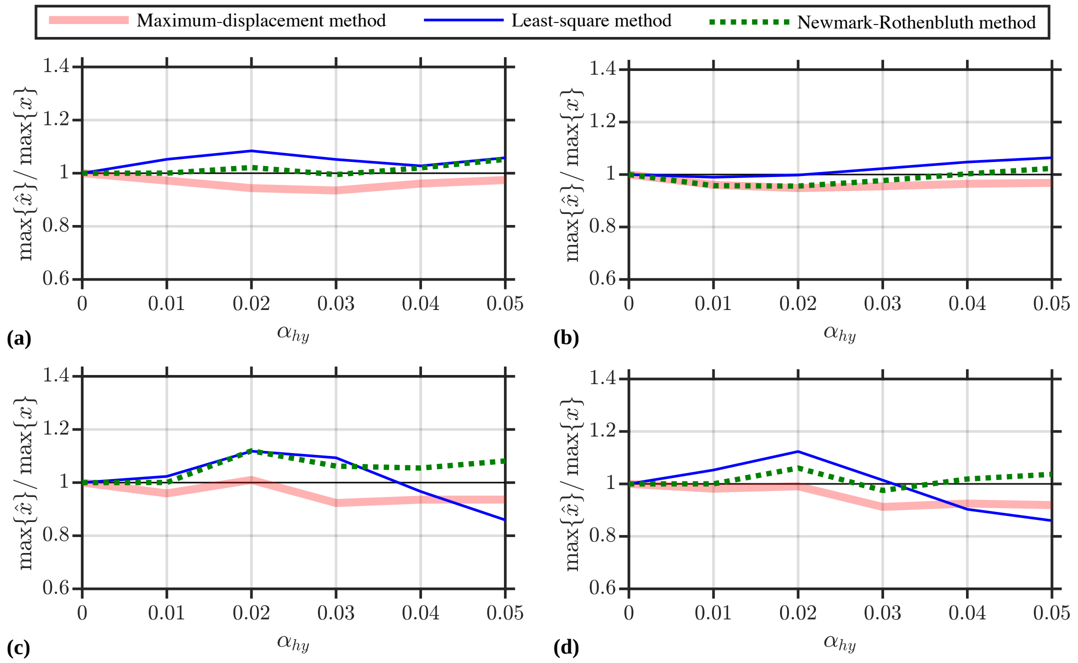

Figure 3.24: Maximum-displacement-stiffness method vs. least-square method vs. Newmark-Rosenblueth method for maximum displacement under Art. Kobe wave : (a) $T_0 = 2$ s and $\zeta_v = 0.05$, (b) $T_0 = 2$ s and $\zeta_v = 0.10$, (c) $T_0 = 4$ s and $\zeta_v = 0.05$, and (d) $T_0 = 4$ s and $\zeta_v = 0.10$

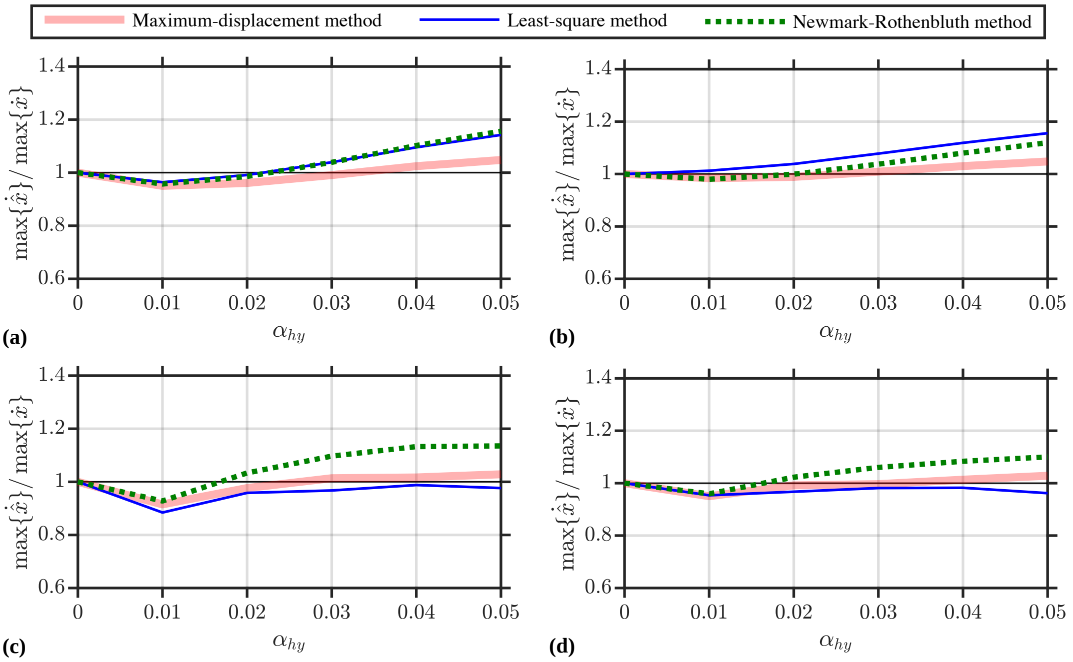

Figure 3.25: Maximum-displacement-stiffness method vs. least-square method vs. Newmark-Rosenblueth method for maximum velocity under Code Hachinohe wave : (a) T_0 = 2 s and ζ_v = 0.05, (b) T_0 = 2 s and ζ_v = 0.10, (c) T_0 = 4 s and ζ_v = 0.05, and (d) T_0 = 4 s and ζ_v = 0.10

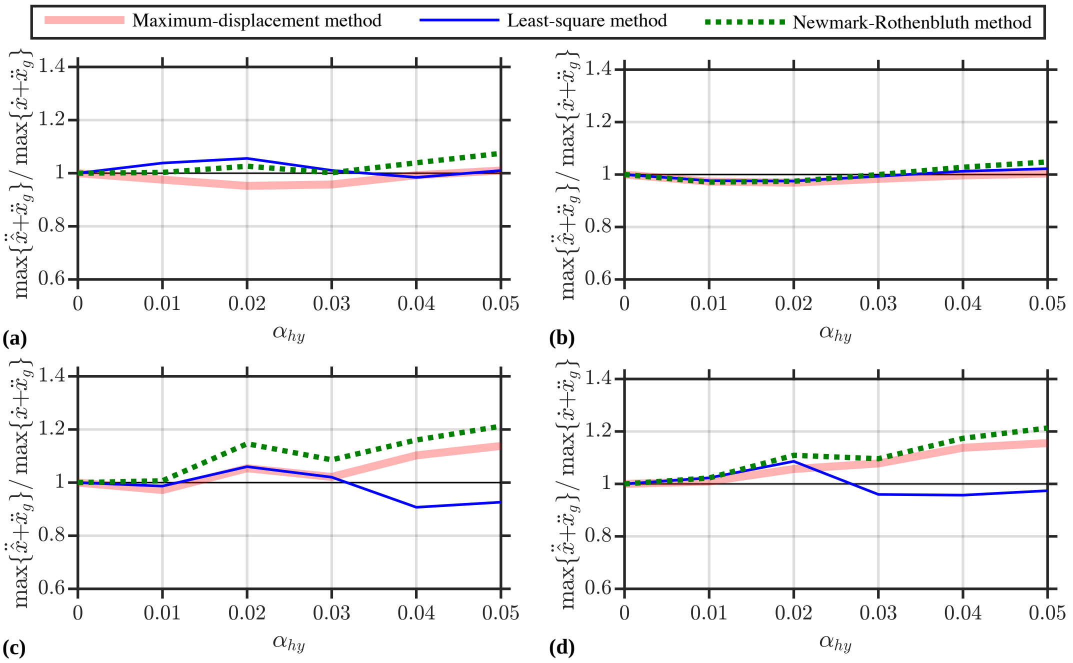

Figure 3.26: Maximum-displacement-stiffness method vs. least-square method vs. Newmark-Rosenblueth method for maximum absolute acceleration under Code Hachinohe wave : (a) T_0 = 2 s, ζ_v = 0.05, (b) T_0 = 2 s, ζ_v = 0.10, (c) T_0 = 4 s, ζ_v = 0.05, and (d) T_0 = 4 s, ζ_v = 0.10

Appendix 3B Estimation error of equivalent linear model ignoring nonlinearity of hysteretic damper

Fig. 3.27~3.30 show the comparison of estimation errors of the equivalent model between the model considering the nonlinearity of the hysteretic damper (Bilinear model) and the model not considering the nonlinearity of the hysteretic damper (1st stiffness only, linear model) subjected to Taft NS, El Centro 1940 NS, JMA Kobe NS, and Code Hachinohe. From Fig. 3.27~3.30, it can be seen that the estimation error is extremely large if do not consider the nonlinearity of the hysteretic damper (only uses its 1st stiffness). Thus, the equivalent linearization is necessary to construct the equivalent linear model of active nonlinear model.

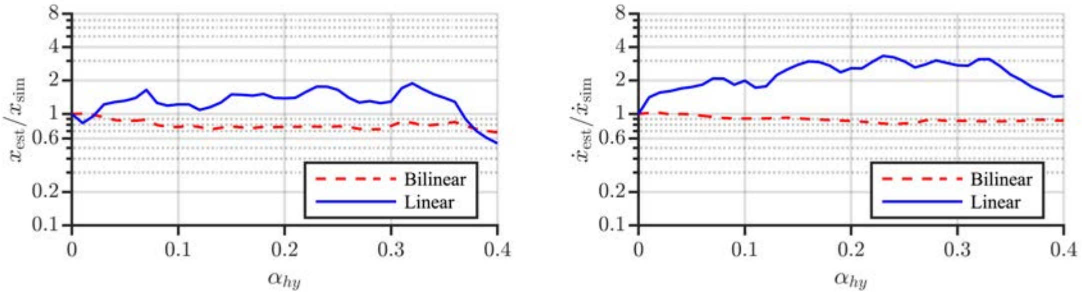

(a) Displacement

(b) Velocity

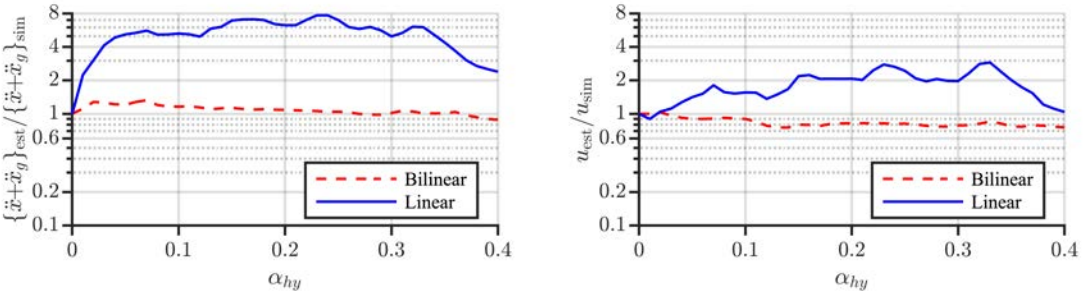

(c) Absolute acceleration

(d) Control force

Figure 3.27: Estimation error of equivalent model (Taft NS): bilinear model vs. linear model

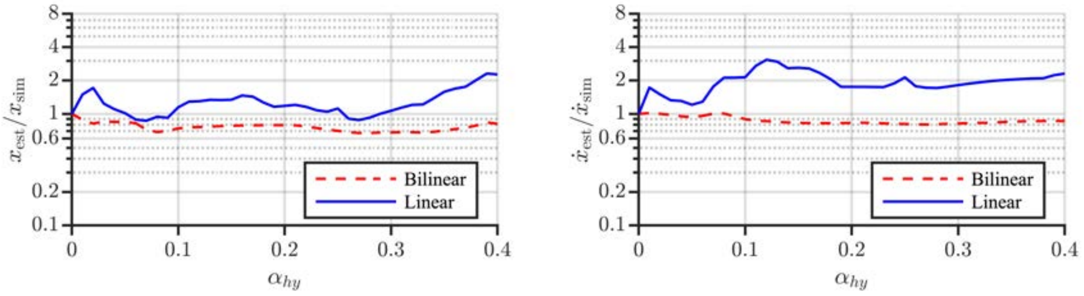

(a) Displacement **(b)** Velocity

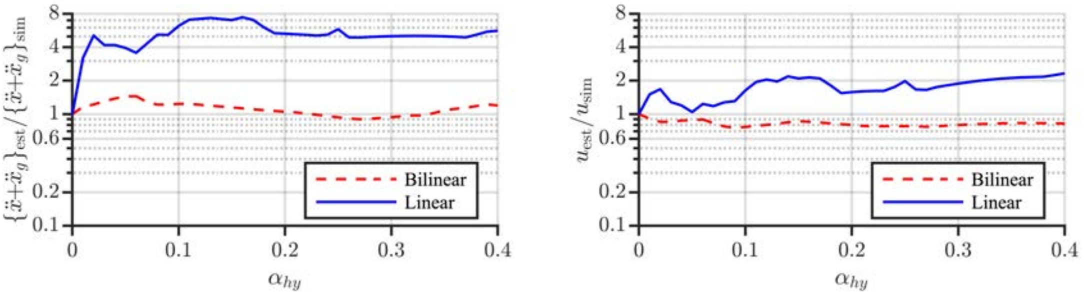

(c) Absolute acceleration **(d)** Control force

Figure 3.28: Estimation error of equivalent model (El Centro 1940 NS): bilinear model vs. linear model

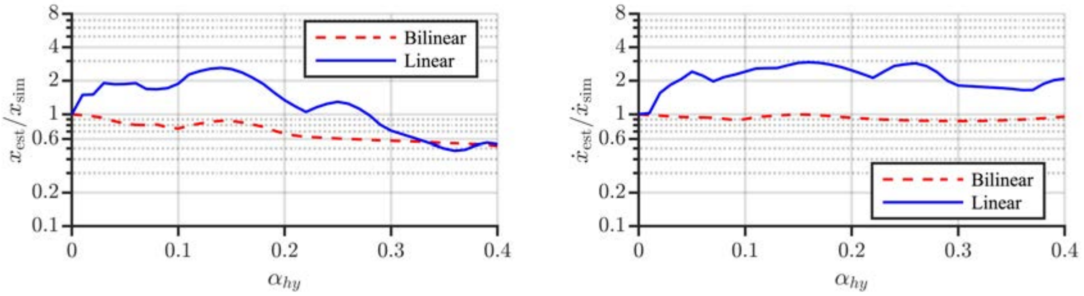

(a) Displacement **(b)** Velocity

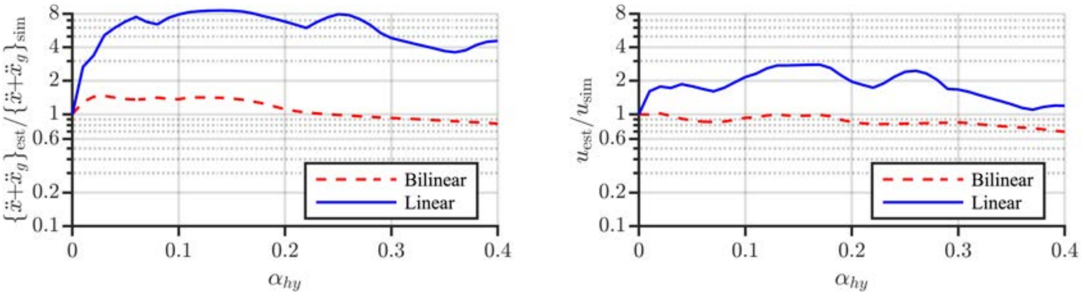

(c) Absolute acceleration **(d)** Control force

Figure 3.29: Estimation error of equivalent model (JMA Kobe NS): bilinear model vs. linear model

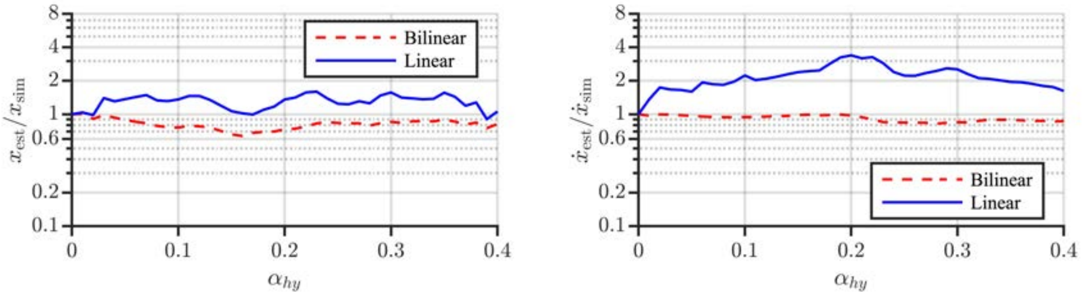

(a) Displacement **(b)** Velocity

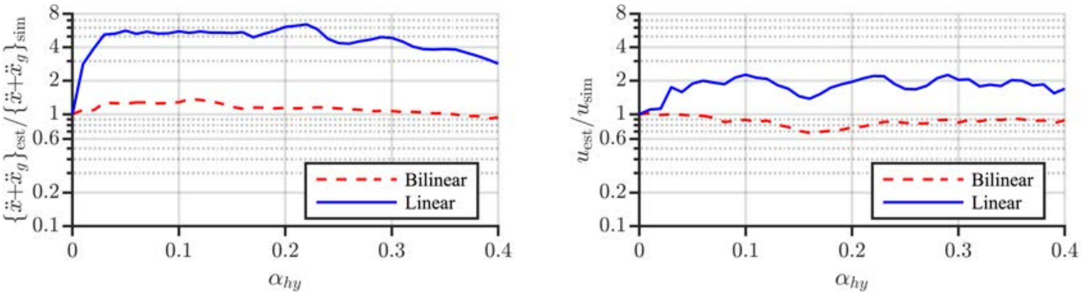

(c) Absolute acceleration **(d)** Control force

Figure 3.30: Estimation error of equivalent model (Code Hachinohe): bilinear model vs. linear model

References

[3.1] A. Salem Milani, M. Dicleli, Systematic development of a new hysteretic damper based on torsional yielding: part I—design and development, Earthquake Engineering & Structural Dynamics 45 (6) (2016) 845–867. `doi:https://doi.org/10.1002/eqe.2684`.

[3.2] X. D. Nguyen, L. Guizani, Analytical and numerical investigation of natural rubber bearings incorporating U-shaped dampers behaviour for seismic isolation, Engineering Structures 243 (2021) 112647. `doi:https://doi.org/`.

[3.3] D. R. Teruna, T. A. Majid, B. Budiono, Experimental study of hysteretic steel damper for energy dissipation capacity, Advances in Civil Engineering 2015 (631726). `doi:10.1155/2015/631726`.

[3.4] Y. Hui, S.-S. Law, W. Zhu, Q. Wang, Internal resonance of structure with hysteretic base-isolation and its application for seismic mitigation, Engineering Structures 229 (2021) 111643. `doi:https://doi.org/10.1016/j.engstruct.2020.111643`.

[3.5] M. Higashino, S. Okamoto, Response Control and Seismic Isolation of Buildings, Routledge, 2006. `doi:10.4324/9780203018866`.

[3.6] M. Omiya, H. Kitamura, Investigation and analysis on the structural characteristics of the recent base isolated buildings corresponding to long-period ground motion [in Japanese], AIJ journal of technology and design 25 (59) (2019) 61–66. `doi:10.3130/aijt.25.61`.

[3.7] A. Shibata, Dynamic analysis of earthquake resistant structures, Tohoku University Press, 2010.

[3.8] N. M. Newmark, E. Rosenblueth, Fundamentals of Earthquake Engineering, Prentice Hall, 1972.

[3.9] W. D. Iwan, N. C. Gates, Estimating earthquake response of simple hysteretic structures, Journal of the Engineering Mechanics Division 105 (3) (1979) 391–405. `doi:10.1061/JMCEA3.0002481`.

[3.10] Architectural Institute of Japan, Design Recommendations for Seismically Isolated Buildings, Architectural Institute of Japan, 2016.

[3.11] J. M. Kelly, Earthquake-Resistant Design with Rubber, Second Edition, Springer, 1997.

CHAPTER 4

Wind-resistant design on along-wind direction

4.1 Introduction

In passive wind-resistant designs, as the along-wind force contains the mean component, the mean displacement response in the along-wind direction can only be calculated using static equilibrium. Moreover, the gust factor approach is a well-developed method to estimate the maximum response along the along-wind direction, based on probability and statistics [4.1, 4.2]. The gust factor approach simplifies the design procedure for wind-resistant designs, because numerical simulations are not required. However, there are three main issues when extending the gust factor approach to include buildings combined with ASC:

(1) To calculate the mean displacement of the control system, the mean control force should also be considered. Therefore, it is necessary to devise a method to estimate the mean control force, without the use of numerical simulations.

(2) Although the gust factor for displacement has been well developed for PBI buildings [4.1], the gust factor for the buildings employing a combination of PBI and ASC has not been analyzed thus far.

(3) Estimating the maximum control force is also significantly important when designing the controller. Hence, it is necessary to determine the gust factor for the control force.

Sato et al. studied the single degree-of-freedom (DOF) control system and presented a method for estimating the maximum control force of the control system under an earthquake, using only the velocity response spectrum [4.3]. However, this method is limited to single-DOF models and cannot be used to estimate the maximum control force for a system under wind disturbances. *Chen et al.* presented a method for estimating the mean control force and mean displacement response for multi-DOFs models under an along-wind force, using the linear quadratic regulator (LQR) method [4.4]. However, this method still requires numerical simulations to calculate the maximum response and control force. Therefore, it is necessary to develop a method that can be used to theoretically calculate the gust factor for displacement and control force, thereby extending the gust factor approach to base-isolated buildings combined with ASC.

In this chapter, a method for estimating the mean control force and mean displacement response using static equilibrium and without the use of numerical simulations, is devised initially. Thereafter, the analytical formulae for estimating the gust factor for the control force of multi-DOFs models is developed. The efficacy of the estimation methods is validated via numerical verifications. Moreover, the gust factor for displacement and control force is proposed to estimate the maximum displacement and maximum control force. Note that, the gust factors proposed in this chapter only considered the condition of 0 degree of wind angle, thus, it can not be used to estimate the maximum responses if the wind angle is not 0 degree. This paper also proposes a design method for PBI buildings combined with ASC, for determining the isolated period, isolated damping ratio, and LQR weighting matrices that satisfy the limits, using an estimation method for mean control force and mean displacement response, and their gust factor. This method requires only static equilibrium and gust factor to estimate the maximum control force and maximum displacement response, thereby simplifying the design procedure. Finally, a design example of a high-rise PBI building with ASC is used to validate the efficacy of the proposed design methodology.

4.2 Mathematics models

4.2.1 Introduction of buildings

This paper uses two high-rise base-isolated buildings as the research targets, the aspect ratio of the superstructure of the buildings are 4 and 5, respectively (A4 building and A5 building). The two A4 and A5 buildings have the same 1st natural period, T_s, and H ($T_s = 2$ s and $H = 100$ m). The width and depth of A4 and A5 building are the same, respectively (25×25 m for A4 building and 20×20 for A5 building). The shape of the superstructure of A4 and A5 buildings are shown at Fig. 4.1. Parameters of superstructure of two buildings are presented in Table 4.1.

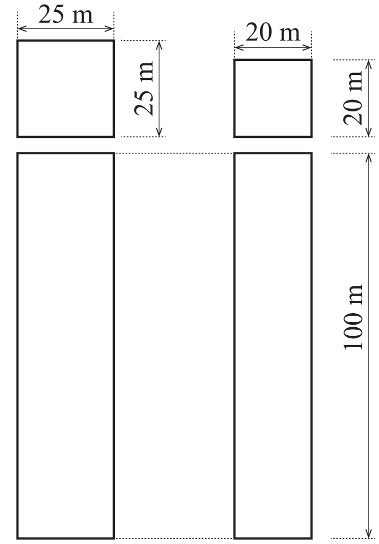

A4 building (aspect ratio is 4) A5 building (aspect ratio is 5)

Figure 4.1: Shape of buildings

Table 4.1
Parameters of superstructures of A4 and A5 buildings

Parameter	Symbol	Unit	A4 building	A5 building
Height	H	m	10	
Area	$B \times D$	m^2	25×25	20×20
Density	ρ_s	kg/m^3	175	
1st natural period	$T_{s,\mathrm{m1}}$	s	2	
1st damping ratio	$\zeta_{s,\mathrm{m1}}$		0.02	

The superstructures of A4 and A5 buildings are described as 10-DOF shear models only considering one direction input, and the height, mass, and stiffness of every story is calculated by following equations:

$$h_i = \frac{H}{10},\ i = 1 \sim 10, \tag{4.1}$$

$$m_i = h_i B D \rho_s \text{ and} \tag{4.2}$$

$$k_i = \begin{cases} \dfrac{\omega^2 m_1 \phi_{\mathbf{s},\mathrm{m1},1} + k_2(\phi_{\mathbf{s},\mathrm{m1},2} - \phi_{\mathbf{s},\mathrm{m1},1})}{\phi_{\mathbf{s},\mathrm{m1},1}} & \text{if } i = 1 \\ \dfrac{\omega^2 m_i \phi_{s,\mathrm{m1},i} + k_{i+1}(\phi_{s,\mathrm{m1},i+1} - \phi_{s,\mathrm{m1},i})}{\phi_{s,\mathrm{m1},i} - \phi_{s,\mathrm{m1},i-1}} & \text{if } i = 2 \sim 9 \\ \dfrac{\omega^2 m_{10} \phi_{\mathbf{s},\mathrm{m1},10}}{\phi_{\mathbf{s},\mathrm{m1},10} - \phi_{\mathbf{s},\mathrm{m1},9}} & \text{if } i = 10, \end{cases} \tag{4.3}$$

where, $\omega_{s,\mathrm{m1}}$ is the 1st natural angular frequency of the superstructures. $\phi_{s,\mathrm{m1}}$ is the 1st mode of superstructure, and this paper assumes the slide mode for $\phi_{s,\mathrm{m1}}$ $\omega_{s,\mathrm{m1}}$ and $\phi_{s,\mathrm{m1}}$ are defined by the following equations:

$$\omega_{s,\mathrm{m1}} = \frac{2\pi}{T_{s,\mathrm{m1}}} \tag{4.4}$$

$$\phi_{\mathbf{s},\mathrm{m1},i} = i. \tag{4.5}$$

Thus, the stiffness matrix of the superstructure, $\mathbf{K_s}$, is defined by the following equation:

$$\mathbf{K_s} = \begin{bmatrix} k_1 + k_2 & -k_2 & & & \\ -k_2 & k_2 + k_3 & -k_3 & & \\ & \ddots & \ddots & \ddots & \\ & & & -k_9 & k_{10} \end{bmatrix} \tag{4.6}$$

The damping of superstructure uses stiffness-proportional damping model, and the damping matrix of superstructure, C_s, is defined by the following equation:

$$\mathbf{C_s} = \frac{2\zeta_{s,\mathrm{m1}}}{\omega_{s,\mathrm{m1}}} \mathbf{K_s}. \tag{4.7}$$

The parameters of height, mass, and stiffness of superstructure is presented in Table 4.2.

Isolation story is installed under the superstructures. The isolation story is made by natural rubber bearing and viscous damper and controller (Fig. 4.2).

Table 4.2
Height, mass, stiffness, and damping coefficient of each story of superstructures for A4 model

Story	h_i [m]	m_i [kg]	k_i [N/m]	c_i [Ns/m]
1	10	1.09×10^6	5.94×10^8	7.56×10^6
2	10	1.09×10^6	5.83×10^8	7.42×10^6
3	10	1.09×10^6	5.61×10^8	7.15×10^6
4	10	1.09×10^6	5.29×10^8	6.73×10^6
5	10	1.09×10^6	4.86×10^8	6.19×10^6
6	10	1.09×10^6	4.32×10^8	5.50×10^6
7	10	1.09×10^6	3.67×10^8	4.67×10^6
8	10	1.09×10^6	2.91×10^8	3.71×10^6
9	10	1.09×10^6	2.05×10^8	2.61×10^6
10	10	1.09×10^6	1.08×10^8	1.37×10^6

Table 4.3
Height, mass, stiffness, and damping coefficient of each story of superstructures for A5 model

Story	h_i [m]	m_i [kg]	k_i [N/m]	c_i [Ns/m]
1	10	7.00×10^5	3.80×10^8	4.84×10^6
2	10	7.00×10^5	3.73×10^8	4.75×10^6
3	10	7.00×10^5	3.59×10^8	4.57×10^6
4	10	7.00×10^5	3.39×10^8	4.31×10^6
5	10	7.00×10^5	3.11×10^8	3.96×10^6
6	10	7.00×10^5	2.76×10^8	3.52×10^6
7	10	7.00×10^5	2.35×10^8	2.99×10^6
8	10	7.00×10^5	1.87×10^8	2.38×10^6
9	10	7.00×10^5	1.31×10^8	1.67×10^6
10	10	7.00×10^5	6.91×10^7	8.80×10^5

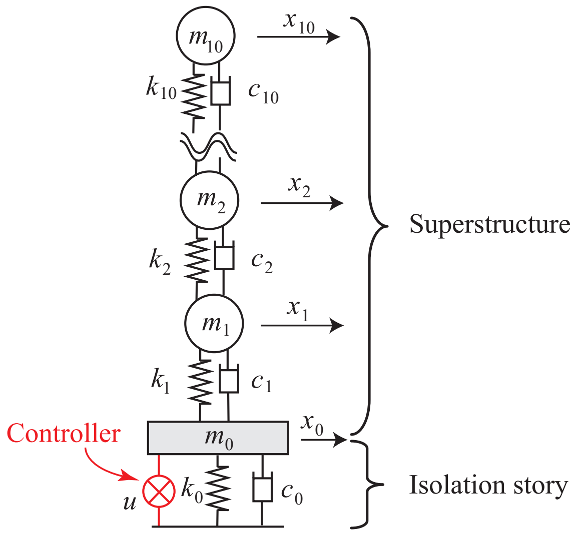

Figure 4.2: 11-DOF model of [(a) NoASC model and (b) ASC model]

The mass stiffness and the damping coefficient of the isolation story (m_0, k_0, and c_0) are given by

$$m_0 = \rho_0 BD \tag{4.8}$$

$$k_0 = \frac{4\pi^2 \sum_{i=0}^{10} m_i}{T_0^2} \tag{4.9}$$

$$c_0 = 2\zeta_0 \sqrt{\sum_{i=0}^{10} m_i k_0} \tag{4.10}$$

where ρ_0 is the mass per area of the isolation story; T_0 and ζ_0 are the isolated period and isolated damping ratio, respectively. Note that isolated period and isolated damping ratio are the natural period and damping ratio of the structure by assuming the superstructure as a rigid body.

The value of mass, stiffness, and coefficient of the isolation story are presented in Tables 4.4 and 4.5.

Table 4.4
Mass, stiffness, and damping coefficient of isolation story (A4 model)

T_0 [s]	m_0 [kg]	k_0 [N/m]	c_0 [Ns/m]		
			$\zeta_0 = 0.01$	$\zeta_0 = 0.05$	$\zeta_0 = 0.10$
3	1.59×10^6	5.50×10^7	5.25×10^5	2.62×10^6	5.25×10^6
4	1.59×10^6	3.09×10^7	3.94×10^5	1.97×10^6	3.94×10^6
5	1.59×10^6	1.98×10^7	3.15×10^5	1.57×10^6	3.15×10^6

Table 4.5
Mass, stiffness, and damping coefficient of isolation story (A5 model)

T_0 [s]	m_0 [kg]	k_0 [N/m]	c_0 [Ns/m]		
			$\zeta_0 = 0.01$	$\zeta_0 = 0.05$	$\zeta_0 = 0.10$
3	1.02×10^7	3.51×10^7	3.36×10^5	1.68×10^6	3.36×10^6
4	1.98×10^7	3.09×10^7	2.52×10^5	1.26×10^6	2.52×10^6
5	1.02×10^7	1.27×10^7	2.02×10^5	1.01×10^6	2.02×10^6

Thus, the models used in this Chapter have 11 DOFs (10 DOFs for the superstructure and 1 DOF for the base isolation).

4.2.2 Construction of Control System

The dynamics of a control system are described by the following equation:

$$\mathbf{M}\ddot{\mathbf{X}}(t) + \mathbf{C}\dot{\mathbf{X}}(t) + \mathbf{K}\mathbf{X}(t) = \mathbf{E_F}\mathbf{F}(t) - \mathbf{E_u}\mathbf{u}(t), \tag{4.11}$$

where,

$$\mathbf{M} = \begin{bmatrix} m_0 & & & \\ & m_1 & & \\ & & \ddots & \\ & & & m_{10} \end{bmatrix} \tag{4.12a}$$

$$\mathbf{K} = \begin{bmatrix} k_0 + k_1 & -k_1 & & \\ -k_1 & k_1 + k_2 & -k_2 & \\ & & \ddots & \\ & & -k_9 & k_{10} \end{bmatrix} \tag{4.12b}$$

$$\mathbf{C} = \begin{bmatrix} c_0 + c_1 & -c_1 & & \\ -c_1 & c_1 + c_2 & -c_2 & \\ & & \ddots & \\ & & -c_9 & c_{10} \end{bmatrix} \tag{4.12c}$$

$$\mathbf{E_F} = \mathbf{I} \tag{4.12d}$$

$$\mathbf{E_u} = \text{diag.} \begin{Bmatrix} 1 & 0 & 0 & \cdots & 0 \end{Bmatrix} \tag{4.12e}$$

The state-space representation of (4.11) is

$$\dot{\mathbf{z}}(t) = \mathbf{A}\mathbf{z}(t) + \mathbf{B_F}\mathbf{F}(t) - \mathbf{B_u}\mathbf{u}(t), \tag{4.13}$$

where state vector, $\mathbf{z}(t)$, system gain, $\mathbf{A}$, input matrix for $u(t)$, $\mathbf{B_u}$, and input gain for $\mathbf{F}(t)$, $\mathbf{B_F}$, are

$$\mathbf{z}(t) = \begin{bmatrix} \mathbf{X}(t) \\ \dot{\mathbf{X}}(t) \end{bmatrix}, \tag{4.14a}$$

$$\mathbf{A} = \begin{bmatrix} \mathbf{0} & \mathbf{I} \\ -\mathbf{K}^{-1}\mathbf{M} & -\mathbf{C}^{-1}\mathbf{M} \end{bmatrix}, \tag{4.14b}$$

$$\mathbf{B_F} = \begin{bmatrix} \mathbf{0} \\ \mathbf{M}^{-1}\mathbf{E_F} \end{bmatrix}, \text{ and} \tag{4.14c}$$

$$\mathbf{B_u} = \begin{bmatrix} \mathbf{0} \\ \mathbf{M}^{-1}\mathbf{E_u} \end{bmatrix}. \tag{4.14d}$$

In this paper, displacement and velocity of every story is assumed to be directly observable (displacement sensors and velocity sensors are set to every story). In addition, if displacement and velocity of every story is not directly observable, a observer is needed to estimate system state.

Figure 4.3 presents the block-diagram of the control system used in this paper.

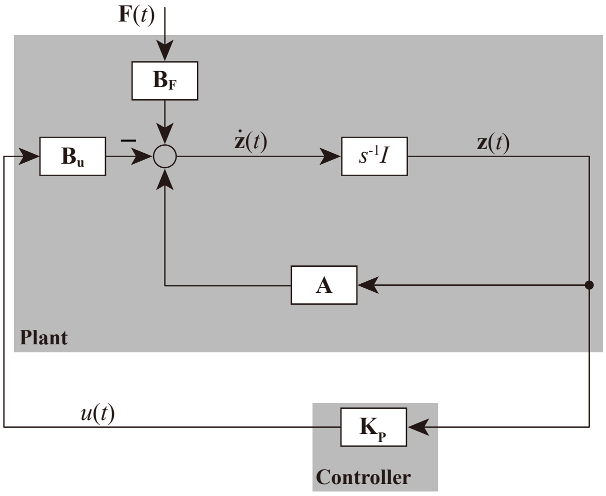

Figure 4.3: Block diagram of control system (wind-resistant design)

Feedback control law

$$u(t) = \mathbf{K_P z}(t) \tag{4.15}$$

is used, where $\mathbf{K_P}$ is the state-feedback gain that is designed using the LQR method, which is widely used in structural control [4.5–4.8]. LQR method is an optimal problem using weighting matrices as its design parameters to determine the state-feedback gain $\mathbf{K_P}$ by minimizing the following performance index [4.9]:

$$\tilde{J} = R\int_0^\infty \left[\mathbf{z}^{\mathrm{T}}(t)\frac{\tilde{\mathbf{Q}}}{R}\mathbf{z}(t) + u^{\mathrm{T}}(t)u(t)\right] \mathrm{d}t, \tag{4.16}$$

where, weighting matrix for control force, R, is positive defined and weighting matrix, $\tilde{\mathbf{Q}}$ is semi-positive defined. In this paper, only one controller is used, so R is a positive scalar.

The problem of optimizing $\tilde{J}$ in (4.16) is equal to that of optimizing

$$J = \int_0^\infty \left[\mathbf{z}^{\mathrm{T}}(t)\mathbf{Q}\mathbf{z}(t) + u^{\mathrm{T}}(t)u(t)\right] \mathrm{d}t. \tag{4.17}$$

So, we can set $R = 1$ and focus on the adjustment of Q:

$$\mathbf{Q} = \frac{1}{R}\tilde{\mathbf{Q}}. \tag{4.18}$$

This study uses the following weighting matrices in order to suppress the displacement of the isolation story:

$$\mathbf{Q} = 10^{\beta}\mathrm{diag.}\{\underset{x_0}{1}\,,\ \underset{x_1}{0}\,,\ \cdots,\ \underset{x_{10}}{0}\ ||\ \underset{\dot{x}_0}{0}\,,\ \cdots,\ \underset{\dot{x}_{10}}{0}\ \}, \tag{4.19a}$$

$$R = 1 \tag{4.19b}$$

Solving (4.17), the feedback gain K_P is given as

$$\mathbf{K_P} = \mathbf{B_u^T P}, \tag{4.20}$$

where $\mathbf{P}$ ($\geq \mathbf{0}$) is the solution of the following algebraic Riccati equitation [4.9]:

$$\mathbf{A^T P} + \mathbf{PA} - \mathbf{PB_u B_u^T P} + \mathbf{Q} = \mathbf{0}. \tag{4.21}$$

4.2.3 Equivalent model of active model

Representing the control law, (4.15), yields

$$u = \mathbf{K_P z}(t) = \begin{bmatrix}\mathbf{K_{PD}} & \mathbf{K_{PV}}\end{bmatrix}\begin{bmatrix}\mathbf{X}(t)\\ \dot{\mathbf{X}}(t)\end{bmatrix} = \mathbf{K_{PD}X}(t) + \mathbf{K_{PV}}\dot{\mathbf{X}}(t). \tag{4.22}$$

Substituting (4.22) into (4.11) yields the dynamics of the equivalent model:

$$\mathbf{M}\ddot{\mathbf{X}}(t) + \mathbf{C}_{\mathrm{eq}}\dot{\mathbf{X}}(t) + \mathbf{K}_{\mathrm{eq}}\mathbf{X}(t) = \mathbf{E_F F}(t), \tag{4.23}$$

where $\mathbf{K}_{\mathrm{eq}}$ and $\mathbf{C}_{\mathrm{eq}}$ are equivalent stiffness matrix and equivalent damping matrix, respectively. $\mathbf{K}_{\mathrm{eq}}$ and $\mathbf{C}_{\mathrm{eq}}$ are defined by the following equation:

$$\mathbf{K}_{\mathrm{eq}} = \mathbf{K} + \mathbf{E_u K_{PD}} \text{ and} \tag{4.24a}$$

$$\mathbf{C}_{\text{eq}} = \mathbf{C} + \mathbf{E}_{\mathbf{u}}\mathbf{K}_{\mathbf{PV}}. \tag{4.24b}$$

4.3 Wind force for simulation

Wind force acting on building is calculated from the observed data of the wind tunnel experiment (WTE) standardized by AIJ Recommendations for Loads on Buildings (AIJ design code [4.1]).

The parameters of the wind force for simulation are given at the Table 4.6. Because the responses of a structure with 1.0 depth-width-ratio subjected a wind force with 0-degree-wind-angle is largest (see, Appendix 4C), this study only uses the wind force with 0-degree-wind-angle. If the depth-width-ratio of the structure is not 1.0, the influence of wind angle is also should be considered. 30 cases of wind force are used for carrying out the numerical simulations. 10-minute wind force are used in this paper, and 50-second envelopes are set before and after 10-minute wind force for each case (see Fig. 4.4). Responses are calculated by the ensemble averages of 30 cases using 10-minute wind force (responses of envelopes are ignored).

Calculation procedure of the wind force from WTE data to simulation are shown at Appendix 4A.

Table 4.6
Parameters of wind force for simulation

Parameter	Symbol	Unit	Value
Return period	t_R	Year	100 and 500
Terrain category			3 and 4
DOF			10
Duration of one wind case		s	600
Cases of ensemble average			30

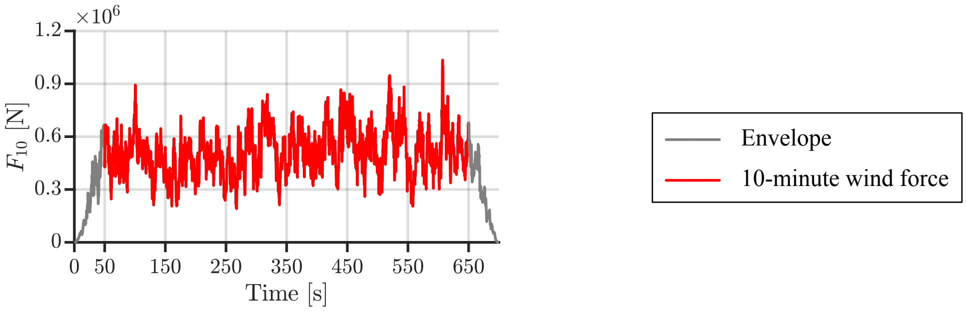

Figure 4.4: One case example of 10th story wind force on along-wind direction

Fig. 4.5 shows the story-wind wind force on along-wind direction. Fig. 4.6 shows the 30 cases ensemble average of power spectral density (PSD) of 10th story-wind force on along-wind direction.

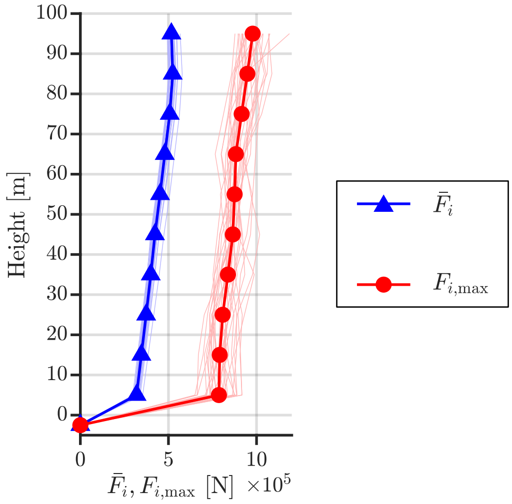

Figure 4.5: Story-wind wind force on along-wind direction

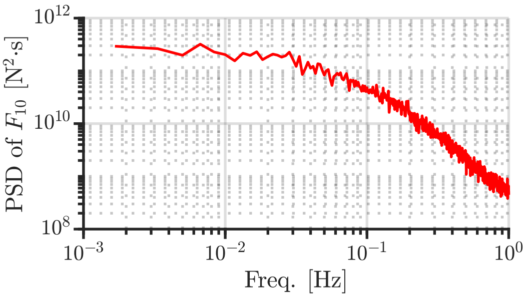

Figure 4.6: PSD of 10th story-wind force on along-wind direction

4.4 Estimation of displacement response

The maximum displacement of the control system is estimated by the following equation:

$$X_{\max} = G_D \bar{X}, \tag{4.25}$$

where $X_{\max}$ is the maximum-displacement vector; G_D is the gust factor for displacement; $\bar{X}$ mean-displacement vector.

Subsection 4.4.1 presents the estimation method for mean displacement using the static balance of the equivalent model. Subsection 4.4.2 introduces the gust effect factor of Japan design code [4.1], and uses it to estimate the maximum displacement of the control system. Subsection 4.4.3 uses numerical examples to show the accuracy of the presented method.

4.4.1 Mean displacement response

Since along-wind force contains mean component, the mean displacement response of a passive building can be estimated with static balance easily. For an active model, the mean displacement, $\bar{X}$, also can be estimated with static balance using the presented equivalent model:

$$\bar{X} = K_{\mathrm{eq}}^{-1}\bar{F}, \tag{4.26}$$

where $\bar{F}$ is the mean-wind-force vector.

4.4.2 Gust factor for displacement

This paper uses the Gust effect factor proposed by the AIJ design code to estimate the gust factor of displacement for the along-wind force G_D [4.1]

$$G_D = 1 + g_D \frac{C_g'}{C_g}\sqrt{1 + \phi_D^2 R_D}, \tag{4.27}$$

where

$$g_D = \sqrt{2\ln(600 v_D) + 1.2}, \tag{4.28a}$$

$$C_g' = 2I_H \frac{0.49 - 0.14\alpha'}{1 + \dfrac{0.63(\sqrt{BH}/L_H)^{0.56}}{(H/B)^k}} \quad \begin{cases} k = 0.07, & (H/B \geq 1) \\ k = 0.15, & (H/B < 1) \end{cases}, \tag{4.28b}$$

$$C_g = \frac{1}{3 + 3\alpha'} + \frac{1}{6}, \tag{4.28c}$$

$$\phi_D = \frac{3}{2 + \tau}\frac{M_{D1}}{M_D}\lambda, \tag{4.28d}$$

$$R_D = \frac{\pi F_D}{4\zeta_D}, \tag{4.28e}$$

$$v_D = f_D\sqrt{\frac{R_D}{1 + R_D}}, \tag{4.28f}$$

$$F_D = \frac{I_H^2 F S_D (0.57 - 0.35\alpha' + 2R\sqrt{0.053 - 0.042\alpha'})}{C_g'^2}, \tag{4.28g}$$

$$R = \frac{1}{1 + 20 + \dfrac{f_D B}{U_H}}, \tag{4.28h}$$

$$F = \frac{4\dfrac{f_D L_H}{U_H}}{\left[1 + 71\left(\dfrac{f_D L_H}{U_H}\right)^2\right]^{5/6}}, \tag{4.28i}$$

$$S_D = \frac{0.9}{\left[1 + 6\left(\frac{f_D H'}{U_H}\right)^2\right]^{0.5}\left(1 + 3\frac{f_D B}{U_H}\right)}, \tag{4.28j}$$

$$\lambda = 1 - 0.4 \ln \tau, \tag{4.28k}$$

$$M_D = \int_0^H m(h)\mu^2(h)\mathrm{d}h, \text{ and} \tag{4.28l}$$

$$\mu(h) = \left(\frac{h}{H}\right)^{\tau}. \tag{4.28m}$$

The variables are defined as follows:

g_D: peak factor of along-wind vibration,

C_g: overturning moment coefficient in along-wind direction,

C'_g: rms overturning moment coefficient in along-wind direction,

ϕ_D: mode shape correction factor for along-wind load,

R_D: resonance factor for along-wind vibration,

v_D [Hz]: level crossing rate,

α': exponent of power law for wind speed profile,

I_H: turbulence intensity at reference height given by Eq. (4.29),

B [m]: building width,

L_H [m]: turbulence scale at reference height given by Eq. (4.32),

F_D: along-wind force spectral factor,

ζ_1: damping ratio for the 1st mode in along-wind direction,

f_1 [Hz]: natural frequency for the 1st mode in along-wind direction,

F: wind force spectrum factor,

S_D: size effect factor,

R: correlation coefficient between wind pressures on the windward and leeward faces,

U_H [m/s]: design wind speed,

τ: exponent of power law for the first translational vibration mode in along-wind direction defined in Eq. (4.33),

M_D [kg]: generalized mass of building for along-wind vibration,

M_{D1} [kg]: generalized mass of building for along-wind vibration calculated based on $\tau = 1$,

λ: mode correction factor of general wind force,

$m(h)$ [kg/m]: mass per unit height at h m,

$\mu(h)$: 1st mode shape of building in each direction.

Note that f_1 and ζ_1 are calculated by the 1st eigenvalue of the control system (Figure 4.7).

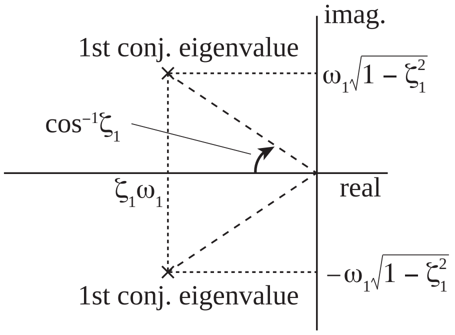

Figure 4.7: 1st natural frequency and 1st damping ratio of the control system [4.10]

The turbulence intensity I_H is defined according to the conditions of the construction site as

$$I_H = I_{rH} E_{gI} \tag{4.29}$$

where I_{rH} is the turbulence intensity at height H for each terrain category defined in Eq. (4.30); E_{gI} is the topography factor defined in Eq. (4.31).

$$I_{rH} = \begin{cases} 0.1 \left(\dfrac{H}{H_G}\right)^{-\alpha'-0.05}, & H_b < H \le H_G, \\ 0.1 \left(\dfrac{H_b}{H_G}\right)^{-\alpha'-0.05}, & H \le H_b, \end{cases} \tag{4.30}$$

where H_b, H_G, and α' are the parameters of the exposure factor as defined in Table 4.7.

Table 4.7
Parameters of the exposure factor [4.1]

Flat terrain categories	I	II	III	IV	V
H_b	3	5	10	20	30
H_G	250	350	450	550	650
α'	0.10	0.15	0.20	0.27	0.35

The topography factor for the turbulence intensity is defined as follows:

$$E_{gI} = \frac{E_I}{E_g}, \tag{4.31}$$

where E_I is the topography factor for the standard deviation of the fluctuating wind speed; E_g is the topography factor. In this section, it is not necessary to consider both topography factors: $E_I = E_g = 1$.

The turbulence scale L_H is defined according to the terrain category of the construction site as

$$L_H = \begin{cases} 100\left(\dfrac{H}{30}\right)^{0.05}, & H_b < H \leq H_G, \\ 100\left(\dfrac{H_b}{30}\right)^{0.05}, & H \leq H_b, \end{cases} \tag{4.32}$$

The value of the exponent of power law for the first translational vibration mode in along-wind direction, τ, is approximated by

$$\beta = 0.51\mu_0^2 - 1.5\mu_0 + 0.99, \tag{4.33}$$

where μ_0 is the mode displacement at the PBI story (Figure 4.8).

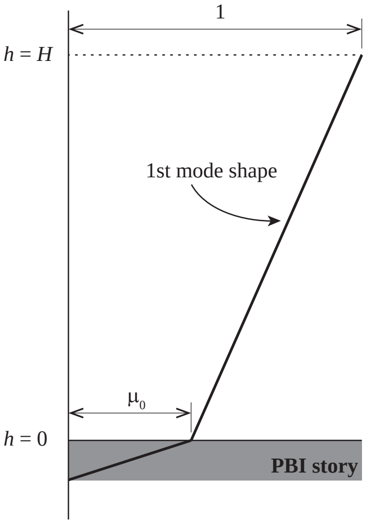

Figure 4.8: Mode displacement at the PBI story μ_0 [4.1]

4.4.3 Numerical verification

This section shows the accuracy of the estimation method for maximum displacement via numerical examples. The parameters of the model and wind force are given below:

Aspect ratio of the superstructure: 4 (A4 building)
Return period of wind force: 500 years
Number of cases for ensemble average: 30
Terrain category of wind force: 3
Natural period of the isolator: 3, 4, and 5 s
Damping ratio of the viscous damper: 0.01, 0.05, and 0.10

Fig. 4.9 shows the story wind force used in this section. Fig. 4.10 shows the 30-cases ensemble average of power spectral density (PSD) of 10th story-wind force.

Fig. 4.11 shows the comparison of the mean displacement of the control system between estimation values and simulation results. From Fig. 4.11, the following results are obtained:

- The estimated values of the mean displacement of isolation story for all models are the same with the simulation results, which confirms the validity of the estimation formula (4.26).
- The mean displacement of isolation story decreases as the weighting entry, β, increases.
- The mean displacement of isolation story increases as the isolated period, T_0, increases, if $\beta < 15$.
- The mean displacement of isolation story are the same for different isolated periods, if $\beta > 15$.

Fig. 4.12 shows the comparison of the gust factor for displacement, G_D, between estimation values and simulation results, and Fig. 4.13 shows the estimation errors of G_D. From Figs. 4.12 and 4.13, the following results are obtained:

- The estimated values of the gust factor for displacement for all models matches well to the simulation results, which confirms the validity of the estimation formula (4.27).
- The gust factor for displacement decreases as the weighting entry, β, increases.

- The gust factor for displacement increases as the isolated period, T_0, increases, if $\beta < 15$.
- The gust factor for displacement increases as the isolated damping ratio, ζ_0, increases, if $\beta < 15$.
- The mean displacement of isolation story are the same for different isolated periods, if $\beta > 15$.
- The mean displacement of isolation story are the same for different isolated damping ratios, if $\beta > 15$.

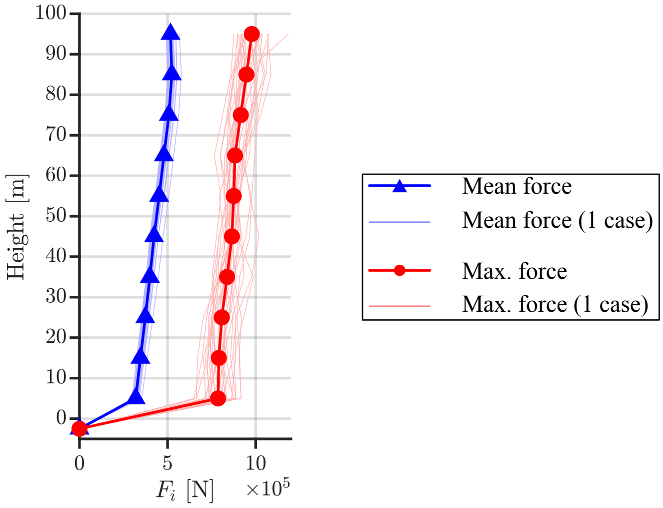

Figure 4.9: Story wind force for numerical verification (along-wind direction)

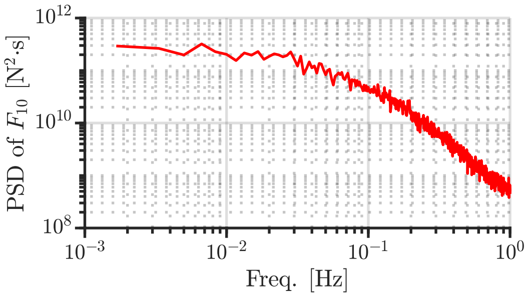

Figure 4.10: PSD of 10th story-wind force (along-wind direction)

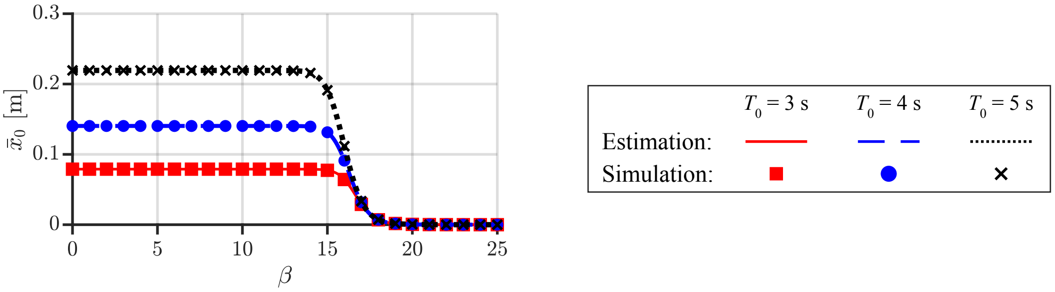

Figure 4.11: Mean displacement: estimation vs. simulation

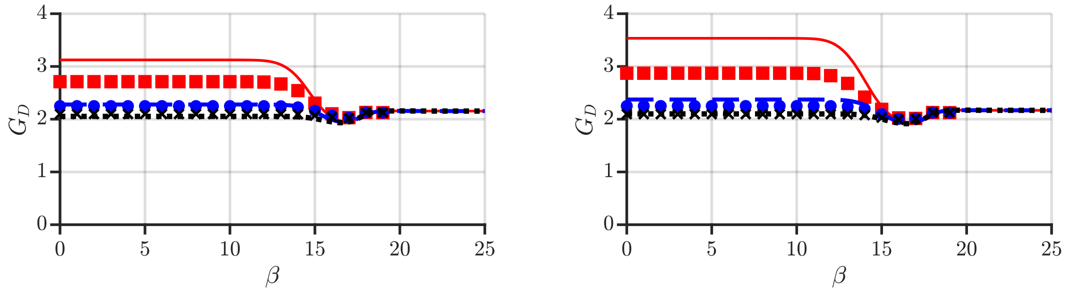

(a) T_0 = 3 s

(b) T_0 = 4 s

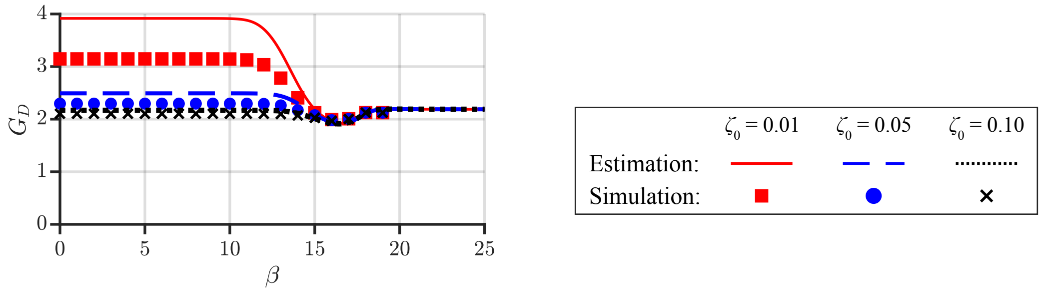

(c) T_0 = 5 s

Figure 4.12: Gust factor for displacement: estimation vs. simulation

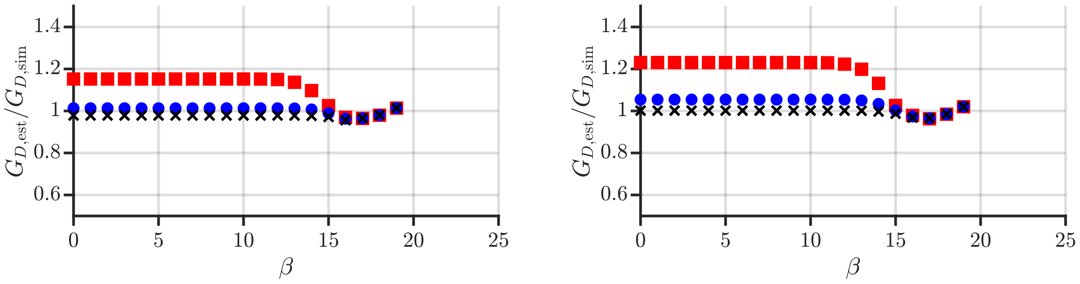

(a) T_0 = 3 s

(b) T_0 = 4 s

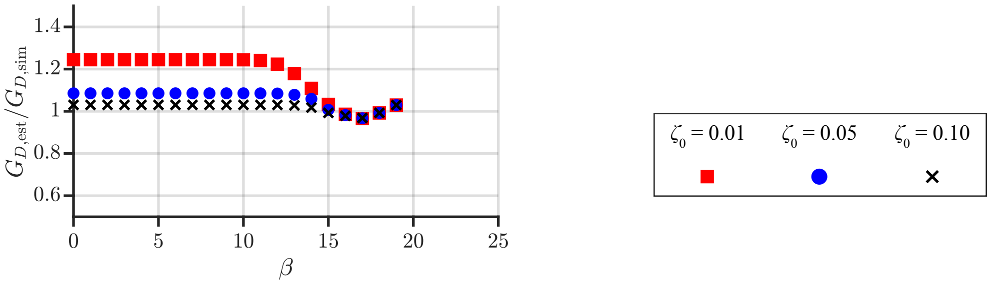

(c) T_0 = 5 s

Figure 4.13: Gust factor for displacement: estimation error

4.5 Estimation of control force

The maximum displacement of the control system is estimated by the following equation:

$$u_{\max} = G_u \bar{u}, \tag{4.34}$$

where $u_{\max}$ is the maximum control force; G_u is the gust factor for displacement; $\bar{u}$ mean control force.

Subsection 4.5.1 presents the estimation method for mean displacement using the static balance of the equivalent model. Subsection 4.5.2 introduces the gust effect factor of Japan design code [4.1], and uses it to estimate the maximum displacement of the control system. Subsection 4.5.3 uses numerical examples to show the accuracy of the presented method.

4.5.1 Mean control force

From the control law, (4.22), the mean control force, $\bar{u}$, is

$$\bar{u} = \mathbf{K_{PD}}\bar{\mathbf{X}} + \mathbf{K_{PV}}\bar{\dot{\mathbf{X}}}, \tag{4.35}$$

where $\bar{\dot{\mathbf{X}}}$ is the mean-velocity vector. Because the velocity response does not contain the mean component ($\bar{\dot{\mathbf{X}}} \approx \mathbf{0}$), the mean control force can be estimated by the following static-balance equation:

$$\bar{u} \approx \mathbf{K_{PD}}\bar{\mathbf{X}} = \mathbf{K_{PD}}\mathbf{K_{eq}^{-1}}\bar{\mathbf{F}} \tag{4.36}$$

4.5.2 Gust factor for control force

The gust factor for control force G_u is defined as

$$\begin{aligned} G_u &= \frac{\max\{u(t)\}}{\bar{u}} \\ &= \frac{\max\{\mathbf{K_{PD}}\mathbf{X}(t) + \mathbf{K_{PD}}\dot{\mathbf{X}}(t)\}}{\mathbf{K_{PD}}\bar{\mathbf{X}} + \mathbf{K_{PV}}\bar{\dot{\mathbf{X}}}} \\ &\leq \frac{\max\{\mathbf{K_{PD}}\mathbf{X}(t)\} + \max\{\mathbf{K_{PD}}\dot{\mathbf{X}}(t)\}}{\mathbf{K_{PD}}\bar{\mathbf{X}} + \mathbf{K_{PV}}\bar{\dot{\mathbf{X}}}}, \end{aligned} \tag{4.37}$$

As the phase difference between the displacement response and velocity response, and the velocity response of a control system does not contain the mean component ($\bar{\dot{\mathbf{X}}} \approx \mathbf{0}$), (4.37) yields

$$
\begin{aligned}
G_u &\leq \frac{\max\{\mathbf{K_{PD}X}(t)\} + \max\{\mathbf{K_{PD}}\dot{\mathbf{X}}(t)\}}{\mathbf{K_{PD}}\bar{\mathbf{X}}} \\
&= \frac{\max\{\mathbf{K_{PD}X}(t)\}}{\mathbf{K_{PD}}\bar{\mathbf{X}}} + \frac{\max\{\mathbf{K_{PD}}\dot{\mathbf{X}}(t)\}}{\mathbf{K_{PD}}\bar{\mathbf{X}}} \\
&= \frac{\mathbf{K_{PD}}\boldsymbol{\phi}_{\mathbf{m1}} x_{0,\max}}{\mathbf{K_{PD}}\boldsymbol{\phi}_{\mathbf{m1}} \bar{x}_0} + \frac{\max\{\mathbf{K_{PD}}\dot{\mathbf{X}}(t)\}}{\mathbf{K_{PD}}\boldsymbol{\phi}_{\mathbf{m1}} \bar{x}_0} \\
&= G_D + \frac{\max\{\mathbf{K_{PD}}\dot{\mathbf{X}}(t)\}}{\mathbf{K_{PD}}\boldsymbol{\phi}_{\mathbf{m1}} \bar{x}_0}.
\end{aligned}
\tag{4.38}
$$

The maximum velocity response can be estimated by

$$
\max\{\dot{\mathbf{X}}(t)\} \approx \left(x_{0,\max} - \bar{x}_0\right) \omega_1 \boldsymbol{\phi}_{\mathbf{m1}}. \tag{4.39}
$$

Substituting (4.39) in (4.38) yields the following expression:

$$
\begin{aligned}
G_u &\approx G_D + \frac{\mathbf{K_{PV}}\boldsymbol{\phi}_{\mathbf{m1}} \left(x_{0,\max} - \bar{x}_0\right) \omega_1}{\mathbf{K_{PD}}\boldsymbol{\phi}_{\mathbf{m1}} \bar{x}_0} \\
&\approx G_D + \frac{\mathbf{K_{PV}}\boldsymbol{\phi}_{\mathbf{m1}} \bar{x}_0 \left(G_D - 1\right) \omega_1}{\mathbf{K_{PD}}\boldsymbol{\phi}_{\mathbf{m1}} \bar{x}_0} \\
&= G_D + G_V,
\end{aligned}
\tag{4.40}
$$

where

$$
G_V = \frac{\mathbf{K_{PV}}\boldsymbol{\phi}_{\mathbf{m1}}}{\mathbf{K_{PD}}\boldsymbol{\phi}_{\mathbf{m1}}} \left(G_D - 1\right) \omega_1. \tag{4.41}
$$

This study uses SRSS method to estimate the gust factor for control force, G_u:

$$
G_u := \sqrt{G_D^2 + G_V^2}. \tag{4.42}
$$

Note that the applicable conditions of (4.42) is that the 1st mode of the control system is dominant.

4.5.3 Numerical verification

This section shows the accuracy of the estimation method for maximum displacement via numerical examples. The parameters of the model and wind force are given below:

Aspect ratio of the superstructure: 4 (A4 building)

Return period of wind force: 500 years

Number of cases for ensemble average: 30

Terrain category of wind force: 3

Natural period of the isolator: 3, 4, and 5 s

Damping ratio of the viscous damper: 0.01, 0.05, and 0.10

The wind force used in this section are shown at Figs. 4.9 and 4.10.

Fig. 4.14 shows the comparison of the mean displacement of the control system between estimation values and simulation results. From Fig. 4.14, the following results are obtained:

- The estimated values of the mean control force for all models are the same with the simulation results, which confirms the validity of the estimation formula (4.36).
- The mean control force increases as the weighting entry, β, increases.
- The mean control force decreases as the isolated period, T_0, increases, if $\beta < 15$.
- The mean control force are the same for different isolated periods, if $\beta > 15$.

Fig. 4.15 shows the comparison of the gust factor for displacement, G_D, between estimation values and simulation results, and Fig. 4.16 shows the estimation errors of G_D. From Figs. 4.15 and 4.16, the following results are obtained:

- The estimated values of the gust factor for control force for all models matches well to the simulation results, which confirms the validity of the estimation formula (4.42).
- The gust factor for control force decreases as the weighting entry, β, increases.
- The gust factor for control force increases as the isolated period, T_0, increases, if $\beta < 15$.
- The gust factor for control force increases as the isolated damping ratio, ζ_0, increases, if $\beta < 15$.
- The mean control force of isolation story are the same for different isolated damping ratios, if $\beta > 15$.

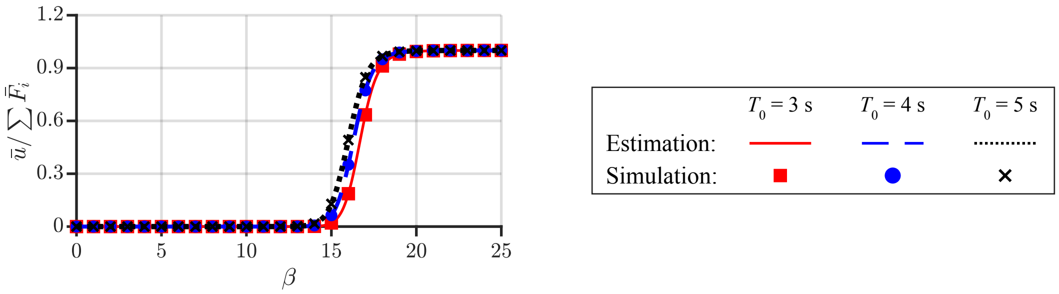

Figure 4.14: Mean control force: estimation vs. simulation

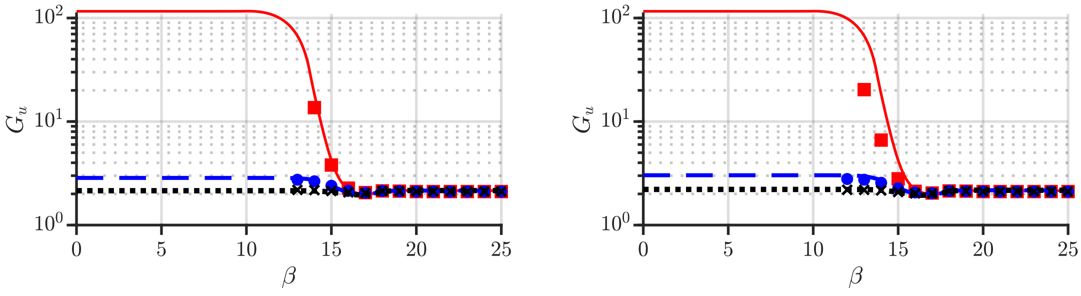

(a) T_0 = 3 s **(b)** T_0 = 4 s

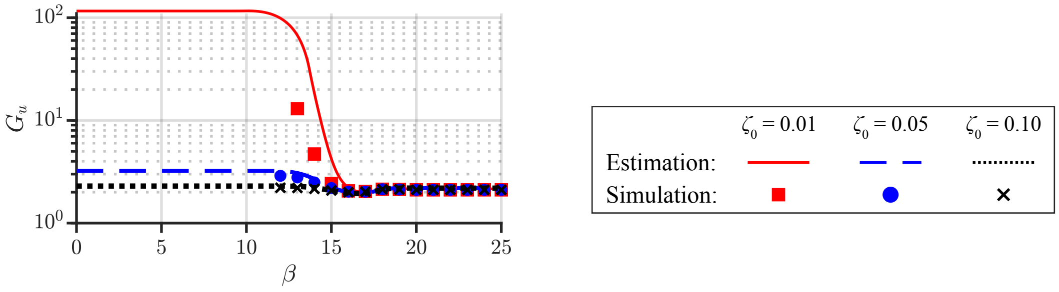

(c) T_0 = 5 s

Figure 4.15: Gust factor for control force: estimation vs. simulation

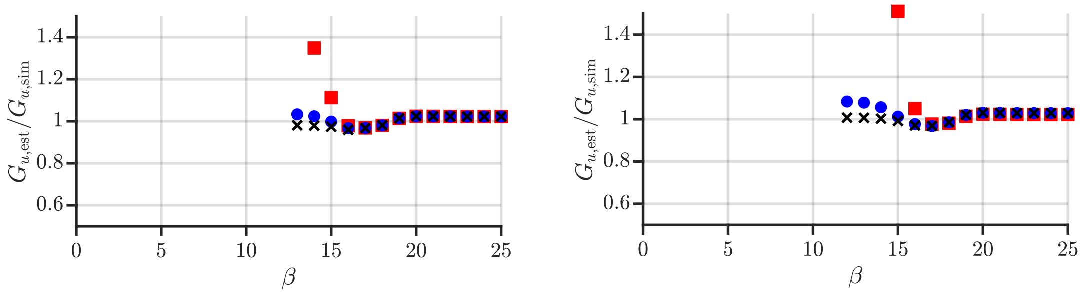

(a) T_0 = 3 s **(b)** T_0 = 4 s

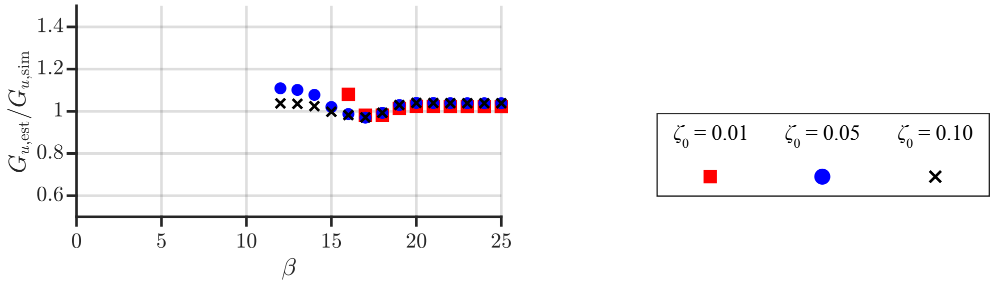

(c) T_0 = 5 s

Figure 4.16: Gust factor for control force: estimation error

4.6 Design method

This section presents the design method for the PBI structure combined with ASC under an along-wind force, for determining the isolated period, isolated damping ratio, and feedback gain that satisfy the limits on the maximum displacement response and control force. Moreover, a design example for a high-rise base-isolated building combined with active control is used to demonstrate the validity of the design method. Fig. 4.17 presents the design flowchart presented in this study.

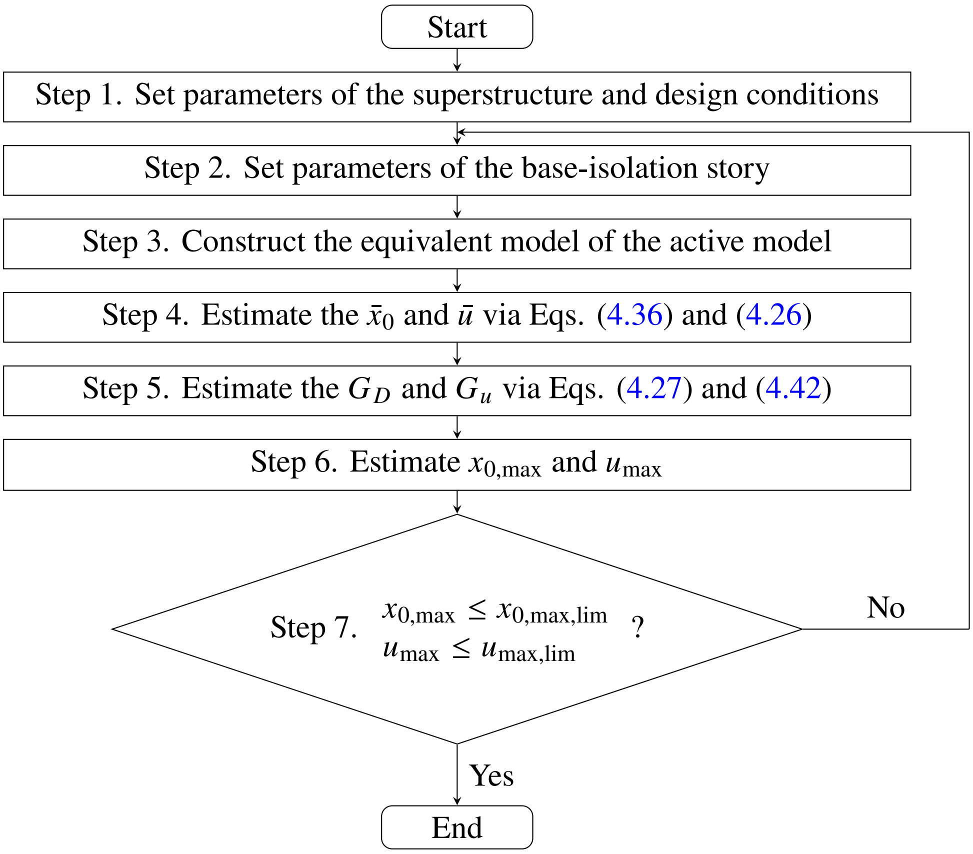

Figure 4.17: Design flowchart (Along-wind direction)

4.6.1 Design algorithm

Step 1. Specify the parameters of the superstructure and design conditions. (i.e., design wind force, design restrictions on the maximum displacement and maximum control force).

Step 2. Specify the parameters of the base-isolation story.

Step 3. Construct the equivalent model of the active model.

Step 4. Use Equation (4.36) and Equation (4.26) to estimate the mean control force and the mean displacement response, respectively.

Step 5. Use Equation (4.42) and Equation (4.27) to calculate the gust factor for the control force and displacement, respectively.

Step 6. Use the estimated values for the mean control force and mean displacement response calculated in Step 4 and the gust factor calculated in Step 5 to estimate the maximum control force and the maximum displacement response, respectively.

Step 7. If the restrictions on the maximum displacement response and maximum control force are satisfied, select the weighting entry β and proceed to the next step. If not, go back to Step 2, thereby decreasing the isolated period or increasing the isolated damping ratio or operating both of them.

Step 8. Design the control system using the isolated period T_0 and the isolated damping ratio ζ_0 determined in Step 2, and the weighting entry β selected in Step 7.

4.6.2 Design example

Step 0. Return period of along-wind force: 500 years (see Figs. 4.9 and 4.10).

Parameters of the superstructure: A4 building (as shown in Figure 4.1, 1st natural period: 2 s, damping ratio for the 1st natural period: 0.02). Parameters of the superstructure used in the design example are presented in Table 4.2.

Step 1. Parameters of the PBI story: $T_0 = 4$ s and $\zeta_0 = 0.05$. Parameters of the PBI story used in the design example are presented in Table 4.4.

Step 2. Restrictions on the maximum control force: 1×10^7 N.

Restrictions on the maximum displacement response of PBI story: 0.03 m.

Step 3. Figure 4.18 presents the estimation values for the mean displacement and mean control force obtained using Equation (4.26) and Equation (4.36).

Step 4. Figure 4.19 presents the estimation values for the gust factor for the mean control force and mean displacement response obtained using Equation (4.42) and Equation (4.27).

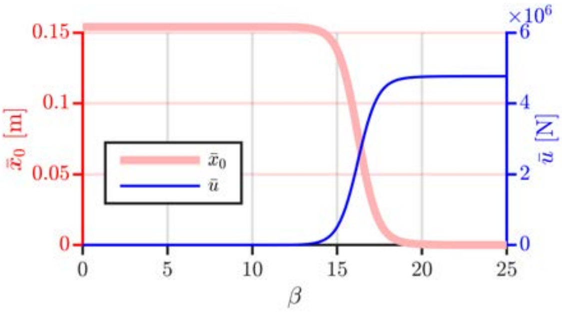

Figure 4.18: Estimated mean displacement and mean control force (Along-wind direction)

Figure 4.19: Estimated peak factor for displacement and control force (Along-wind direction)

Step 5. Based on Figs. 4.18 and 4.19, the estimation values for the maximum control force of the control system are depicted in Fig. 4.20.

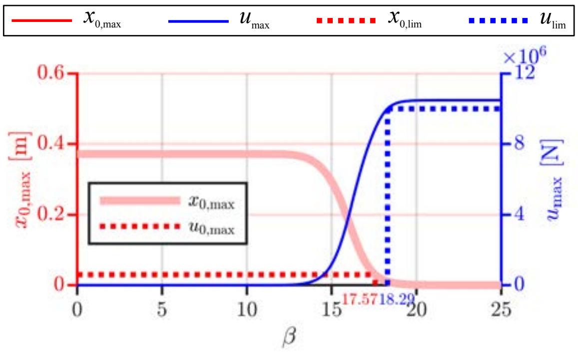

Figure 4.20: Estimated maximum displacement and maximum control force (Along-wind direction)

Step 6. From Fig. 4.20, it can be observed that if $\beta \in [17.57, 18.29]$, the restrictions on the maximum control force and maximum displacement response are satisfied. this paper selects $\beta = 18.1$.

Step 7. Using the values of β selected in Step 7 to determine the feedback gain K_P. This paper uses `lqr` function provided by MATLAB to calculate the feedback gain.

Fig. 4.21 shows responses of the design example model of each story. Fig. 4.22 shows time-history waves of responses (base-isolation story) and control force of design example model of each story. From Figs. 4.21 and 4.22, it can be seen that the responses of the model are suppressed by active control, and all design limitations are satisfied. Thus, the efficiency of the design method is confirmed.

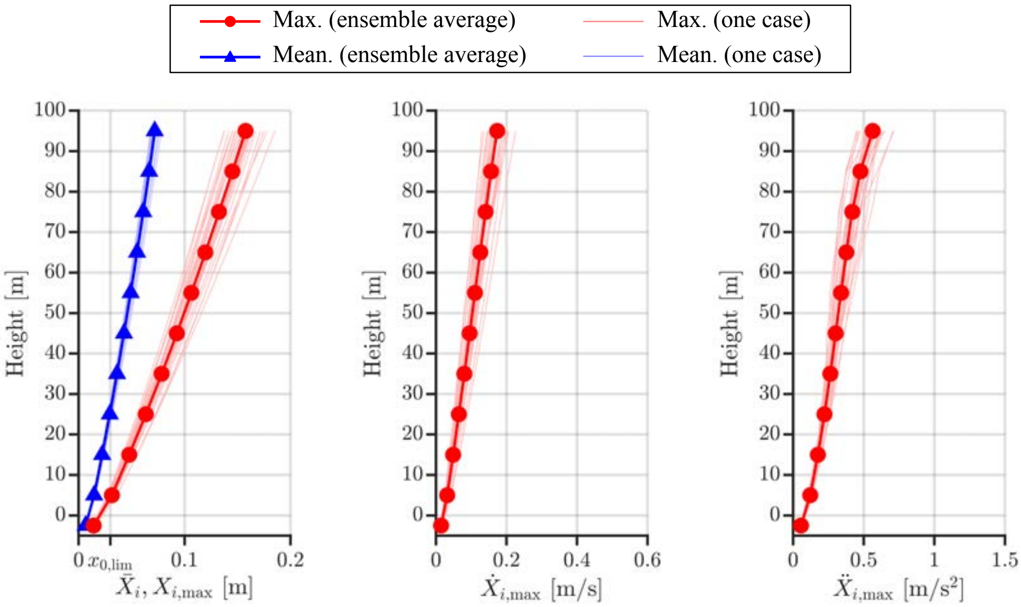

(a) Displacement **(b)** Velocity **(c)** Acceleration

Figure 4.21: Responses of design example model of each story (along-wind direction)

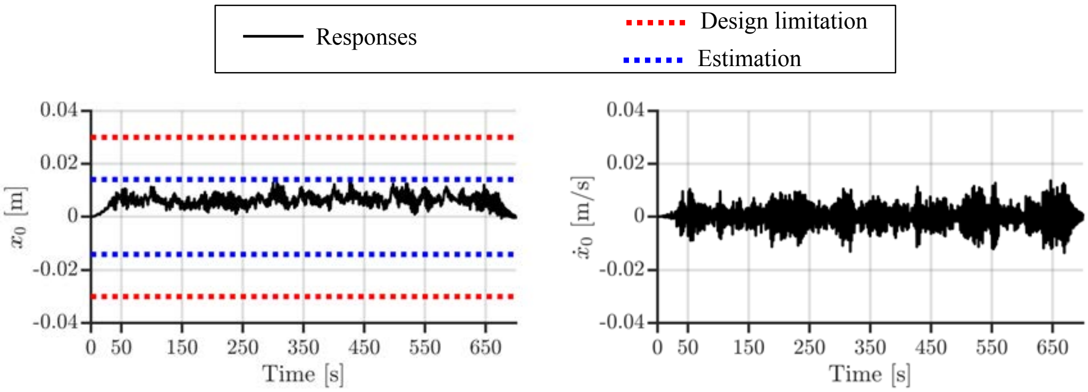

(a) Displacement **(b)** Velocity

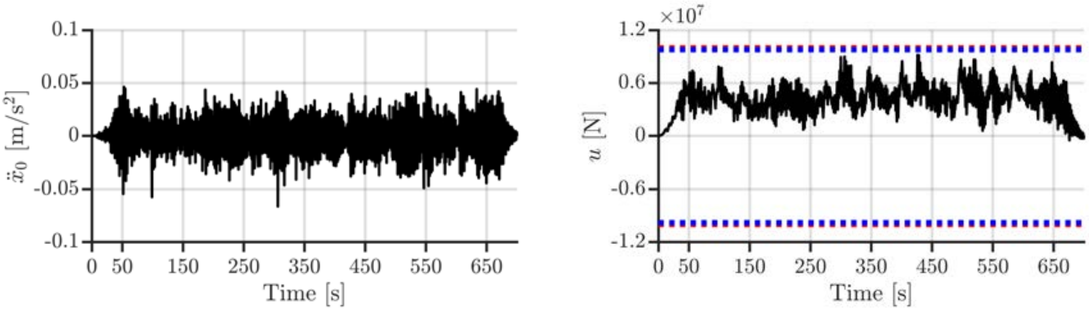

(c) Acceleration **(d)** Control force

Figure 4.22: Time-history waves of responses (base-isolation story) and control force of design example model of each story (along-wind direction, one case)

4.7 Conclusion

This section presents a method to estimate the mean control force of an active control system on along-wind direction only using static equilibrium, without any numerical simulations. Furthermore, a method to estimate the gust factor for displacement and control force was developed. The numerical examples confirmed the validity of the estimation methods. Finally, a design method was proposed for PBI buildings with ASC against an along-wind force, for determining the isolated period, isolated damping ratio, and feedback gain under restrictions on the maximum displacement response and maximum control force. The numerical design example validated the efficiency of the design method. Moreover, the following five points were also clarified based on the numerical examples:

(1) The displacement response and control force of the control system under an along-wind force contains the mean components; however, the velocity response and acceleration response do not contain the mean components.

(2) The mean control force can be estimated by only using static equilibrium. However, the estimation equation does not have analytical solutions for a multi-DOFs system because the inverse of the stiffness matrix of the structure is used.

(3) The estimation of the gust factor for displacement can be extended to buildings with ASC, because the simulation results are similar to the estimated values.

(4) A method of estimating the gust factor for control force is proposed, and the numerical simulations confirm the validity of this method.

(5) The design method simplifies the design procedure for PBI buildings with ASC, because it meets the restrictions on maximum displacement as well as maximum control force, and it does not require numerical simulations.

Appendix 4A Calculation procedure of wind force for simulation

This section shows the calculation procedure of wind force for simulation. Wind tunnel experiments (WTEs) are used to estimate the wind force acting on A4 and A5 buildings (Fig. 4.1).

4A.1 Summary of wind tunnel experiment

The WTEs use a 1/250-scaled model for A4 model and 1/200-scaled model for A5 model (Figs. 4.23 and 4.24). The mean wind velocity of WTEs are 10 m/s. Table 4.8 shows the height distribution of the sensors of WTE models, and Table 4.9 shows other experiment conditions of WTEs.

Table 4.8

Sensor location of WTE models

Story	Height [m]	
	A5 model	A4 model
1	0.025	0.025
2	0.075	0.075
3	0.125	0.125
4	0.175	0.175
5	0.225	0.225
6	0.275	0.275
7	0.325	0.325
8	0.375	0.375
9	0.425	–
10	0.475	–

Table 4.9

parameters of WTE models

Item	Symbol	Unit	A4 model	A5 model
Height	H_{WTE}	[m]	0.4	0.5
Area	A_{WTE}	[m^2]	0.1×0.1	
Wind velocity	$U_{H,\mathrm{WTE}}$	[m/s]	10	
Sampling frequency	f_{WTE}	[Hz]	1000	

The WTEs record time-history data of story-wind coefficient containing mean component on along-wind direction. The detail of experiment method and experiment condition is presented at [4.11, 4.12].

Experimental airflow is made by referring Architecture Institute of Japan Recommendation for Loads on Buildings (AIJ recommendation [4.1]).

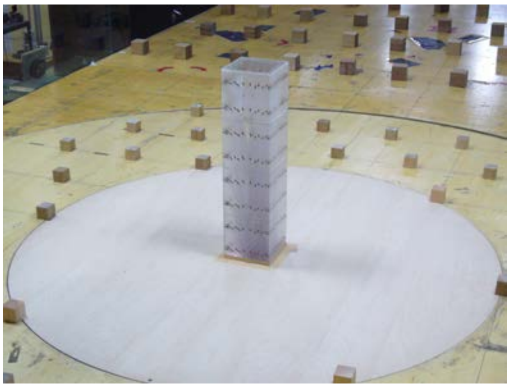

Figure 4.23: Wind tunnel model for A4 model

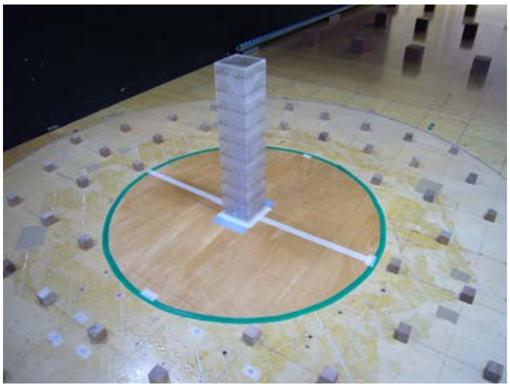

Figure 4.24: Wind tunnel model for A5 model

This subsection calculates story wind force using wind tunnel experiment (WTE) data.

4A.2 Wind force for simulation

The wind force for simulation is determined by the following equation:

$$F_i(t) = C_{F,i}(t) q_H B h_i \tag{4.43}$$

where $C_{F,i}(t)$ is the wind coefficient of ith story observed by the sensors located on WTE models; q_H is the speed pressure of wind velocity.

The speed pressure of wind velocity, q_H, is defined by the following equation:

$$q_H = \frac{1}{2}\rho_a U_H^2 \tag{4.44}$$

where ρ_a is the density of the air (this paper uses $\rho_a = 1.22$ m/kg^3); U_H is the design wind velocity referred to AIJ recommendation.

From AIJ recommendation, design wind velocity, U_H, is calculated by following equation:

$$U_H = U_0 K_{\mathrm{D}} E_H k_{\mathrm{R}w}, \tag{4.45}$$

where, U_0 [m/s] is basic wind velocity. K_{D} is wind direction factor. E_H is wind velocity profile factor. $k_{\mathrm{R}w}$ is conversion factor of return period.

Basic wind velocity U_0 is mean wind force of 10 minutes with return period of 100 years at 10 m above the ground when flat terrain category is II.

Wind direction factor K_{D} reflects strong wind characteristics of different directions, which is affected by such as geographical position of the construction site and large-scale terrain. This paper does consider the influence of these parameters, thus, $K_\mathrm{D} = 1$.

Wind velocity profile factor E_H is calculated by following equation:

$$E_H = E_\mathrm{r} E_\mathrm{g}. \tag{4.46}$$

where, E_r and E_g are parameters for determining E_H respectively.

E_r is calculated by

$$E_\mathrm{r} = \begin{cases} 1.7\left(\dfrac{Z_d}{Z_\mathrm{G}}\right)^\alpha & Z_\mathrm{b} < Z \leq Z_\mathrm{G} \\ \\ 1.7\left(\dfrac{Z_\mathrm{b}}{Z_\mathrm{G}}\right)^\alpha & Z \leq Z_\mathrm{b} \end{cases}, \tag{4.47}$$

Z_d [m] is height of building above the ground. Z_b [m], Z_G [m] and α is parameters for determining E_r, and these values are obtained from table 4.10.

Table 4.10
Parameters for calculating wind velocity profile factor

Flat terrain category	I	II	III	IV	V
Z_b [m]	3	5	10	20	30
Z_G [m]	250	350	450	550	650
α	0.1	0.15	0.2	0.27	0.35

E_g is calculated by

$$\begin{aligned} E_\mathrm{g} =& (C_1 - 1)\left\{C_2\left(\frac{Z_d}{H_\mathrm{S}} - C_3\right) + 1\right\}\ldots \\ & \exp\left\{-C_2\left(\frac{Z_d}{H_\mathrm{S}} - C_3\right)\right\} + 1, \text{ and over than } 1, \end{aligned} \tag{4.48a}$$

$$\theta_\mathrm{S} = \tan^{-1}\frac{H_\mathrm{S}}{2L_\mathrm{S}} \tag{4.48b}$$

where, H_S is height of slope and L_S is horizontal length between top of slope and half of slope. C_1, C_2 and C_3 are parameters for determining E_g. This paper does not consider the influence of season, thus, $E_\mathrm{g} = 1$.

Conversion factor of return period $k_{\mathrm{R}w}$ is calculated by following equations:

$$k_{\mathrm{R}w} = 0.63(\lambda_\mathrm{U} - 1)\ln t_\mathrm{R} - 2.9\lambda_\mathrm{U} + 3.9 \text{ and} \tag{4.49a}$$

$$\lambda_\mathrm{U} = \frac{U_{500}}{U_0}, \tag{4.49b}$$

where, t_R is return period of design, and U_{500} [m/s] is mean wind force of 10 minutes with return period of 500 years at 10 m above the ground, when flat terrain category is II.

Note that the time step, $\mathrm{d}t_\mathrm{WTE}$, of wind force for simulation is determined by solving the following equation:

$$\frac{\mathrm{d}t_\mathrm{WTE} \cdot U_{H,\mathrm{WTE}}}{\sqrt{A_\mathrm{WTE}}} = \frac{\mathrm{d}t_\mathrm{AIJ} \cdot U_{H,\mathrm{AIJ}}}{\sqrt{A_\mathrm{AIJ}}}. \tag{4.50}$$

where, $U_{H,\mathrm{WTE}}$ is wind velocity of WTE. A_WTE is area of WTE model. $U_{H,\mathrm{AIJ}}$ is design wind velocity. A_AIJ is area of building.

4A.3 Mean wind force and mean wind velocity of AIJ recommendation

mean story wind force and mean story wind velocity of AIJ recommendation is calculated by the following equation:

$$\bar{U}_{H,i} = U_H C_{\mathrm{D},i} \text{ and} \tag{4.51a}$$

$$\bar{F}_i = q_H C_{\mathrm{D},i} B h_i, \tag{4.51b}$$

where, q_H is the velocity pressure calculated by 4.44; U_H is the wind velocity calculated by 4.44 $C_{\mathrm{D},i}$ is wind force factor of i^th story.

The story wind factor C_D is calculated by following equation:

$$C_\mathrm{D} = C_\mathrm{pe1} - C_\mathrm{pe2}, \tag{4.52}$$

where, C_pe1 and C_pe2 are external pressure factors, and these values is determined by Table 4.11.

4A.4 Calculation Result

This subsection calculate design wind velocity with return period of 500 years. The assumed construction site is Tokyo, and the terrain category is III.

Table 4.11
external pressure factor

(a) C_{pe}

	$B \geq D$	$B < D$
C_{pe1}	$0.8k_Z$	
C_{pe2}	-0.5	-0.35

(b) k_Z

$Z \leq Z_{\mathrm{b}}$	$Z_{\mathrm{b}} < Z < 0.8H$	$Z \geq 0.8H$
$(Z_{\mathrm{b}}/H)^{2\alpha}$	$(Z/H)^{2\alpha}$	$0.8^{2\alpha}$

From AIJ recommendation, value of U_0 and U_{500} are

$$U_0 = 36 \text{ m/sand} \tag{4.53a}$$

$$U_{500} = 42 \text{ m/s.} \tag{4.53b}$$

This section uses the maximum value of wind direction factor in Tokyo, and does not consider the influence of season:

$$K_{\mathrm{D}} = 1. \tag{4.54a}$$

$$E_{\mathrm{g}} = 1. \tag{4.54b}$$

From table 4.10, value of Z_{b}, Z_{G} and β are

$$Z_{\mathrm{b}} = 10 \text{ [m]}, \tag{4.55a}$$

$$Z_{\mathrm{G}} = 450 \text{ [m]and} \tag{4.55b}$$

$$\alpha = 0.2. \tag{4.55c}$$

Substituting (4.55) into (4.47) yields

$$E_r = 1.7\left(\frac{100}{450}\right)^{0.2} = 1.26. \tag{4.56}$$

Substituting (4.54b) and (4.56) into (4.46) yields

$$E_H = 1.26 \times 1 = 1.26. \tag{4.57}$$

Substituting (4.53) into (4.49) yields

$$\lambda_{\mathrm{U}} = \frac{36}{42} = 1.17\text{and} \tag{4.58}$$

$$\begin{aligned} k_{\mathrm{R}w} &= 0.63 \times (1.17 - 1) \ln 500 - 2.9 \times 1.17 + 3.9 \\ &= 1.17. \end{aligned} \tag{4.59}$$

Substituting (4.53a), (4.54a), (4.57) and (4.59) into (4.45), mean wind velocity of 200 m is

$$U_H = 38 \times 1 \times 1.445 \times 1.160 = 52.97\ [\mathrm{m/s}]. \tag{4.60}$$

Substituting (4.60) into (4.44) yields

$$q_H = 0.5 \times 1.22 \times 63.7^2 = 1711.30\ [\mathrm{N/m^2}]. \tag{4.61}$$

From table 4.9, time step of WTE, $\mathrm{d}t_{\mathrm{WTE}}$, is

$$\mathrm{d}t_{\mathrm{WTE}} = \frac{1}{f_{\mathrm{WTE}}} = 0.001\ [\mathrm{s}], \tag{4.62}$$

and area of WTE model, A_{WTE}, is

$$A_{\mathrm{WTE}} = 0.1 \times 0.1 = 0.01\ [\mathrm{m^2}]. \tag{4.63}$$

Area of building, A, is

$$A = 20 \times 20 = 400\ [\mathrm{m^2}]. \tag{4.64}$$

Substituting (4.62), (4.63), (4.60)and (4.64) into (4.50) yields

$$\frac{0.001 \times 10}{\sqrt{0.01}} = \frac{\mathrm{d}t \cdot 52.97}{\sqrt{400}}. \tag{4.65}$$

Solving (4.65), time step of WTE $\mathrm{d}t_{\mathrm{e}}$ [s] is

$$\mathrm{d}t = 0.0378\ [\mathrm{s}]. \tag{4.66}$$

Substituting (4.61) into (4.43), story wind force of WTE is

$$
\begin{aligned}
F_i(t) &= C_{f,i}(t) \times 1711.30 \times 20 \times 10, \\
&= C_{f,i}(t) \times 3.42 \times 10^5 \text{ [N]}.
\end{aligned}
\tag{4.67}
$$

Wind force for simulation vs. AIJ recommendation

Fig. 4.25 shows the comparison of mean story-wind force between results calculated by WTE (Appendix 4A.4) and AIJ recommendation. Fig. 4.27 shows the comparison of turbulence intensity between results calculated by WTE (Appendix 4A.4) and AIJ recommendation.

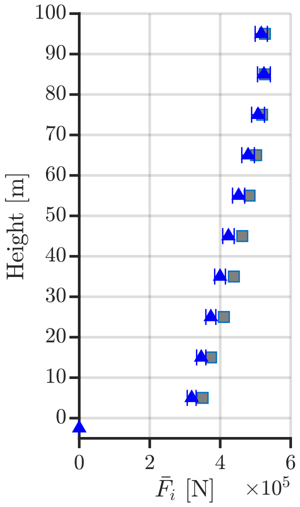

Figure 4.25: WTE wind force vs. AIJ recommendation: mean story-wind force

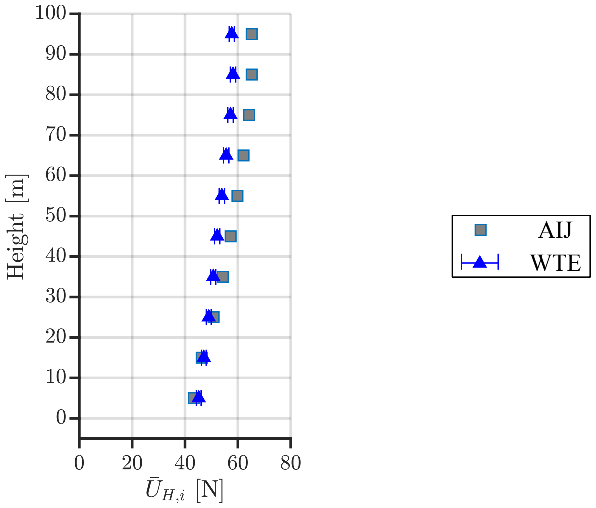

Figure 4.26: WTE wind force vs. AIJ recommendation: mean velocity

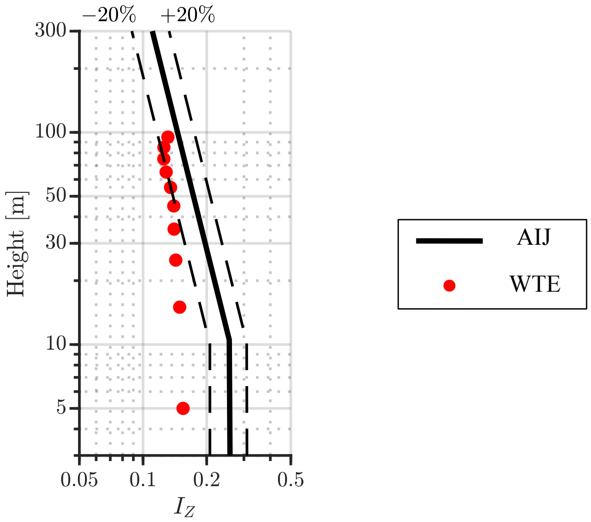

Figure 4.27: WTE wind force vs. AIJ recommendation: turbulence intensity

Appendix 4B Numerical verifications for different aspect ratio and terrain category

This section shows numerical verifications of the mean displacement, gust factor for displacement, mean control force, gust factor for control force between estimation values and simulation results, using following combinations:

Aspect ratio: 4, terrain category: 4

Aspect ratio: 5, terrain category: 3

Fig. 4.28 shows the comparison of the mean displacement of the isolation story, $\bar{x}_0$, between estimation values and simulation results. Figs. 4.29 and 4.30 shows the comparison of the gust factor for displacement of the base-isolation story, $G_{D,0}$, between estimation values and simulation results. Fig. 4.31 shows the comparison of the mean control force of the isolation story, $\bar{u}_0$, between estimation values and simulation results. Figs. 4.32 and 4.33 shows the comparison of the gust factor for control force of the base-isolation story, G_u, between estimation values and simulation results. Note that the results of Figs. 4.28~4.33 is for the cases, which aspect ratio is 4 and terrain category is 4.

Moreover, Figs. 4.34~4.39 show the comparison results for the cases, which aspect ratio is 5 and terrain category is 3.

From Figs. 4.28~4.39, it can be seen that the estimation values match to the simulation results for the cases that have different aspect ratios and terrain categories also have a high validity.

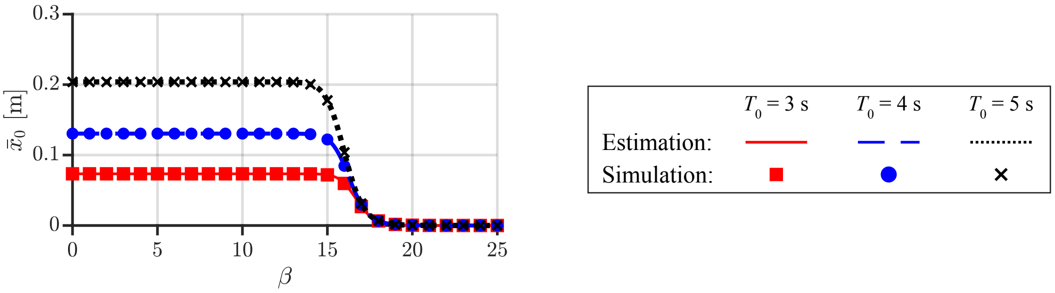

Figure 4.28: Mean displacement: estimation vs. simulation (aspect ratio: 4, terrain category: 4)

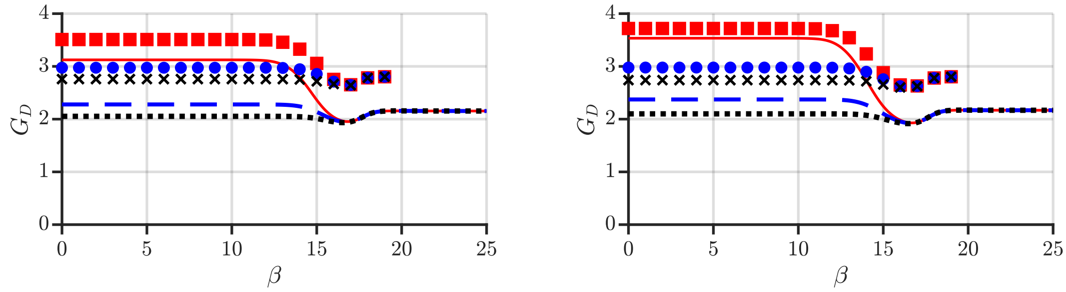

(a) T_0 = 3 s

(b) T_0 = 4 s

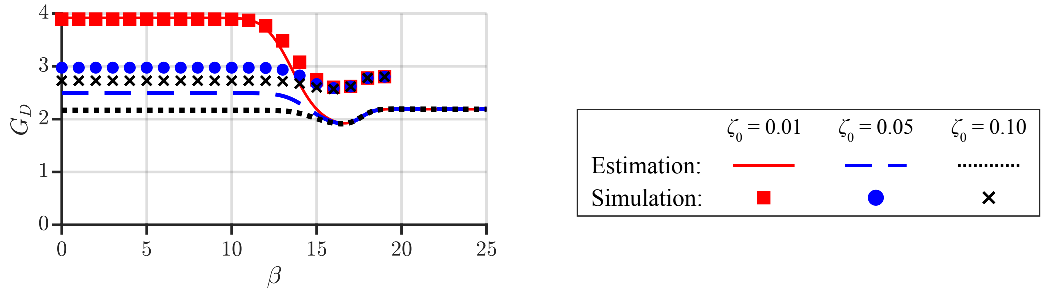

(c) T_0 = 5 s

Figure 4.29: Gust factor for displacement: estimation vs. simulation (aspect ratio: 4, terrain category: 4)

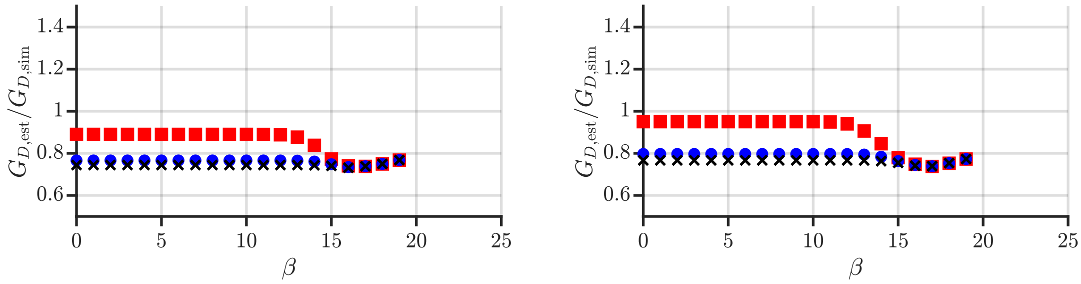

(a) T_0 = 3 s

(b) T_0 = 4 s

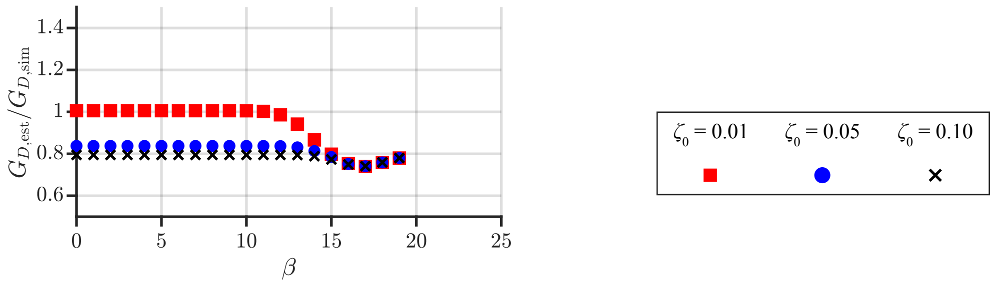

(c) T_0 = 5 s

Figure 4.30: Gust factor for displacement: estimation error (aspect ratio: 4, terrain category: 4)

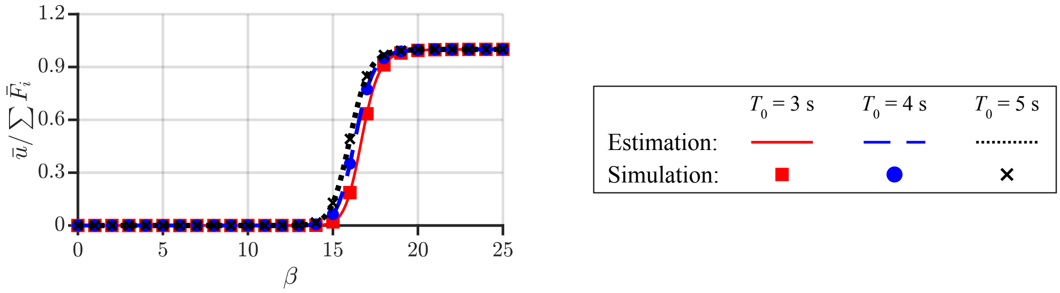

Figure 4.31: Mean control force: estimation vs. simulation (aspect ratio: 4, terrain category: 4)

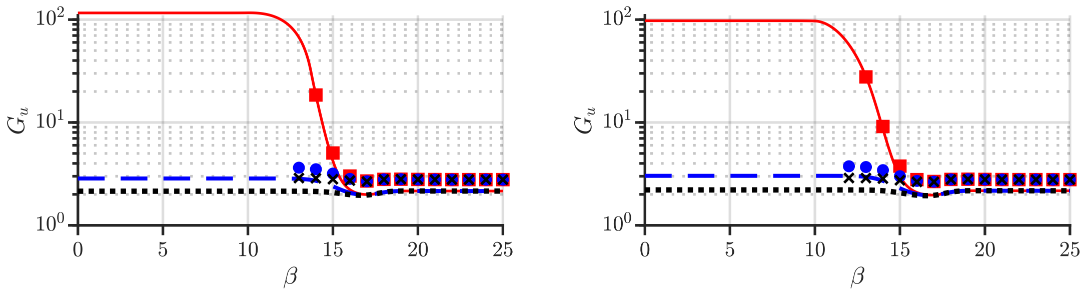

(a) T_0 = 3 s

(b) T_0 = 4 s

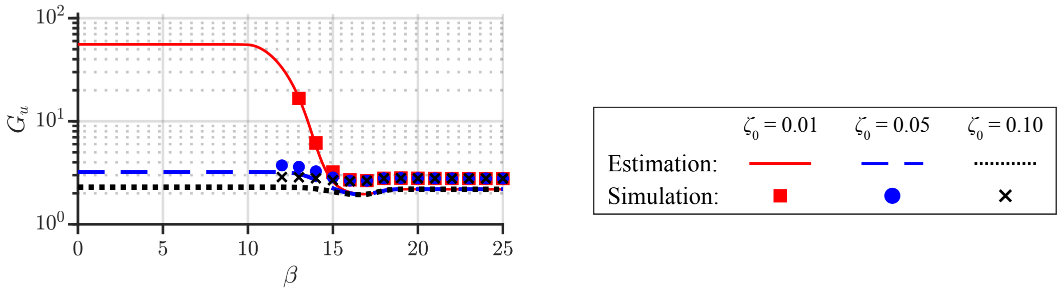

(c) T_0 = 5 s

Figure 4.32: Gust factor for control force: estimation vs. simulation (aspect ratio: 4, terrain category: 4)

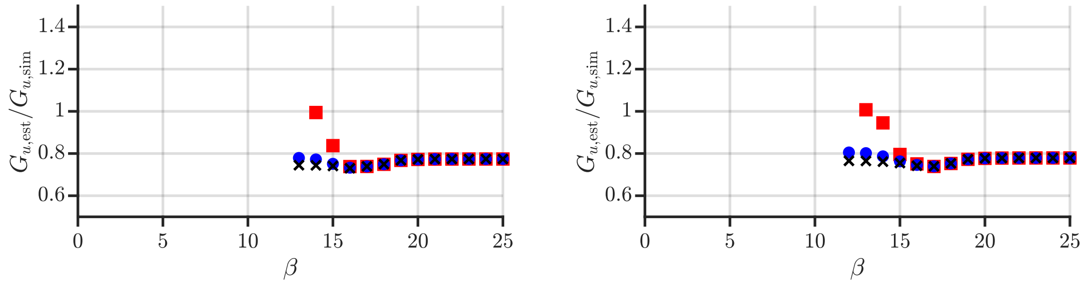

(a) T_0 = 3 s

(b) T_0 = 4 s

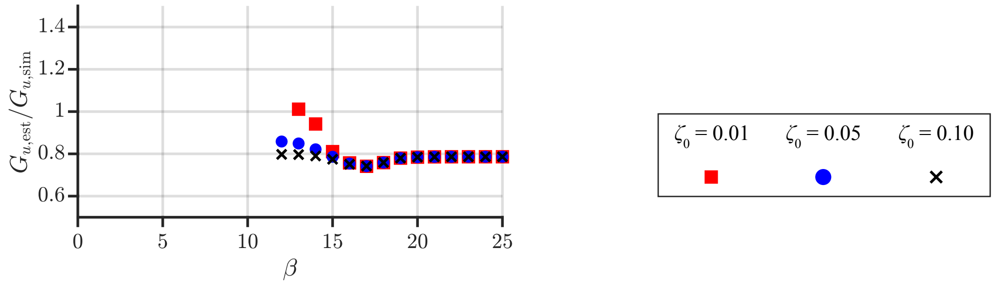

(c) T_0 = 5 s

Figure 4.33: Gust factor for control force: estimation error (aspect ratio: 4, terrain category: 4)

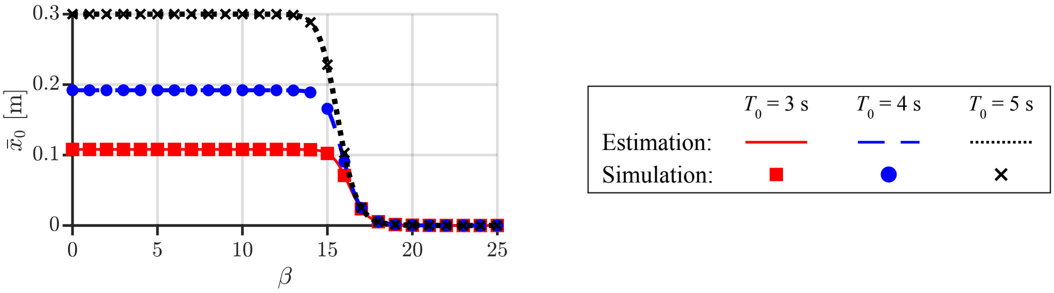

Figure 4.34: Mean displacement: estimation vs. simulation (aspect ratio: 5, terrain category: 3)

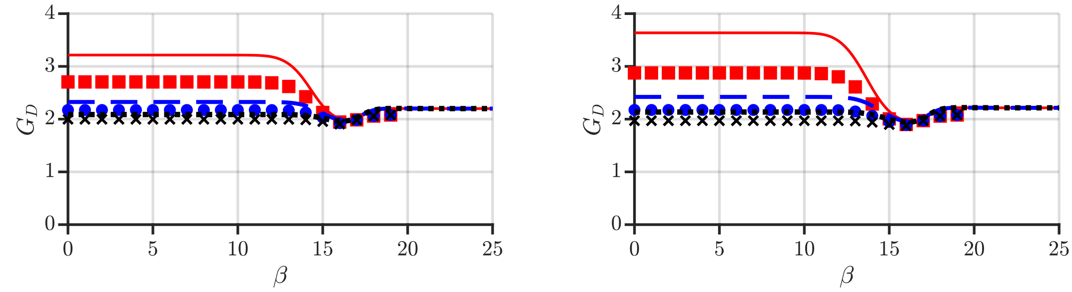

(a) T_0 = 3 s **(b)** T_0 = 4 s

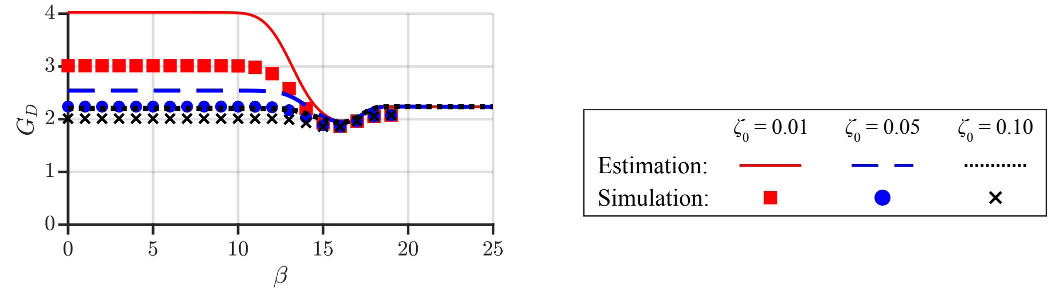

(c) T_0 = 5 s

Figure 4.35: Gust factor for displacement: estimation vs. simulation (aspect ratio: 5, terrain category: 3)

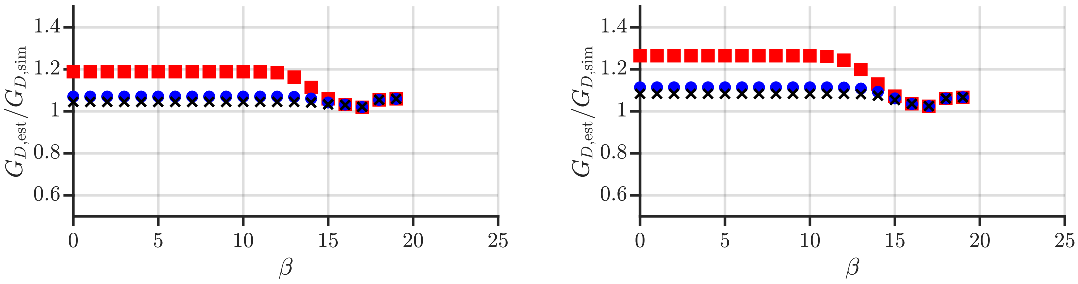

(a) T_0 = 3 s **(b)** T_0 = 4 s

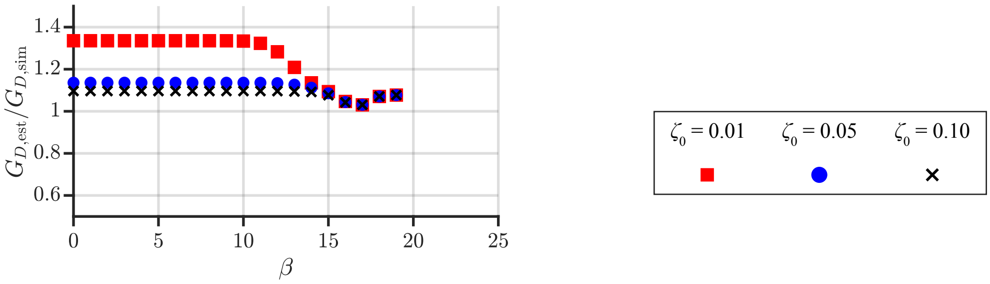

(c) T_0 = 5 s

Figure 4.36: Gust factor for displacement: estimation error (aspect ratio: 5, terrain category: 3)

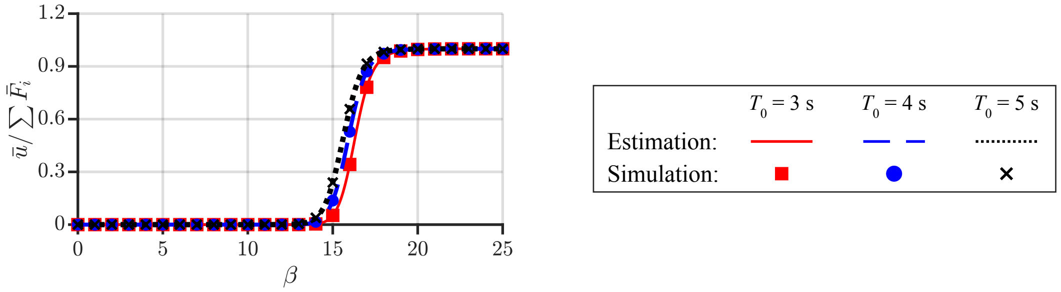

Figure 4.37: Mean control force: estimation vs. simulation (aspect ratio: 5, terrain category: 3)

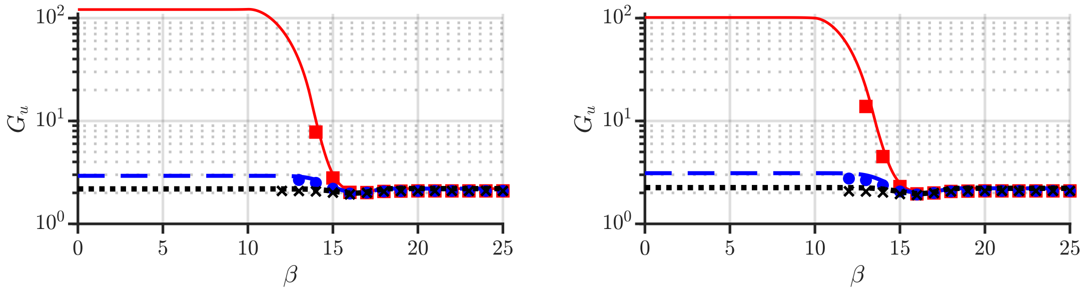

(a) T_0 = 3 s **(b)** T_0 = 4 s

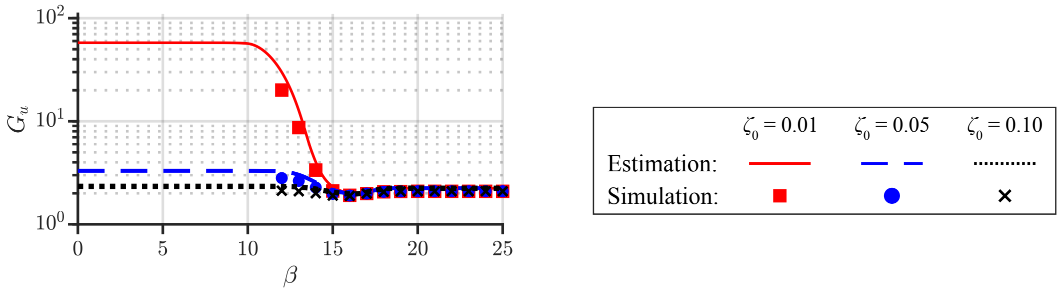

(c) T_0 = 5 s

Figure 4.38: Gust factor for control force: estimation vs. simulation (aspect ratio: 5, terrain category: 3)

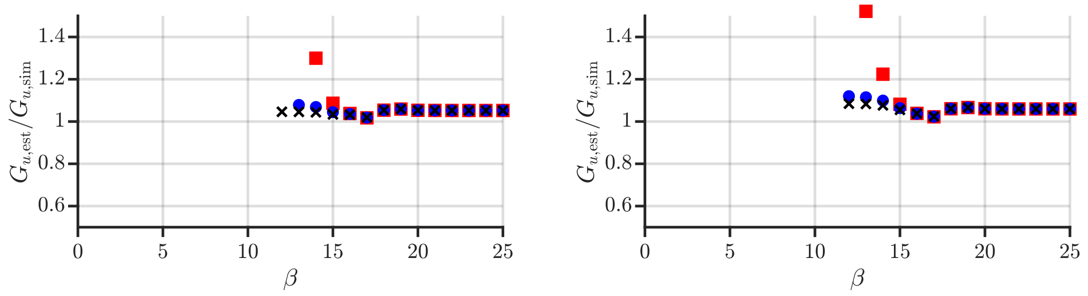

(a) T_0 = 3 s **(b)** T_0 = 4 s

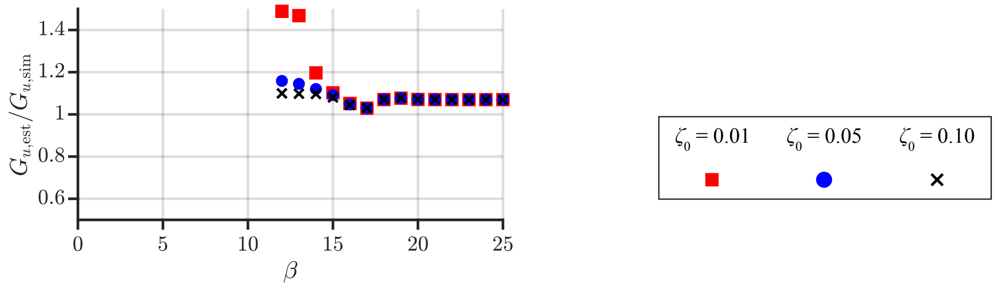

(c) T_0 = 5 s

Figure 4.39: Gust factor for control force: estimation error (aspect ratio: 5, terrain category: 3)

Appendix 4C Responses of different wind angle

The wind angle of a typhoon event is changes (see Fig. 4.40), and the wind angle also affects the responses of the structure. The structure used in this study has the same depth and width (see Fig. 4.1 and Table 4.1), the responses subjected to a wing force with 0-degree of wind force (both X-direction and Y-direction) is the largest.

Figs. 4.41~4.43 show the responses of the control system of X-direction with 0 degree, 22.5 degree, and 45 degree of wind force, and Fig. 4.44~4.46 show that of Y-direction. Fig. 4.47 shows the time-history waves of control force (1st case only) of X-direction of X-direction with 0 degree, 22.5 degree, and 45 degree of wind force, and Fig. 4.48 shows that of Y-direction. Note that the value of weighting entries is 18.1 (selected at Subsection 4.6.2 *"Design example"*). From Figs. 4.41~4.48, it can be seen that the responses and control force of 0-degree of wind-angle is the largest one. Thus, this study uses wind force of 0 degree of wind angle to carry out for analysis.

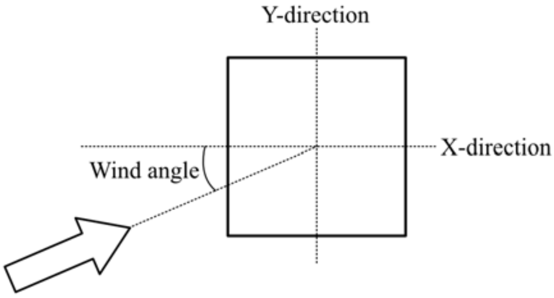

(a) Definition of wind angle and response direction

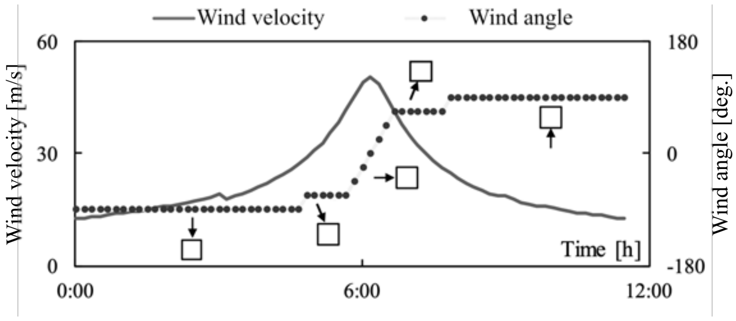

(b) Wind angle and wind velocity

Figure 4.40: An example of time-history wave of wind angle and wind velocity of typhoon event

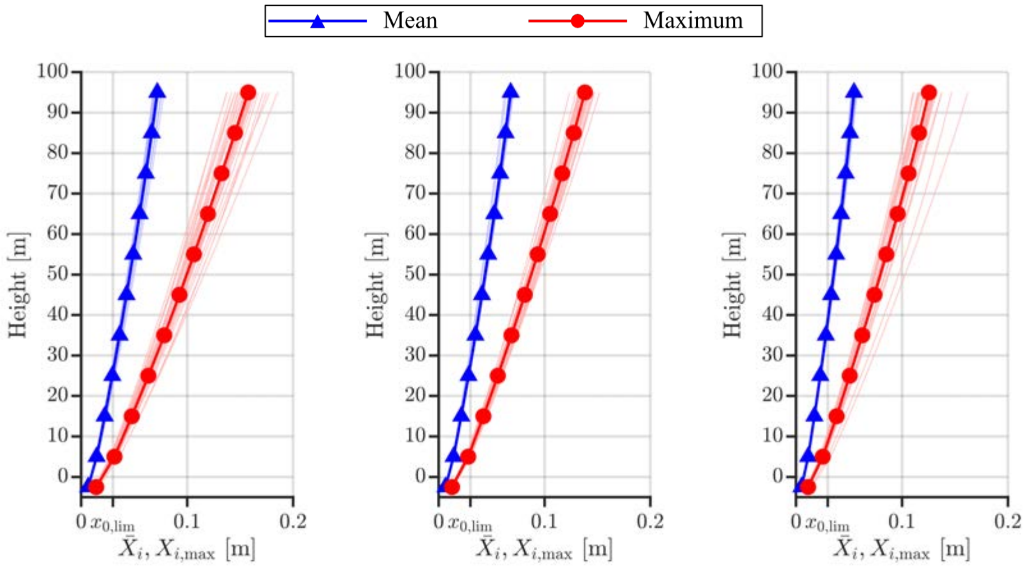

(a) Wind angle: 0 deg. **(b)** Wind angle: 22.5 deg. **(c)** Wind angle: 45 deg.

Figure 4.41: Story distribution of displacement on X-direction (β = 18.1)

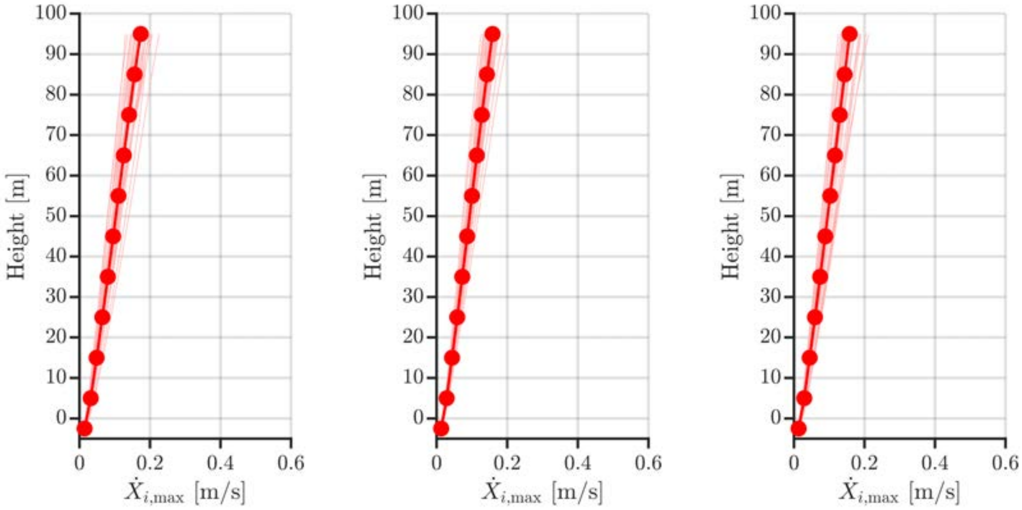

(a) Wind angle: 0 deg. **(b)** Wind angle: 22.5 deg. **(c)** Wind angle: 45 deg.

Figure 4.42: Story distribution of velocity on X-direction (β = 18.1)

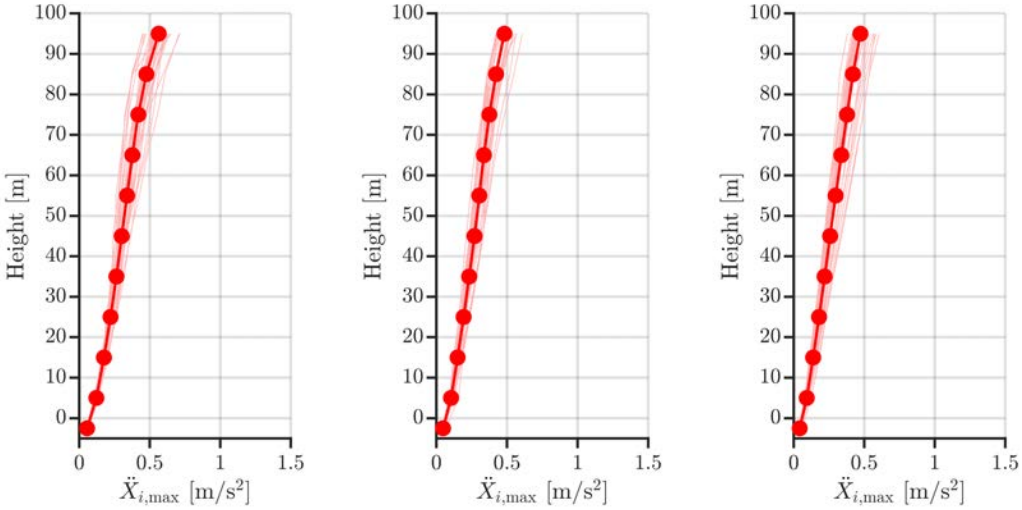

(a) Wind angle: 0 deg. **(b)** Wind angle: 22.5 deg. **(c)** Wind angle: 45 deg.

Figure 4.43: Story distribution of acceleration on X-direction (β = 18.1)

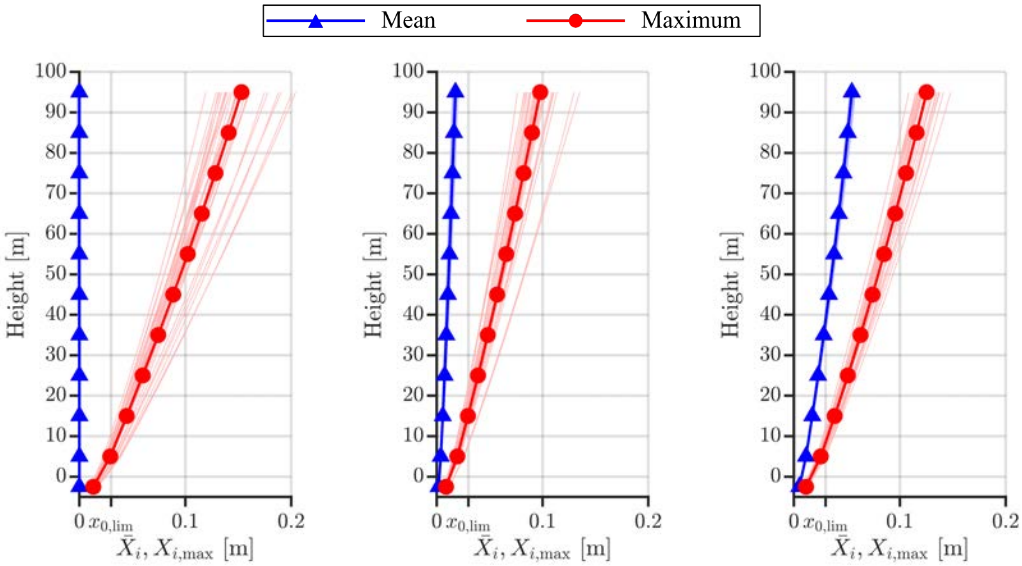

(a) Wind angle: 0 deg. **(b)** Wind angle: 22.5 deg. **(c)** Wind angle: 45 deg.

Figure 4.44: Story distribution of displacement on Y-direction (β = 18.1)

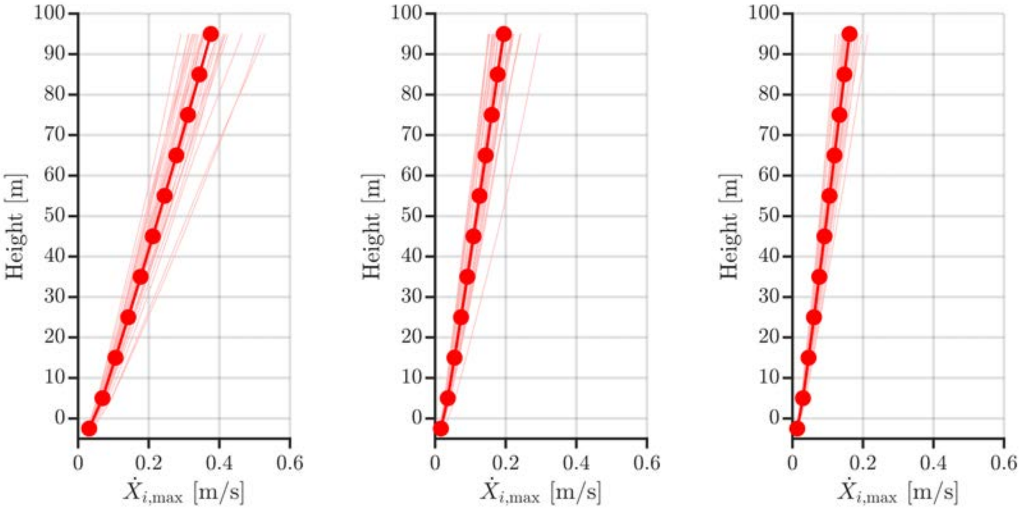

(a) Wind angle: 0 deg. **(b)** Wind angle: 22.5 deg. **(c)** Wind angle: 45 deg.

Figure 4.45: Story distribution of velocity on Y-direction (β = 18.1)

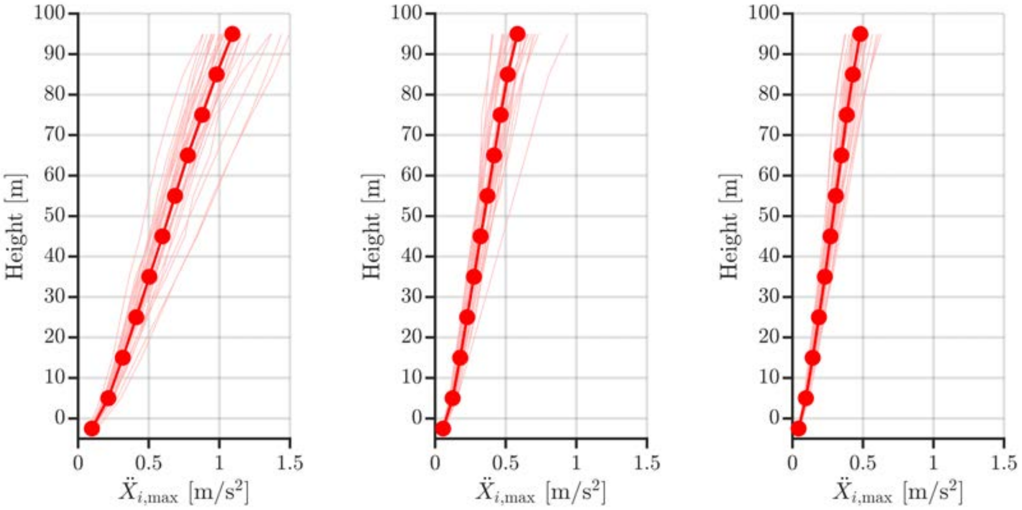

(a) Wind angle: 0 deg. **(b)** Wind angle: 22.5 deg. **(c)** Wind angle: 45 deg.

Figure 4.46: Story distribution of acceleration on Y-direction (β = 18.1)

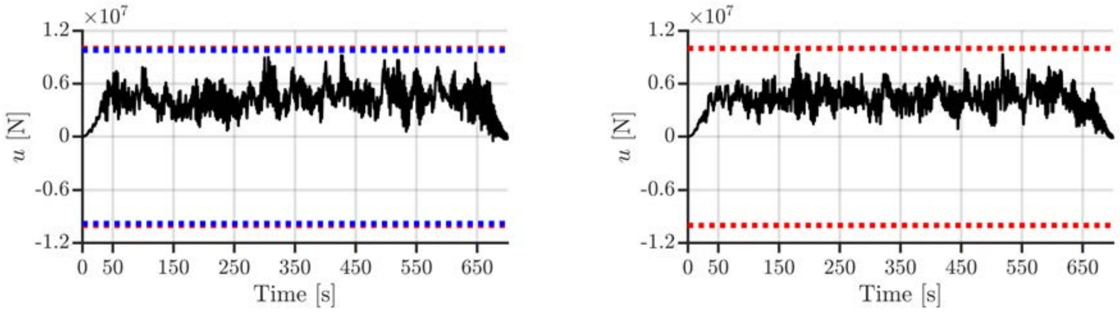

(a) Wind angle: 0 deg.

(b) Wind angle: 22.5 deg.

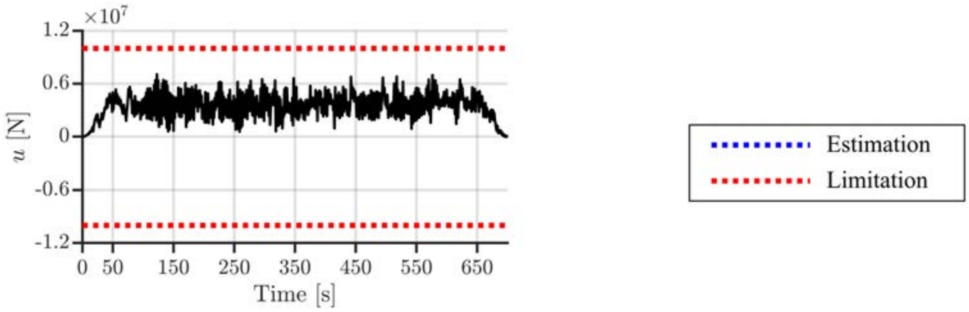

(c) Wind angle: 45 deg.

Figure 4.47: Time-history waves of control force on X-direction (β = 18.1)

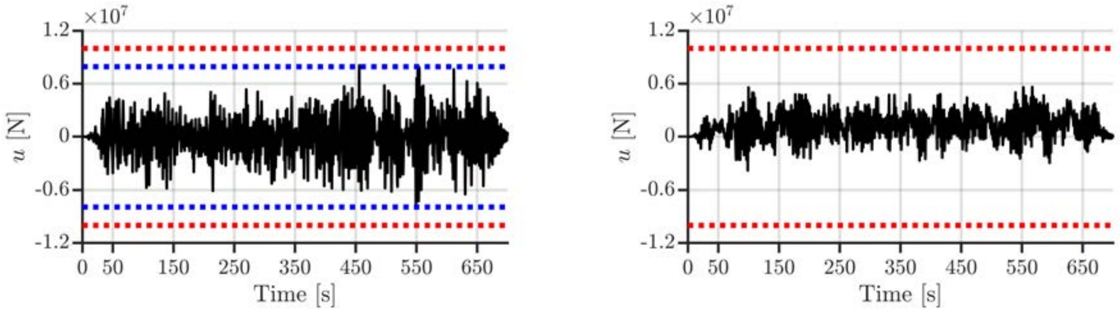

(a) Wind angle: 0 deg.

(b) Wind angle: 22.5 deg.

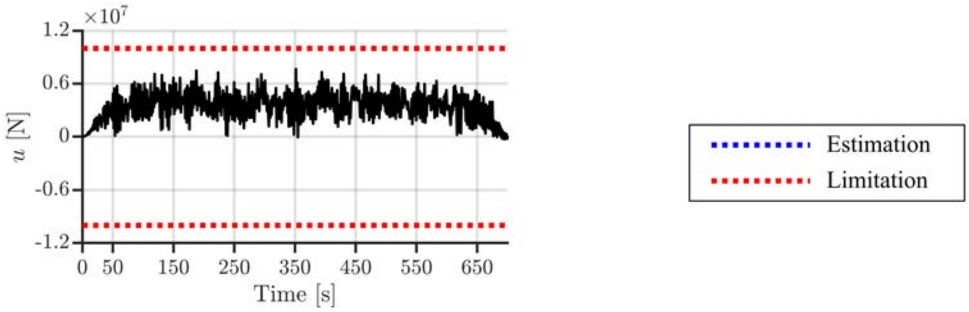

(c) Wind angle: 45 deg.

Figure 4.48: Time-history waves of control force on Y-direction (β = 18.1)

References

[4.1] Architectural Institute of Japan, AIJ Recommendations for Loads on Buildings, Architectural Institute of Japan, 2015.

[4.2] A. Kareem, Y. Zhou, Gust loading factor—past, present and future, Journal of Wind Engineering and Industrial Aerodynamics 91 (12) (2003) 1301 – 1328, eNGINEERING SYMPOSIUM To Honour ALAN G. DAVENPORT for his 40 Years of Contributions. `doi:10.1016/j.jweia.2003.09.003`.

[4.3] D. Sato, Y. Chen, K. Miyamoto, J. She, A spectrum for estimating the maximum control force for passive-base-isolated buildings with lqr control, Engineering Structures 199 (2019) 109600. `doi:10.1016/j.engstruct.2019.109600`.

[4.4] Y. Chen, D. Sato, K. Miyamoto, J. She, Method of designing control system for high-rise seismically isolated buildings with active control under along-wind force [in Japanese], Journal of Structural Engineering (Transactions of AIJ) 64B (2018) 199–206.

[4.5] S. Korkmaz, A review of active structural control: challenges for engineering informatics, Computers & Structures 89 (23) (2011) 2113 – 2132. `doi:10.1016/j.compstruc.2011.07.010`.

[4.6] K. Miyamoto, D. Sato, J. She, A new performance index of LQR for combination of passive base isolation and active structural control, Engineering Structures 157 (2018) 280 – 299. `doi:10.1016/j.engstruct.2017.11.070`.

[4.7] K. Miyamoto, J. She, J. Imani, X. Xin, D. Sato, Equivalent-input-disturbance approach to active structural control for seismically excited buildings, Engineering Structures 125 (2016) 392 – 399. `doi:10.1016/j.engstruct.2016.07.028`.

[4.8] F. Casciati, J. Rodellar, U. Yildirim, Active and semi-active control of structures – theory and applications: A review of recent advances, Journal of Intelligent Material Systems and Structures 23 (11) (2012) 1181–1195. `doi:10.1177/1045389X12445029`.

[4.9] A. Preumont, A. Seto, Active control of structures, John Wiley & Sons, Inc., 2008.

[4.10] R. Dorf, R. Bishop, Modern Control Systems, 13th Edition, Pearson, 2017.

[4.11] G. Saito, D. Sato, K. Yoshie, T. Ohkuma, J. Katagiri, H. Kitamura, Influence of number of wind-force samples on response of high-rise base-isolated building using elastoplastic model [in Japanese], AIJ Journal of Technology and Design 23 (2017) 65–70. `doi:10.3130/aijt.23.65`.

[4.12] H. Marukawa, T. Ohkuma, H. Kitimura, K. Yoshie, T. Tsurumi, D. Sato, 20097 energy input of local wind forces for high-rise building based on wind tunnel test : Part.2 local wind force characteristics of rectangular high-rise buildings [in Japanese], in: Summaries of technical papers of annual meeting of Architectural Institute of Japan, Architectural Institute of Japan, 2010, pp. 193–194.
URL `https://www.aij.or.jp/paper/detail.html?productId=204006`

CHAPTER 5

Wind-resistant design on across-wind direction

5.1 Introduction

Chapter 4 presented the method for estimating the maximum displacement and maximum control force using the mean responses caculated by static balance and gust factors on along-wind direction. However, wind force on across-wind direction does not contain a mean component, the gust factor can not be used on across-wind direction.

Japan wind-resistant design code [5.1] provides the peak-factor method for estimating the maximum displacement of a passive base-isolated structure. The peak-factor method estimates the standard deviation of displacement via power spectral density (PSD) and transfer function of the structure. Japan wind-resistant design code [5.1] also provides the equation for estimating the peak factor for displacement. Thus, the maximum displacement can be estimated by the multiplication of the standard deviation and peak factor. Only the 1st mode response are used to estimate the maximum displacement for multi-DOFs models, because the influence of the 1st mode is dominant subjecting to wind loading [5.2].

This chapter construct an equivalent model of a multi-DOFs active model using the method provided at Chapter 4 (Eq. (4.24)). Modal analysis is used to obtain the 1st mode of the equivalent model, and this chapter uses the method presented in Japan wind-resistant design code [5.1] to calculate the standard deviation and peak factor of the 1st mode. Moreover, this chapter also proposes a new estimation equation of the standard deviation of control force using the transfer function of control force. This chapter only uses the maximum response and maximum control force of the 1st mode to estimate the maximum response and maximum control force of the multi-DOFs model. Thus, using the extend peak-factor method, both the maximum displacement and maximum control force are estimated without numerical simulations. Furthermore, This chapter devises a design method for determining the design parameters of the control system that satisfies the design limitations requires no trial-and-error approaches and numerical simulations.

5.2 Mathematics models

5.2.1 Introduction of buildings

The buildings used in this Chapter are the same with Chapter 4. The parameters of A4 and A5 buildings are shown at Table 4.4.

5.2.2 Construction of Control System

The control systems used in this chapter are the same with Chapter 4

5.2.3 Equivalent model of active model

This section uses the same method to construct the equivalent model of the active model.

5.3 Wind force for simulation

5.3.1 Summary of wind force

Wind force on across direction is determined by the WTE. The calculation procedure is shown at Appendix 4A.2.

5.4 Estimation of displacement response

This section shows the peak-factor method for estimating the maximum displacement of the control system on along-wind direction, and uses numerical simulations to verify the validity of the estimation method.

5.4.1 Estimation procedure

The maximum displacement of the control system is estimated using the peak-factor method:

$$x_{\max,i} = g_D \sigma_{D,i}, \tag{5.1}$$

where $X_{\max}$ is the maximum-displacement vector; g_D is the peak factor for displacement; σ_D standard deviation of displacement.

The estimation procedure are given below:

Step. 1 Construction the equivalent model of the active model:
Calculate the equivalent stiffness matrix and equivalent damping matrix (K_{eq} and C_{eq}) using (4.24).

Step. 2 Calculating the dynamic parameters of the 1st mode of the equivalent model by modal analysis:

(1) Calculate the 1st mode vector, $\phi_{\text{eq,m1}}$, via generalized eigenvectors of the equivalent stiffness matrix, K_{eq}, and mass matrix, M. Note that this paper uses non-proportional damping models, complex modal analysis are required for the theory. But, this method ignores the influence of non-proportional damping, and only carries out real number solutions:

$$\begin{aligned} \text{eig.}(\mathbf{K_{eq}}, \mathbf{M}) &= \begin{bmatrix} \boldsymbol{\phi}_{\mathbf{eq,m1}} & \cdots & \boldsymbol{\phi}_{\mathbf{eq,m11}} \end{bmatrix} \\ &= \begin{bmatrix} \phi_{\text{eq,m1,0}} & \cdots & \phi_{\text{eq,m11,0}} \\ \vdots & \ddots & \vdots \\ \phi_{\text{eq,m1,10}} & \cdots & \phi_{\text{eq,m11,10}} \end{bmatrix}. \end{aligned} \tag{5.2}$$

(2) Calculate the mass, stiffness, and damping coefficient of the 1st mode of equivalent model ($m_{\mathrm{eq,m1}}$, $k_{\mathrm{eq,m1}}$, and $c_{\mathrm{eq,m1}}$) by the following equation:

$$m_{\mathrm{eq,m1}} = \phi^{-1}_{\mathbf{eq,m1}}\mathbf{M}\phi_{\mathbf{eq,m1}}, \tag{5.3a}$$

$$k_{\mathrm{eq,m1}} = \phi^{-1}_{\mathbf{eq,m1}}\mathbf{K}_{\mathbf{eq}}\phi_{\mathbf{eq,m1}}, \text{ and} \tag{5.3b}$$

$$c_{\mathrm{eq,m1}} = \phi^{-1}_{\mathbf{eq,m1}}\mathbf{c}_{\mathbf{eq}}\phi_{\mathbf{eq,m1}}. \tag{5.3c}$$

(3) Calculate the natural frequency and damping ratio of the 1st mode of the equivalent model ($f_{\mathrm{eq,m1}}$ and $\zeta_{\mathrm{eq,m1}}$):

$$f_{\mathrm{eq,m1}} = \frac{2\pi}{\omega_{\mathrm{eq,m1}}}, \tag{5.4a}$$

$$\zeta_{\mathrm{eq,m1}} = \frac{c_{\mathrm{eq,m1}}}{2m_{\mathrm{eq,m1}}\omega_{\mathrm{eq,m1}}}, \text{ and} \tag{5.4b}$$

$$\omega_{\mathrm{eq,m1}} = \frac{k_{\mathrm{eq,m1}}}{c_{\mathrm{eq,m1}}}. \tag{5.4c}$$

where $\omega_{\mathrm{eq,m1}}$ is the natural angular frequency of the 1st mode of the equivalent model.

Step. 3 Calculate the standard deviation of the displacement for the 1st mode of the equivalent model, $\sigma_{D,0}(f)$,:

(1) Calculate the wind force of the 1st mode of the equivalent model:

$$F_{\mathrm{eq,m1}}(t) = \phi^{-1}_{\mathbf{eq,m1}}\mathbf{F}(t). \tag{5.5}$$

(2) Calculate the PSD of $F_{\mathrm{eq,m1}}(t)$: $S_{f,\mathrm{eq,m1}}(f)$.

(3) Calculate the transfer function of the 1st mode from input to displacement, $H_{D,\mathrm{eq,m1}}$:

$$H_{D,\mathrm{eq,m1}}(f) = \frac{1}{1-\left(f/f_{\mathrm{eq,m1}}\right)^2 + 2\mathrm{i}\,\zeta_{\mathrm{eq,m1}}\left(f/f_{\mathrm{eq,m1}}\right)} \cdot \frac{1}{k_{\mathrm{eq,m1}}}. \tag{5.6}$$

(4) Calculate the PSD of displacement of the base-isolation layer, $S_{D,0}(f)$:

$$S_{D,0}(f) = \left|H_{D,\mathrm{eq,m1}}(f)\right|^2 S_{f,\mathrm{eq,m1}}(f)\ \phi_{\mathrm{eq,m1,0}}. \tag{5.7}$$

(5) Calculate $\sigma_{D,0}$ by the following equation:

$$\sigma_{D,0} = \sqrt{\int_0^{\infty} S_{D,0}(f)\,\mathrm{d}f}. \tag{5.8}$$

Step. 4 Calculate the peak factor for displacement of the 1st mode of equivalent model $g_{D,\mathrm{eq}}$ using the AIJ design code [5.1]:

$$g_{D,\mathrm{eq,m1}} = \sqrt{2\ln(600 f_{\mathrm{eq,m1}}) + 1.2}. \tag{5.9}$$

Step. 5 Calculate the estimation value of the maximum displacement of the base-isolation story by the following equation:

$$x_{0,\mathrm{max,est}} = g_{D,\mathrm{eq,m1}}\ \sigma_{D,0}. \tag{5.10}$$

5.4.2 Numerical verification

This section shows the accuracy of the estimation method for maximum displacement via numerical examples. The parameters of the model and wind force are given below:

Aspect ratio of the superstructure: 4 (A4 building)
Return period of wind force: 500 years
Number of cases for ensemble average: 30 [5.3–5.5]
Terrain category of wind force: 3
Natural period of the isolator: 3, 4, and 5 s
Damping ratio of the viscous damper: 0.01, 0.05, and 0.10

Fig. 5.1 shows the story wind force used in this section. Fig. 5.2 shows the 30-cases ensemble average of power spectral density (PSD) of 10th story-wind force.

Figs. 5.3 and 5.4 shows the comparison of the standard deviation of displacement of the isolation story, $\sigma_{D,0}$, between estimation values and simulation results. From Figs. 5.3

and 5.4, The following results are obtained:

- The estimated standard deviation of displacement of isolation story, $\sigma_{D,0}$, by the equivalent model matches well to the values calculated by numerical simulations. Thus, the validity of the presented equation, (5.8), is confirmed.
- $\sigma_{D,0}$ decreases as the weighting entry, β, increases.
- $\sigma_{D,0}$ increases as the isolated period, T_0, increases, if $\beta < 15$.
- $\sigma_{D,0}$ decreases as the damping ratio, ζ_0, increases.
- The values of $\sigma_{D,0}$ are the same for different isolated periods and damping ratios, if $\beta > 15$.

Figs. 5.5 and 5.6 shows the comparison of the peak factor for displacement of the base-isolation story, $g_{D,0}$, between estimation values and simulation results. From Figs. 5.5 and 5.6, The following results are obtained:

- The estimated peak factor of displacement of isolation story, $g_{D,0}$, by the equivalent model matches well to the values calculated by numerical simulations. Thus, the validity of the presented equation, (5.9), is confirmed.
- $g_{D,0}$ increases as the weighting entry, β, increases.
- The values of $\sigma_{D,0}$ are the same for different isolated periods and damping ratios, if $\beta > 15$.
- The simulation values of peak factor have peak values around $\beta = 17$, however, the estimation values do not have. The reason for it are explained at Appendix 5B.

Figs. 5.7 and 5.8 shows the comparison of the maximum displacement of the isolation story, $\sigma_{D,0}$, between estimation values and simulation results. From Figs. 5.7 and 5.8, The following results are obtained:

- The estimated maximum displacement of isolation story, $x_{0,\max}$, by the equivalent model matches well to the values calculated by numerical simulations. Thus, the validity of the presented equation, (5.10), is confirmed.

- $x_{0,\max}$ decreases as the weighting entry, β, increases.
- $x_{0,\max}$ decreases as the isolated damping ratio, ζ_0, increases.
- $x_{0,\max}$ increases as the isolated natural period, T_0, increases.
- The values of $\sigma_{D,0}$ are the same for different isolated periods and damping ratios, if $\beta > 15$.

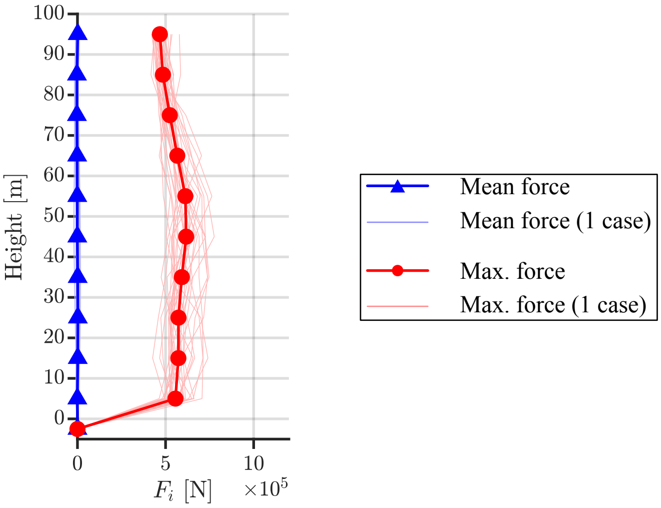

Figure 5.1: Story wind force for numerical verification (across-wind direction)

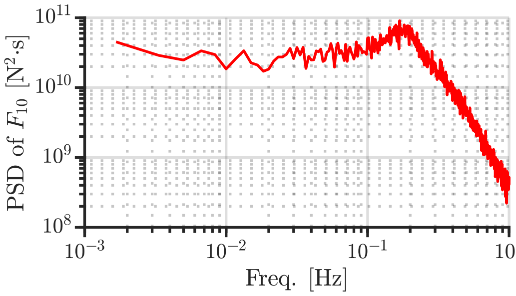

Figure 5.2: PSD of 10th story-wind force (across-wind direction)

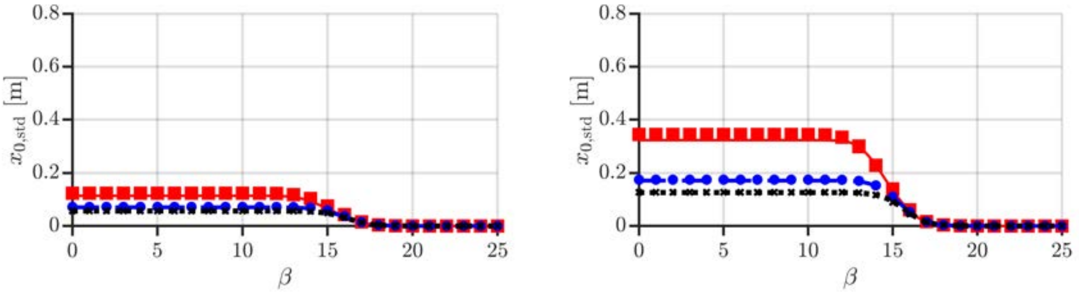

(a) T_0 = 3 s

(b) T_0 = 4 s

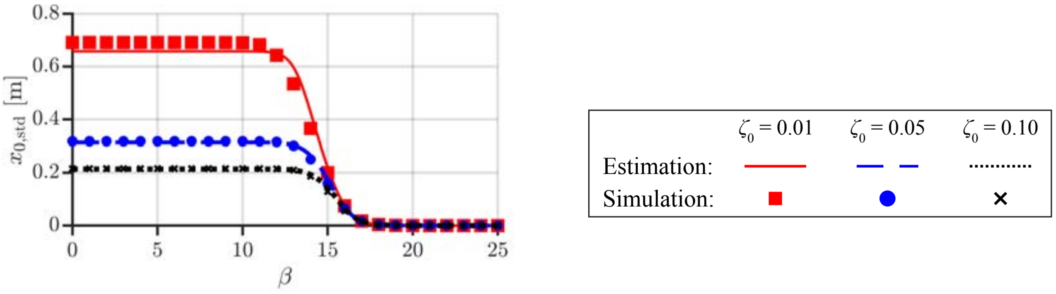

(c) T_0 = 5 s

Figure 5.3: Standard deviation of displacement of isolation story: estimation vs. simulation (across-wind direction)

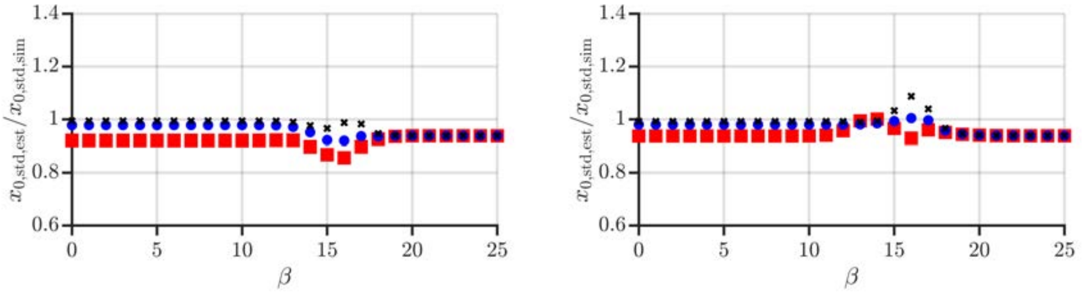

(a) T_0 = 3 s

(b) T_0 = 4 s

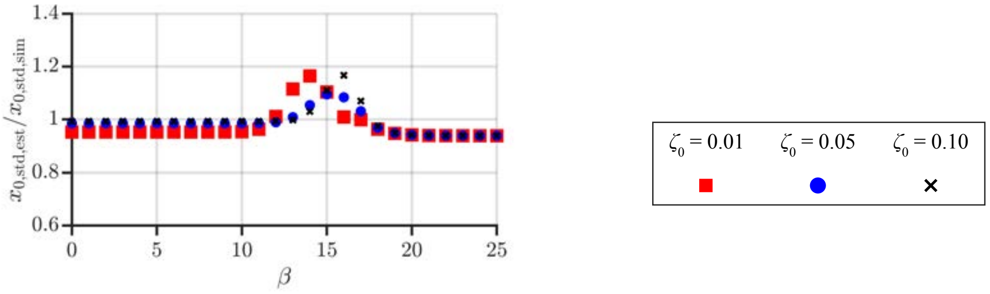

(c) T_0 = 5 s

Figure 5.4: Estimation error of standard deviation of displacement of isolation story (across-wind direction)

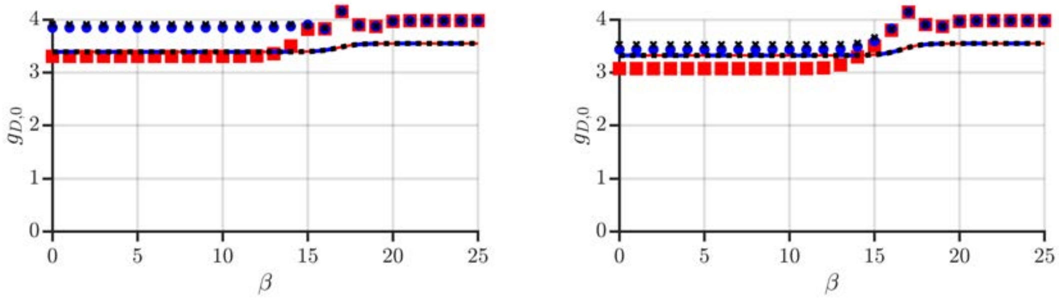

(a) T_0 = 3 s **(b)** T_0 = 4 s

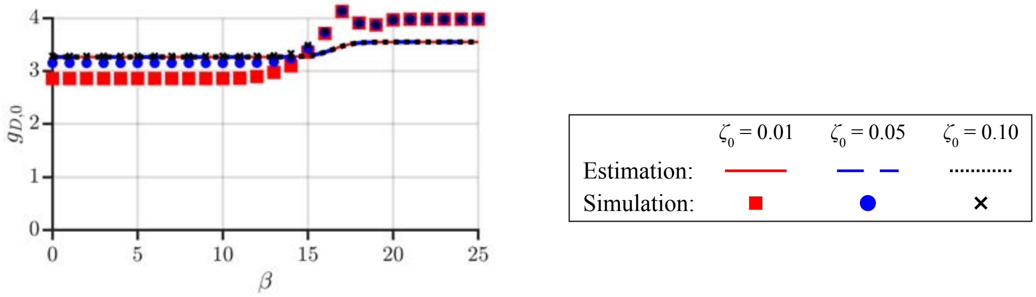

(c) T_0 = 5 s

Figure 5.5: Peak factor for displacement of isolation story: estimation vs. simulation (across-wind direction)

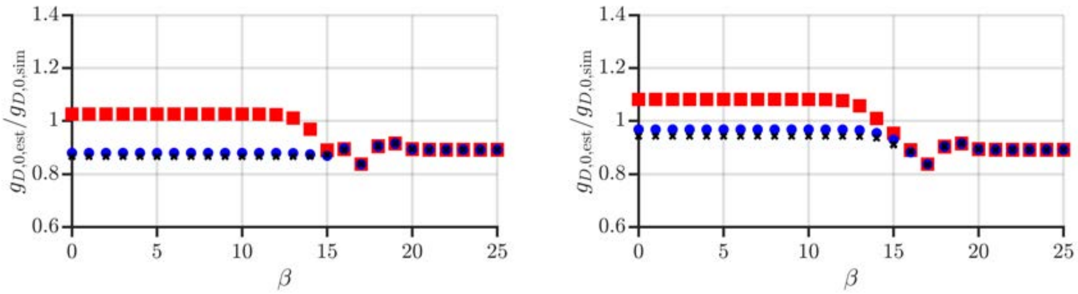

(a) T_0 = 3 s **(b)** T_0 = 4 s

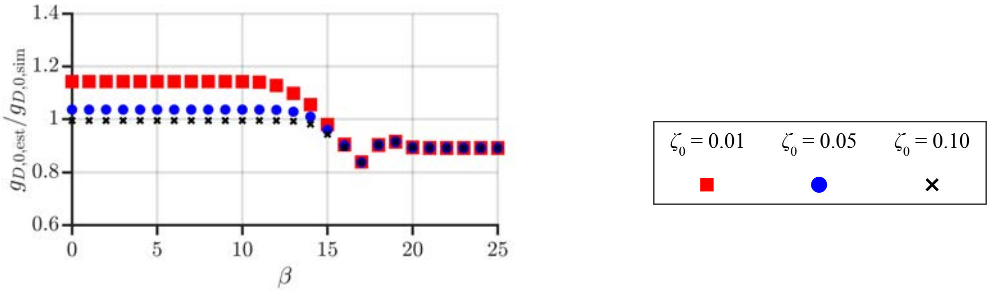

(c) T_0 = 5 s

Figure 5.6: Estimation error of peak factor for displacement of isolation story (across-wind direction)

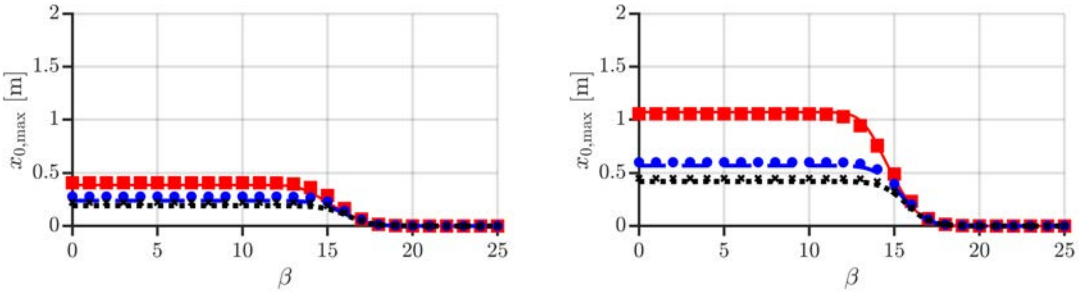

(a) T_0 = 3 s **(b)** T_0 = 4 s

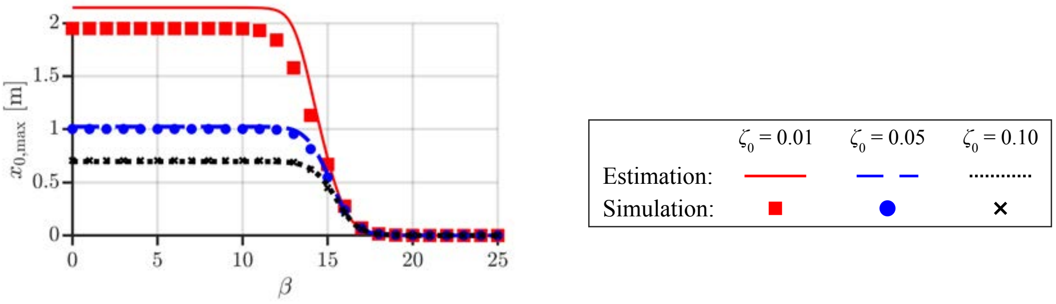

(c) T_0 = 5 s

Figure 5.7: Maximum displacement of isolation story: estimation vs. simulation (across-wind direction)

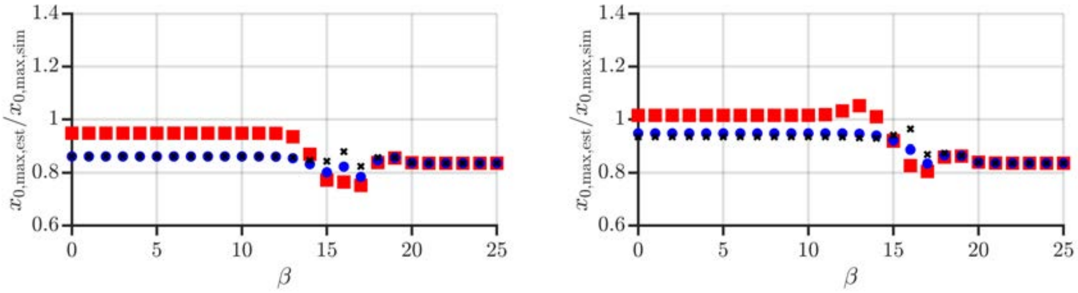

(a) T_0 = 3 s **(b)** T_0 = 4 s

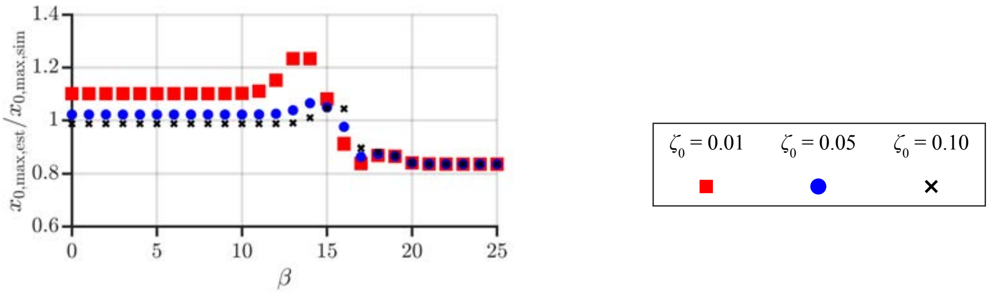

(c) T_0 = 5 s

Figure 5.8: Estimation error of maximum displacement of isolation story: estimation vs. simulation (across-wind direction)

5.5 Estimation of control force

This section shows the peak-factor method for estimating the maximum control force on across-wind direction, and uses numerical simulations to verify the validity of the estimation method.

5.5.1 Estimation procedure

The maximum control force is estimated using the peak-factor method:

$$u_{\max} = g_u \sigma_u, \tag{5.11}$$

where $u_{\max}$ is the maximum control force; g_u is the peak factor for control force; σ_u standard deviation of control force.

The estimation procedure are given below:

Step. 1 Construction the equivalent model of the active model:

Calculate the equivalent stiffness matrix and equivalent damping matrix ($\mathbf{K_{eq}}$ and $\mathbf{C_{eq}}$) using (4.24).

Step. 2 Calculating the dynamic parameters of the 1st mode of the equivalent model by modal analysis (refer to Subsection 5.4.1).

Step. 3 Calculate the natural frequency and damping ratio of the 1st mode of the equivalent model ($f_{\mathrm{eq,m1}}$ and $\zeta_{\mathrm{eq,m1}}$, refer to Subsection 5.4.1).

Step. 4 Calculate the standard deviation of control force for the 1st mode of the equivalent model, $\sigma_u(f)$,:

(1) Calculate the wind force of the 1st mode of the equivalent model:

$$F_{\mathrm{eq,m1}}(t) = \phi^{-1}_{\mathbf{eq,m1}} F(t). \tag{5.12}$$

(2) Calculate the PSD of $F_{\mathrm{eq,m1}}(t)$: $S_{f,\mathrm{eq,m1}}(f)$.

(3) Calculate the transfer function of the 1st mode from input to displacement, $H_{u,\mathrm{eq,m1}}$. From the control law, (4.15), $H_{u,\mathrm{eq,m1}}$ is

$$\begin{aligned} H_{u,\mathrm{eq,m1}}(f) &= K_{PD} H_{D,\mathrm{eq,m1}}(f) + K_{PV} H_{V,\mathrm{eq,m1}}(f) \\ &= K_{PD} H_{D,\mathrm{eq,m1}}(f) + K_{PV} \dot{H}_{D,\mathrm{eq,m1}}(f) \\ &= (K_{PD} + K_{PV}\mathrm{i}f) H_{D,\mathrm{eq,m1}}(f) \end{aligned} \tag{5.13}$$

(4) Calculate the PSD of control force of the 1st mode of the base-isolation layer, $S_{u,\mathrm{eq,m1}}(f)$:

$$S_{u,\mathrm{eq,m1}}(f) = \left| H_{u,\mathrm{eq,m1}}(f) \right|^2 S_{f,\mathrm{eq,m1}}(f)\ \phi_{\mathrm{eq,m1,0}}. \tag{5.14}$$

(5) Calculate $\sigma_{u,\mathrm{eq,m1}}$ by the following equation:

$$\sigma_{u,\mathrm{eq,m1}} = \sqrt{\int_0^\infty S_{u,\mathrm{eq,m1}}(f)\,\mathrm{d}f}. \tag{5.15}$$

Step. 5 Use the peak factor of the 1st mode of equivalent model $g_{u,\mathrm{eq}}$ using the AIJ design code [5.2] to estimate the peak factor of control force:

$$g_{u,\mathrm{eq,m1}} = g_{D,\mathrm{eq,m1}} = \sqrt{2\ln(600 f_{\mathrm{eq,m1}}) + 1.2}. \tag{5.16}$$

Step. 6 Calculate the estimation value of the maximum displacement of the base-isolation story by the following equation:

$$u_{\mathrm{max,est}} = g_{u,\mathrm{eq,m1}}\ \sigma_{u,\mathrm{eq,m1}}. \tag{5.17}$$

5.5.2 Numerical verification

This section shows the accuracy of the estimation method for maximum displacement via numerical examples. The parameters of the model and wind force are given below:

Aspect ratio of the superstructure: 4 (A4 building)

Return period of wind force: 500 years

Number of cases for ensemble average: 30

Terrain category of wind force: 3

Natural period of the isolator: 3, 4, and 5 s

Damping ratio of the viscous damper: 0.01, 0.05, and 0.10

Fig. 5.1 shows the story wind force used in this section. Fig. 5.2 shows the 30-cases ensemble average of power spectral density (PSD) of 10th story-wind force.

Figs. 5.9 and 5.10 shows the comparison of the standard deviation of displacement of the isolation story, σ_u, between estimation values and simulation results. From Figs. 5.9 and 5.10, The following results are obtained:

- The estimated standard deviation of control force, σ_u, by the equivalent model matches well to the values calculated by numerical simulations. Thus, the validity of the presented equation, (5.15), is confirmed.
- σ_u increases as the weighting entry, β, increases.
- σ_u are the same for different isolated damping ratios, ζ_0.
- The values of σ_u are the same for different isolated periods and damping ratios, if $\beta > 16$.

Figs. 5.11 and 5.12 shows the comparison of the peak factor for displacement of the base-isolation story, g_u, between estimation values and simulation results. From Figs. 5.11 and 5.12, The following results are obtained:

- The estimated peak factor of control force, g_u, by the equivalent model matches well to the values calculated by numerical simulations. Thus, the validity of the presented equation, (5.16), is confirmed.
- g_u increases as the weighting entry, β, increases.
- The values of σ_u are the same for different isolated periods and damping ratios, if $\beta > 15$.

Figs. 5.13 and 5.14 shows the comparison of the maximum displacement of the isolation story, $\sigma_{D,0}$, between estimation values and simulation results. From Figs. 5.13 and 5.14, The following results are obtained:

- The estimated maximum control force, $u_{\max}$, by the equivalent model matches well to the values calculated by numerical simulations. Thus, the validity of the presented equation, (5.17), is confirmed.
- $u_{\max}$ increases as the weighting entry, β, increases.
- The values of $u_{\max}$ are the same for different damping ratios, ζ_0.
- The values of $u_{\max}$ are the same for different isolated periods and damping ratios, if $\beta > 18$.

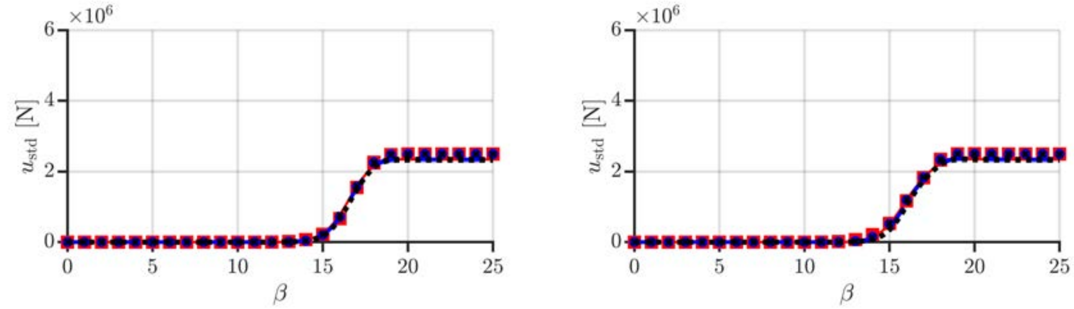

(a) T_0 = 3 s **(b)** T_0 = 4 s

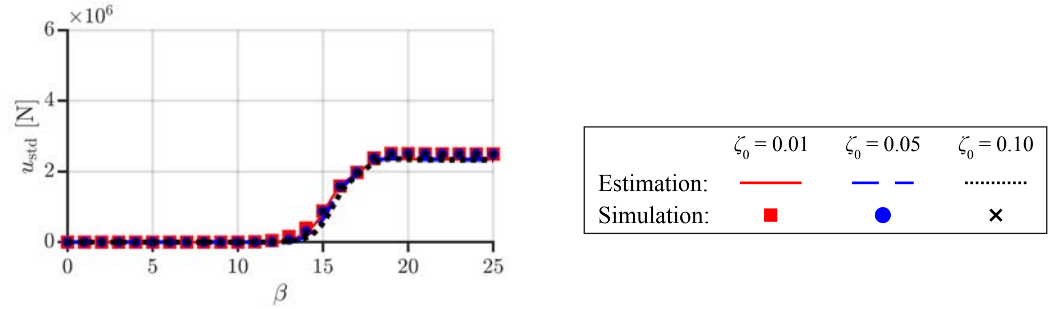

(c) T_0 = 5 s

Figure 5.9: Standard deviation of control force: estimation vs. simulation (across-wind direction)

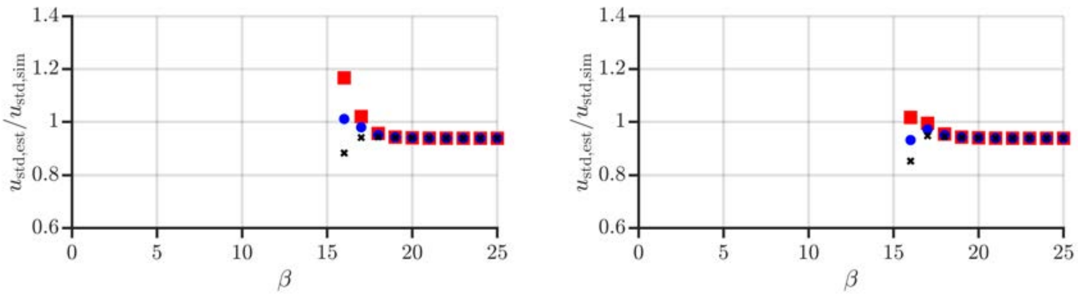

(a) T_0 = 3 s **(b)** T_0 = 4 s

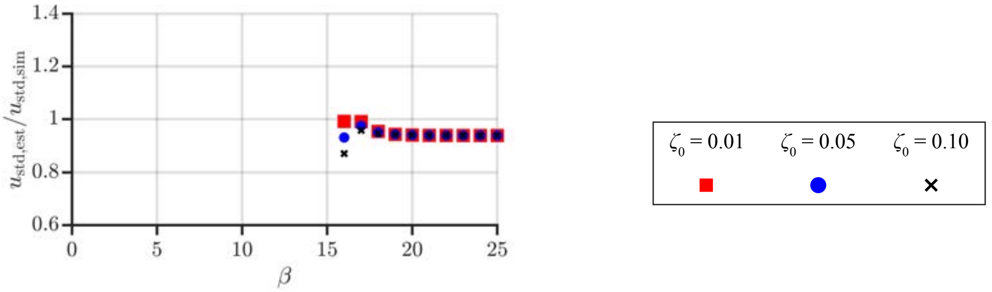

(c) T_0 = 5 s

Figure 5.10: Estimation error of standard deviation of control force (across-wind direction)

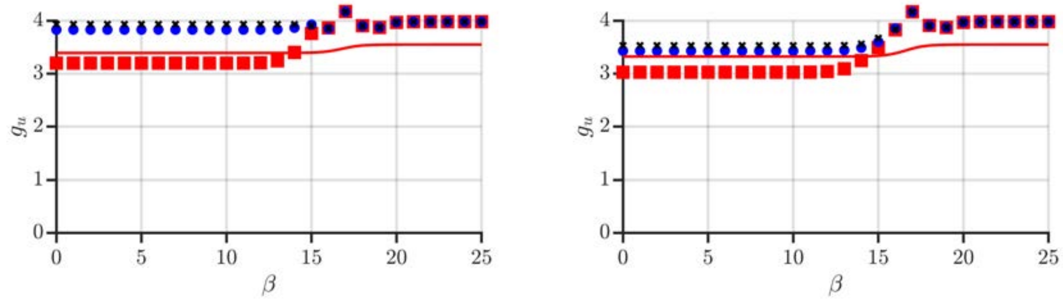

(a) T_0 = 3 s **(b)** T_0 = 4 s

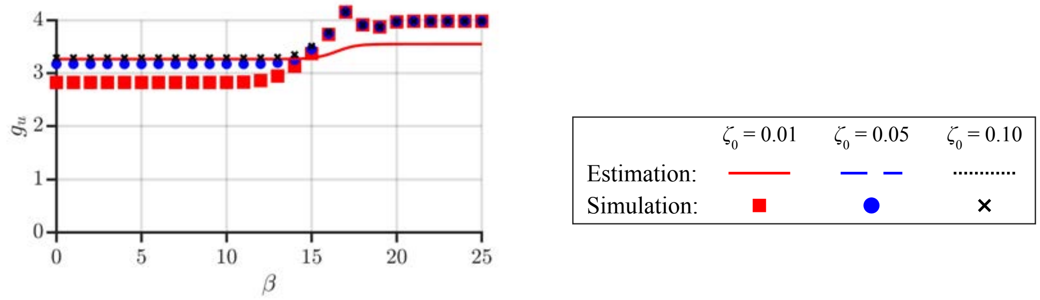

(c) T_0 = 5 s

Figure 5.11: Peak factor for control force: estimation vs. simulation (across-wind direction)

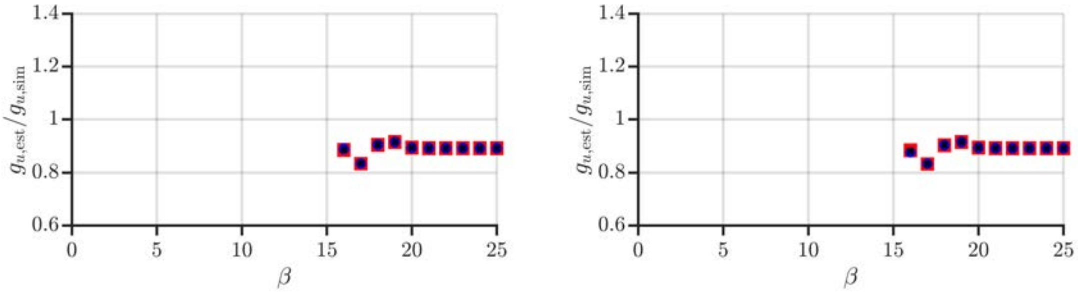

(a) T_0 = 3 s **(b)** T_0 = 4 s

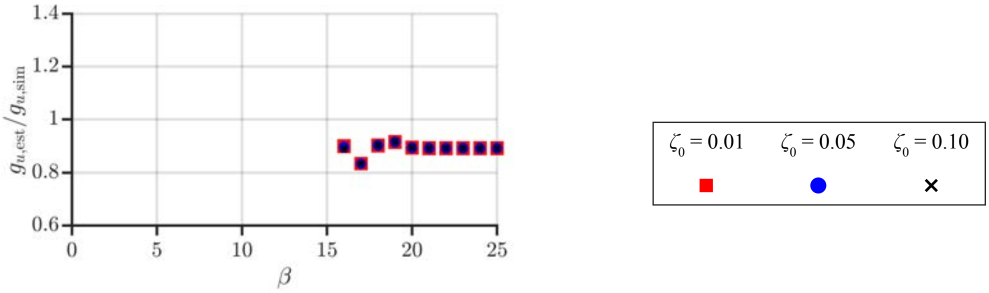

(c) T_0 = 5 s

Figure 5.12: Estimation error of peak factor for control force (across-wind direction)

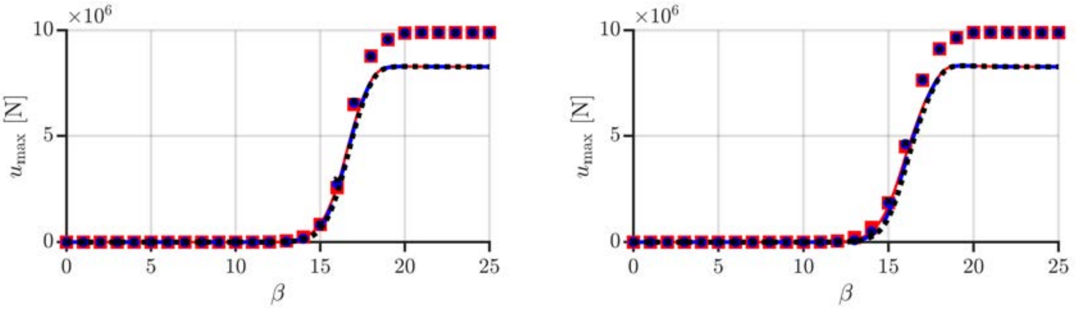

(a) T_0 = 3 s

(b) T_0 = 4 s

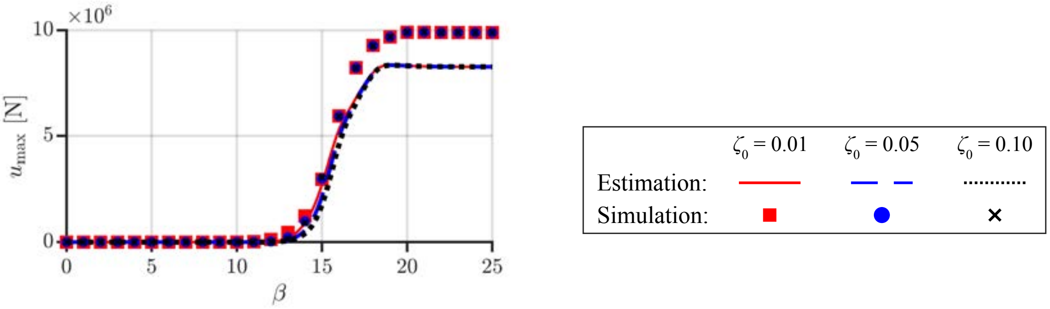

(c) T_0 = 5 s

Figure 5.13: Maximum control force: estimation vs. simulation

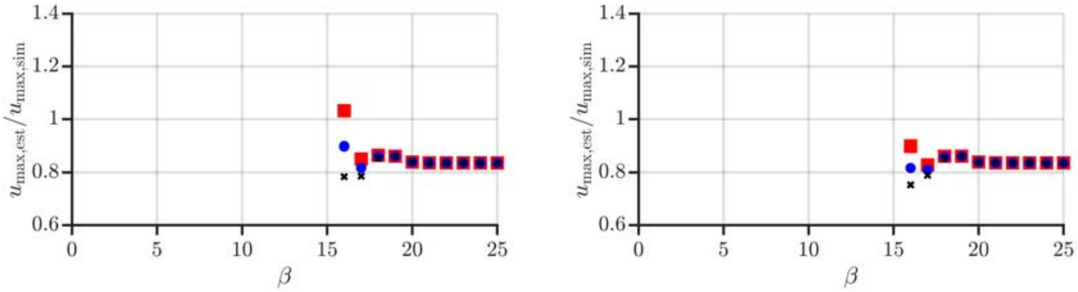

(a) T_0 = 3 s

(b) T_0 = 4 s

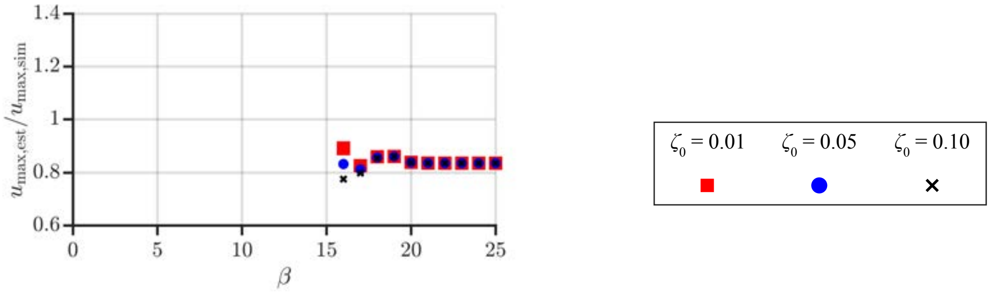

(c) T_0 = 5 s

Figure 5.14: Estimation error of maximum control force: estimation vs. simulation (across-wind direction)

5.6 Design method

This section presents the design method for the PBI structure combined with ASC under an along-wind force, for determining the isolated period, isolated damping ratio, and feedback gain that satisfy the limits on the maximum displacement response and control force. Moreover, a design example for a high-rise base-isolated building combined with active control is used to demonstrate the validity of the design method. Fig. 5.15 presents the design flowchart presented in this study.

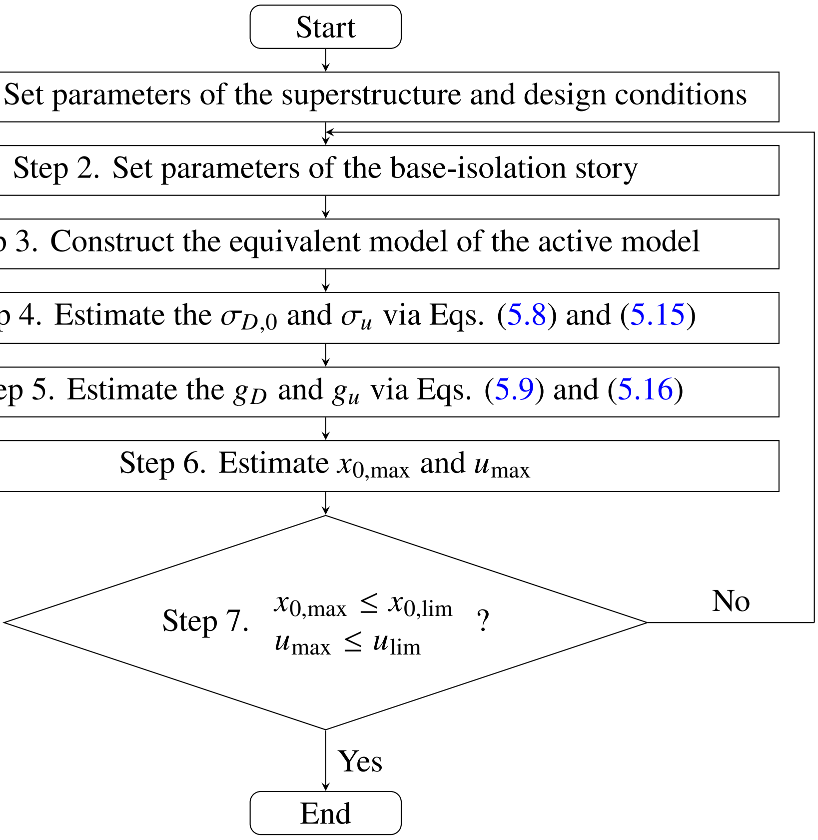

Figure 5.15: Design flowchart (Across-wind direction)

5.6.1 Design algorithm

Step 1. Specify the parameters of the superstructure and design conditions. (i.e., design wind force, design restrictions on the maximum displacement and maximum control force).

Step 2. Specify the parameters of the base-isolation story.

Step 3. Construct the equivalent model of the active model.

Step 4. Use Equation (5.8) and Equation (5.15) to estimate the standard deviation of displacement and control force, respectively.

Step 5. Use Equation (5.9) and Equation (5.16) to calculate the peak factor for displacement and control force, respectively.

Step 6. Use the estimated values for the standard deviation of displacement and control force calculated in Step 4 and the gust factor calculated in Step 5 to estimate the maximum control force and the maximum displacement response, respectively.

Step 7. If the restrictions on the maximum displacement response and maximum control force are satisfied, select the weighting entry β and proceed to the next step. If not, go back to Step 2, thereby decreasing the isolated period or increasing the isolated damping ratio or operating both of them.

Step 8. Design the control system using the isolated period T_0 and the isolated damping ratio ζ_0 determined in Step 2, and the weighting entry β selected in Step 7.

5.6.2 Design example

Step 1. Return period of along-wind force: 500 years (see Figs. 5.1 and 5.2).

Parameters of the superstructure: A4 building (as shown in Figure 4.1, 1st natural period: 2 s, damping ratio for the 1st natural period: 0.02). Parameters of the superstructure used in the design example are presented in Table 4.2.

Restrictions on the maximum control force: 1×10^7 N.

Restrictions on the maximum displacement response of PBI story: 0.03 m.

Step 2. Parameters of the PBI story: $T_0 = 4$ s and $\zeta_0 = 0.05$. Parameters of the PBI story used in the design example are presented in Table 4.4.

Step 3. Figure 5.16 presents the estimation values for the standard deviation of displacement and control force obtained using Equation (5.8) and Equation (5.15).

Step 4. Figure 5.17 presents the estimation values for the peak factor for the displacement and control force obtained using Equation (5.9) and Equation (5.16).

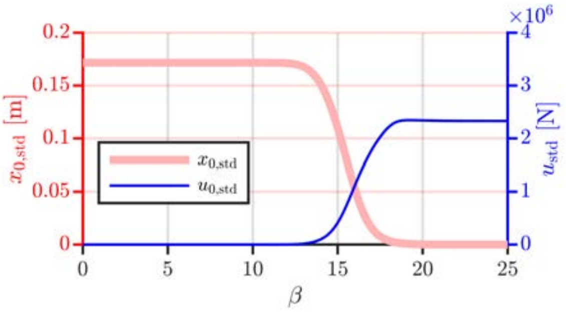

Figure 5.16: Estimated standard deviation of displacement and control force (across-wind direction)

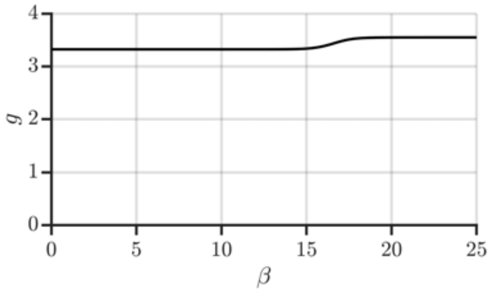

Figure 5.17: Estimated peak factor for displacement and control force (across-wind direction)

Step 5. Based on Figs. 5.16 and 5.17, the estimation values for the maximum displacement and control force of the control system are depicted in Fig. 5.18.

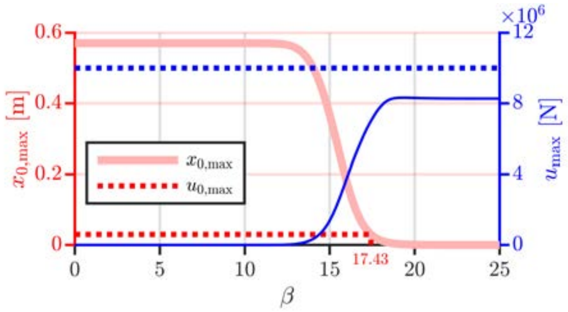

Figure 5.18: Estimated maximum displacement and maximum control force (across-wind direction)

Step 6. From Fig. 5.18, it can be observed that if $\beta > 17.03$, the restrictions on the maximum control force and maximum displacement response are satisfied. this paper selects $\beta = 20$.

Step 7. Using the values of β selected in Step 7 to determine the feedback gain K_P. This paper uses `lqr` function provided by MATLAB to calculate the feedback gain.

Fig. 5.19 shows responses of the design example model of each story. Fig. 5.20 shows time-history waves of responses (base-isolation story) and control force of design example model of each story. From Figs. 5.19 and 5.20, it can be seen that the responses of the model are suppressed by active control, and all design limitations are satisfied. Thus, the efficiency of the design method is confirmed.

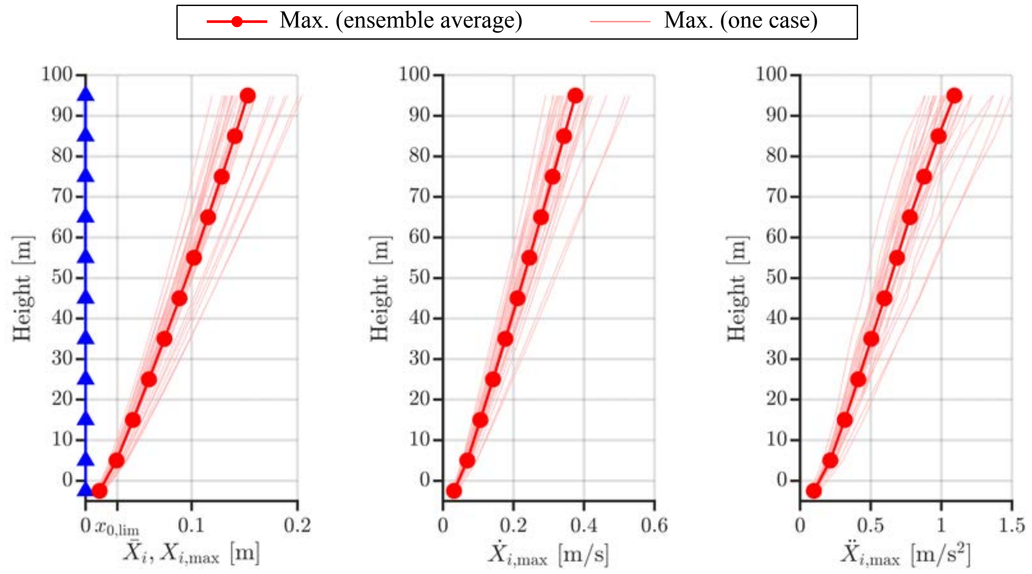

(a) Displacement **(b)** Velocity **(c)** Acceleration

Figure 5.19: Responses of design example model of each story (across-wind direction)

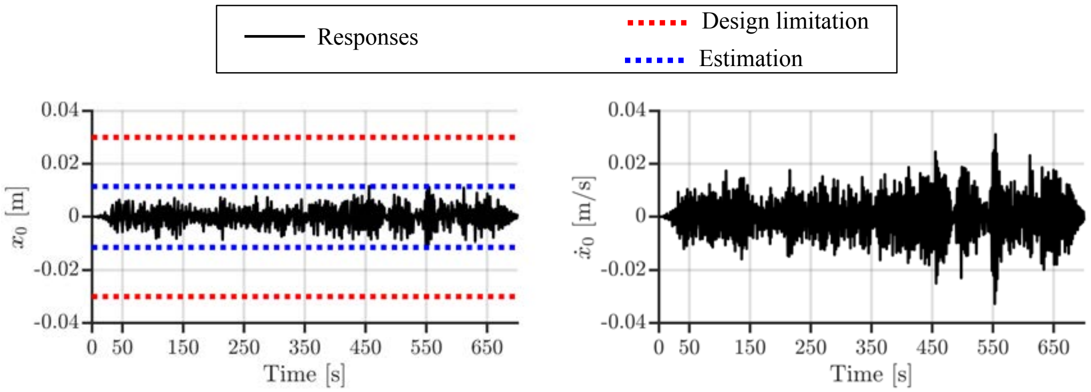

(a) Displacement **(b)** Velocity

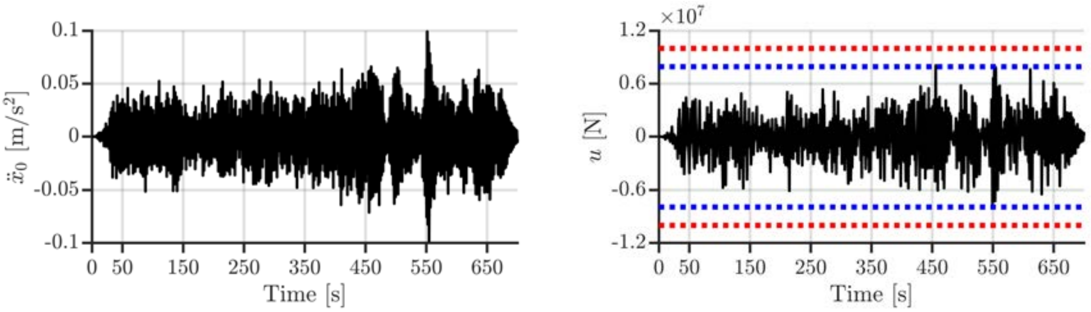

(c) Acceleration **(d)** Control force

Figure 5.20: Time-history waves of responses (base-isolation story) and control force of design example model of each story (across-wind direction, one case)

5.7 Conclusion

This section extends the peak-factor method to the base-isolated buildings with active structural control. The equivalent model of an multi-DOFs buildings with active control was constructed to demonstrate the dynamic characteristics of the control system. Moreover, A method to estimate the standard deviation and peak factor for displacement and control force was proposed in this section using modal analysis method of the constructed equivalent models. This method requires no trial-and-error approached nor numerical simulations, and using the estimated standard deviation and peak factor, the maximum displacement and maximum control force are obtained. The numerical examples confirmed the validity of the estimation methods. Finally, a design method was proposed for base-isolated buildings with active control on across-wind direction, for determining the isolated period, isolated damping ratio, and feedback gain that satisfies the restrictions on the maximum displacement response and maximum control force. The numerical design example validated the efficiency of the design method. Moreover, the following five points were also clarified based on the numerical examples:

(1) The estimation of the peak factor for displacement can be extended to buildings with active control, because the simulation results are similar to the estimated values.

(2) A method of estimating the peak factor for control force is proposed, and the numerical simulations confirm the validity of this method.

(3) The design method simplifies the design procedure for base-isolated buildings with active control, because it meets the restrictions on maximum displacement as well as maximum control force, and it does not require numerical simulations.

Appendix 5A Numerical verifications for different aspect ratio and terrain category

This section shows numerical verifications of the standard deviation of displacement, peak factor for displacement, maximum displacement, standard deviation of control force, peak factor for control force, maximum control force, between estimation values and simulation results, setting aspect ratio to 5 and terrain category to 3.

Figs. 5.21 and 5.22 show the comparison of the standard deviation of displacement of the isolation story, $\sigma_{D,0}$, between estimation values and simulation results. Figs. 5.23 and 5.24 show the comparison of the peak factor for displacement of the base-isolation story, $g_{D,0}$, between estimation values and simulation results. Figs. 5.25 and 5.26 show the comparison of the maximum displacement of the isolation story, $\sigma_{D,0}$, between estimation values and simulation results.

Figs. 5.27 and 5.28 show the comparison of the standard deviation of control force of the isolation story, $\sigma_{D,0}$, between estimation values and simulation results. Figs. 5.23 and 5.24 show the comparison of the peak factor for control force of the base-isolation story, $g_{D,0}$, between estimation values and simulation results. Figs. 5.31 and 5.32 show the comparison of the maximum control force of the isolation story, $\sigma_{D,0}$, between estimation values and simulation results.

From Figs. 5.27~5.32, it can be seen that the estimation values match to the simulation results for the cases that the aspect ratio is 5 and the terrain category is 3.

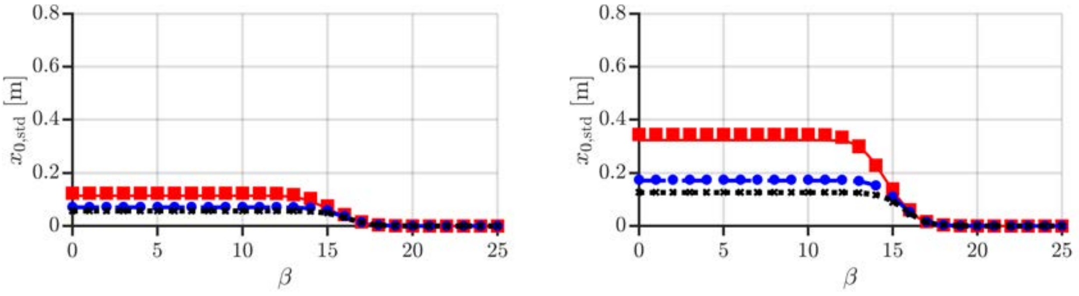

(a) T_0 = 3 s

(b) T_0 = 4 s

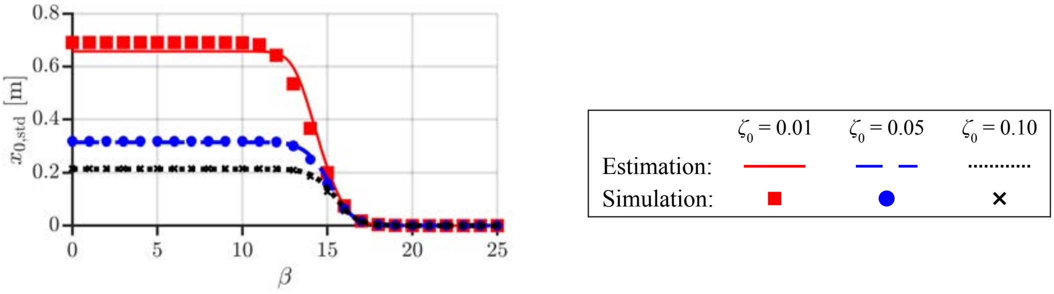

(c) T_0 = 5 s

Figure 5.21: Standard deviation of displacement of isolation story: estimation vs. simulation (across-wind direction, aspect ratio: 4, terrain category: 4)

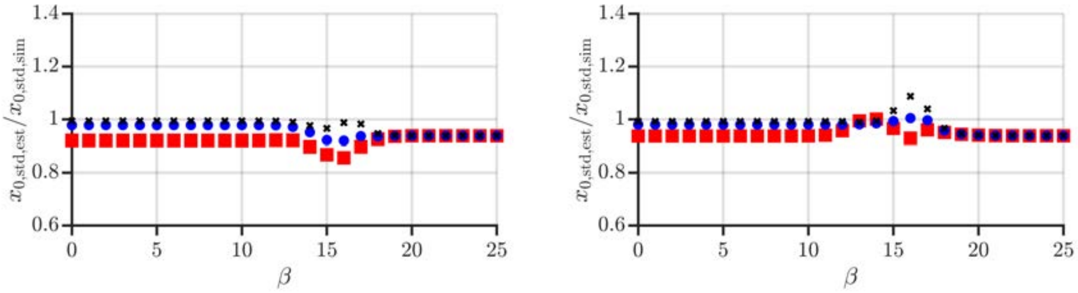

(a) T_0 = 3 s

(b) T_0 = 4 s

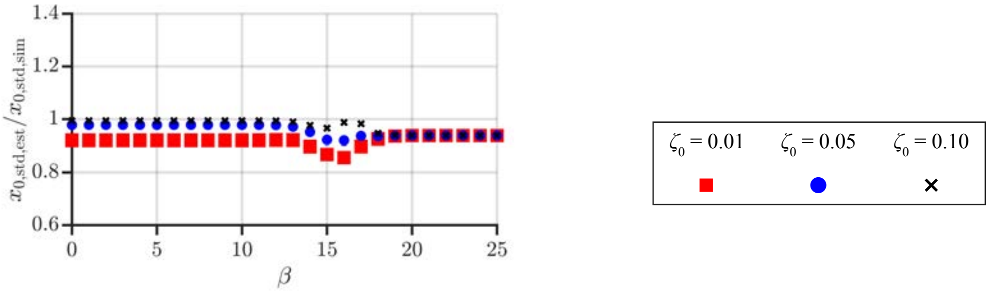

(c) T_0 = 5 s

Figure 5.22: Estimation error of standard deviation of displacement of isolation story (across-wind direction, aspect ratio: 4, terrain category: 4)

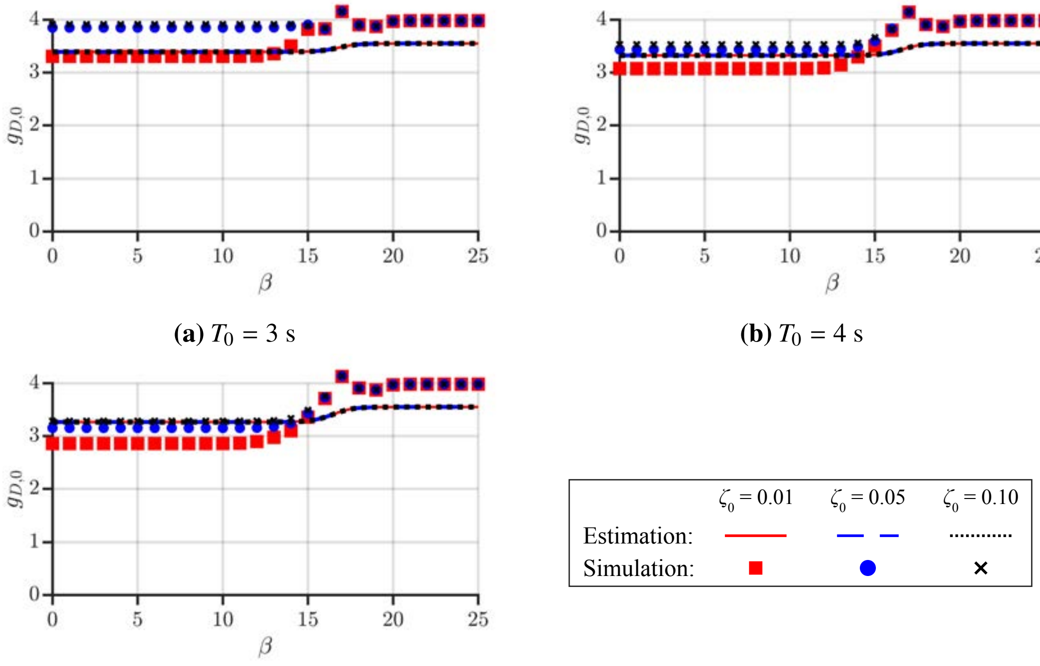

(a) T_0 = 3 s

(b) T_0 = 4 s

(c) T_0 = 5 s

Figure 5.23: Peak factor for displacement of isolation story: estimation vs. simulation (across-wind direction, aspect ratio: 4, terrain category: 4)

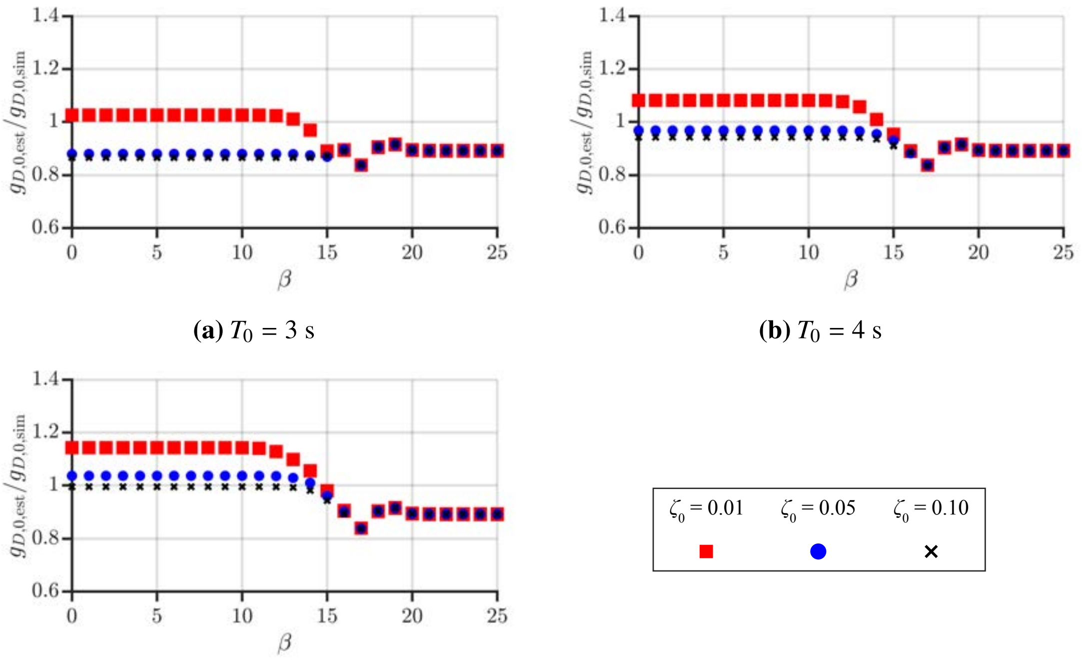

(a) T_0 = 3 s

(b) T_0 = 4 s

(c) T_0 = 5 s

Figure 5.24: Estimation error of peak factor for displacement of isolation story (across-wind direction, aspect ratio: 4, terrain category: 4)

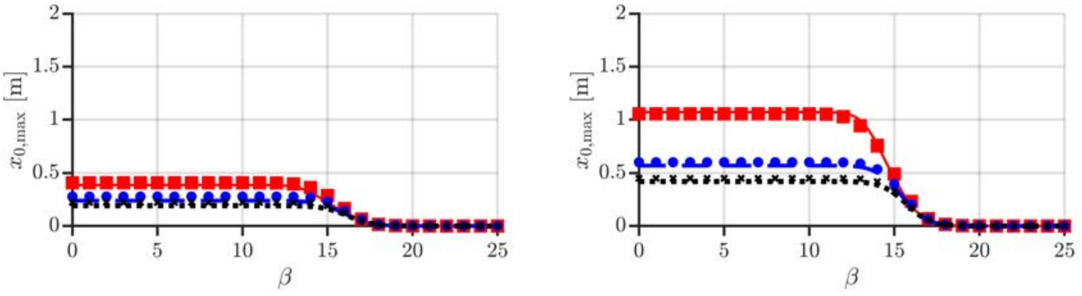

(a) T_0 = 3 s **(b)** T_0 = 4 s

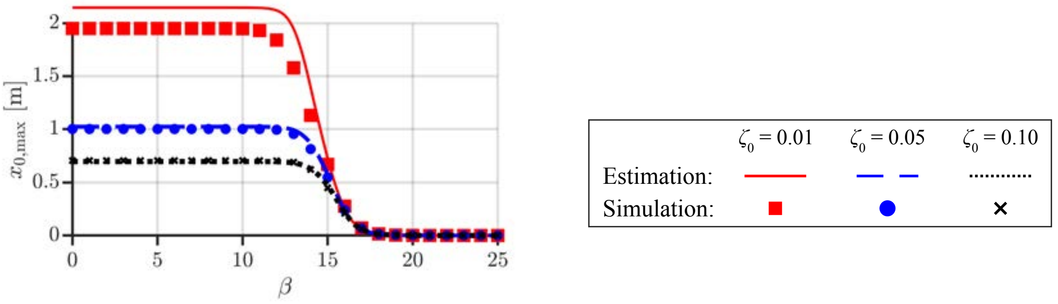

(c) T_0 = 5 s

Figure 5.25: Maximum displacement of isolation story: estimation vs. simulation (across-wind direction)

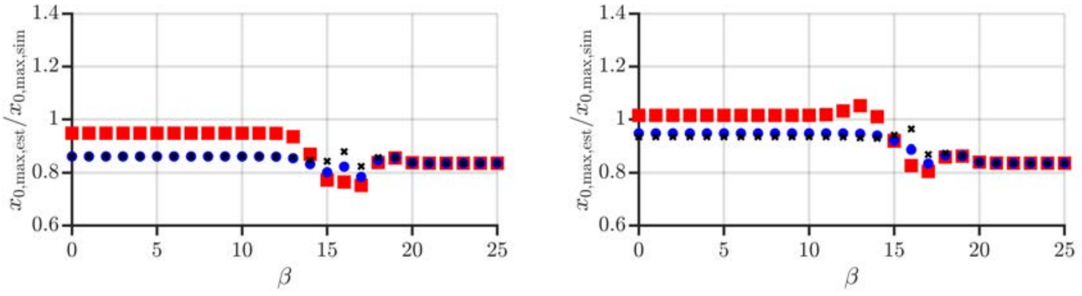

(a) T_0 = 3 s **(b)** T_0 = 4 s

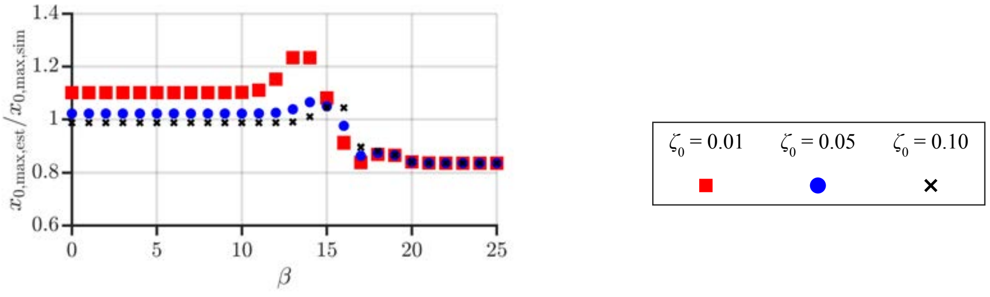

(c) T_0 = 5 s

Figure 5.26: Estimation error of maximum displacement of isolation story: estimation vs. simulation (across-wind direction, aspect ratio: 4, terrain category: 4)

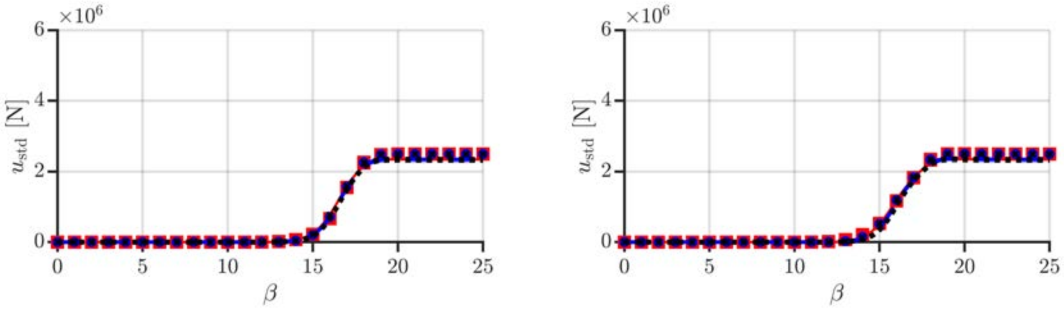

(a) T_0 = 3 s **(b)** T_0 = 4 s

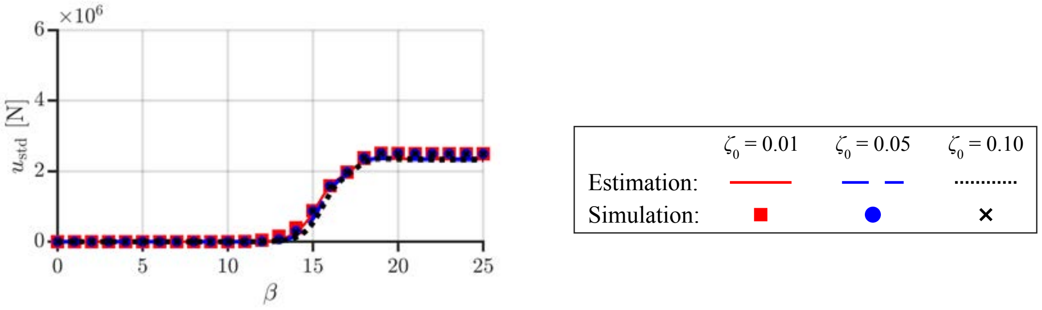

(c) T_0 = 5 s

Figure 5.27: Standard deviation of control force: estimation vs. simulation (across-wind direction, aspect ratio: 5, terrain category: 3)

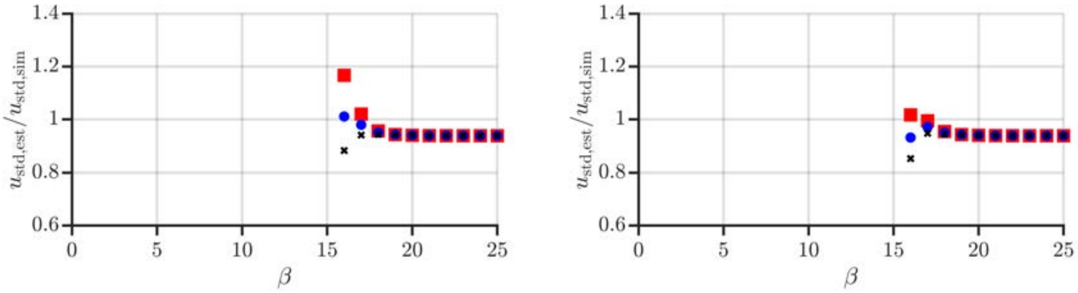

(a) T_0 = 3 s **(b)** T_0 = 4 s

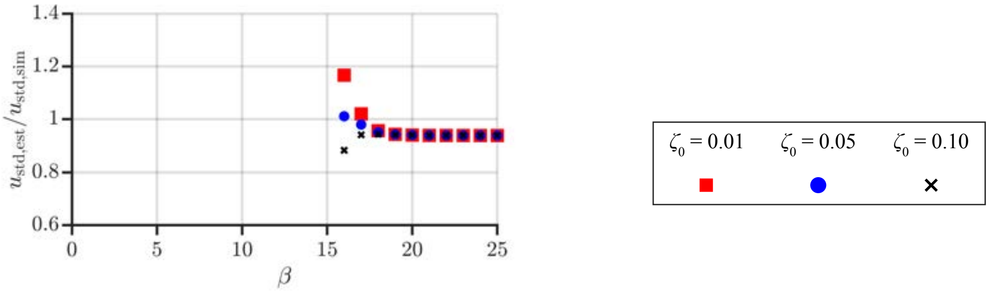

(c) T_0 = 5 s

Figure 5.28: Estimation error of standard deviation of control force (across-wind direction, aspect ratio: 5, terrain category: 3)

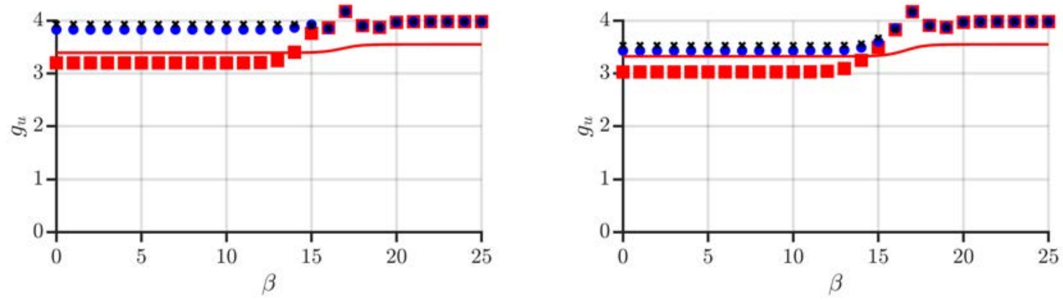

(a) T_0 = 3 s **(b)** T_0 = 4 s

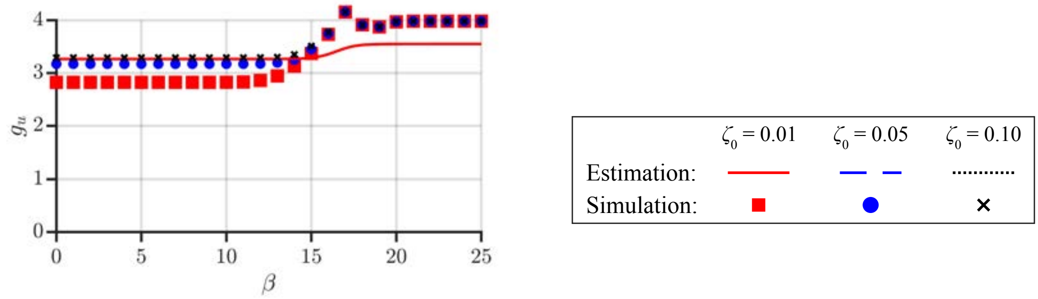

(c) T_0 = 5 s

Figure 5.29: Peak factor for control force: estimation vs. simulation (across-wind direction, aspect ratio: 5, terrain category: 3)

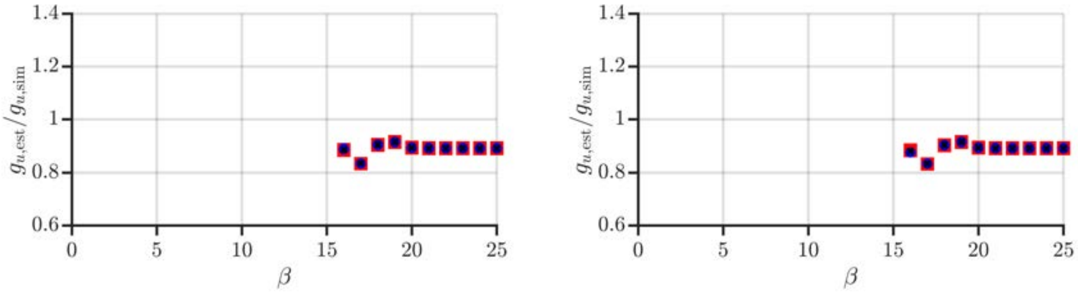

(a) T_0 = 3 s **(b)** T_0 = 4 s

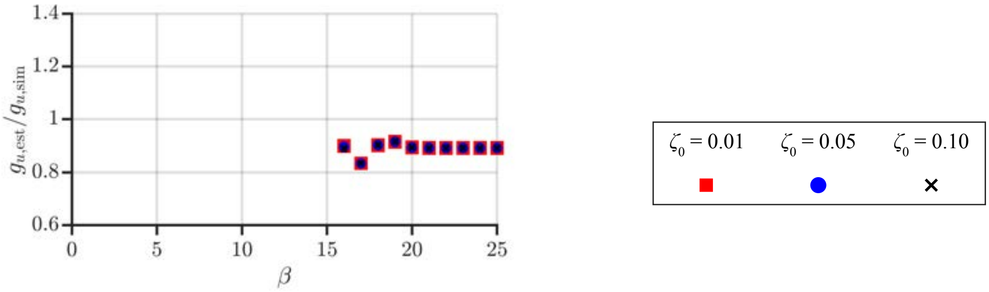

(c) T_0 = 5 s

Figure 5.30: Estimation error of peak factor for control force (across-wind direction, aspect ratio: 5, terrain category: 3)

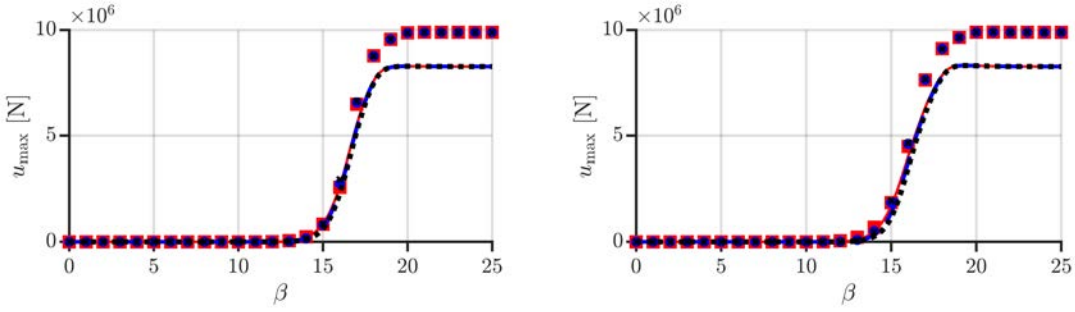

(a) T_0 = 3 s **(b)** T_0 = 4 s

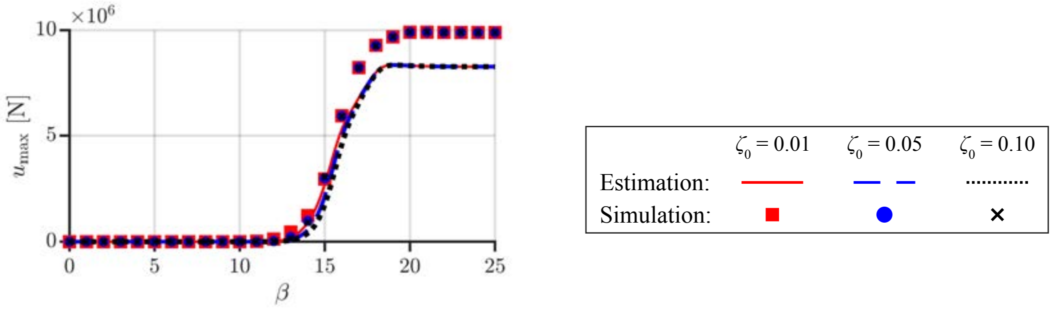

(c) T_0 = 5 s

Figure 5.31: Maximum control force: estimation vs. simulation (across-wind direction, aspect ratio: 5, terrain category: 3)

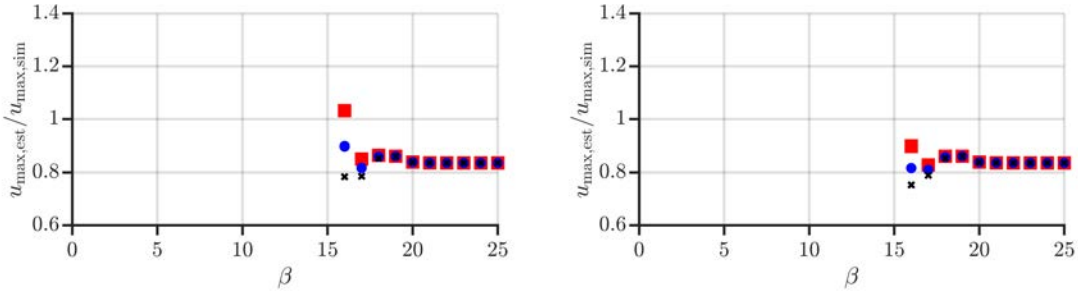

(a) T_0 = 3 s **(b)** T_0 = 4 s

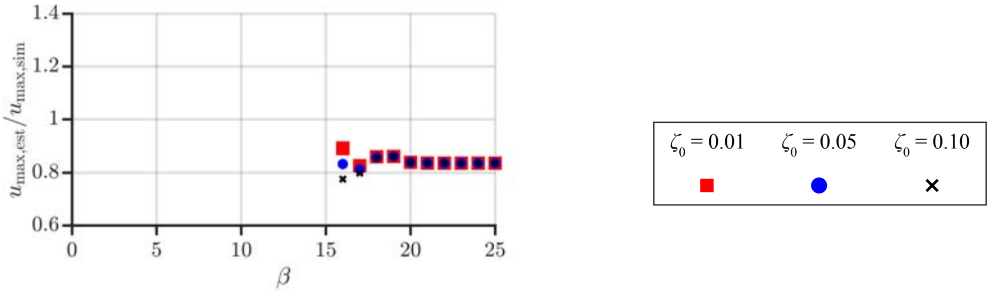

(c) T_0 = 5 s

Figure 5.32: Estimation error of maximum control force: estimation vs. simulation (across-wind direction, aspect ratio: 5, terrain category: 3)

Appendix 5B Analysis of peak values of numerical simulation of peak factor

This section explains the reason of that the simulation values of peak factor have peak values around $\beta = 17$, however, the estimation values do not have (see Figs. 5.5, 5.11, 5.23, and 5.29).

This chapter uses the peak factor presented by Japan design code (AIJ Recommendations for Loads on Buildings [5.1]) for estimation. The estimation equation is given below:

$$g_{D,\mathrm{eq,m1}} = \sqrt{2\ln(600 f_{\mathrm{eq,m1}}) + 1.2}, \qquad \text{(Re. 5.9)}$$

where $f_{\mathrm{eq,m1}}$ is the natural frequency of the 1st mode of the equivalent model.

From (5.9), we can know that the estimation values of the gust factor is only related to the 1st natural frequency (1st natural period) of the system. Fig. 5.33 shows the relationship of the natural period of the 1st mode of the control system, $T_{\mathrm{eq,m1}}$, and weighting entry, β. From Fig. 5.33, it can be seen that the 1st natural period of the control system, $T_{\mathrm{eq,m1}}$, converges to the 1st natural period of the superstructure (2s, see Table 4.1) as weighting entry, β, increases. This is because increasing the weighting entry, β, adds the equivalent stiffness to the isolation layer to suppress the displacement of isolation layer, resulting the isolation layer approximation as a rigid body. As the β-$T_{\mathrm{eq,m1}}$ relationship is a flat curve that does not have peak values, the estimation values of peak factor do not have peak values.

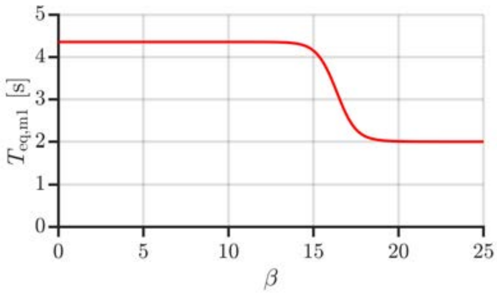

Figure 5.33: 1st natural period against weighting entry

However, the simulation results of gust factors are related to both natural period and damping ratio [5.1]. Figs. 5.34 and 5.35 show the dependency of gust factor on 1st natural period and 1st damping ratio of passive-controlled structures. From Figs. 5.34 and 5.35, the following results are obtained:

- The simulation results of peak factor decreases as 1st natural period increases.
- The simulation results of peak factor decreases as 1st damping ratio increases.

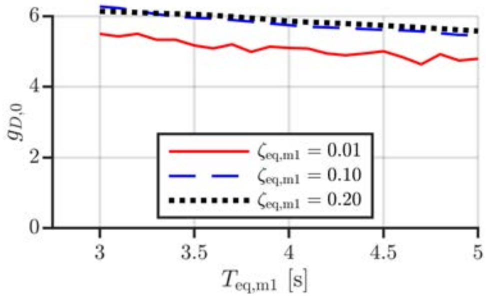

Figure 5.34: Dependency of gust factor on 1st natural period (passive structure)

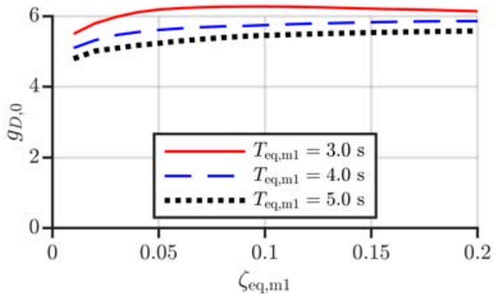

Figure 5.35: Dependency of gust factor on 1st damping ratio (passive structure)

Fig. 5.36 shows the relationship of the damping ratio of the 1st mode of the control system, $\zeta_{\mathrm{eq,m1}}$, and the weighting entry, β. From Fig. 5.36, it can be seen that the 1st damping ratio, $\zeta_{\mathrm{eq,m1}}$, of the control system has a peak value around $\beta = 17$. If $\beta < 17$, the 1st damping ratio, $\zeta_{\mathrm{eq,m1}}$ increases as the weighting entry, β, increases. This is because increasing the weighting entry, β, adds the equivalent damping coefficient to the isolation layer, resulting the 1st damping ratio, $\zeta_{\mathrm{eq,m1}}$, increasing. If $\beta > 17$, the 1st damping ratio, $\zeta_{\mathrm{eq,m1}}$ decreases as the weighting entry, β, increases, and finally converges to the 1st damping ratio of the superstructure (0.02, see Table 4.1). This is because the isolation layer converges to be a rigid body, thus, the 1st damping ratio converges to the 1st damping of the superstructure although the equivalent damping coefficient increases.

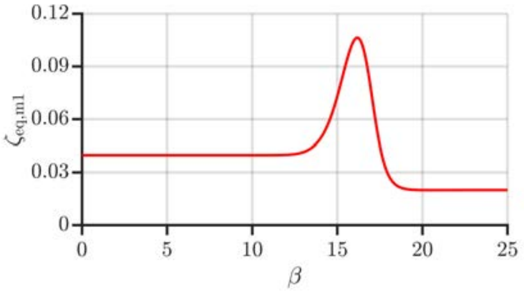

Figure 5.36: 1st damping ratio against weighting entry

Therefore, the simulation results of gust factors have a peak value around $\beta = 17$.

Note that this study uses the following weighting matrices, and selecting other sets of weighting matrices will have different results.

$$\mathbf{Q} = 10^{\beta}\text{diag.}\{\, \underset{x_0}{1}\,,\ \underset{x_1}{0}\,,\ \cdots\,,\ \underset{x_{10}}{0}\ \|\ \underset{\dot{x}_0}{0}\,,\ \cdots\,,\ \underset{\dot{x}_{10}}{0}\,\}, \tag{4.19a}$$

$$R = 1 \tag{4.19b}$$

References

[5.1] Architectural Institute of Japan, AIJ Recommendations for Loads on Buildings, Architectural Institute of Japan, 2015.

[5.2] Architectural Institute of Japan, Design Recommendations for Seismically Isolated Buildings, Architectural Institute of Japan, 2016.

[5.3] K. YOSHIE, H. KITAMURA, T. OKUMA, A. WADA, 20097 energy input of local wind forces for high-rise building based on wind tunnel test: Part.2 local wind force characteristics of rectangular high-rise buildings [in Japanese], in: Summaries of Technical Papers of Annual Meeting, Architectural Institute of Japan, 2005, pp. 233–234.

[5.4] H. HIRAI, K. YOSHIE, D. SATO, J. KATAGIRI, T. TSURUMI, H. KITAMURA, T. OHKUMA, Influence of number of experimental wind force samples on wind response analysis of a tall building [in Japanese], AIJ journal of technology and design 18 (39) (2012) 489–494. `doi:10.3130/aijt.18.489`.

[5.5] G. Saito, D. Sato, K. Yoshie, T. Ohkuma, J. Katagiri, H. Kitamura, Influence of number of wind-force samples on response of high-rise base-isolated building using elastoplastic model [in Japanese], AIJ Journal of Technology and Design 23 (2017) 65–70. `doi:10.3130/aijt.23.65`.

CHAPTER 6

Switch of feedback gain

6.1 Introduction

This study uses separated design approaches for earthquake-resistant design and wind-resistant design, respectively. In earthquake-resistant design, the design method prefer to construct a softer system than the non-control system to avoid the dominant natural period of earthquake disturbance. On the other hand, wind-resistant design prefer to add equivalent stiffness to the isolation layer to suppress the displacement of isolation layer. Therefore, the responses and control force of the system designed by earthquake-resistant design may increases subjected wind disturbance, and responses and control force of the system designed by wind-resistant design also may increases subjected earthquake disturbance To solve this problem, this study uses a switch-type controller to change the feedback gain for earthquake-resistant design and wind-resistant design. Because of predictability of typhoon events, this study considers to keep earthquake-resistant pattern as usual and switch to wind-resistant pattern when a typhoon is predicted to occur.

This Chapter shows the switch-type of the control system. Moreover, the responses and control force of the control system subjected to a disturbance that is different from the disturbance considered at design.

6.2 Responses and control force of control system with wind controller subjected to earthquake disturbance

Figure 6.1 shows the block diagram of the switch-type control system used in this study.

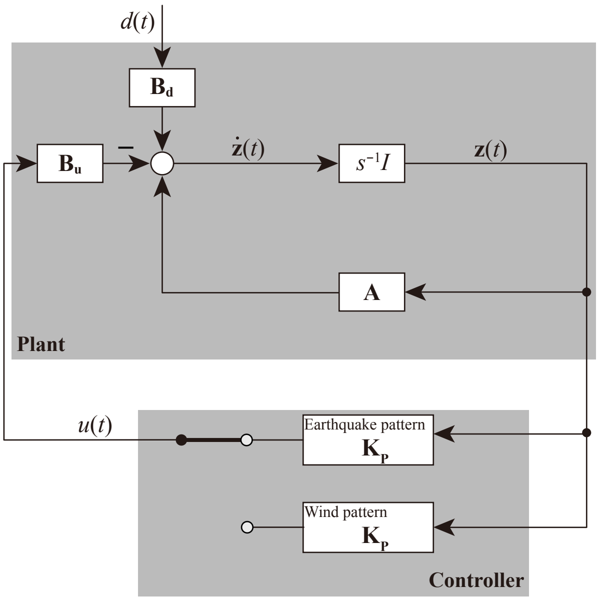

Figure 6.1: Block diagram: switch of feedback gain

The state equation of the control system is given below:

$$\dot{\mathbf{z}}(t) = \mathbf{A}\mathbf{z}(t) + \mathbf{B_d}d(t) - \mathbf{B_u}u(t), \tag{6.1}$$

where $d(t)$ is the disturbance (wind or earthquake) and $\mathbf{B_d}$ is the input matrix for $d(t)$. The definition of $d(t)$ and $\mathbf{B_d}$ for earthquake-resistant design and wind-resistant design are given below:

Earthquake-resistant design

$$d(t) = \ddot{x}_g(t) \text{ and} \tag{6.2a}$$

$$\mathbf{B_d} = \mathbf{B_g} = \begin{bmatrix} \mathbf{0} \\ \mathbf{-1} \end{bmatrix} \tag{6.2b}$$

Earthquake-resistant design

$$d(t) = \mathbf{F}(t) \text{ and} \tag{6.3a}$$

$$\mathbf{B_d} = \mathbf{B_F} = \mathbf{M}^{-1}\mathbf{E_F} = \mathbf{M}^{-1}\mathbf{I} \tag{6.3b}$$

From Fig. 6.1, the control system can switch from earthquake pattern to wind pattern when a typhoon is predicted to occur.

6.3 Responses and control force of control system with earthquake controller subjected to earthquake disturbance

The block diagram of the control systems used in this section is shown at Fig. 6.2.

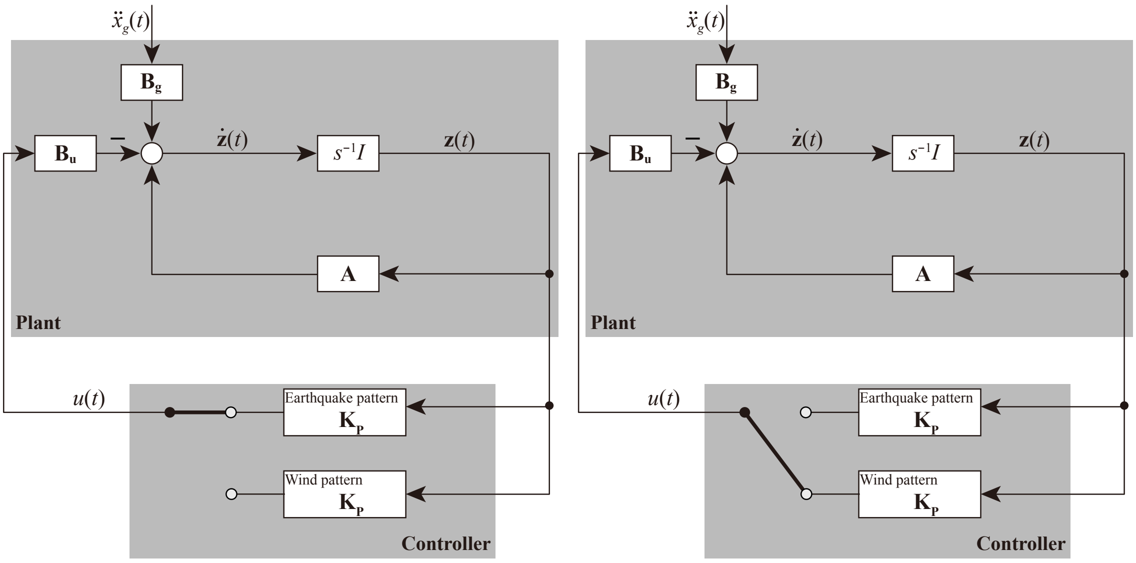

(a) Earthquake controller **(b)** Wind controller

Figure 6.2: Block diagram of control system with earthquake controller and wind controller

Figs. 6.3~6.6 show the comparison of responses (displacement, velocity, and absolute acceleration) of control systems subjected to earthquake waves between non-control system, earthquake controller, and wind controller. Fig. 6.7 show the comparison of control force of control systems subjected to earthquake waves between earthquake controller and wind controller. From Figs. 6.3~6.7, the following results are obtained:

- Compared to the pattern of without control, the all responses (displacement, velocity, and absolute acceleration) of the control system are suppressed by earthquake controller.

- Compared to the pattern of without control, the displacement and velocity responses of the isolation layer are suppressed by wind controller. However, the responses of the upper stories with wind controller is larger than that non-control system.

- The absolute acceleration responses of the system with wind controller are significantly compared to non-control system.

- The required control force of wind controller is significantly larger than that of earthquake controller.

Therefore, the control performance of the control system with a wind controller is even much inferior to an non-control system.

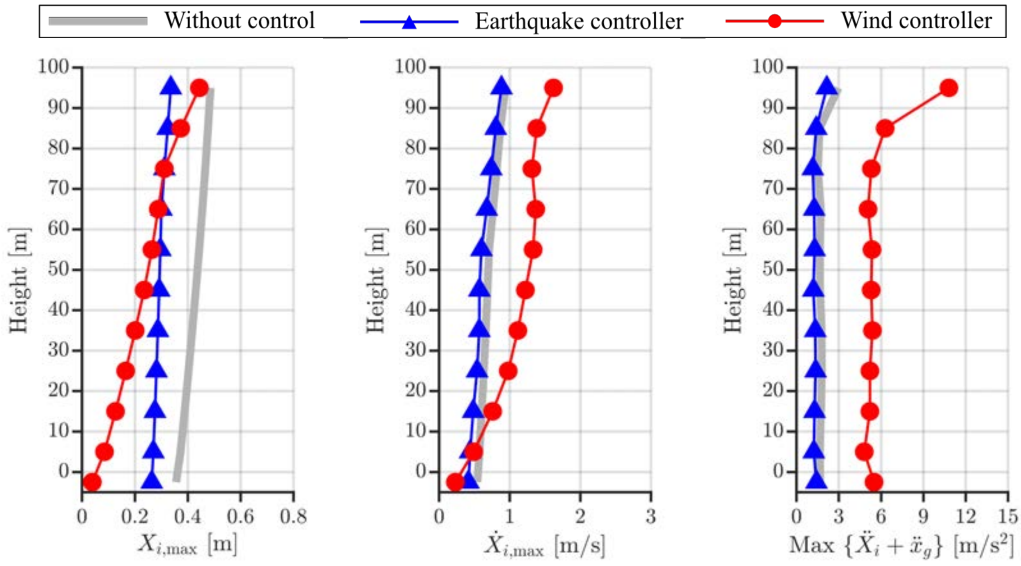

(a) Displacement **(b)** Velocity **(c)** Abs. acceleration

Figure 6.3: Responses subjected to Taft NS: without control vs. earthquake controller vs. wind controller

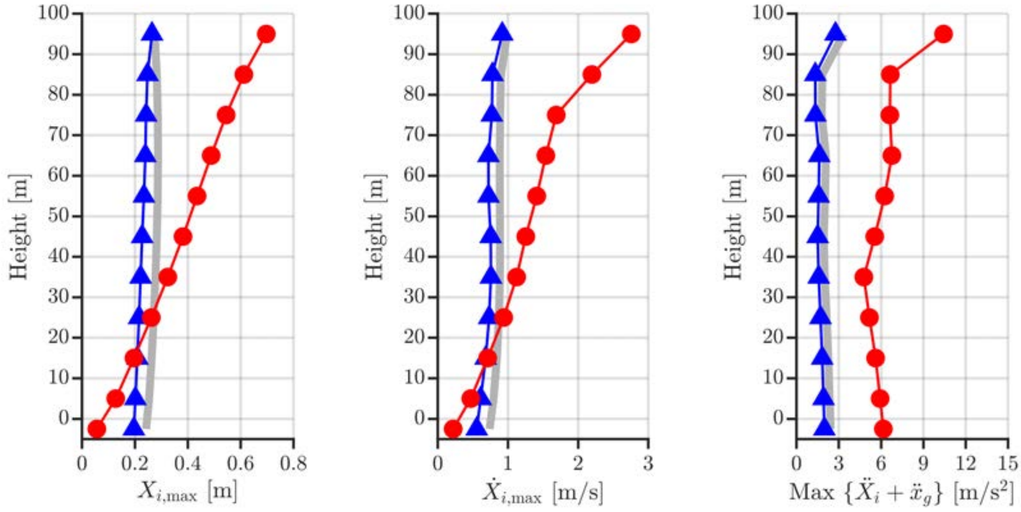

(a) Displacement **(b)** Velocity **(c)** Abs. acceleration

Figure 6.4: Responses subjected to El Centro 1940 NS: without control vs. earthquake controller vs. wind controller

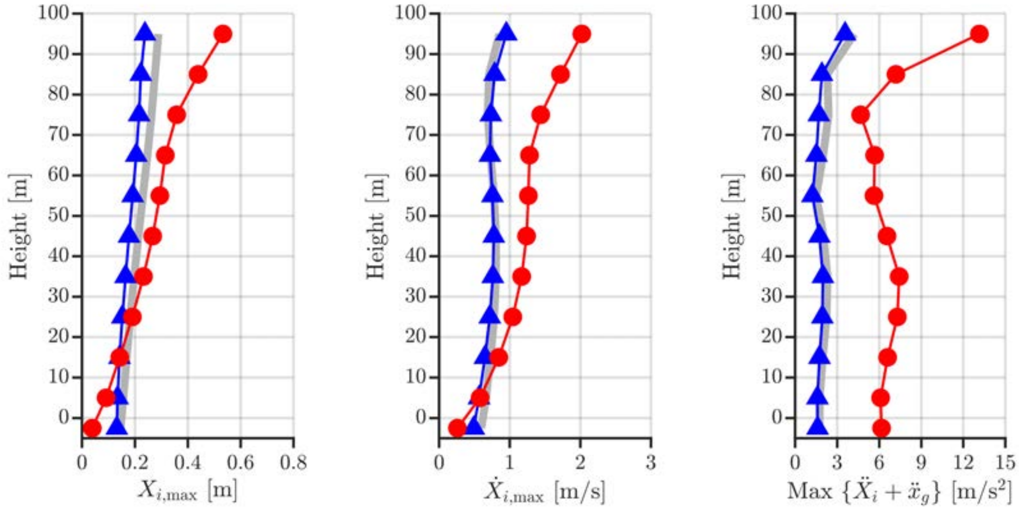

(a) Displacement **(b)** Velocity **(c)** Abs. acceleration

Figure 6.5: Responses subjected to JMA Kobe NS: without control vs. earthquake controller vs. wind controller

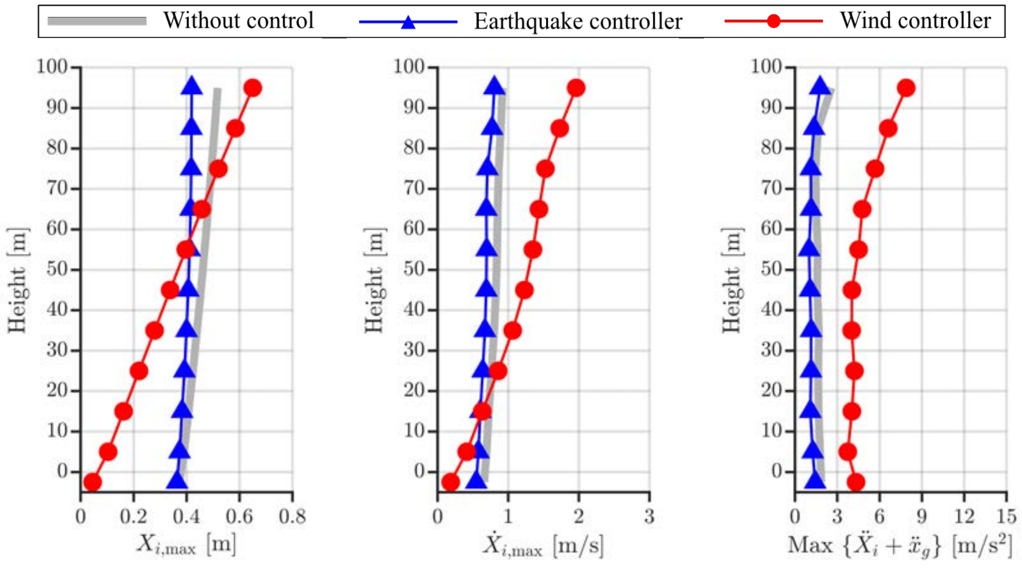

(**a**) Displacement (**b**) Velocity (**c**) Abs. acceleration

Figure 6.6: Responses subjected to Code Hachinohe: without control vs. earthquake controller vs. wind controller

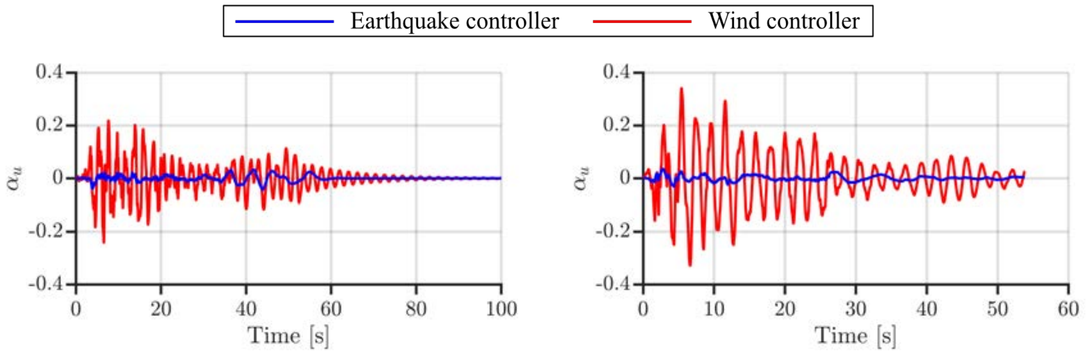

(**a**) Taft NS (**b**) El Centro 1940 NS

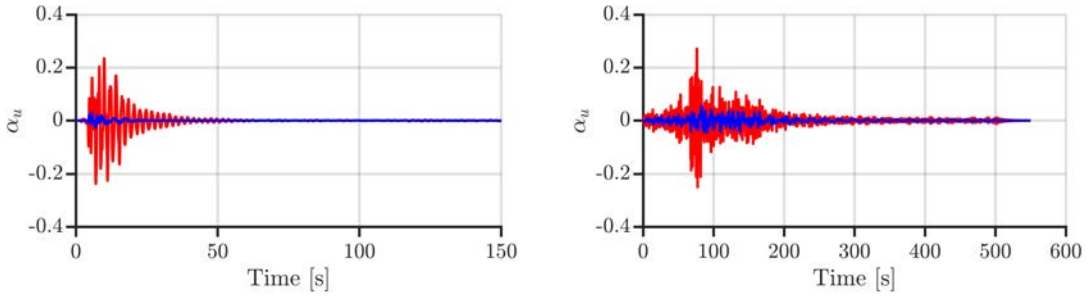

(**c**) JMA Kobe NS (**d**) Code Hachinohe

Figure 6.7: Control force subjected to earthquake: earthquake controller vs. wind controller

6.4 Responses and control force of control system with earthquake controller subjected to wind disturbance

The block diagram of the control systems used in this section is shown at Fig. 6.8.

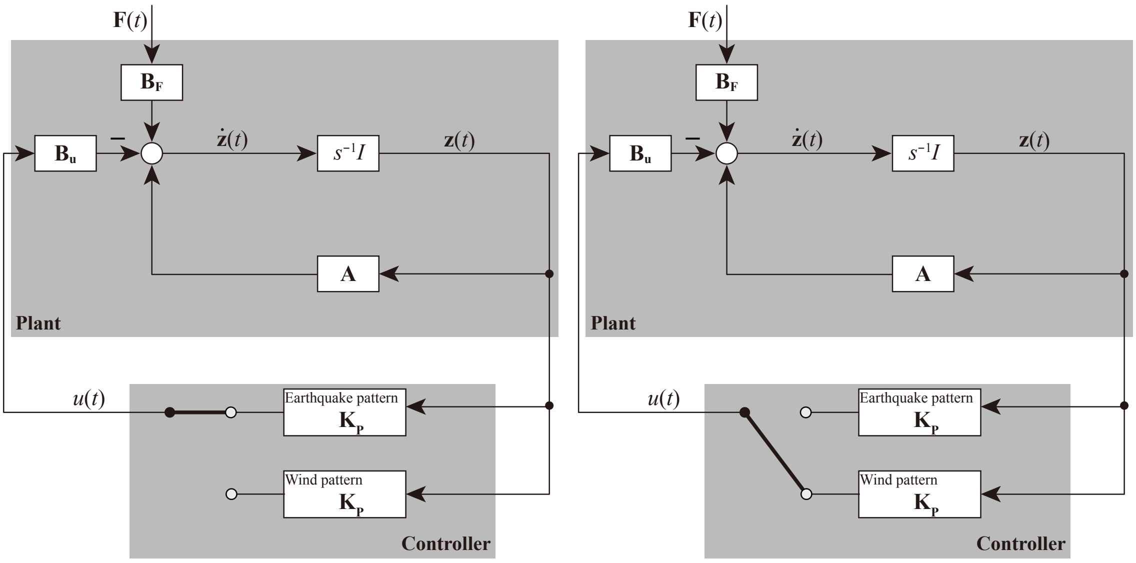

(a) Earthquake controller **(b)** Wind controller

Figure 6.8: Block diagram of control system with earthquake controller and wind controller

Figs. 6.9~6.10 show the comparison of responses (displacement, velocity, and absolute acceleration) of control systems subjected to wind force between non-control system, earthquake controller, and wind controller. Fig. 6.11 show the comparison of control force of control systems subjected to wind force between between non-control system, earthquake controller, and wind controller. From Figs. 6.3~6.7, the following results are obtained:

- Compared to the non-control system, the velocity and acceleration responses of the control system using earthquake controller are suppressed, but, the displacement responses enlarges.
- Compared to the non-control system, the displacement response of the control system using wind controller are suppressed, but, the acceleration responses enlarges.
- The required control force of earthquake controller and wind controller are almost the same.

Because the displacement response subjected to wind force is sensitive for a building, the control performance of the control system with a earthquake controller is even inferior to an non-control system.

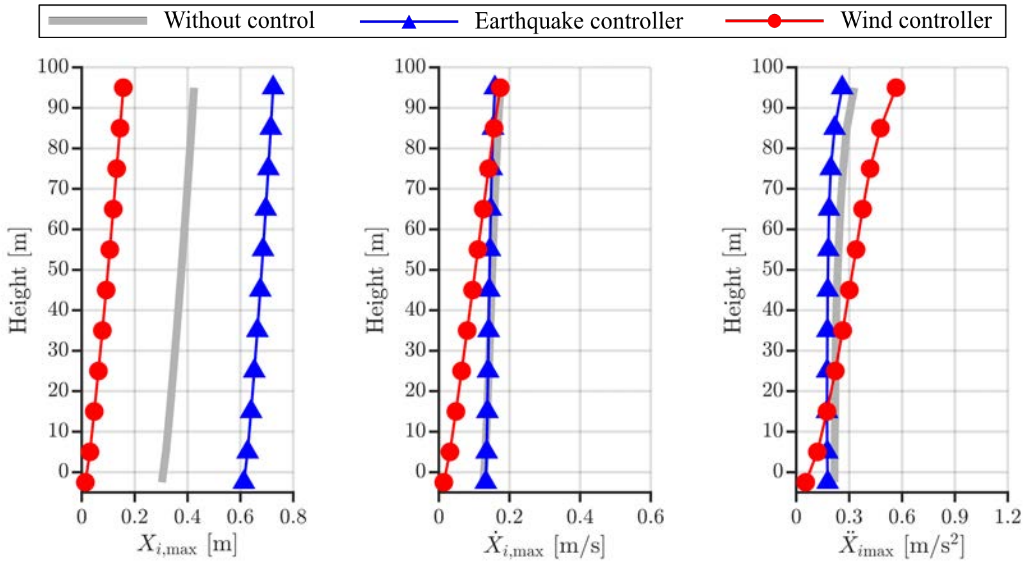

(a) Displacement **(b)** Velocity **(c)** Abs. acceleration

Figure 6.9: Responses subjected to along-wind force: without control vs. earthquake controller vs. wind controller

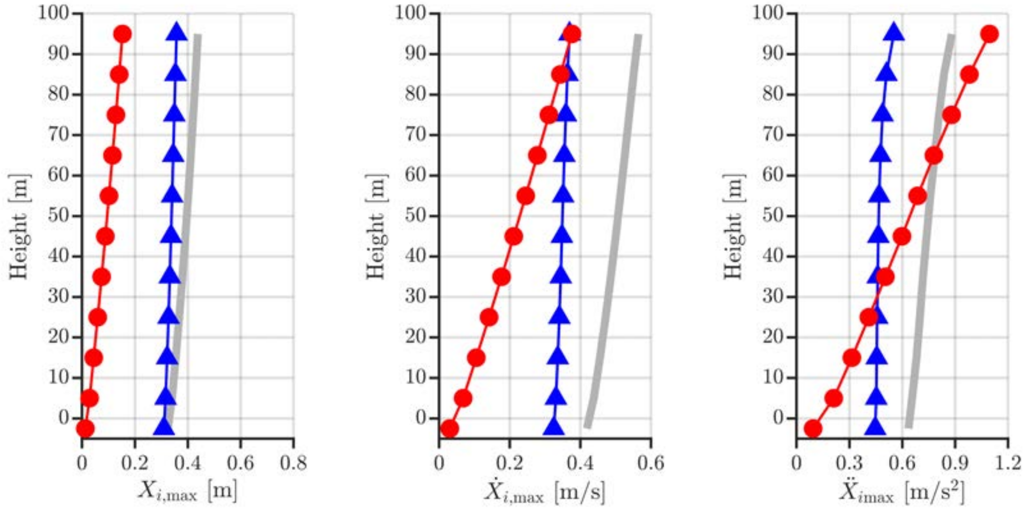

(a) Displacement **(b)** Velocity **(c)** Abs. acceleration

Figure 6.10: Responses subjected to along-wind force: without control vs. earthquake controller vs. wind controller

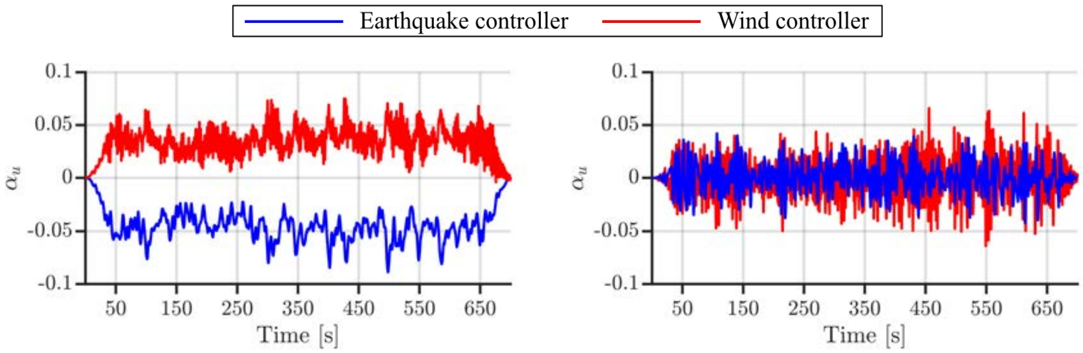

(a) Taft NS **(b)** El Centro 1940 NS

Figure 6.11: Control force subjected to wind force: earthquake controller vs. wind controller

6.5 Conclusion

This chapter showed the switch-type of the control system. Moreover, the responses and control force of the control system subjected to a disturbance that is different from the disturbance considered at design. From simulation results, the following results are obtained:

- Compared to the pattern of without control, the all responses (displacement, velocity, and absolute acceleration) of the control system are suppressed by earthquake controller.
- Compared to the pattern of without control, the displacement and velocity responses of the isolation layer are suppressed by wind controller. However, the responses of the upper stories with wind controller is larger than that non-control system.
- The absolute acceleration responses of the system with wind controller are significantly compared to non-control system.
- The required control force of wind controller is significantly larger than that of earthquake controller.
- Compared to the non-control system, the velocity and acceleration responses of the control system using earthquake controller are suppressed, but, the displacement responses enlarges.
- Compared to the non-control system, the displacement response of the control system using wind controller are suppressed, but, the acceleration responses enlarges.
- The required control force of earthquake controller and wind controller are almost the same.

Therefore, the control performance of a control system subjected to a disturbance that is different from the disturbance considered at design will become worse than an non-control system.

CHAPTER 7
Conclusion

7.1 Contributions of this study

This study presented simple design methods for high-rise base-isolated buildings with active control subjected to earthquake and wind disturbance, respectively. The equivalent model of an active control system was constructed to theoretically express the dependency of the maximum responses and maximum control force on the design parameters of both passive structure and controller. This study extended the conventional passive design methods for earthquake-resistant design and wind-resistant design to active-controlled system.

For earthquake-resistant design, the devised design method simplifies the conventional design procedure by the following points:

(1) The maximum responses (displacement, velocity and absolute acceleration) are estimated by response spectra, which was wildly used in conventional passive earthquake-resistant design, using the equivalent model of control system.

(2) This study proposed a new spectrum, control-force spectrum, for estimating the maximum control force. This study the control-force spectrum only using the response spectra eliminating the requirement of carrying numerical simulations.

(3) This study devised a formula for determining the feedback gain that achieves the target dynamic characteristics without trial-and-error approaches.

(4) This study presented a equivalent linearization method to replace the nonlinear hysteretic dampers with a linear spring and linear dash-pot considering the combination of base-isolation and active control.

(5) This study developed a design method for determining the design parameters for both passive structure and controller that satisfies design limitations on maximum responses and maximum control force requiring no trial-and-error approaches and numerical simulations.

This study also used numerical examples and design examples to validate the effectiveness of the proposed estimation methods and design methods.

For wind-resistant design, the devised design method simplifies the conventional design procedure by the following points:

(1) This study presented the estimation equation for mean displacement and mean control force of active control systems using the static balance of the equivalent model (along-wind direction).

(2) This study extended the gust factor for displacement to active control systems using the dynamic characteristics of the equivalent model that estimates the maximum displacement without numerical simulations (along-wind direction).

(3) This study devised a new gust factor, gust factor for control force, of active control systems using the equivalent model that estimates the maximum control force without numerical simulations (along-wind direction).

(4) This study shown the estimation equation for standard deviation of displacement and control force of active control systems using the equivalent model (across-wind direction).

(5) This study extended the peak factor for displacement to active control systems using the dynamic characteristics of the equivalent model that estimates the maximum displacement without numerical simulations (across-wind direction).

(6) This study devised a new peak factor, peak factor for control force, of active control systems using the equivalent model that estimates the maximum control force without numerical simulations (across-wind direction).

(7) This study developed design methods for determining the design parameters for both passive structure and controller that satisfies design limitations on maximum responses

and maximum control force requiring no trial-and-error approaches and numerical simulations (both along-wind and across-wind directions).

This study also used numerical examples and design examples to validate the effectiveness of the proposed estimation methods and design methods.

Furthermore, chapter 6 showed the the switch-type control system to change the feedback gain to control the earthquake-induced vibration and wind-induced vibration, respectively. Chapter 6 also showed the responses and control force of the control system subjected to a disturbance that is different from the disturbance considered at design. From the simulation examples, it can be seen that the control performance of a control system subjected to a disturbance that is different from the disturbance considered at design will become worse than an non-control system. Thus, it illustrates the importance of the switch timing.

7.2 Future works

Recommendations for future works are given following:

- This paper assumed that the displacement and velocity can be directly. If theses responses can not be observed by sensors, the control system should use a state observer to estimate all responses. The design method for state observer also need be considered.

- Chapter 5 only uses real modal analysis to estimate the response and control force of the 1st mode. As the the model of Chapter 5 uses non-proportional damping, the complex-modal analysis should be considered.

- Chapters 4 and 5 used a shear-model only considering 1-direction wind force. However, a practical structure is simultaneously subjected to 3-direction wind force (along-wind, across-wind, and torsion). The responses of a model that simultaneously subjected to 3-direction wind force also should be checked by numerical simulation.

- The method proposed at Chapters 4 and 5 limited to linear models. the estimation method for nonlinear models also need be considered.